New Avenues in Atmospheric Modelling of Exoplanets

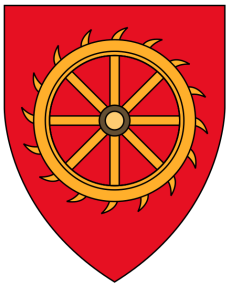

Siddharth Gandhi

Supervisor: Dr. Nikku Madhusudhan

Institute of Astronomy
University of Cambridge

This dissertation is submitted for the degree of
Doctor of Philosophy

St Catharine's College

May 2019

Declaration

This thesis is the result of my own work and includes nothing which is the outcome of work done in collaboration except as declared in the Preface and specified in the text. It is not substantially the same as any that I have submitted, or, is being concurrently submitted for a degree or diploma or other qualification at the University of Cambridge or any other University or similar institution except as declared in the Preface and specified in the text. I further state that no substantial part of my thesis has already been submitted, or, is being concurrently submitted for any such degree, diploma or other qualification at the University of Cambridge or any other University or similar institution except as declared in the Preface and specified in the text. It does not exceed the prescribed word limit for the relevant Degree Committee.

Siddharth Gandhi
May 2019

New Avenues in Atmospheric Modelling of Exoplanets

Siddharth Nandkumar Gandhi

In this thesis I explore various aspects of atmospheric characterisation of exoplanets with the primary goal of understanding their chemical compositions and physical processes. My research led to the development of new self-consistent models of exoplanetary atmospheres, a new paradigm for atmospheric retrievals of thermal emission spectra, as well as chemical detections using both high-resolution Doppler spectroscopy as well as low-resolution transit spectroscopy.

I firstly computed the molecular and atomic cross sections of various species prevalent in the atmospheres of such exoplanets in order to compute their spectra. The absorption cross sections were calculated through the broadening of spectral lines obtained from high resolution line lists. These cross sections and subsequent spectral models have led to the detections of numerous chemical species (HCN, TiO, Li, Na, K, CO, and H_2O) in the atmospheres of several exoplanets.

Recent advances in observations have heralded the need for accurate models of exoplanetary atmospheres. I have built a new self-consistent atmospheric model, GENESIS, custom built for exoplanets and demonstrated for irradiated and non-irradiated atmospheres over a wide range of atmospheric parameter space. The model treats line-by-line radiative transfer through the Feautrier method and radiative-convective equilibrium through the Rybicki Complete Linearisation method in a plane parallel atmosphere. This model allows for a detailed exploration of radiative processes and chemical compositions and their effects on observed emission spectra. I compared this model against several others in the literature and found good agreement between the atmospheric properties and emission spectra.

Thermal inversions have been seen on the dayside atmospheres of some hot Jupiters and have been predicted to be caused by TiO or VO due to their visible opacity. I used the GENESIS model to investigate the effect of visible opacity and deduced that many new species (AlO, CaO, NaH and MgH), hitherto unexplored, are also capable of

causing thermal inversions on hot Jupiters. I have explored the effect of these species as a function of their overall atmospheric abundance as well as determining the required abundance for each of these species to form an inversion. Secondly, I show that a low infrared opacity caused by a low H_2O abundance can also lead to strong thermal inversions even with sub-solar abundances of these visible absorbers due to the change in infrared opacity. As a demonstration of this work I have shown that the thermal inversion on WASP-121b can be explained by all the visible absorbers listed above. These thermal inversions are of great importance as the species responsible may be observed with current observational capabilities, thus providing testable observations for these species.

I have also developed a new hybrid retrieval method for exoplanetary emission spectra, HyDRA. This uses the latest atmospheric modelling tools to fit the observed spectra of exoplanet atmospheres. We explore a wide range of parameter space and determine the temperature profile and abundances of various species present in the dayside atmosphere through the emission spectra. These retrieved abundances are then used to explore disequilibrium processes which may be present through integration into the GENESIS self-consistent model. Such a framework allows constraints on departures of the temperature structures from radiative-convective equilibrium as well as chemical compositions from thermochemical equilibrium. I explored HST and Spitzer observations of WASP-43b and confirmed the data were in agreement with radiative-convective equilibrium in the dayside atmosphere.

The HyDRA retrieval framework has also been extended to model the atmospheres of ultra-hot Jupiters with temperatures in excess of 2500 K. Such high temperatures can cause molecular species such as H_2O to thermally dissociate and for ionic species such as H- to form. Such effects have been used to explain the largely featureless WFC3 spectra seen for many ultra-hot Jupiters. I have included both of these effects into the HyDRA retrieval model to retrieve the atmosphere of the planet WASP-18b. I find that the retrieved abundances for H_2O and CO and the thermal inversion in the atmosphere do not change significantly compared to previous retrievals of WASP-18b which did not include thermal dissociation or H- opacity. I also see no significant evidence for H- or thermal dissociation in the atmosphere. With future instrumentation we may be more likely to constrain such effects in the emission spectra.

I have also used the HyDRA retrieval framework to perform a set of homogeneous retrievals for eight well known hot Jupiters with high precision HST WFC3 spectra. These planets all also have Spitzer observations which I also use to explore the atmospheric temperature profile and chemical composition, in particular explore the H_2O

abundance. The eight explored planets span a wide range of equilibrium temperatures, including four which fall into the category of ultra-hot Jupiters. We find that the coolest planets in the study generally have better constrained H_2O abundances near solar composition due to strong H_2O absorption features. On the other hand, three of the hottest exoplanets exhibit thermal inversions and indicate very poorly constrained or sub-solar H_2O abundances. This study shows that even currently explored exoplanets exhibit a wide range of atmospheric properties and that we will be able to explore this diversity further with more exoplanetary spectra coming up in the next few years.

Finally, I have used the GENESIS model to enable chemical detections of molecular species using high resolution Doppler spectroscopy of hot Jupiters. I generated high resolution emission spectra of the hot Jupiters HD189733b and HD209458b for cross correlation with the data obtained with the VLT CRIRES spectrograph. This helped us find evidence for H_2O, CO and HCN in the atmosphere of both planets. In the future this method has great potential for new chemical detections due to its sensitivity to trace species and shows great promise in the detection of biosignatures on smaller rocky planets.

Acknowledgements

I would firstly like to thank my supervisor Nikku Madhusudhan for putting up with me for four years and passing on some of his infinite wisdom and humour. I would also like to acknowledge all of my collaborators, who have helped me immeasurably throughout this work. In particular, Avi Mandell and Kyle Sheppard have provided the observational data and expertise for the retrievals of WASP-18b and WASP-19b. I would also like to thank Ivan Hubeny for numerous fruitful discussions and expertise on self-consistent modelling. I would also like to thank all of the people within the exoplanet group within Cambridge at the IoA, Luis Welbanks, Anjali Piette, Ryan MacDonald and Arazi Pinhas, for discussions and expertise on various topics related to atmospheric modelling. In particular I'd like to thank George Hawker and Sam Cabot, who developed the high resolution data analysis pipeline over both of the VLT CRIRES spectral ranges. I'd also like to thank Adam Jermyn for teaching me the joys and pitfalls of atmospheric modelling with Python and C++ respectively throughout my time at the IoA.

I'd also like to thank the many people for keeping me distracted from my work throughout my time at the IoA. The numerous games and chat provided by my office-mates, Aneesh Naik, Cameron Lemon and Andrew Winter, certainly kept me sane when work was mounting, and I'd particularly like to thank Holly Preece for providing my fix of rowing chat when I was away from the river. Luis Welbanks also helped me to catch 'em all in Pokemon Go over the years. I'd also like to thank all of the folks that I played cricket with in the summer afternoons for making sure that when work was failing I could at least release my frustrations on a ball. The Netflix, games and other shenanigans provided by my housemates, Dave Baker, Lizzie Pearmain, Simon Matthews and Anthony Shillito also helped with making sure I didn't get too much work done when I returned home in the evenings. I'd also like to thank the many rowers I have coxed over the years for making sure that I didn't get stressed about work by making me stressed about bumps and other races. Finally, thanks for the support of Thomasina Ball who made sure that I stayed together throughout the final year when finishing my PhD.

Table of contents

List of figures **xvii**

List of tables **xxxiii**

1 Introduction **1**
1.1 Exoplanet Diversity . . . 1
1.2 Detection Methods . . . 2
1.3 Detecting the Atmospheres of Exoplanets . . . 3
1.3.1 Transit Spectroscopy . . . 3
1.3.2 High Resolution Spectroscopy . . . 8
1.3.3 Direct Imaging . . . 9
1.4 Atmospheric and Formation Processes . . . 10
1.5 Atmospheric Modelling of Exoplanets . . . 12
1.6 Scope of this Thesis . . . 14
1.6.1 Atmospheric Opacities . . . 14
1.6.2 Self-Consistent Atmospheric Models: GENESIS . . . 15
1.6.3 Retrievals of Emission Spectra: HyDRA . . . 16
1.6.4 High Resolution Spectroscopy . . . 17
1.6.5 Conclusions . . . 18

2 Sources of Opacity in Hot Giant Exoplanets **19**
2.1 Introduction . . . 19
2.2 Cross Section Calculations . . . 21
2.2.1 Infrared Opacity . . . 24
2.2.2 Visible opacity . . . 25
2.2.3 High Resolution Cross Sections . . . 26
2.3 H- opacity . . . 27
2.4 Collisionally Induced Absorption . . . 29

2.5 Rayleigh Scattering due to Molecular Hydrogen 30

3 GENESIS: Self-Consistent Models of Exoplanetary Spectra 31
3.1 Previous Work on Self-Consistent Modelling 31
3.2 The GENESIS Model 33
3.3 Methods 35
3.3.1 Basic Equations 37
3.3.2 Overview of the Methods 38
3.3.3 Radiative Transfer 40
3.3.4 Radiative-Convective Equilibrium 42
3.3.5 Chemical Composition 48
3.3.6 Opacities 51
3.3.7 Stellar Flux 52
3.3.8 Model Validation 53
3.4 Results 56
3.4.1 Irradiated Atmospheres 58
3.4.2 Models of Known Irradiated Planets - Effect of System Properties 65
3.4.3 Non-irradiated Atmospheres 66
3.5 Summary and Discussion 71

4 New Avenues for Thermal Inversions in hot Jupiters 75
4.1 Introduction to Thermal Inversions 75
4.2 Theory of Thermal Inversions 81
4.2.1 Signatures of Thermal Inversions in Emission Spectra 81
4.2.2 Analytic Model 82
4.2.3 Self-Consistent Models 84
4.3 Effect of Visible Opacity on Inversions 88
4.3.1 Other Sources of Visible Opacity 89
4.3.2 Effects on Equilibrium Profile 89
4.3.3 Inversions on Very Hot Planets 91
4.3.4 Inversions on Cooler Planets 92
4.4 Effect of Infrared Opacity 93
4.4.1 Chemical Equilibrium of Volatile Species 93
4.4.2 Thermal Inversions with Super-Solar C/O Ratio 94
4.5 Case Study: Hot Jupiter WASP-121b 96
4.6 Discussion and Conclusion 97

5 Retrieval of Exoplanet Emission Spectra with HyDRA 107
5.1 Background . . . 107
5.2 Methods . . . 109
5.2.1 Geometry . . . 111
5.2.2 Model Parameters . . . 113
5.2.3 Opacities . . . 115
5.2.4 Radiative Transfer . . . 117
5.2.5 Stellar Spectrum . . . 119
5.2.6 Generating Model Data . . . 120
5.2.7 Parameter Estimation and Statistical Inference . . . 121
5.2.8 Constraints on Disequilibrium . . . 123
5.3 Retrievals with Simulated Data . . . 125
5.3.1 Retrieved Abundances . . . 128
5.3.2 Retrieved $P-T$ Profile . . . 130
5.3.3 Radiative-Convective Disequilibrium . . . 131
5.3.4 Chemical Disequilibrium . . . 131
5.4 Results . . . 134
5.4.1 Constraints on Chemical Abundances . . . 134
5.4.2 Retrieved $P-T$ Profile . . . 137
5.4.3 Radiative-Convective Disequilibrium . . . 138
5.4.4 Chemical Disequilibrium . . . 140
5.5 Discussion and Summary . . . 140

6 On the effect of H- in Ultra-hot Jupiters 145
6.1 Introduction . . . 145
6.2 Methods . . . 147
6.2.1 Thermal dissociation . . . 148
6.2.2 H- opacity . . . 149
6.2.3 Data and Retrieval Setup . . . 150
6.3 Results . . . 150
6.3.1 H_2O abundances . . . 152
6.3.2 H- abundances . . . 155
6.3.3 CO abundances . . . 155
6.3.4 $P-T$ Profile . . . 157
6.3.5 Constraints on other species . . . 158
6.4 Discussion and Conclusion . . . 159

7 Homogeneous Retrievals of Exoplanets 163
7.1 Introduction . . . 163
7.2 Methods . . . 164
7.2.1 $P-T$ Profile . . . 165
7.2.2 Molecular Mixing Ratios . . . 165
7.2.3 Radiative Transfer . . . 166
7.2.4 Target Sample . . . 167
7.3 WASP-19b WFC3 Data Analysis . . . 168
7.4 Results . . . 172
7.4.1 Spectral Fits . . . 177
7.4.2 Molecular Abundance Inferences . . . 177
7.4.3 $P-T$ Profile . . . 182
7.5 Discussion and Conclusions . . . 185
7.5.1 Retrieved Abundances . . . 186
7.5.2 Retrieved $P-T$ Profile . . . 188
7.5.3 Mass-Metallicity Relation . . . 189

8 Detecting Species in Hot Jupiters with High Resolution Spectroscopy 191
8.1 Introduction . . . 191
8.2 Observations and Reduction . . . 193
8.2.1 Detrending . . . 194
8.3 Spectral Modelling . . . 195
8.4 Results . . . 200
8.4.1 HD209458b . . . 201
8.4.2 HD189733b . . . 202
8.4.3 Robustness of HRS Detections . . . 203
8.5 Discussion and Conclusion . . . 204

9 Conclusions 209
9.1 Molecular Opacity . . . 209
9.2 Self-Consistent Modelling . . . 210
9.2.1 GENESIS . . . 210
9.2.2 New Avenues for Thermal Inversions . . . 211
9.2.3 Future Directions . . . 211
9.3 Retrievals . . . 213
9.3.1 HyDRA . . . 213
9.3.2 High Temperature Retrievals . . . 214

9.3.3 Future Directions 214
9.4 High Resolution Spectroscopy 215
9.4.1 Future Directions 216
9.5 Landscape of Atmospheric Characterisation 216

References **219**

Appendix A Computational Methods for Self-consistent Atmospheric Modelling **235**
A.1 Solving the Transfer Equation 235
A.2 Complete Linearisation 236

List of figures

1.1 Planetary mass as a function of semi-major axis for the currently known exoplanets, with the colour of each point indicating the planetary radius (where known). The data was obtained from exoplanets.org. 2
1.2 Schematic of a transiting exoplanet. A primary eclipse or transit occurs when the planet passes in front of the star as seen by the observer. On the other hand, a secondary eclipse occurs as the planet passes behind the host star in its orbit. Atmospheric observations can be carried out under transmission at primary eclipse or just prior to secondary eclipse, where we observe emission emanating from the dayside of the planet. Figure by S. Seager (Seager and Deming, 2010). 4
1.3 Molecular absorption cross sections for the prominent volatile molecules in giant planetary atmospheres. Cross sections are shown for representative hot Jupiter conditions of T =1000 K and P =1 bar. 5
1.4 Planet/star flux ratios for some of the most prominent hot Jupiters obtained using the HST WFC3 spectrograph. The black points indicate the data and their associated error, while the blue curves indicate fits to the observations. The solid blue line denotes the best fit spectrum and the dark and light shaded contours show the 1 and 2σ spectral fits respectively (see chapter 7). Sources of data: Kreidberg *et al.* (2014) for WASP-43b, Line *et al.* (2016) for HD209458b, Evans *et al.* (2017) for WASP-121b and Sheppard *et al.* (2017) for WASP-18b. 7
1.5 Detection of CO in the non-transiting planet τ Boötis b using VLT observations. The white cross-hairs denote the peak in the significance, while the black plus indicates the expected planetary and systemic velocity from Brogi *et al.* (2012). Figure obtained from Cabot *et al.* (2019). 8

1.6 The various processes which occur within the atmospheres of extra-solar giant planets. The left hand side shows the temperature as a function of pressure for various profiles, with and without thermal inversions. The dashed curve shows the atmospheric temperature profile for a brown dwarf/non-irradiated planet. The right hand side shows the wavelengths that each region of the spectrum probes, along with the various chemical species and physical processes which occur at such depths within the atmosphere. Figure obtained from Madhusudhan (2019). 11

2.1 Molecular cross sections of chemical species with strong absorption cross sections in the visible. The cross sections were calculated at representative conditions of 0.1 bar pressure and 2000 K. 25
2.2 High resolution molecular cross section for the 2.3 μm and 3.2 μm band for HCN, H_2O and CO. These opacities formed the basis for high resolution cross correlation spectral templates (see chapter 8). 27
2.3 Abundance weighted cross section for H- at a temperature of 2900 K and 0.33 bar pressure. The abundance weighted cross sections of H_2O, TiO and CO are also shown. The abundances have been calculated from the dissociation model by Parmentier *et al.* (2018) discussed in chapter 6. 28

3.1 The GENESIS Modelling Framework. The flowchart shows the key components of the model and the steps followed to converge to radiative-convective equilibrium. The description of each step is given in section 3.3.2. 36
3.2 Schematic of the model atmosphere. The plane-parallel model comprises of ND layers, with the stellar flux incident at the top ($F_{\rm ext}$) and the internal heat flux at the bottom denoted by $F_{\rm int}$, corresponding to temperature $T_{\rm int}$. The specific intensity is I, J is the mean intensity, and F_p is the emergent flux from the top of the atmosphere. 39

3.3 Demonstration of the radiative and convective zones in atmospheres of irradiated vs non-irradiated giant planets. A Jupiter-sized planet is considered with solar elemental abundances in chemical and radiative-convective equilibrium. The irradiated planet has an equilibrium temperature of 1000 K (left) and the one with no irradiation has an internal flux corresponding to 1000 K (right). The solid lines are the converged pressure-temperature profiles, the blue shaded region represents the radiative zone, and the red region near the bottom of the atmosphere is the convective zone, with the transition point shown by the black circle. 44

3.4 Molecular mixing ratios of prominent molecules in H_2-rich atmospheres in chemical equilibrium. The dependence of the mixing ratios on the temperature is shown for a nominal pressure of 1 bar assuming solar elemental abundances, as discussed in section 3.3.5. 49

3.5 Comparison of GENESIS models with published results. A model of the hot Jupiter HD 189733 b from Fig. 1 and Fig. 4 of Burrows *et al.* (2008) is shown in the left panel, and a model of HD 209458 b from Fig. 12 of Fortney *et al.* (2008) is shown on the right. The planet-star flux ratios and the $P-T$ profiles in the inset show good agreement. The models assume chemical equilibrium with solar elemental abundances. . 52

3.6 Model spectra and $P-T$ profiles for a hot Jupiter with $T_{\rm eq} = 1500$ K computed at different spectral and spatial resolutions. ND denotes the number of layers in the model atmosphere and NF denotes the number of frequency points with the corresponding spectral resolution $\mathrm{R} = \nu/d\nu$ given at $1.4\,\mu$m, near the centre of a strong H_2O band as well as of the HST WFC3 G141 spectrograph. Six models are considered with different ND and NF, as discussed in section 3.3.8. The left hand side (top) shows the flux ratio overlaid with circles indicating binned model points in the HST WFC3 bandpass. The bottom figure on the left shows the differences in the binned points for each model relative to the highest resolution model. The right hand plot shows the corresponding $P-T$ profiles, with the radiative-convective boundary for each model marked with a circle of the corresponding colour. 54

3.7 Self-consistent model spectra and $P-T$ profiles of hot Jupiters with different levels of irradiation, represented by the equilibrium temperatures. The left plot shows the planet-star flux ratio as a function of wavelength for equilibrium temperatures of $T_{\rm eq} = 1000$ K (blue) to $T_{\rm eq} = 3000$ K (red). The right panel shows the converged $P-T$ profiles. The mass and radius of this test planet are taken to be that of Jupiter, and the host star and the overall atmospheric metallicity is modelled as solar. The onset of convection is represented by a circle, and is only visible in the figure for the lowest equilibrium temperature; higher temperatures suppress convective regions to higher pressures due to the incident irradiation. . 55

3.8 Effect of metallicity on the planet-star flux ratio and $P-T$ profile of a hot Jupiter. The metallicity is explored between 1-30× solar, with the left panel showing models with equilibrium temperature of 1000 K and the right showing 1500 K. The inset plots show the converged $P-T$ profiles. 57

3.9 Effect of C/O ratio on the planet-star flux ratio and $P-T$ profile of a hot Jupiter. Two models are considered, with equilibrium temperatures of 1000 K (left) and 1500 K (right). The O/H is fixed at solar value and the C/H is varied to obtain the required C/O ratio; the solar C/O ratio is 0.5. 58

3.10 Effect of Na/K and TiO visible opacity on the emergent spectrum and $P-T$ profile of a hot Jupiter. The left plot shows a hot Jupiter without sodium or potassium (blue) and with sodium+potassium included at solar abundances (yellow). The right hand side shows the same blue curve (without any visible absorbers) and the red curve with TiO at solar abundances. In each case the equilibrium temperature was 1500 K, with an identical incident stellar flux for all the cases shown. The inset shows the converged radiative-convective equilibrium $P-T$ profiles. The transition to the convective zone for the red curve is marked on the plot with a circle. 60

3.11 Model spectra and $P-T$ profiles for several known hot Jupiters. The planetary and stellar parameters are given in Table 3.3. The models are discussed in section 3.4.2. 63

3.12 Effect of TiO absorption on the spectrum and $P-T$ profile of a hot Jupiter. A model with equilibrium temperature of 1500 K is considered with varying levels of TiO in the atmosphere with the mixing ratio ranging from zero to 10^{-7}. 64
3.13 Comparison between an irradiated and a non-irradiated giant planet. The two models show the emergent spectra and $P-T$ profiles for an irradiated hot Jupiter with an equilibrium temperature of 1500 K (blue) and a non-irradiated Jupiter with an internal temperature of 1500 K (red), as discussed in section 3.4.3. Both the planets are assumed to be 10 pc away from the observer. The circle in the $P-T$ profile indicates the radiative-convective boundary. 68
3.14 Effect of internal heat on emergent spectra and $P-T$ profiles of non-irradiated planets. A Jupiter placed at 10 A.U. is modelled with different internal heat fluxes represented by $T_{\rm int}$. The emergent flux is shown for the source at 10 pc from the observer. The corresponding $P-T$ profiles are shown in the inset. The circles denote the radiative-convective boundary. 69
3.15 Effect of metallicity and C/O ratio on emergent spectra and $P-T$ profiles for non-irradiated planets. A jupiter-sized planet with an internal temperature of 1500 K is considered. The metallicity is explored between 1-30 ×solar and the C/O ratio spans 0.5-1.5. 70

4.1 Schematic showing the effect of a thermal inversion on the observed planet/star flux ratio. Lower regions in the atmosphere, where the temperature is cooler, are probed in opacity windows, i.e. wavelengths with low opacity. At wavelengths where molecular absorption is stronger, emission features occur due to the flux being emitted from higher up in the atmosphere where temperature is higher in the case of a thermal inversion (see section 4.2.1). 83
4.2 Effect of varying the TiO abundance on the equilibrium P-T profile of a hot Jupiter. The P-T profiles are generated with the GENESIS model of a hot Jupiter with equilibrium temperature of 2000 K and solar equilibrium abundances for the volatile species. In this model we assume TiO is the sole source of the visible opacity. 85

4.3 Radiative equilibrium P-T profiles of model atmospheres with varying abundances of metallic species. The model assumes a hot Jupiter with an equilibrium temperature of 2000 K and a solar C/O ratio of 0.5. The left panel shows the effect of solar mixing fractions for the inversion-causing refractory species. In the right panel, the abundances of the inversion-causing species are such that the ratio of visible to infrared opacity was 10. The volatile species were assumed to be in chemical equilibrium with solar abundances, and in each model the species was included in the atmosphere by itself with no other visible absorbers. . . 100

4.4 Equilibrium mixing ratios for the 7 volatile species which have significant absorption in the infrared as a function of the C/O ratio. This was calculated at a temperature of 2000 K and 0.1 bar pressure. 101

4.5 Required molecular abundance for a thermal inversion for each of the metallic species as a function of the C/O ratio. These were calculated assuming the analytic model such that the visible opacity equals the infrared opacity. The model atmosphere was assumed to have an equilibrium temperature of 2000 K. 101

4.6 Radiative equilibrium P-T profiles of model atmospheres with varying abundances of metallic species for C/O = 1. The model assumes a hot Jupiter with an equilibrium temperature of 2000 K. The left panel shows the effect of solar mixing fractions of the metallic species, and the right panel shows the abundances such that the ratio of visible to infrared opacity was 10. The volatile species were assumed to be in chemical equilibrium at C/O = 1, and in each model the species was included in the atmosphere by itself with no other visible absorbers. 102

4.7 Radiative equilibrium P-T profiles of model atmospheres with varying abundances of metallic species for C/O = 1.5. The model assumes a hot Jupiter with an equilibrium temperature of 2000 K. The left panel shows the effect of solar mixing fractions of the metallic species, and the right panel shows the abundances such that the ratio of visible to infrared opacity was 10. The volatile species were assumed to be in chemical equilibrium at C/O = 1.5, and in each model the species was included in the atmosphere by itself with no other visible absorbers. . . 103

4.8 Radiative-convective equilibrium P-T profiles for the planet WASP-121b for a C/O ratio of 0.5 (left) and 1 (right) that most closely match the observed spectrum. In each model the species was included in the atmosphere by itself with no other visible absorbers. 104
4.9 Planet/star flux ratios for the radiative-convective equilibrium models of WASP-121b for a C/O ratio of 0.5 (left) and 1 (right). The green points indicate the Hubble WFC3 and Spitzer photometric observations. The corresponding P-T profiles are shown in fig. 4.8. 105

5.1 The HyDRA modelling and retrieval framework. The model parameters, discussed in section 5.2.2, are used to compute the atmospheric structure (see section 5.2.2 and 5.2.2), the opacities (section 5.2.3) and the emergent spectrum for a model atmosphere (section 5.2.4 and 5.2.6). The likelihood is computed using the data and the model spectrum binned to the resolution of the data. The statistical inference, including parameter estimation and model selection, is conducted using the nested sampling algorithm implemented using the MultiNest package, as discussed in section 5.2.7. Once the retrieval is completed the retrieved $P-T$ profile and chemical compositions are used in tandem with the GENESIS self-consistent equilibrium model to compute deviations from radiative-convective equilibrium and chemical equilibrium, as discussed in section 5.2.8. 110
5.2 Schematic of thermal emission from an atmosphere. The lower diagram shows a model pressure-temperature profile and the upper diagram shows the corresponding observed spectrum. If the emission occurs from lower in the atmosphere (where the temperature is greater) the emitted flux is greater (red regions) and vice versa for cooler (blue) regions. Thus, features in molecular bands where the opacity is greater appear as absorption features in the flux spectrum if the temperature decreases with height and originate higher up in the atmosphere. 112
5.3 Molecular absorption cross sections for the 7 volatile species considered in our retrievals. These are shown at 1600K, approximately WASP-43b's expected temperature, and at a pressure of 0.1 bar, where most of the emission from the planet originates. The cross sections have been gaussian smoothed in the figure for clarity. 116

5.4 Theoretical emergent flux spectra (top) and residuals (bottom) for various choices of the radiative transfer model shown compared to the full Feautrier radiative transfer solver in chapter 3. The markers indicate the binned WFC3 spectrum at the resolution of the WASP-43b data. 2000 wavelength points between 1.1 and 1.7 μm were used to generate the spectra with 100 atmospheric layers. The choice of model parameters are given in table 5.1. 120

5.5 Marginalised posterior distribution for the synthetic retrieval on the emergent dayside spectrum of WASP-43b, with the simulated spectrum taken from our self-consistent model GENESIS (chapter 3) so as to be in radiative equilibrium. The red lines indicate the actual value of each parameter in the posterior corner plot and the histograms show the retrieved values and their error. The blue error bars indicate the median and 1σ error bars. Over 10^6 models were run with 4000 live samples and 4000 wavelength points between 1 and 5.5 μm, with the model atmosphere consisting of 100 atmospheric layers. The table on the left shows the actual and retrieved parameters along with their associated uncertainty. The $P-T$ profile parameters are described in section 5.2.2 and the abundances and opacity calculations are described in section 5.2.3. 126

5.6 Retrieved emergent spectrum from the simulated data of WASP-43b. The spectrum used for our retrieval was taken from the self-consistent model shown in cyan. The best-fitting model is shown in blue along with its binned data points as yellow diamonds. The dark and light purple contours show the 1σ and 2σ spread of 4000 parameter combinations from the posterior. The green markers indicate the spectral data points for the WFC3 (see inset) and Spitzer 3.6 μm and 4.5 μm channels and their associated error. The noise on the data is identical to the actual spectrum for the planet. 127

5.7 Retrieved dayside $P-T$ profile from the simulated spectrum of WASP-43b, with the actual $P-T$ profile used to generate the simulated data shown in cyan. The blue line indicates the median fit and the dark and light purple contours show the 1σ and 2σ spread in the results drawn from the posterior. 128

5.8 Retrieved $P-T$ profiles (purple) and theoretical radiative equilibrium calculations performed with GENESIS (in green) for the dayside of WASP-43b shown on the left. The cyan line indicates the $P-T$ profile of the simulated data. The right hand side shows the temperature difference between the median retrieved and equilibrium models, and the associated 1 and 2 σ confidence contours. The retrieval's solution was used to run the equilibrium model with retrieved chemistry, to determine the radiative-convective profile and hence the equilibrium profile. The spread in the equilibrium model's $P-T$ profile is due to the chemical variations in the retrieval's solution. The sodium and potassium abundances were set to solar compositions for the equilibrium calculations. 132

5.9 Comparison of retrieved chemical abundances and theoretical chemical equilibrium models for simulated data. The cyan line indicates the actual mixing ratio used to generate the spectrum that was retrieved, the dark and light purple contours show the 1 and 2σ errors for the retrieval respectively, and the dark and light green the corresponding equilibrium mixing fractions for each species. Where a molecule was detected in the retrieval, the median fit value is also plotted in blue, and where no abundance could be constrained, the 2σ upper bound is shown with an arrow. 1000 randomly sampled retrieval points were used, and 100 layers taken for the model atmosphere. The $P-T$ profile was fixed for each random sample from the posterior. 133

5.10 Marginalised posterior distribution of WASP-43b's atmosphere under emission spectroscopy. The data set used for the retrieval was obtained from Kreidberg *et al.* (2014) and considers the Hubble WFC3 and Spitzer 3.6 μm and 4.5 μm channels. We considered 7 molecular volatile species and six parameters describing the $P-T$ profile of the atmosphere. 4000 evenly spaced points in wavelength were used to generate spectra between 1 μm and 5.5 μm, with 4000 live points used for the nested sampling and 100 atmospheric layers, with over 10^6 models run in total. The histograms and relative correlations between the retrieval parameters is shown on the top right hand side. The table shows the retrieved values and their associated 1σ error bars. The upper limits where shown are 2σ upper bounds. 135

5.11 Retrieved emission spectrum of WASP-43b, showing the median fit spectrum and the 1 and 2σ uncertainty. The green markers indicate the data set and the corresponding error bars, and the yellow diamonds the binned median model. The top left inset shows the WFC3 bandpass and the corresponding data points and spectral fit. The bottom right inset shows the retrieved $P-T$ profile and the corresponding retrieved error on the temperature. 136

5.12 Deviation from 1-D radiative-convective equilibrium present on WASP-43b. The left hand side shows the retrieved $P-T$ profiles in purple and theoretical radiative equilibrium calculations performed with GENESIS in green, with the chemistry fixed to the retrieved values. The right hand side shows the difference between the retrieved and the equilibrium temperatures, with the darker and lighter shade representing the 1 and 2σ uncertainties respectively. 1000 randomly sampled points from the retrieval were used to generate the equilibrium models and the sodium and potassium abundances (not retrieved) were set to solar compositions. 139

5.13 Retrieved chemical abundances and theoretical chemical equilibrium calculations performed with GENESIS. The dark and light purple contours show the 1 and 2σ errors for the retrieval respectively, and the dark and light green the corresponding thermochemical equilibrium mixing fractions with the $P-T$ profile fixed to the retrieved values. Where a molecule was detected using our Bayesian analysis, the median fit value is also plotted in blue, and where there was no significant detection, the 2σ upper bound is shown by an arrow. 1000 randomly sampled retrieval points were used, and 100 layers taken for the model atmosphere. The atomic abundances were kept at solar values for C, O and N during the equilibrium calculations. 141

6.1 Abundance weighted cross sections for the prominent species in our retrieval at a temperature of 2900K and 0.33 bar pressure. The abundances have been calculated from the dissociation model by Parmentier *et al.* (2018) and the cross sections derived in chapter 2. The H- opacity is calculated in section 6.2.2. We also show the abundance weighted H- cross section from Arcangeli *et al.* (2018). 148

6.2 Planet/star flux ratio as a function of wavelength for the WFC3 bandpass for each of the retrievals conducted for the hot Jupiter WASP-18b. The inset in each panel shows the Spitzer IRAC photometric points. The top left panel shows the three datasets together with black body curves at 2800 K (dotted line), 2900 K (dashed line) and 2950 K (solid line). The other three panels show each of the retrievals, with the dark and light colours indicating the 1σ and 2σ uncertainty respectively. The solid line shows the median best fit curve for each. The final three HST WFC3 points for the Sheppard *et al.* (2017) dataset have not been included into our retrievals for comparisons given that the other two do not have data at these wavelengths. 151

6.3 Histogram showing the undissociated H_2O, CO and H- abundance probability distribution functions in the photosphere ($P = 0.1$ bar) for the various retrievals conducted for WASP-18b. In each retrieval the H_2O and H- were thermally dissociated with pressure and temperature according to the model in section 6.2.1. The red dashed line shows the expected abundance assuming solar composition for each of the species (Parmentier *et al.*, 2018). 152

6.4 Posterior distribution of WASP-18b's retrieved dayside emission spectrum. The dataset was obtained from Sheppard *et al.* (2017) and considers HST WFC3 and four Spitzer photometric channels between 3.6-8 μm. We retrieved six chemical species, H_2O, CO, CO_2, TiO ,VO and H-, and parametrised the atmospheric temperature profile with six parameters, as discussed in section 5.2.2. 153

6.5 Retrieved pressure-temperature profiles for the retrievals conducted for WASP-18b. In each case the dark and light colours indicate the 1σ and 2σ uncertainty respectively, with the solid black line showing the median best fit. 157

7.1 Analysis of the temporal correlated noise in each spectral bin for WASP-19b. The data is binned up in time and the RMS of the light curve residuals is calculated; the results are then normalized by the RMS of the light curve with minimal binning (i.e, one point per bin) and compared with the predicted trend assuming there is no correlation in time ($RMS_0/\sqrt{N}$, where N is the number of exposures per bin). Most light curves show no evidence of correlated noise; only the bin at 1.329 μm) shows any excess noise, but the effect is only seen at large bin sizes. 169

7.2 Band-integrated light curve (left) and a sample spectral bin light curve (right) for HST WFC3 observations of WASP-19b. The top panels show the raw data with the best-fit model overplotted, and the middle panels show the light curve and model after detrending systematic effects. The bottom panels show the difference between the observations and the best-fit model at each point in the time series and give the standard deviation of those residuals (RMS). 170

7.3 Retrieved spectral fits and HST WFC3 data for each system. The flux ratio is shown against the wavelength in the 1.1-1.7 μm range. The data and its associated error is shown in black and the median fit to the data is shown with the blue curve. The dark and light shaded regions represent the 1 and 2σ uncertainty in the retrieved flux ratio for each planet. 173

7.4 Retrieved H_2O abundances for each planet in our study, coloured according to their equilibrium temperature. Each plot shows the undissociated abundance, and the pressure and temperature dependent H_2O abundance has been calculated from the dissociation model discussed in chapter 6.2.1. The shaded regions show the probability density distribution and the blue error bar represents its median value along with its associated 1σ uncertainty. Also shown on the red dashed line is the solar value of H_2O at the planet equilibrium temperature and 0.1 bar pressure. 174

7.5 Posterior distribution of HD209458b's retrieved dayside emission spectrum. The dataset was obtained from Line *et al.* (2016) and considers HST WFC3 and four Spitzer photometric channels between 3.6-8 μm. We retrieved seven volatile chemical species, H_2O, CH_4, NH_3, CO, HCN, CO_2 and C_2H_2, and parametrised the atmospheric temperature profile with six parameters, as discussed in section 5.2.2. 175

7.6 Posterior distribution of Kepler-13Ab's retrieved dayside emission spectrum. The dataset was obtained from Beatty *et al.* (2017a) and considers HST WFC3 and two Spitzer photometric channels between ∼3.6-5 μm. We retrieved six chemical species, H_2O, CO, CO_2, TiO ,VO and H-, and parametrised the atmospheric temperature profile with six parameters, as discussed in section 5.2.2. 176

7.7 H_2O abundance versus temperature at 100 mbar. These abundances are normalised relative to the metallicity of the host star. These are shown with their 1σ uncertainty. The five hottest planets show the dissociated H_2O abundances. Planets with a thermal inversion have been shown in red and ones without are blue. The left panel also shows the equilibrium chemical abundances for a range of C/O ratios at a pressure of 100 mbar as a function of the temperature (see chapter 3.3.5). The right panel shows the H_2O abundance in the photosphere as a function of temperature from thermal dissociation (Parmentier *et al.*, 2018). These are shown at planetary gravity ranging from $\log(g) = 3-4$ (cgs). 179

7.8 Retrieved H- abundances for the ultra-hot Jupiters in our study, coloured according to their equilibrium temperature. Each plot shows the undissociated abundance, and the pressure and temperature dependent abundance has been calculated from the dissociation model discussed in chapter 6.2.1. The shaded regions show the probability density distribution and the blue error bar represents its median value along with its associated 1σ uncertainty. Also shown on the red dashed line is the solar value of H- at the planet equilibrium temperature and 0.1 bar pressure. 181

7.9 Retrieved $P-T$ profiles for each of the planets in our study. The black curve represents the median temperature profile and the dark and light shaded regions the 1 and 2σ uncertainties respectively. 183

7.10 Retrieved O/H ratio for the hot Jupiters against mass (shown in blue). Also shown for reference are the metallicities for the solar system giant planets. 189

8.1 Stages of detrending for the observations of HD209458b, for detectors 1–4 and the set of VLT CRIRES observations taken on 2011 July 25. The x-axis corresponds to wavelength, and the y-axis corresponds to frame number, increasing in time. Panel (a): spectra immediately after reduction of nodding frames. Heavy telluric contamination is evident (e.g. at 3.1915 μm). Poor seeing conditions manifest as dark horizontal bands. Panel (b): reduced spectra after wavelength calibration, alignment, additional cleaning, normalisation, and masking. This image (excluding masked regions) is the input of our detrending algorithm. Panel (c): data subject to column-wise mean subtraction, the optimal number of SYSREM iterations, a 15-pixel standard-deviation high-pass filter, and column-wise standard-deviation division. Panel (d): the same as in Panel (c), but with the injection of our planet model at 40x its nominal strength prior to detrending. The preserved planetary absorption features appear as dark trails that stretch over $\sim 0.0008\,\mu$m. 196

8.2 Frame-by-frame cross correlation values as a function of velocity for the observations of HD209458b. The CCFs are shifted into the planetary rest frame by the peak significance K_p, for each model template (HCN, H_2O, CO, and their combination). The right panel shows the CCF with a model injection at two times nominal strength. Each CCF contains a dark vertical trail at approximately the known systemic velocity of -14.8 km s^{-1} from alignment between the model template and intrinsic features. 197

8.3 Planetary spectra of the model atmosphere of HD189733b with different molecular species present. Panel a shows the 2.28-2.35 μm spectral range and panel b shows the 3.18-3.27 μm range. Spectra were generated with HCN (turquoise), H_2O (blue) and CO (red) with a wavenumber spacing of 0.01 cm^{-1} using the GENESIS code (chapter 3). Panel c shows the $P-T$ profile used to generate the spectra. 198

8.4 High-resolution model spectra of HD209458b showing line features of HCN, H_2O, and CO in the observed bands at 2.28-2.35 μm and 3.18-3.27 μm. 199

8.5 Cross correlation S/N for CO, H_2O, and HCN as a function of systemic velocity and peak radial velocity of HD209458b. Cross correlation in the 2.29-2.35 μm spectral band yields an S/N of 5.1 with the CO template, and 4.4 with H_2O individually. A combined CO + H_2O model yields a boosted S/N of 5.3. HCN yields an S/N of 4.7 in the 3.18-3.27 μm spectral band. The white crosshairs denote the K_p and V_{sys} for the peak S/N which agree with the black cross corresponding to known orbital parameters. 200

8.6 Molecular detection significances for HD189733b using the two detrending methods. From left to right: detection significances of CO in the 2.3 μm band, and of H_2O, HCN, and combined H_2O + HCN in the 3.2 μm band. The black plus indicates the expected planetary K_p and V_{sys}. The top row of detections are made using the SYSREM detrending method. The bottom row of detections use airmass fitting. 207

List of tables

2.1 The temperature and pressure grid for the cross sections, which are the same as those used in Hedges and Madhusudhan (2016). 24
2.2 References for the line lists/opacity sources for each of the species considered in this work. 30

3.1 Comparison of prominent atmospheric models in the literature including strong irradiation. Details of the methods used by Fortney et al. can be found in Toon *et al.* (1989) and McKay *et al.* (1989), Burrows et al. in Sudarsky *et al.* (2003) with their methods in Hubeny and Mihalas (2014), Barman *et al.* (2001) describe their methods in Hauschildt and Baron (1999), Malik et al. in Malik *et al.* (2017) and Heng *et al.* (2014), Seager et al. in Seager and Sasselov (1998) with methods in Vaz and Nordlund (1985) and Mollière et al. in Mollière *et al.* (2015); Mollière *et al.* (2017). The model used by Drummond *et al.* (2016) can be found in the paper and Amundsen *et al.* (2014).
[1] Radiative Transfer solver used in the model.
[2] Temperature correction scheme used to ensure radiative-convective equilibrium.
The remaining columns describe other aspects, including whether convection and clouds are incorporated in the model, and whether the opacities are treated in a line-by-line or using the correlated-k approximation. See section 3.1 for a discussion of the different models.
[†]In the present work we only consider weak scattering, due to gaseous H_2 Rayleigh scattering. 34

3.2 The inputs, outputs and key features of GENESIS. $R_{\rm star}$, $\log(g_{\rm star})$, $T_{\rm eff,star}$ and $Z_{\rm star}$ are the radius, log(gravity), metallicity, and effective temperature of the planet hosting star. $R_{\rm planet}$, $\log(g_{\rm planet})$, $T_{\rm int,planet}$ and $a_{\rm planet}$ are the radius, log(gravity), internal temperature, and the orbital separation of the planet. d is the distance to the system. The stellar redistribution factor $f_{\rm r}$ denotes the fraction of the insolation received by the dayside atmosphere, accounting for spherical geometry, day-night energy redistribution, etc. The mixing length for the convection l (usually taken to be the scale height) and the elemental abundances relative to atomic hydrogen {X/H} are also inputs. The model has the option to either fix the molecular abundances of the main gaseous species at equilibrium values or set them to other specified values for each layer. The outputs are the emergent spectrum, either the planet-star flux ratio or the planet flux alone, the pressure-temperature ($P-T$) profile and the chemical profiles. Clouds/hazes have not been included in the present work. 37

3.3 System parameters of known hot Jupiters modelled in section 3.4.2 and Fig. 3.11. $Z_{\rm star}$ is the stellar metallicity, $T_{\rm eff}$ is the effective temperature of the star and $T_{\rm eq}$ is the equilibrium temperature of the planet. The equilibrium temperature is calculated assuming the albedo is 0, and complete redistribution of flux over the planet, $T_{\rm eq} = T_{\rm eff}\sqrt{R_{\rm star}/(2a)}$. The system parameters are obtained from exoplanets.org. 66

4.1 Summary of developments in the theory of thermal inversions in strongly irradiated giant planets. 76

4.2 Table showing the solar atomic log mixing ratio and the required molecular log mixing ratios of each metallic species in order to form a thermal inversion for various C/O ratios. The solar atomic abundances were obtained from Asplund *et al.* (2009). The required volume mixing ratios were determined from eqn. 4.12 and thermochemical equilibrium of the volatile infrared species at 2000K and 0.1 bar. In each model the species with strong visible opacity was included by itself with no other visible absorbers present. 88

5.1 The set of parameters we choose in order to test our model. These were chosen so as to explore the model in the region of the parameter space in which we would expect the results to lie and taken from a self-consistent equilibrium profile. The first 7 values are the mixing fractions of the molecular species (section 5.2.2) and the total absorption coefficient calculation is given in section 5.2.3. The final six generate the $P-T$ profile described in section 5.2.2. As the original $P-T$ profile to generate the data set is from the self-consistent model, the analytic profile parameters are the closest fit. 113

5.2 Weights and angles (μ) used for each integration scheme. The angles for the integration with the Feautrier method can be found in chapter 3 and are the same as triple ray quadrature. 119

6.1 Retrieved parameters for the various runs conducted on the emission spectrum of WASP-18b. In each case the parameter is shown with its 1σ uncertainty. In models with dissociation the dissociated 100 mbar abundance is shown. We also show the Bayesian comparison for each model versus our reference case. 161

7.1 Planet parameters, retrieved properties and data sources for the hot Jupiters we consider in our study. The mass and radius parameters have been obtained from exoplanet.org, and the equilibrium temperature has been calculated assuming full redistribution of the incident flux. The retrieved photospheric temperature temperature and H_2O abundances for each planet were calculated using the retrieval method in chapters 5 and 6 and discussed in section 7.2. The reference for each data source is also shown in the final column. 171

Chapter 1

Introduction

"That's no moon..."
- Obi Wan Kenobi

The study of exoplanets and in particular their atmospheres is a major emerging frontier in science. Numerous observational surveys in the last decade have led to the detection of thousands of exoplanets, revealing that exoplanets are extremely common and extremely diverse in their masses, radii, and orbital architectures (Fischer *et al.*, 2016). New surveys in the near future, such as the TESS, CHEOPS, ARIEL and PLATO space missions and several ground-based surveys, are expected to find thousands more planets orbiting nearby stars. The proximity of these host stars allows for detailed characterisation of their planetary atmospheres. Thus exoplanetary science is now entering an exciting time as low mass planets are already being discovered in the habitable zones of nearby stars (Anglada-Escudé *et al.*, 2016; Gillon *et al.*, 2016), thereby opening the possibility of detecting biosignatures in their atmospheres in the future.

1.1 Exoplanet Diversity

Figure 1.1 shows some of the currently known exoplanets obtained through numerous surveys. These surveys have shown that exoplanets are indeed extremely common, with many thousands of exoplanets discovered since the first planet detected around a Sun-like star (Mayor and Queloz, 1995). As these numerous exoplanets have been discovered, we have seen that these planets occupy a significant range in parameter space, much more so than naively expected from studying the solar system planets. Our own solar system has three distinct classifications, that of small close in rocky planets

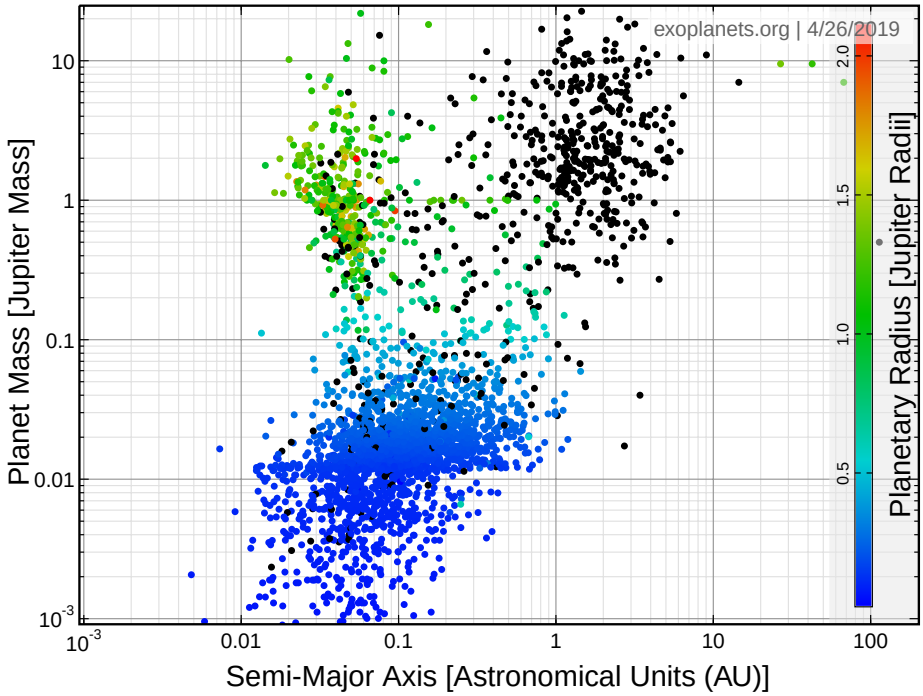

Fig. 1.1 Planetary mass as a function of semi-major axis for the currently known exoplanets, with the colour of each point indicating the planetary radius (where known). The data was obtained from exoplanets.org.

with masses $\lesssim$1 Earth mass, followed by the gas giants Jupiter and Saturn further out and then finally the ice giants Uranus and Neptune. However, as fig. 1.1 shows, exoplanetary sizes, orbital distances and planetary masses all fall into a continuum. For instance we have observed numerous gas giants and Neptune sized planets closer in than the orbit of Mercury. We have also detected planets known as Super-Earths, which fall in between the rocky planets and ice giants in our solar system. Whether their internal structure is rocky or icy remains a mystery. This has opened up questions as to the composition and classification of such planets, and indeed how such planets may form at a given location within a protoplanetary disk and migrate to their current locations. Key to answering this is the accurate detection and characterisation of these exoplanets. We now discuss the ways in which we detect exoplanets historically and in the coming years.

1.2 Detection Methods

A number of ways exist to detect exoplanets. The most successful to date are the radial velocity and transit method. The radial velocity method involves the detection

of the Doppler shift of the stellar absorption lines as the planet and star orbit their common centre of mass. This was used to detect the first exoplanet orbiting a Sun-like star (Mayor and Queloz, 1995). The transit method on the other hand observes exoplanets through the dimming of the stellar light as the planet traverses in front of the star as observed by us. This technique is advantageous given that the planetary radius can be measured and the atmosphere can be characterised easily at various points in the planet's orbit (see section 1.3.1 below). However, this does require the system to be aligned such that transits can occur, which is only a small subset of the overall population of potential exoplanets. This is particularly disadvantageous for detecting exoplanets at large orbital separations. Another technique is the direct imaging of exoplanets (e.g. Konopacky *et al.*, 2013; Macintosh *et al.*, 2015). Like radial velocity, this does not require favourable orbital alignment for transit, but only the very brightest planets at large separations have been successfully detected this way given that the planetary signal needs to be strong enough to be distinguished from the stellar signal. With such techniques we have a wealth of exoplanets over a wide range in orbital parameter space. The focus of research has now shifted towards exploring the compositions of such planets through their atmospheres. A detailed review of detection methods can be found in Fischer *et al.* (2016).

1.3 Detecting the Atmospheres of Exoplanets

Detecting the atmosphere of an exoplanet requires a sensitivity that is orders of magnitude better than the detection of the planet itself. However, the atmosphere allows us to explore a large number of processes occurring on the exoplanet. It offers us the opportunity to explore numerous species and conditions in the atmosphere. There are three key ways in which the atmospheres of exoplanets have been explored, transit spectroscopy, high resolution spectroscopy and direct imaging of exoplanets. These different means of characterising exoplanetary atmospheres are all poised to receive a major boost with upcoming large facilities, such as the James Webb Space Telescope (JWST) and the large ground-based telescopes (e.g., ELT, TMT, etc). We discuss each of these methods below.

1.3.1 Transit Spectroscopy

Atmospheric detections are much more difficult than planetary detections, as the strength of the atmospheric signals are significantly weaker than the planetary signal.

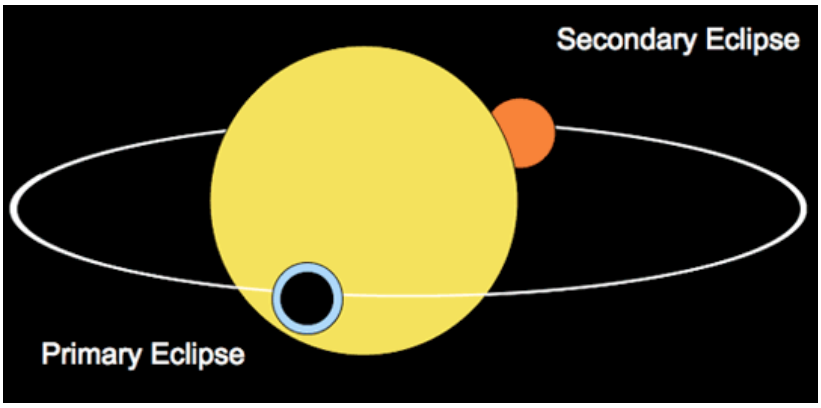

Fig. 1.2 Schematic of a transiting exoplanet. A primary eclipse or transit occurs when the planet passes in front of the star as seen by the observer. On the other hand, a secondary eclipse occurs as the planet passes behind the host star in its orbit. Atmospheric observations can be carried out under transmission at primary eclipse or just prior to secondary eclipse, where we observe emission emanating from the dayside of the planet. Figure by S. Seager (Seager and Deming, 2010).

The first detection of the atmosphere of an exoplanet was achieved through the transit method (Charbonneau *et al.*, 2002). A schematic of a transiting exoplanet is shown in fig. 1.2. This method involves observing the flux received from the system as the planet orbits the host star. At primary eclipse, the planet will block some of the light from the star. The occultation or transit depth (Seager, 2010) is given by

$$\Delta = \frac{R_p^2}{R_{\text{star}}^2}, \tag{1.1}$$

where R_p and R_{star} represent the radius of the planet and star respectively. A small fraction of this light will also pass through the atmosphere of the planet. At certain wavelengths where the atmosphere is opaque to radiation the planetary radius will appear larger than wavelengths which are transparent. Therefore Δ will be larger at these wavelengths. If the atmospheric height is given by H, the transit depth at these opaque wavelengths now becomes

$$\Delta = \frac{(R_p + H)^2}{R_{\text{star}}^2} \approx \frac{R_p^2 + 2HR_p}{R_{\text{star}}^2}, \tag{1.2}$$

assuming that the atmospheric height is much lower than the radius of the planet. The planetary scale height is often used to gauge the extent of the atmosphere. This scale height is given by $k_b T/\mu g$, where k_b is the Boltzmann constant, T is the temperature, μ is the molecular weight and g is the surface gravity (Seager, 2010). This means

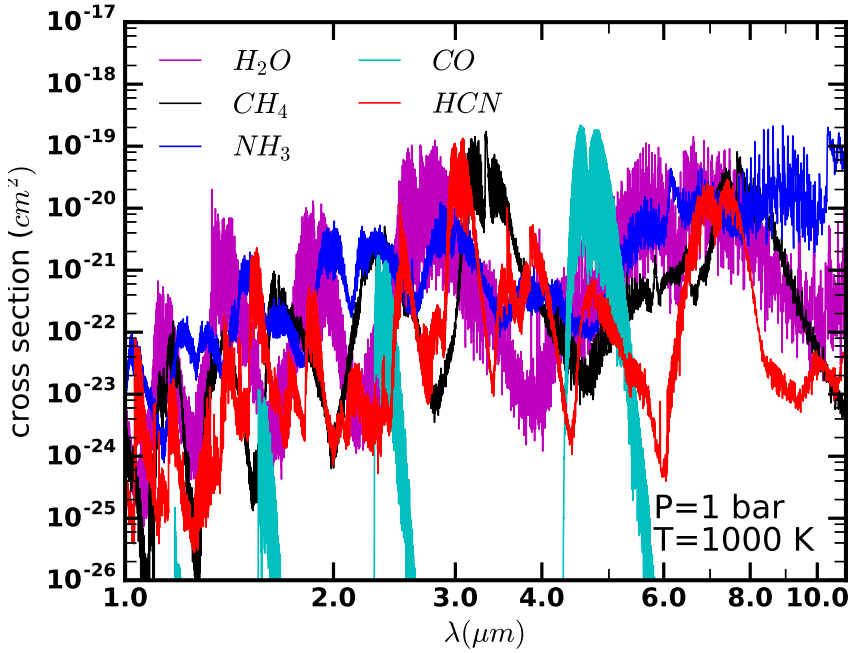

Fig. 1.3 Molecular absorption cross sections for the prominent volatile molecules in giant planetary atmospheres. Cross sections are shown for representative hot Jupiter conditions of T =1000 K and P =1 bar.

that to maximise the scale height, the temperature must be high and/or the planetary gravity and mean molecular weight must be low. This is why very large hot planets are the most well studied thus far. Typically, atmospheres are 7-10 scale heights in extent. By observing the variation in Δ with wavelength, we are able to constrain the spectroscopically active species within it, which only absorb at certain wavelengths and make the atmosphere opaque. Fig. 1.3 shows the cross section of some of the prominent volatile species for conditions typical on hot Jupiters. Numerous species, particularly H_2O and CO, have strong absorption cross sections between ~1-10 μm. Each has their own unique spectral signature that allows for conclusive detections given sufficient spectral coverage in the near infrared. Through these we may also determine the abundance of each species, the atmospheric temperature, clouds/hazes and various other processes which occur from the variation in the transit depth with wavelength.

The transit method has been particularly successful in probing planetary atmospheres in multiple configurations. A transmission spectrum, obtained when the planet transits in front of the star, probes the atmosphere at the day-night terminator region of the planet. On the other hand, an emission spectrum obtained, just prior to secondary eclipse when the planet passes behind the star, probes the dayside atmosphere of the

planet. The eclipse depth (Seager, 2010), which is the ratio of flux received from the planet to the star, is given by

$$F_p/F_{\rm star} = \frac{R_p^2 B(T_p, \lambda)}{R_{\rm star}^2 B(T_{\rm star}, \lambda)}, \tag{1.3}$$

where $T_{\rm p}$ and $T_{\rm star}$ are the brightness temperatures of the planet and star respectively at the given wavelength. $B(T, \lambda)$ is the Planck function for a given temperature T and wavelength λ. Thus to obtain a strong planetary signal we must observe exoplanets where this factor is maximised. Hot Jupiters are prime candidates for such a study as they have atmospheric temperatures $\gtrsim$1000 K. These planets are very close to their host star which also maximises their chances for transit as well. We observe such planets in the infrared, where the stellar flux is weaker and hence the planet-star flux contrast is higher. For such planets the peak thermal emission from the atmosphere also occurs in the infrared and is thus ideal for observations. Typically, hot Jupiter emission spectra have planet/star flux ratios of $\gtrsim 10^{-4}$ and are thus detectable even with current facilities. Smaller, cooler planets remain out of reach of current observations, but with greater capabilities on the horizon we will soon be able to observe such planets in the next decade.

Thermal emission spectra observed at secondary eclipse have the advantage of providing rigorous constraints on the temperature profile as well as chemical composition of the dayside atmosphere. This is because the temperature gradients in the dayside atmosphere directly lead to spectral features of the chemical species present through their influence on the Planck function $B(T, \lambda)$. The lack of any features in observed emission spectra can indicate an isothermal temperature profile in the atmosphere. Furthermore, positive or negative temperature gradients with altitude in the photosphere cause emission and absorption features respectively. With the advent of high precision data, e.g using the Hubble Space Telescope's Wide Field Camera 3 (HST WFC3) spectrograph (see fig. 1.4), and detailed retrieval techniques, strong constraints have been obtained for the atmospheric temperature profile and chemical species present in the dayside atmospheres. The imminent arrival of JWST is expected to further enhance our ability to constrain such physical and chemical properties.

Recent Observations

The success seen in the characterisation of exoplanetary atmospheres in recent years is due to the tremendous progress in the observations and characterisation of transiting exoplanetary atmospheres (Crossfield *et al.*, 2016; Heng and Showman, 2015; Mad-

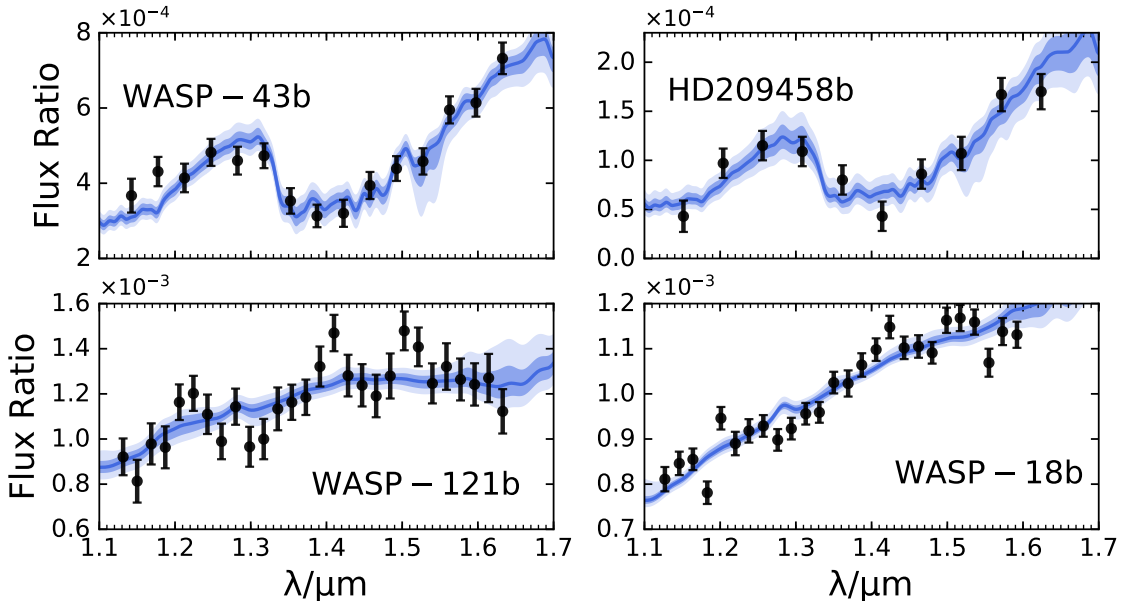

Fig. 1.4 Planet/star flux ratios for some of the most prominent hot Jupiters obtained using the HST WFC3 spectrograph. The black points indicate the data and their associated error, while the blue curves indicate fits to the observations. The solid blue line denotes the best fit spectrum and the dark and light shaded contours show the 1 and 2σ spectral fits respectively (see chapter 7). Sources of data: Kreidberg *et al.* (2014) for WASP-43b, Line *et al.* (2016) for HD209458b, Evans *et al.* (2017) for WASP-121b and Sheppard *et al.* (2017) for WASP-18b.

husudhan, 2019; Madhusudhan *et al.*, 2014a). A wealth of new high quality observations have become available thanks to space based telescopes such as the Hubble Space Telescope (HST) (Deming *et al.*, 2013; Kreidberg *et al.*, 2014; Madhusudhan *et al.*, 2014b). These observations are a substantial improvement over the previous years when largely broadband photometric or low-resolution observations were available (see e.g. Madhusudhan *et al.*, 2014a). High precision spectra have now been observed both in primary transit and in secondary eclipse using an array of facilities. These and other observations have led to the detections of atomic and molecular species, clouds/hazes, thermal inversions, day-night circulation patterns, and exospheres (e.g., Ehrenreich *et al.*, 2015; McCullough *et al.*, 2014; Sing *et al.*, 2016; Stevenson *et al.*, 2014; Wyttenbach *et al.*, 2015).

Fig. 1.4 shows HST Wide Field Camera 3 (WFC3) emission spectra for four of the most well studied hot Jupiters spanning a range in equilibrium temperature between 1500-3000 K. These spectra highlight the diversity of hot Jupiter atmospheres, with two showing strong H_2O absorption at 1.4 μm whilst the other two showing weaker

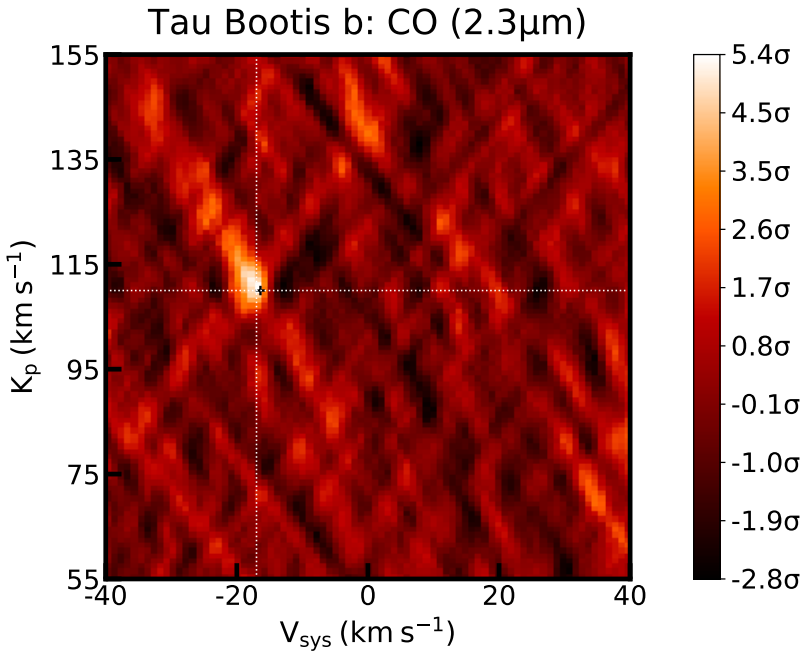

Fig. 1.5 Detection of CO in the non-transiting planet τ Boötis b using VLT observations. The white cross-hairs denote the peak in the significance, while the black plus indicates the expected planetary and systemic velocity from Brogi *et al.* (2012). Figure obtained from Cabot *et al.* (2019).

emission features. The emission features constrain thermal inversions (or stratospheres) (Evans *et al.*, 2017; Haynes *et al.*, 2015; Sheppard *et al.*, 2017), whilst strong absorption features can constrain the H_2O abundance as well as the temperature profile (Kreidberg *et al.*, 2014; Line *et al.*, 2016). Such constraints are providing key insights into the various processes and chemistry in the atmosphere and we are now even able to carry out ensemble studies to explore the variation of these parameters from numerous observations of hot Jupiter atmospheres (Pinhas *et al.*, 2019).

1.3.2 High Resolution Spectroscopy

High resolution spectroscopy (HRS) has recently been used to detect a number of species in the atmosphere of hot Jupiters (e.g. Birkby *et al.*, 2017; Brogi *et al.*, 2012; Snellen *et al.*, 2010). This involves observing numerous spectral lines within a narrow wavelength range as the planet traverses the star. These spectral lines from the planet are generated from the molecular and atomic absorption of the species present within the atmosphere. They are Doppler shifted as the planet moves around in its orbit. By observing the Doppler shift of these lines, we are able to constrain the various species

which may be present within the atmosphere (see e.g. review by Birkby, 2018). This technique has recently come to the fore thanks improvements in high resolution infrared spectroscopy using large new ground based observational facilities, such as the Keck Observatory and VLT (Brogi *et al.*, 2016; Nugroho *et al.*, 2017). The high resolution spectrographs observe the system at R$\sim$100,000 and detect the small variations within the planetary signal due to their sensitivity. Key to extracting the planetary signal over the noise from the strong stellar signal is the detrending method (Birkby, 2018). This removes the strong stellar lines and the telluric features from absorption from the Earth's atmosphere to leave the planetary signal.

Such observations have led to detections of several molecules, most notably H_2O and CO, in several hot Jupiters (Birkby *et al.*, 2013, 2017; Brogi *et al.*, 2012; Rodler *et al.*, 2013; Snellen *et al.*, 2010). TiO has also recently been observed in the strongly irradiated hot Jupiter WASP-33b (Nugroho *et al.*, 2017). As well as molecular species, atomic species have also been observed from high resolution visible observations (Hoeijmakers *et al.*, 2018). This has shown signs of Ti, Fe and even evidence for some of their ionic counterparts in the atmosphere of KELT-9b, one of the hottest known exoplanets with an atmospheric temperature of $\sim$4500 K (Gaudi *et al.*, 2017). This technique has also been used to constrain winds and dynamical processes on exoplanets thanks to the high resolution of the observations, capable of resolving the broadening of spectral features accurately (Brogi *et al.*, 2016; Snellen *et al.*, 2010).

Doppler spectroscopy also has a particularly powerful scope given that it does not require the planet to transit. Numerous detections of species have been possible thanks to this technique which have not been possible with the transit method. For example, CO was observed in τ Boötis b (see fig. 1.5) and H_2O in 51 Pegasi b (Birkby *et al.*, 2017; Brogi *et al.*, 2012). By exploring a large grid of velocities, we are able to constrain the planetary velocity (speed of the orbit around the star) and systemic velocity (of the whole planet and star system as it recedes/approaches us) with each detection. This can be used to determine the orbital inclination of the system. The ability to detect and characterise non-transiting planets is thus opening up a greater proportion of potential exoplanets for characterisation.

1.3.3 Direct Imaging

The direct imaging of exoplanets has only recently been possible for a handful of systems within the last decade. We directly observe planets only if they are very bright and their orbital separation is large. This allows for the planetary signal to be resolved from the star. The very bright planets observable through direct imaging thus have

large radii and a high photospheric temperature, similar to hot Jupiters discussed above. Such planets are rare given that they are so far away from their host star, and are thus only detectable in young systems as they still have substantial residual heat from their formation. These planets thus provide ideal laboratories for studying the formation and migration pathways for exoplanets.

There has been significant progress in detecting molecules and investigating the temperature profiles through direct imaging of exoplanets (e.g. Konopacky *et al.*, 2013; Macintosh *et al.*, 2015). The most prominent system explored with direct imaging is HR8799, with three planets initially detected (Marois *et al.*, 2008) with a fourth discovered later (Marois *et al.*, 2010). Lavie *et al.* (2017) recently investigated the chemical composition and temperature profiles of each of the planets in the system further. These constraints on species led to constraints on the overall C/O ratio of the planets which showed that some formation mechanisms for such planets are preferred over others from the observed abundances (see below). Ground based direct imaging with the next generation of large 30-40m ground based telescopes will allow for formation pathways to be further explored for such newly formed exoplanets.

1.4 Atmospheric and Formation Processes

The atmospheres of exoplanets can be used as a laboratory to explore a multitude of effects. We can explore physicochemical effects such as atmospheric chemistry, mixing/circulation, atmospheric escape and even study the history of the planet, i.e the formation and migration mechanisms, through the observations of the atmospheres. Different spectral ranges encode the atmospheric behaviour in various regions of the atmosphere, allowing us to explore these specific depths within the atmosphere where such processes can occur.

Fig. 1.6 shows the various processes which occur in exoplanetary atmospheres. The right hand side of the figure shows the regions of the atmosphere probed by each wavelength. Generally, longer wavelength observations are able to explore deeper regions of the atmosphere. This is because the optical depth of each species present in the atmosphere sets the location at which spectra are generated. For instance, infrared observations ($\sim$0.9-20 μm) have been used to constrain molecular species in the deep atmospheres of exoplanets at $\sim$1 bar pressure, where the atmosphere is at or near chemical equilibrium. Shorter wavelengths such as the visible ($\sim$0.4-0.9 μm) probe lower pressures (P$\sim$0.01 bar), where metals and metallic compounds are prevalent in the spectra (e.g. Charbonneau *et al.*, 2002; Hoeijmakers *et al.*, 2018; Nugroho

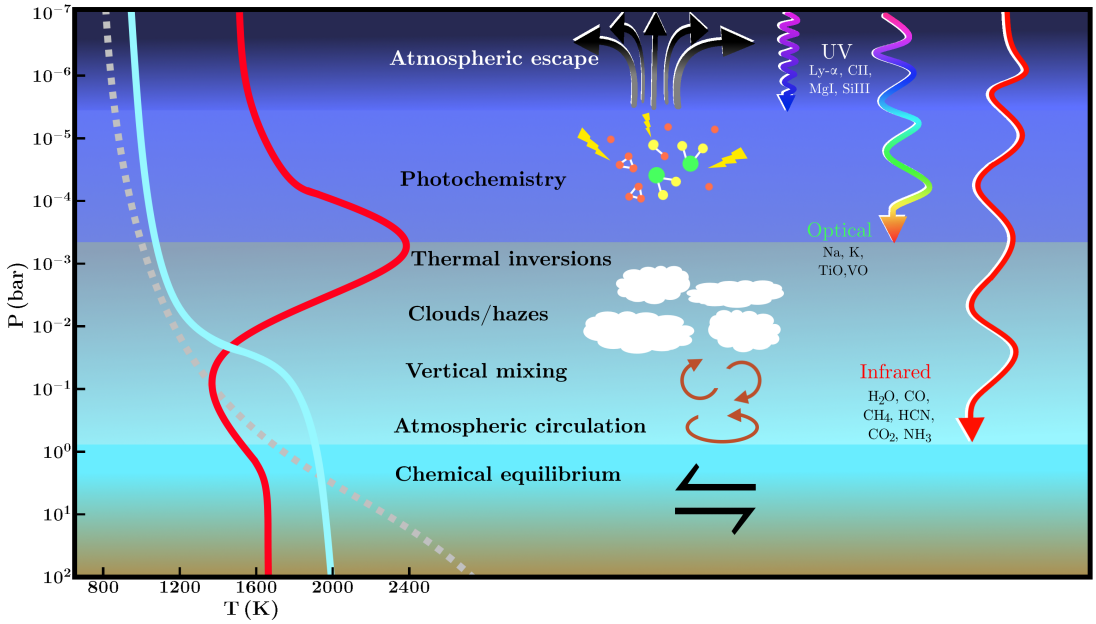

Fig. 1.6 The various processes which occur within the atmospheres of extra-solar giant planets. The left hand side shows the temperature as a function of pressure for various profiles, with and without thermal inversions. The dashed curve shows the atmospheric temperature profile for a brown dwarf/non-irradiated planet. The right hand side shows the wavelengths that each region of the spectrum probes, along with the various chemical species and physical processes which occur at such depths within the atmosphere. Figure obtained from Madhusudhan (2019).

et al., 2017). The atmosphere here at these higher altitudes is also more affected by disequilibrium processes, thermal inversions (stratospheres) and clouds/hazes (e.g. Evans *et al.*, 2017; Pinhas *et al.*, 2019) as shown on the left hand side of fig. 1.6. Further up in the atmosphere, photochemical effects begin to dominate, particularly for the hot planets with strong stellar irradiation observed to date (e.g. Moses *et al.*, 2013). Indeed, exospheres from atmospheric escape of gas have also been observed for many planets (Ehrenreich *et al.*, 2015; Owen, 2018). Thus atmospheric characterisation has explored many such phenomena over a wide range of regions within exoplanet atmospheres. With future improvements in ground based and spaced based observational facilities, there will be an exponential growth in this field in the coming years.

The compositional estimates obtained from the various detections are beginning to provide constraints not only on the atmospheric processes but also on the formation processes (Lavie *et al.*, 2017; Madhusudhan *et al.*, 2014c). Such conditions of temperature and composition are not seen in our own solar system, where the giant planets have a temperature of $\lesssim$100 K. These lower temperatures mean that species that can be used as chemical tracers of planetary formation, such as H_2O, CO and HCN, are condensed out (Atreya *et al.*, 2016; Wong *et al.*, 2004) and/or present in trace quantities (Cavalié *et al.*, 2008, 2010; Moreno *et al.*, 2003; Moses *et al.*, 2010). These species are however likely to be present in their gaseous form at significant abundances on hot Jupiters due to the higher temperatures. Therefore measuring the abundances of these species can provide key insights into planetary formation (Madhusudhan *et al.*, 2016). For instance, constraints on the C/O ratio can tell us where within a protoplanetary disk a planet may have formed, given that the C/O ratio varies with orbital distance within the gas in the disk as species condense out (Öberg *et al.*, 2011). These and other constraints on trace species can also tell about the migration of the planet to its current location close to its host star (Madhusudhan *et al.*, 2014c).

1.5 Atmospheric Modelling of Exoplanets

Central to the characterisation of exoplanetary atmospheres is the availability of high fidelity spectral models which are able to capture all of the relevant processes which may occur in planetary atmospheres. Two modelling approaches have been developed over time to address complementary needs: forward models and retrieval methods (see e.g., reviews by Heng and Showman, 2015; Madhusudhan *et al.*, 2014a, 2016). Forward models attempt to self-consistently model detailed physical and chemical processes in the atmospheres under various assumptions for chemical abundances,

energy transport mechanisms, chemical equilibrium/non-equilibrium, etc. Such models are extremely useful for a priori theoretical understanding of atmospheric processes in exoplanets under varied conditions, for predicting observable signatures to aid in planning observations, and for initial interpretation of data. The complexity of these models varies significantly, ranging from 1-D atmospheres (e.g. Burrows *et al.*, 2008; Fortney *et al.*, 2008; Mollière *et al.*, 2015; Seager *et al.*, 2005) to full 3-D general circulation models (e.g. Kataria *et al.*, 2015; Showman *et al.*, 2009). While such forward models are highly beneficial they are however limited in their capability to directly interpret observations.

Atmospheric retrieval on the other hand involves deriving the atmospheric properties of an exoplanet given an observed spectrum. The methods generally involve a parametric model, with the pressure-temperature ($P-T$) profile and abundances of chemical species as free parameters, with no prior assumptions about chemical or radiative equilibrium. The model is coupled to a statistical inference algorithm to explore the model space and estimate the parameters. A variety of statistical methods have been used in the literature with varying levels of sophistication and have resulted in constraints on temperature profiles and chemical abundances in several exoplanets (Evans *et al.*, 2017; Haynes *et al.*, 2015; Line *et al.*, 2014; Madhusudhan and Seager, 2009; Madhusudhan *et al.*, 2011a, 2014b). These retrieval methods have been the workhorse for deriving statistical estimates of atmospheric chemical abundances and temperature profiles from exoplanetary spectra in recent years (e.g. Benneke, 2015; Lavie *et al.*, 2016; Lee *et al.*, 2012; Line *et al.*, 2013; Madhusudhan *et al.*, 2014b; Waldmann *et al.*, 2015). However, such models do not regularly explore the physical plausibility of such observations or investigate the processes which may lead to such atmospheric conditions.

Both forward models (or 'self-consistent' models) and retrieval methods have their own strengths and limitations and are essential for thorough characterisation of exoplanetary atmospheres. The constraints on atmospheric properties derived from observations using retrieval methods need to be checked against self-consistent forward models to understand the conformance or deviations of the constrained solutions with respect to the assumptions of self-consistent models. The differences, if any, could lead to refinement of the models, constraints on non-equilibrium phenomena, and/or to discover new physical and chemical effects unaccounted for in the forward models. Efficient forward models of exoplanetary spectra are therefore vital to gain a good insight into exoplanetary atmospheres, particularly of those quite hostile worlds

stretching our current knowledge at the extremes of atmospheric conditions well beyond those encountered in the solar system.

1.6 Scope of this Thesis

This thesis explores both self-consistent atmospheric models and retrievals of exoplanetary atmospheres. I have developed both of these modelling frameworks in tandem, and used them to predict dayside atmospheric compositions and analyse the atmospheres of real systems via their datasets. I have also developed tools to generate atmospheric opacity tables for various prominent species expected on such planets. In addition to this, I have also generated high resolution emission spectra for multiple hot Jupiters for cross correlation in Doppler spectroscopy. Here I will briefly provide a broad outline and motivation for the work and the chapters contained herein.

1.6.1 Atmospheric Opacities

Central to the characterisation of spectra are the molecular, atomic and ionic opacities which are used to determine the emergent spectrum from an atmosphere. Chapter 2 details the calculations for each source of opacity in hot Jupiter atmospheres. These frequency dependent opacities result in spectral features in the spectra of these exoplanets, and leave an impression on the observed spectrum regarding the atmospheric composition. Accurate and complete line lists from databses such as HITEMP (Rothman *et al.*, 2010), EXOMOL (Tennyson *et al.*, 2016) and HITRAN (Rothman *et al.*, 2013) are vital for many of the detections within this thesis and provide the foundation for the retrieval and self-consistent models discussed below. I detail the theoretical basis for the spectral broadening of molecular lines and also discuss the sources of the line lists. The line lists form the basis for the calculation of the opacity of each chemical species with wavelength. These chemical species (e.g. H_2O and CO) dominate the spectra thanks to their high abundance and strong opacity. I pre-compute cross section tables for all of these species as a function of wavelength for pressures and temperatures typically expected in the photospheres of hot Jupiters. These tables are shared between all of my models in the subsequent chapters. I also include contribution from additional opacity sources such as collisionally induced absorption and Rayleigh scattering from the hydrogen and helium dominated atmospheres.

1.6.2 Self-Consistent Atmospheric Models: GENESIS

In chapter 3 I describe my work on self-consistent modelling of exoplanetary atmospheres. Such models of exoplanetary atmospheres have recently entered a new era. With high precision and high resolution observations both from the ground and space we are in detail able to probe the atmospheres of giant extra-solar planets. With such observations we see that planets have an extremely diverse chemistry, in many cases deviating from solar composition (e.g. Madhusudhan *et al.*, 2014b; Pinhas *et al.*, 2019; Sheppard *et al.*, 2017). Many of the most prominent previous works on self-consistent modelling (e.g. Burrows *et al.*, 2008; Fortney *et al.*, 2008; Hubeny *et al.*, 2003) have modelled atmospheres at solar composition and chemistry. There is thus a growing need for a new generation of models capable of encompassing a wide range of planetary atmospheres and compositions. The new radiative-convective equilibrium atmospheric forward model developed in this work, GENESIS, is capable of modelling irradiated and non-irradiated planets encompassing a wide range of parameters. This was demonstrated by modelling both hot Jupiters and brown dwarfs, over a wide range of chemical abundances and temperatures. I have explored the effect of C/O ratio, thermal inversions (stratospheres), equilibrium temperature and modelled the emission spectra for several prominent hot Jupiters. I have additionally modelled non-irradiated planets over a range of metallicities, C/O ratios and internal fluxes.

Previous work on self-consistent models has also shown that numerous species are capable of giving rise to stratospheres, or thermal inversions, in hot Jupiter atmospheres (e.g. Fortney *et al.*, 2008; Hubeny *et al.*, 2003; Lothringer *et al.*, 2018; Zahnle *et al.*, 2009). These inversions are of particular importance given that they have a strong influence on the emergent dayside spectrum and that the species which may be responsible are now being detected from ground based observations (Nugroho *et al.*, 2017; Sedaghati *et al.*, 2017). Even trace quantities of gaseous species such as TiO and VO are capable of giving thermal inversions thanks to their strong opacity. I have used GENESIS to explore thermal inversions further through the effect of visible and infrared opacity. Chapter 4 details many new species, hitherto not fully explored, which are capable of causing stratospheres on strongly irradiated giant exoplanets. Central to this has been the availability of new and more complete line lists for these metal rich species such as AlO, CaO, MgH and NaH (see chapter 2). In addition, I also explore the effect of varying the infrared opacity through the C/O ratio, and find that thermal inversions require much lower abundances for these metal-rich species for an atmospheric C/O ratio of 1.

1.6.3 Retrievals of Emission Spectra: HyDRA

In chapter 5 I present an atmospheric retrieval framework for dayside emission spectra. Numerous previous retrievals use chemically free retrieval models to explore a wide range of compositions (e.g. Haynes *et al.*, 2015; Madhusudhan *et al.*, 2014b) while others have used chemically consistent models (e.g. Line *et al.*, 2016), which restrict the atmospheric composition depending on the temperature profile and metallicity. Whilst the former is able to explore chemical species without biasing the results, the latter is able to obtain a more consistent solution when the datasets do not allow for many constraints. However, both of these have their disadvantages, either not exploring the physical plausibility of solutions or not allowing the exploration of the full range of parameter space. Given the diversity of hot Jupiter atmospheres that we already see, a framework that allows us to achieve both is advantageous but challenging. I have thus developed a new retrieval model, HyDRA, for emission spectra of hot Jupiters. This has been combined with the GENESIS self-consistent model to explore radiative-convective and chemical disequilibrium in exoplanetary atmospheres. The retrieval model has been developed alongside GENESIS and shares the underlying architecture. This was done to allow integration of the two models to explore non-equilibrium processes using the latest statistical analysis tools such as nested sampling (Feroz and Hobson, 2008; Feroz *et al.*, 2009, 2013). I demonstrate HyDRA by retrieving the emission spectrum of WASP-43b, a hot Jupiter with some of the most precise observations to date. I explore a wide range of atmospheric parameters to retrieve the best fitting parameters for the observations. I then proceed to test these retrieved parameters against chemical and radiative equilibrium to place constraints on any disequilibrium processes which may occur in the atmosphere.

I have also extended the HyDRA retrieval model to analyse the spectra of very strongly irradiated planets in chapter 6. This work was motivated by recent spectra of such ultra-hot planets, which show largely featureless HST WFC3 spectra (Arcangeli *et al.*, 2018; Evans *et al.*, 2017; Kreidberg *et al.*, 2018). These so called "ultra-hot Jupiters" have dayside temperatures in excess of 2500 K, which may lead to species such as H_2O thermally dissociating. In addition, H- may form in the atmosphere and affect the extent of spectral features. I have included both of these features into the HyDRA retrieval model and tested this by retrieving the dayside spectrum of WASP-18b, an ultra-hot Jupiter with some of the most precise WFC3 spectra available. In particular I explore the H_2O, CO and H- abundances retrieved as well as the thermal inversion present on the dayside. The study of such hot planets is particularly important given

that we have no such analogue in our own solar system to explore such extreme physics in planetary atmospheres.

Chapter 7 discusses a set of homogeneous retrievals that I have run using HyDRA for eight well known hot Jupiters with some of the most precise HST WFC3 and Spitzer photometric observations. These include some planets in the class of "ultra-hot Jupiters", such as WASP-18b, WASP-103b, WASP-121b and Kepler-13Ab. The numerous high precision observations recently made with the HST WFC3 spectrograph has motivated this work. With this influx of high quality observations we are now able to carry out these ensemble studies for hot Jupiters and explore how their dayside parameters vary with irradiation, stellar type and planetary mass and radius. In particular I retrieve the H_2O abundances and the temperature profiles as well as some constraints on several other species in each of the eight planets studied. These retrieved abundances and temperature profiles are tested against several planetary parameters to determine correlations therein. This marks one of the first studies of its kind to perform ensemble studies on emission spectra of hot Jupiter atmospheres. With many new facilities and a greater number of exoplanetary spectra on the horizon, such a study is highly relevant for future observations.

1.6.4 High Resolution Spectroscopy

High resolution spectroscopy from large ground based telescopes has recently yielded high significance detections of molecular species in the atmospheres of numerous hot Jupiters. Species such as CO, H_2O and TiO have been observed in the atmospheres from the Doppler shifting of atmospheric absorption lines as the planet traverses around its host star (e.g Birkby *et al.*, 2017; Brogi *et al.*, 2012; Nugroho *et al.*, 2017). These detections can be made at strong significance even at trace atmospheric abundance thanks to the uniqueness and sensitivity of the absorption lines in the spectrum. Central to these detections has been the spectral models for cross correlation against the very high resolution ($R\sim10^5$) observations. I have generated grids of high resolution model spectra, discussed in chapter 8, encompassing a wide range in atmospheric temperature and composition. These were generated with the GENESIS model for cross correlation against ground based VLT CRIRES observations. These models were used to identify several species in the atmospheres of two well studied transiting hot Jupiters, HD209458b and HD189733b. We explore H_2O, CO and HCN detections in both of these planets and detail robust statistical techniques in order to avoid false positives in the cross correlation. Such high resolution observations show

great promise for detection of many new species in the future given their sensitivity to trace abundances and their complementarity to low resolution observations.

1.6.5 Conclusions

The final chapter presents my concluding remarks, summarising the work and outlining potential future directions. In particular with many new planetary spectra and new instruments on the way, I discuss the implications for atmospheric characterisation of self-consistent and retrieval models as well as high resolution spectroscopy in the years to come.

Chapter 2

Sources of Opacity in Hot Giant Exoplanets

"I think I can safely say that no one understands quantum mechanics."
- Richard Feynman

This chapter describes the work I have done on generating cross sections of various chemical species present on hot Jupiters. The theoretical line list calculations have been published in Gandhi and Madhusudhan (2017), and subsequent co-authored works using these cross sections have detected numerous species through retrievals or through cross correlation with high resolution spectra (Cabot *et al.*, 2019; Chen *et al.*, 2018; Hawker *et al.*, 2018; Pinhas *et al.*, 2019; Sedaghati *et al.*, 2017; Sheppard *et al.*, 2017).

2.1 Introduction

In this chapter we discuss the sources of the opacity data in our model atmosphere. This wavelength dependent opacity is crucial as it determines the spectrum of the planet. The emission or transmission spectrum, as discussed in chapter 1, are our only means to probe the atmosphere's structure. Hence an understanding of all of the relevant processes by which the observations may be influenced is vital to gain an accurate understanding of the atmosphere's composition and structure. For any model atmosphere, the opacity is expressed in the form of the *absorption* and/or the *scattering* coefficient. The former determines the loss of photons from a beam of incident radiation by absorption of the species and the latter determines the loss from scattering of radiation. The sum of these is the *extinction* coefficient, which determines the total loss from the beam of incident radiation. Other processes can also act to

introduce radiation from scattering into the beam as well as thermal emission of a given species. We determine the cross sections and contributions to the opacity from all of the relevant species for hot Jupiter atmospheres in this chapter.

All of the species considered in the atmospheric modelling throughout this thesis are given in table 2.2 along with the quantum mechanical line lists used for each. The extinction coefficient of the atmosphere and therefore the emergent spectrum are strongly influenced by absorption from the many gaseous species present as well as collisionally induced absorption from H_2-H_2 and H_2-He and Rayleigh scattering from H_2. Molecular species such as H_2O, CH_4 and CO have opacity due to their ro-vibrational transition lines, which cause incoming photons to be absorbed and the molecule to enter an excited state. On the other hand, atomic species such as Na and K do not have ro-vibrational transitions, and instead electronic transitions absorb the incoming radiation. All of these transitions are highly important as they have been used to detect various species in the atmospheres of exoplanets through their emergent spectra (e.g. Charbonneau *et al.*, 2002; Madhusudhan *et al.*, 2014b). The total absorption and/or scattering coefficient in a given layer of the atmosphere is the sum of the contributions from all the various species present.

Two approaches have been used for opacity calculations in radiative transfer codes for modelling exoplanetary atmospheres. Some models (Drummond *et al.*, 2016; Fortney *et al.*, 2007; Malik *et al.*, 2017; Mollière *et al.*, 2015) use the k-distribution method which is commonly used in models of planetary and satellite atmospheres in the solar system (e.g., McKay *et al.*, 1989). In this approach, the molecular cross sections are reordered in wavelength bins and resampled on a coarser grid. This allows a small number of wavelength points to sample the opacity distribution function and, hence, lower computation times. It does however make the approximation that spectral lines of different molecules are perfectly correlated with each other in the bin, which is only accurate when the bins chosen are small enough in frequency space. In this work however we adopt the so-called line-by-line approach. Other groups (Barman *et al.*, 2001; Burrows *et al.*, 2008; Seager and Sasselov, 1998) have also used this approach, using the sampled opacity cross sections directly. Although common terminology in the exoplanetary atmospheres literature, strictly speaking this is not line-by-line as the cross sections are not computed from a native line list at each pressure and temperature for every model atmosphere. In the stellar atmospheres literature this technique is known as opacity sampling. The details of each method and the advantages and disadvantages are discussed in Hubeny and Mihalas (2014).

In recent years there has been significant progress towards determining the molecular opacities of prominent species in exoplanet atmospheres through very accurate and more complete line lists (Rothman *et al.*, 2010; Tennyson *et al.*, 2016). These line lists are very important for determining the atmospheric spectrum and therefore can influence detections of many species from spectroscopic observations of the exoplanets. New databases such as EXOMOL have been set up to explore high temperature opacity from various chemical species (e.g. Barber *et al.*, 2006; Yurchenko *et al.*, 2011, 2013). These offer more complete and accurate molecular opacity data for temperatures exceeding 1000 K expected to exist on hot Jupiters. Along with developments in the line positions and strengths, there has also been development in broadening parameters for each of these lines in H_2 rich atmospheres (e.g. Barton *et al.*, 2017; Faure *et al.*, 2013). These offer more accurate molecular cross sections over standard air or self broadening given that hot Jupiter atmospheres are H_2/He rich. We now discuss the calculations to work out the molecular cross section of a given species at various temperatures and pressures.

2.2 Cross Section Calculations

This section describes the molecular and atomic cross section calculations for each species through from their line list. The frequency-dependent absorption cross sections of a given molecule depend on both the temperature and pressure which contribute to the broadening of a transition line. These line lists have been obtained from the HITEMP (Rothman *et al.*, 2010), EXOMOL (Tennyson *et al.*, 2016) and HITRAN (Rothman *et al.*, 2013) databases. These databases provide high temperature line lists and their corresponding partition functions. Each ro-vibrational transition is spectrally broadened with respect to pressure and temperature resulting in a wavelength dependent cross section for each $P-T$ combination. Numerous works have explored the broadening of spectral lines due to pressure and temperature (Grimm and Heng, 2015; Hill *et al.*, 2013; Yurchenko *et al.*, 2018). We calculate the cross sections from these line lists following a similar method to Hedges and Madhusudhan (2016).

The line strengths, $S_0 \equiv S(T_{\rm ref})$ in the database are typically given at a reference temperature (commonly 296 K) and are converted to a general temperature by (Rothman *et al.*, 1998),

$$S(T) = S_0 \frac{Q(T_{\rm ref})}{Q(T)} \frac{\exp(-E_{\rm lower}/k_b T)}{\exp(-E_{\rm lower}/k_b T_{\rm ref})} \frac{1-\exp(-h\nu_0/k_b T)}{1-\exp(-h\nu_0/k_b T_{\rm ref})}, \tag{2.1}$$

where E_{lower} is the lower energy state of the transition, ν_0 is the frequency of the transition line ($E_{\text{upper}} - E_{\text{lower}} = h\nu_0$) and Q is the partition function,

$$Q(T) = \sum_j g_j \exp(-E_j/k_b T) \tag{2.2}$$

with the degeneracy of the state j given by g_j and where k_b is the Boltzmann constant.

Once the line strength is obtained, the broadening of the line needs to be taken into account. At a given temperature, thermal motion of the molecule from a Maxwell-Boltzmann type distribution will result in a Doppler shift of the line. This will blur out the transition line, so instead of a sharp absorption peak, a Gaussian shape will be observed. For a molecule of mass m, the Gaussian profile f_D is given by

$$f_D(\nu - \nu_0) = \frac{1}{\gamma_G\sqrt{\pi}} \exp\left(-\frac{(\nu - \nu_0)^2}{\gamma_G^2}\right), \tag{2.3}$$

$$\gamma_G \equiv \sqrt{\frac{2k_b T}{m}} \frac{\nu_0}{c}. \tag{2.4}$$

In this case the full width half maximum of the gaussian is given by $\sqrt{2}\gamma_G$, and the frequency ν and the central line frequency ν_0 are given in cm^{-1}. The line will also become broadened due to the pressure of the gas. This will result in a Lorentzian profile,

$$f_P(\nu - \nu_0) = \frac{1}{\pi} \frac{\gamma_L}{(\nu - \nu_0)^2 + \gamma_L^2}, \tag{2.5}$$

$$\gamma_L \equiv \left(\frac{T_{\text{ref}}}{T}\right)^n P \sum_b \gamma_{L,b}\, p_b, \tag{2.6}$$

with $\gamma_{L,b}$ the Lorentzian HWHM from a specific broadening molecule, and n a temperature scaling factor. Pressure broadening can be more difficult to calculate, as the parameters n and $\gamma_{L,b}$ are needed, and depend not just on the line, but also the main constituent of the atmosphere. Given that we are modelling giant planet atmospheres, ideally we would need pressure broadening parameters due to H_2. However, such data is only now becoming available and for only a couple of molecules (Barton *et al.*, 2017; Faure *et al.*, 2013; Wilzewski *et al.*, 2015). Therefore, in the present work we have instead used parameters for air broadening for all the molecules for a uniform analysis. We tested for H_2O cross sections with H_2 broadening to find that the differences are not significant for the current analysis. Nevertheless, our opacity database is continually updated with new broadening data.

The full broadening of a line will be the convolution of the Gaussian and Lorentzian profiles, known as the Voigt function,

$$f_V(\nu - \nu_0) = \int_{-\infty}^{\infty} f_D(\nu' - \nu_0) f_P(\nu - \nu') d\nu'. \tag{2.7}$$

The characteristic width of the function is given approximately by $\gamma_V \approx 0.5346\gamma_L + \sqrt{0.2166\gamma_L^2 + \gamma_G^2}$. Defining new variables

$$u = \frac{\nu - \nu_0}{\gamma_G}, \tag{2.8}$$

$$a = \frac{\gamma_L}{\gamma_G}, \tag{2.9}$$

the Voigt function can be cast in terms of the normalised Faddeeva function $w(z)$ (see Grimm and Heng, 2015; Hedges and Madhusudhan, 2016),

$$f_V(\nu, \gamma_L, \gamma_G) = \frac{\mathrm{Re}(w(u + ia))}{\gamma_G\sqrt{\pi}}. \tag{2.10}$$

The cross section at a certain frequency ν, for a particular line including broadening is then

$$\sigma_\nu = S(T) f_V(\nu, \gamma_L, \gamma_G). \tag{2.11}$$

The total cross section is then the combination of σ_ν from each line. The σ_ν values were calculated on a fine resolution grid with a frequency spacing determined from the characteristic width of a line at $500\,\mathrm{cm}^{-1}$ at each pressure and temperature that we considered, i.e., taking the spacing of the frequency grid to be $\gamma_V(500\,\mathrm{cm}^{-1}, T, P)/6$, which typically is much less than $0.1\,\mathrm{cm}^{-1}$. When this spacing proved to be larger than $0.1\,\mathrm{cm}^{-1}$, e.g. for strong pressure broadening, a minimum spacing of $0.1\,\mathrm{cm}^{-1}$ was used. The cut-off for the line wings was chosen to be at $\pm 250\gamma_V$ for $P < 1$ bar and $\pm 500\gamma_V$ for $P \geq 1$ bar for every line in the database. The reasoning behind these choices are given in detail in Hedges and Madhusudhan (2016). An alternative approach combining multiple transition lines through the concept of super-lines is explored in Yurchenko *et al.* (2017) and Rey *et al.* (2016) and offers the advantage of computational efficiency when line lists are large.

Our cross section database spans a wide range in P, T, and frequency to encompass wide ranging scenarios for planetary atmospheres and observations. Table 2.1 shows the P and T grid over which the cross sections were computed for each molecular species,

T(K)	300	400	500	600	700	800	900	1000
	1200	1400	1600	1800	2000	2500	3000	3500
P(bar)	10^{-5}	10^{-4}	10^{-3}	10^{-2}	10^{-1}	1	10	100

Table 2.1 The temperature and pressure grid for the cross sections, which are the same as those used in Hedges and Madhusudhan (2016).

and spans the ranges relevant for giant exoplanetary and brown dwarf atmospheres. The pressure grid ranged from 10^{-5} bar to 100 bar, in 7 steps equally spaced in log pressure. The temperature grid spanned 300 - 3500 K. Some of the partition functions do not go up as high as the highest temperatures considered here and in such cases an extrapolation is done by a cubic. The line-by-line cross sections were ultimately binned down and stored at a resolution of $0.1\,\mathrm{cm}^{-1}$ in the spectral range of $25000\,\mathrm{cm}^{-1}$ ($0.4\ \mu$m) to $200\,\mathrm{cm}^{-1}$ ($50\ \mu$m). While this resolution is adequate for our current purpose higher resolution can be easily achieved as need be. For example, while interpreting high resolution spectra of R$\sim 10^5$ we compute cross sections with a wavenumber spacing of 0.01 cm^{-1} as discussed in chapter 8.

The molecular cross section of each species is multiplied by the number density of the species $n_i = \mathrm{X}_i n$, to give the *absorption* coefficient for species i,

$$\kappa_i(\nu) = \mathrm{X}_i n \sigma_\nu(P, T). \tag{2.12}$$

Here, X_i is the volume mixing fraction of species i and n is the number density of gas.

2.2.1 Infrared Opacity

Figure 1.3 shows the molecular cross section for some of the prominent volatile species typically expected in the atmospheres of hot Jupiters. These cross sections have been determined at a representative temperature and pressure through the broadening of the molecular lines from their relevant line lists (as given in table 2.2). They clearly show the absorption cross sections for each species, which show the molecular bands for each species. Each species is dominant over the others in certain wavelength ranges. H_2O for instance shows strong absorption at $\sim$1.4 μm, in the Hubble Space Telescope's Wide Field Camera 3 (HST WFC3) spectral range and thus its abundance can be well constrained. On the other hand, CO shows the strongest cross section at $\sim$5 μm, where it is dominant over the other species. This can be used to constrain its abundance through Spitzer photometric observations between $\sim$3.6-10 μm. The other species such

as CH_4, NH_3 and HCN also show strong absorption cross sections, but their expected atmospheric abundance is lower than that for H_2O or CO (Moses *et al.*, 2013). They are therefore expected to have a smaller influence on the observed spectrum due to their weaker spectral features. With future telescopes such as JWST on the horizon, a much greater spectral range will be probed, allowing for tighter constraints on numerous trace species.

2.2.2 Visible opacity

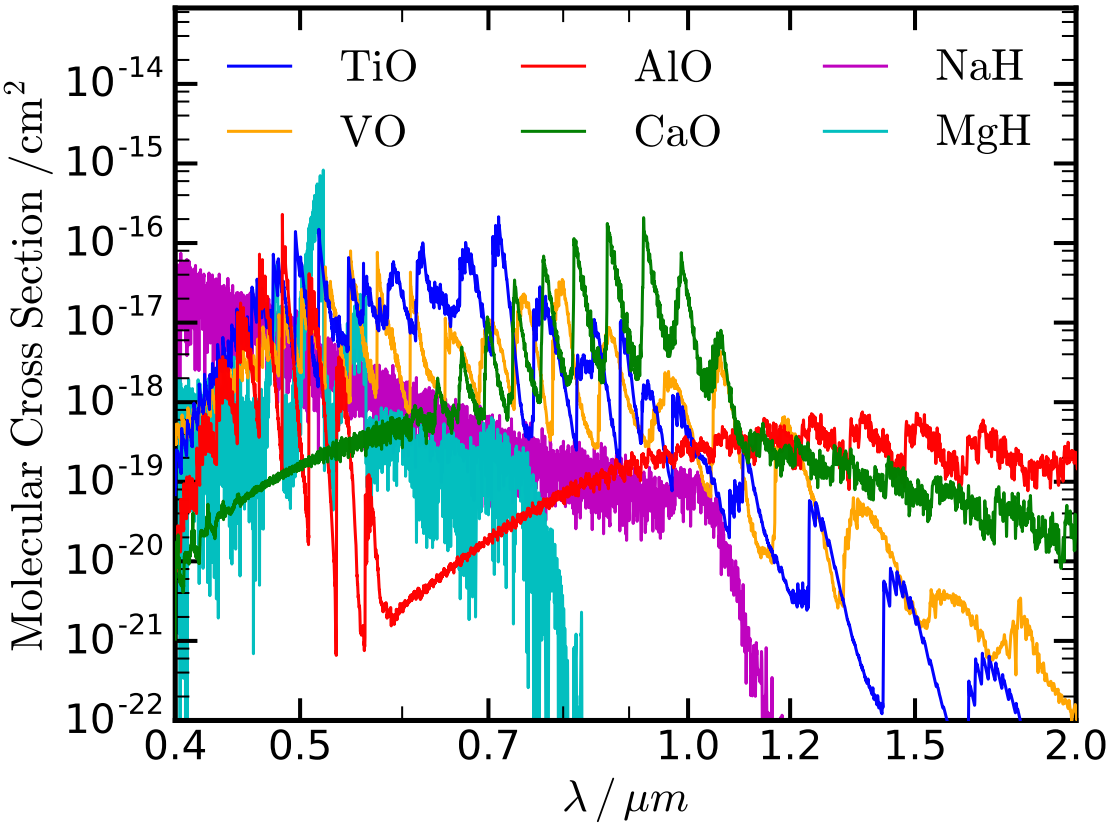

Fig. 2.1 Molecular cross sections of chemical species with strong absorption cross sections in the visible. The cross sections were calculated at representative conditions of 0.1 bar pressure and 2000 K.

Species such as TiO and VO have long been theorised to cause thermal inversions (stratospheres) in the atmospheres of hot Jupiters (Fortney *et al.*, 2008; Hubeny *et al.*, 2003; Spiegel *et al.*, 2009). Recently, detections of TiO have been made thanks to ground based VLT observations (Sedaghati *et al.*, 2017). Such species are capable of

strong absorption of the incident stellar radiation due to their large cross section in the visible. This heats these upper layers of the atmosphere leaving ones underneath cool and thus results in a thermal inversion. This inversion has a strong influence on the emergent spectrum (see chapter 4) and is therefore of great importance in the study of emergent dayside spectra.

As well as TiO and VO, strong visible opacity can arise from a number of different species such as AlO, CaO, NaH and MgH (see fig. 2.1). These cross sections have been derived from the EXOMOL line lists for each molecule (Patrascu *et al.*, 2015; Rivlin *et al.*, 2015; Yadin *et al.*, 2012; Yurchenko *et al.*, 2016). They all have distinct cross sections, but over the visible spectrum they provide similar strong opacity. AlO has a peak cross section near $\sim$0.5 μm, and CaO has a peak nearer 1 μm. Even though these molecules are often present at much lower abundances than the volatiles such as H_2O, CO and CH_4, they are all capable of causing thermal inversions in the stratosphere thanks to their cross section. An in depth discussion of the effect of the infrared and visible opacity on thermal inversions can be found in chapter 4.

2.2.3 High Resolution Cross Sections

Recently, very high resolution spectra of R$\sim$100,000 have been obtained for a number of hot Jupiters through ground based observations using instruments such as VLT CRIRES (Birkby *et al.*, 2013; Brogi *et al.*, 2012, 2017; Snellen *et al.*, 2010). These studies involve observing the planet over a very small spectral range, typically $\Delta\lambda \sim 0.1\,\mu$m. Despite the relatively small spectral range of the observations, detections of multiple species in the atmospheres of extra-solar giant planets has been made possible. This has been achieved as observations are able to resolve individual transition lines in molecules present within the atmosphere, and are sensitive even to trace quantities of species. Spectral templates are constructed for cross correlation against these observations to detect the various species in the atmosphere. These spectral templates require very high resolution in order to resolve the molecular transition lines in the observations.

Therefore, very high resolution and precision spectra and thus cross sections are required in order to resolve individual transition lines for each species. To achieve this we have also generated molecular cross sections for the volatile species, namely H_2O, CH_4, NH_3, CO, HCN and CO_2, at a wavenumber spacing of 0.01 cm^{-1}. This corresponds to a spectral resolution of R$\sim$400,000 at 2.3 μm (K band) and R$\sim$300,000 at 3.2 μm (L band), and hence these cross sections are capable of resolving the transitions in the R$\sim10^5$ observations. These high resolution cross sections are shown for H_2O, CO and HCN in fig. 2.2. We used these high resolution cross sections as the basis for

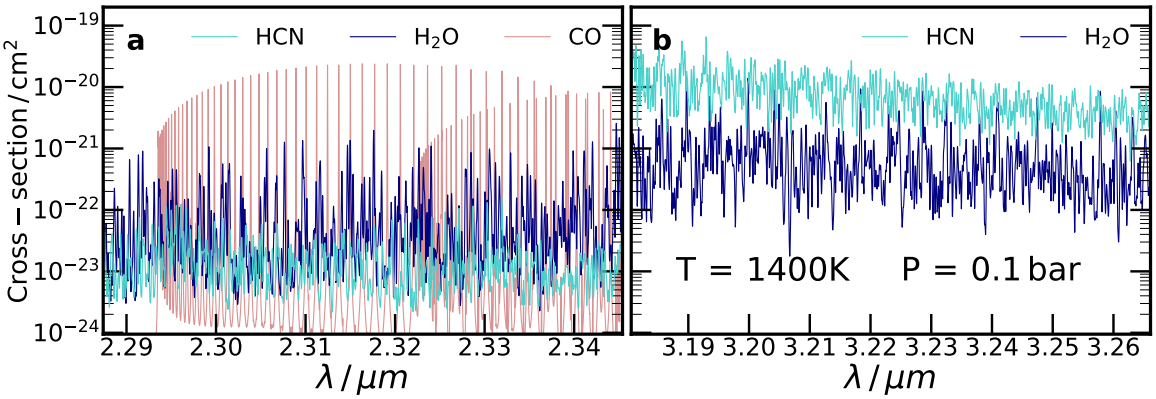

Fig. 2.2 High resolution molecular cross section for the 2.3 μm and 3.2 μm band for HCN, H_2O and CO. These opacities formed the basis for high resolution cross correlation spectral templates (see chapter 8).

the spectra which detected H_2O, CO and HCN in the atmospheres of two of the most well studied hot Jupiters, HD209458b and HD189733b (see chapter 8).

2.3 H- opacity

As well as molecular and atomic species, ionic species such as H- may also be present in sufficient quantities to affect the emergent spectrum. The H- has a strong cross section and thus can have strong absorption even when present at trace abundances. This opacity becomes relevant only for the very hottest of exoplanets, with equilibrium temperatures in excess of 2500 K, where H- may form in the atmosphere through thermal dissociation of H_2 (Lothringer *et al.*, 2018; Parmentier *et al.*, 2018). Fig. 2.3 shows the abundance weighted cross section for H- at a pressure and temperature typical for such hot exoplanets. The H- cross section arises as a result of two separate sources of opacity, bound-free photo-detachment and free-free transitions. Both of these sources of opacity result in broad features in the cross section, unlike with molecular cross sections which consist of many millions of broadened transition lines. The bound-free transitions have strong absorption at λ<1.64 μm, up to the photo-detachment threshold wavelength, and are in fact the dominant source of opacity in cool stars (Wishart, 1979). At higher wavelengths, the free-free transitions are the only contributors to the cross section of H-. Both of these opacity contributions are summed to give the total cross section of H-.

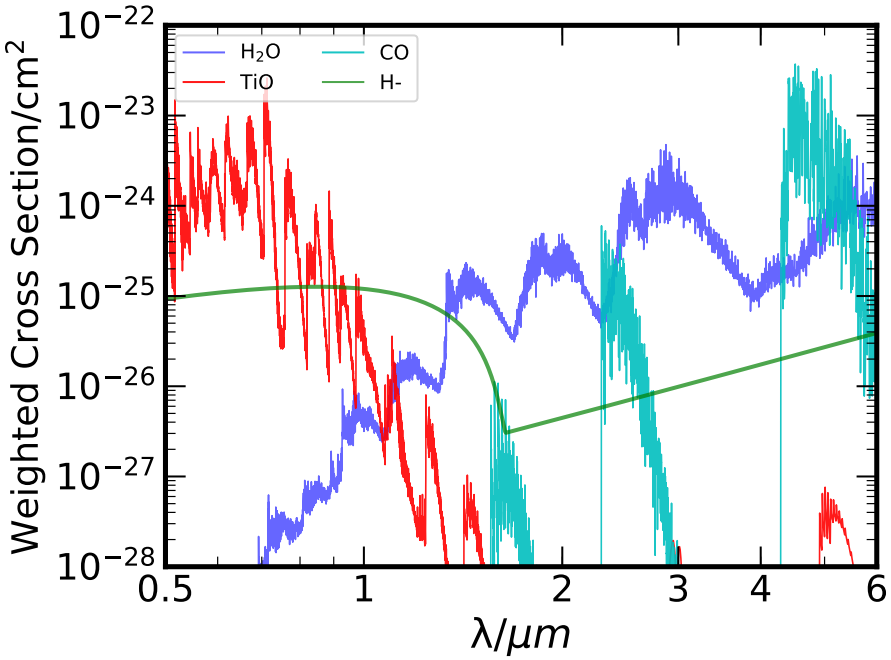

Fig. 2.3 Abundance weighted cross section for H- at a temperature of 2900 K and 0.33 bar pressure. The abundance weighted cross sections of H_2O, TiO and CO are also shown. The abundances have been calculated from the dissociation model by Parmentier *et al.* (2018) discussed in chapter 6.

The bound-free opacity arises due to the absorption of a photon by H-,

$$h\nu + \text{H-} \rightarrow \text{H} + \text{e}^-.$$

The cross section of this reaction, $\sigma_{\text{H}-}$, is given by

$$\sigma_{\text{H}-}(\lambda < \lambda_0) = 10^{-18}\lambda^3\left(\frac{1}{\lambda} - \frac{1}{\lambda_0}\right)^{3/2} f(\lambda)\text{cm}^2, \tag{2.13}$$

where λ represents the wavelength in μm, $\lambda_0 = 1.6419\mu$m is the photo-detachment threshold and $f(\lambda)$ is a slowly varying function (John, 1988). These bound-free transitions result in a cutoff in the opacity at the photo-detachment threshold, with a strong cross section at $\lambda < \lambda_0$ as shown in fig. 2.3. This cutoff is of particular importance given that λ_0 is within the HST WFC3 bandpass (1.1-1.7 μm).

The free-free transitions on the other hand occur due to the following chemical interaction (Bell and Berrington, 1987)

$$h\nu + \mathrm{e}^- + \mathrm{H} \rightarrow \mathrm{H} + \mathrm{e}^-.$$

These transitions are important sources of infrared opacity for late spectral stars (Bell and Berrington, 1987). This opacity may also be important on ultra-hot Jupiters given the similar temperature range, particularly for the Spitzer photometric observations at longer wavelengths where this cross section is stronger (see fig. 2.3). A more detailed study of the free-free absorption due to H- can be found in John (1988) and Bell and Berrington (1987). The overall *absorption* coefficient is given by

$$\kappa_{\mathrm{H}^-}(\nu) = \mathrm{X}_{\mathrm{H}^-} n \sigma_{\mathrm{H}^-}(P, T, \nu). \tag{2.14}$$

2.4 Collisionally Induced Absorption

As well as molecular absorption, collisionally induced absorption from the H_2 and He rich atmosphere is also required. This H_2-H_2 and H_2-He absorption is obtained from the HITRAN database (Abel *et al.*, 2011, 2012; Karman *et al.*, 2019; Richard *et al.*, 2012). This opacity is different to the molecular cross sections calculated above in a number of ways. Firstly, given that there are no transition lines the absorption is smooth and continuous with wavelength. Secondly, as this opacity scales quadratically with the number density of H_2 and H_2/He, spectra from the atmosphere now result in a continuum opacity at very high optical depth given that this now dominates other sources at deep pressures where the number density of species is very high. The absorption coefficient for H_2-H_2 and H_2-He collisionally induced absorption is given by

$$\kappa_{\mathrm{H_2-H_2}}(\nu) = \mathrm{X}_{\mathrm{H_2}} \mathrm{X}_{\mathrm{H_2}} n \sigma_{\mathrm{CIA,H_2-H_2}}(T, \nu), \tag{2.15}$$

$$\kappa_{\mathrm{H_2-He}}(\nu) = \mathrm{X}_{\mathrm{H_2}} \mathrm{X}_{\mathrm{He}} n \sigma_{\mathrm{CIA,H_2-He}}(T, \nu), \tag{2.16}$$

where $\sigma_{\mathrm{CIA,H_2-He}}$ and $\sigma_{\mathrm{CIA,H_2-H_2}}$ are obtained from Richard *et al.* (2012).

Species	Reference	Species	Reference
H_2O	Rothman *et al.* (2010) and Barber *et al.* (2006)	TiO	Kurucz (1992)
CH_4	Yurchenko *et al.* (2013)	VO	McKemmish *et al.* (2016)
NH_3	Yurchenko *et al.* (2011)	AlO	Patrascu *et al.* (2015)
CO	Rothman *et al.* (2010)	CaO	Yurchenko *et al.* (2016)
HCN	Harris *et al.* (2006) and Barber *et al.* (2014)	NaH	Rivlin *et al.* (2015)
CO_2	Rothman *et al.* (2010)	MgH	Yadin *et al.* (2012)
C_2H_2	Rothman *et al.* (2013)	Na	Kramida *et al.* (2018)
H-	Wishart (1979) and John (1988)	K	Kramida *et al.* (2018)

Table 2.2 References for the line lists/opacity sources for each of the species considered in this work.

2.5 Rayleigh Scattering due to Molecular Hydrogen

We also consider Rayleigh scattering due to molecular hydrogen in the atmosphere. This has the most significant effect on the emergent and transmission spectrum at short wavelengths in the visible range. At such wavelengths, where the stellar flux is strongest, the Rayleigh scattering can also influence the equilibrium $P-T$ profiles of the atmosphere by scattering the incoming radiation. We use the work by Dalgarno and Williams (1962) to determine the scattering from H_2. This is given by

$$\kappa_{\text{Rayleigh}} = \mathrm{X}_{\mathrm{H}_2} n \left(\frac{8.14 \times 10^{-53}}{\lambda^4} + \frac{1.28 \times 10^{-66}}{\lambda^6} + \frac{1.61 \times 10^{-80}}{\lambda^8} \right), \tag{2.17}$$

where λ is the wavelength in m and κ_{Rayleigh} represents the *scattering* coefficient in m^{-1}. As before, n represents the number density of gas which, for an ideal gas, is given by $n = P/(k_b T)$ and $\mathrm{X}_{\mathrm{H}_2}$ represents the volume mixing ratio of H_2.

Chapter 3

GENESIS: Self-Consistent Models of Exoplanetary Spectra

"In the beginning the Universe was created. This has made a lot of people very angry and been widely regarded as a bad move."
- D. Adams, The Hitchhiker's Guide to the Galaxy

This chapter introduces my GENESIS self-consistent model, which generates dayside spectra of exoplanetary atmospheres in radiative-convective and chemical equilibrium. This work is published in Gandhi and Madhusudhan (2017). GENESIS is also used in chapters 4 and 5 to simulate equilibrium processes for planets under various conditions. The model has also been used to generate grids of spectra for cross correlation against high resolution VLT observations, discussed in chapter 8.

3.1 Previous Work on Self-Consistent Modelling

Over the past two decades various groups have developed self-consistent models with different levels of complexity and accuracy. Here we discuss some of the prominent plane-parallel self-consistent forward models of atmospheric spectra in the field that take into account strong irradiation, as relevant for currently known transiting exoplanets (Barman *et al.*, 2001; Burrows *et al.*, 2008; Drummond *et al.*, 2016; Fortney *et al.*, 2007; Malik *et al.*, 2017; Mollière *et al.*, 2015; Mollière *et al.*, 2017; Seager and Sasselov, 1998; Sudarsky *et al.*, 2003). Table 3.1 shows a comparison of these models, many of which have been adapted from pre-existing forward models originally built to model radiative transfer in stellar atmospheres (e.g., Hauschildt, 1992; Hubeny and Lanz, 1995; Vaz and Nordlund, 1985), atmospheres of planets in the solar system (Marley and McKay, 1999)

or circumstellar discs (Dullemond, C. P. *et al.*, 2002). Typically, such models assume a given chemical composition and solve for the temperature profile and emergent spectrum of the atmosphere under assumptions of radiative-convective equilibrium, hydrostatic equilibrium, and local thermodynamic equilibrium (LTE), for given system parameters and boundary conditions. Typically, models assume thermochemical equilibrium to determine the chemical composition for assumed elemental abundances.

The differences between the various forward models in Table 3.1 lie in the sophistication of their numerical methods and assumptions therein. Some key aspects where differences lie include the approaches for solving the radiative transfer equation (RTE) and for ensuring radiative-convective equilibrium, the opacities used (e.g. line-by-line vs correlated-k approximation), and the incorporation of physical processes such as clouds, convection, etc. Models adapted from pre-existing stellar atmosphere codes (e.g., Barman *et al.*, 2005; Burrows *et al.*, 2008), such as TLUSTY or PHOENIX, have the advantage of very accurate radiative transfer solvers and temperature correction procedures. On the other hand, such models are based on pre-computed opacity grids with assumed chemical compositions, e.g. of chemical equilibrium with solar abundances, and hence less flexible/efficient to explore a wide range in chemical parameter space. On the other hand, codes adapted from planetary applications (Fortney *et al.*, 2008; Marley *et al.*, 2012) assume the two-stream source function approximation to solve the RTE, with two distinct beams of radiation directed inwards and outwards from the planet atmosphere. This is computationally efficient but not as accurate as a full angle dependent solution (see e.g. Hubeny (2017); Hubeny and Mihalas (2014)).

More recent models have been custom-built for exoplanetary atmospheres. Mollière *et al.* (2015) and Mollière *et al.* (2017) developed a model based on the methods of Dullemond, C. P. *et al.* (2002), originally developed for radiative transfer in protoplanetary discs. They solve the RTE using the Feautrier method and determine the temperature profile in equilibrium using the variable Eddington factor approach, and include scattering due to condensate species along with opacities computed using the k-distribution method. Drummond *et al.* (2016) have constructed a model that uses accelerated lambda iteration for their radiative transfer, and also including scattering from condensate species (Ackerman and Marley, 2001). Another recently developed code, HELIOS (Malik *et al.*, 2017), adopts the two-stream approximation for the radiative transfer, which assumes two distinct beams of radiation emanating from and travelling into the planet's atmosphere. Their work also the correlated-k approximation for opacities, albeit with differences in temperature correction methods and treatment of scattering. Malik *et al.* (2017) have implemented an analytic solution of the transfer

equation that allows one to specify an arbitrary number of streams in the limit of pure absorption. A detailed comparison of these different models can be found in Hubeny (2017). These recent codes (Drummond *et al.*, 2016; Malik *et al.*, 2017; Mollière *et al.*, 2017) are customised to explore a wide range of chemical compositions (e.g. metallicities and C/O ratios) motivated by recent suggestions of the importance of these quantities (Madhusudhan, 2012; Moses *et al.*, 2013).

3.2 The GENESIS Model

There is a need for a new generation of models that build upon the past successes to address the new wave of current and upcoming high quality data. The most desirable spectral code arguably is one that obtains an accurate formal solution of the radiative transfer equation (e.g. using the Feautrier method) and robustly derives the temperature correction for radiative-convective equilibrium, e.g. using a formal Rybicki procedure or accelerated Lambda Iteration (see e.g. Hubeny, 2017), and considers high density opacity sampling or "line-by-line" opacities, with flexible chemistry. Such a model is highly desirable for the planning and interpretation of high-precision and high-resolution spectroscopic observations expected from current and upcoming large facilities. On the other hand, such a code would also be invaluable to be integrated into detailed higher dimensional models of non-equilibrium chemistry and general circulation models to understand chemical and physical processes in exoplanetary atmospheres at high resolution. Finally, there is great value to a coherently developed model architecture where all the components, from radiative transfer, energy balance, and chemistry, to line-by-line broadened opacities, are developed with the latest computing practices and languages, and all tuned to exoplanet conditions. Efforts in this direction have been made by several groups worldwide (Drummond *et al.*, 2016; Malik *et al.*, 2017; Mollière *et al.*, 2017).

Model	**R-T Solver**[1]	**T-correction**[2]	**Parent code**	**Opacity**	**Convection**	**Clouds**	**Scattering**
Seager et al. 1998, 2005	Feautrier	Entropy conservation	UMA	line-by-line	Yes	Yes	Yes
Barman et al. 2001, 2005	Short characteristics+ALI	Unsöld-Lucy correction	PHOENIX	line-by-line	Yes	Yes	Yes
Fortney et al. 2006, 2008	2-stream source function	Linearise flux transfer	McKay et al. 1989	corr.-k	Yes	Yes	Yes
Burrows et al. 2008	Feautrier/DFE+ALI	Rybicki	TLUSTY	line-by-line	Yes	Yes	Yes
Mollière et al. 2015, 2017	Feautrier	Variable Eddington factor	New	corr.-k	Yes	Yes	Yes
Drummond et al. 2016	ALI	Local flux balance	New	corr.-k	Yes	Yes	Yes
Malik et al. 2017	2-stream approximation	Local flux balance	New	corr.-k	No	Yes	Yes
This work	Feautrier	Rybicki	New	line-by-line	Yes	No	Yes[†]

Table 3.1 Comparison of prominent atmospheric models in the literature including strong irradiation. Details of the methods used by Fortney et al. can be found in Toon *et al.* (1989) and McKay *et al.* (1989), Burrows et al. in Sudarsky *et al.* (2003) with their methods in Hubeny and Mihalas (2014), Barman *et al.* (2001) describe their methods in Hauschildt and Baron (1999), Malik et al. in Malik *et al.* (2017) and Heng *et al.* (2014), Seager et al. in Seager and Sasselov (1998) with methods in Vaz and Nordlund (1985) and Mollière et al. in Mollière *et al.* (2015); Mollière *et al.* (2017). The model used by Drummond *et al.* (2016) can be found in the paper and Amundsen *et al.* (2014).
[1] Radiative Transfer solver used in the model.
[2] Temperature correction scheme used to ensure radiative-convective equilibrium.
The remaining columns describe other aspects, including whether convection and clouds are incorporated in the model, and whether the opacities are treated in a line-by-line or using the correlated-k approximation. See section 3.1 for a discussion of the different models.
[†]In the present work we only consider weak scattering, due to gaseous H_2 Rayleigh scattering.

In this chapter we report a new state-of-the-art forward model of exoplanetary atmospheres. We introduce GENESIS, a plane-parallel, line-by-line, self-consistent exoplanetary atmospheric modelling code built upon accurate numerical techniques and the latest opacities and chemical resources. The radiative transfer is solved using Feautrier's method, which is second-order accurate, and the radiative-convective equilibrium is established using Rybicki's method with complete linearisation (Hubeny and Mihalas, 2014). The molecular opacity is calculated from contemporary line lists available to compute the latest high-temperature cross sections with accurate prescriptions for temperature and pressure broadening. The chemical abundances are derived assuming thermochemical equilibrium with variable elemental abundances, in order to facilitate efficient exploration of the chemical phase space (spanning C/O ratios, metallicities, visible absorbers, etc.). The code self-consistently and simultaneously treats both incident irradiation and internal flux so that it is applicable to both irradiated exoplanets as well as isolated planets.

In order to demonstrate the GENESIS code we focus on cloud-free giant exoplanets, both irradiated and non-irradiated, and explore a range of model parameters. All components of the code are extensively tested for accuracy and convergence and provide good match to published models. We generate high-resolution emergent spectra and pressure-temperature ($P-T$) profiles for models over a wide range in equilibrium temperature (i.e., degree of irradiation), metallicity, C/O ratio and internal flux, spanning both planets with and without strong irradiation. Additionally, for planets with strong irradiation we explore the dependence of the models on the visible absorption, via Na/K and TiO opacity. In particular, we demonstrate how the strength of thermal inversions depend on the TiO abundance. We also report model spectra and $P-T$ profiles for several known hot Jupiters.

In what follows we first describe in section 3.3 the various components of the GENESIS code and the numerical methods used to model the atmosphere. We present the model grid and results in section 3.4, including models of several known systems. We present a summary of the results and a discussion of ongoing and future work in section 3.5.

3.3 Methods

We model a fully self-consistent plane parallel atmosphere in radiative-convective equilibrium, local thermodynamic equilibrium and chemical equilibrium. Our goal is to compute model emergent spectra and the atmospheric profiles of temperature, pressure,

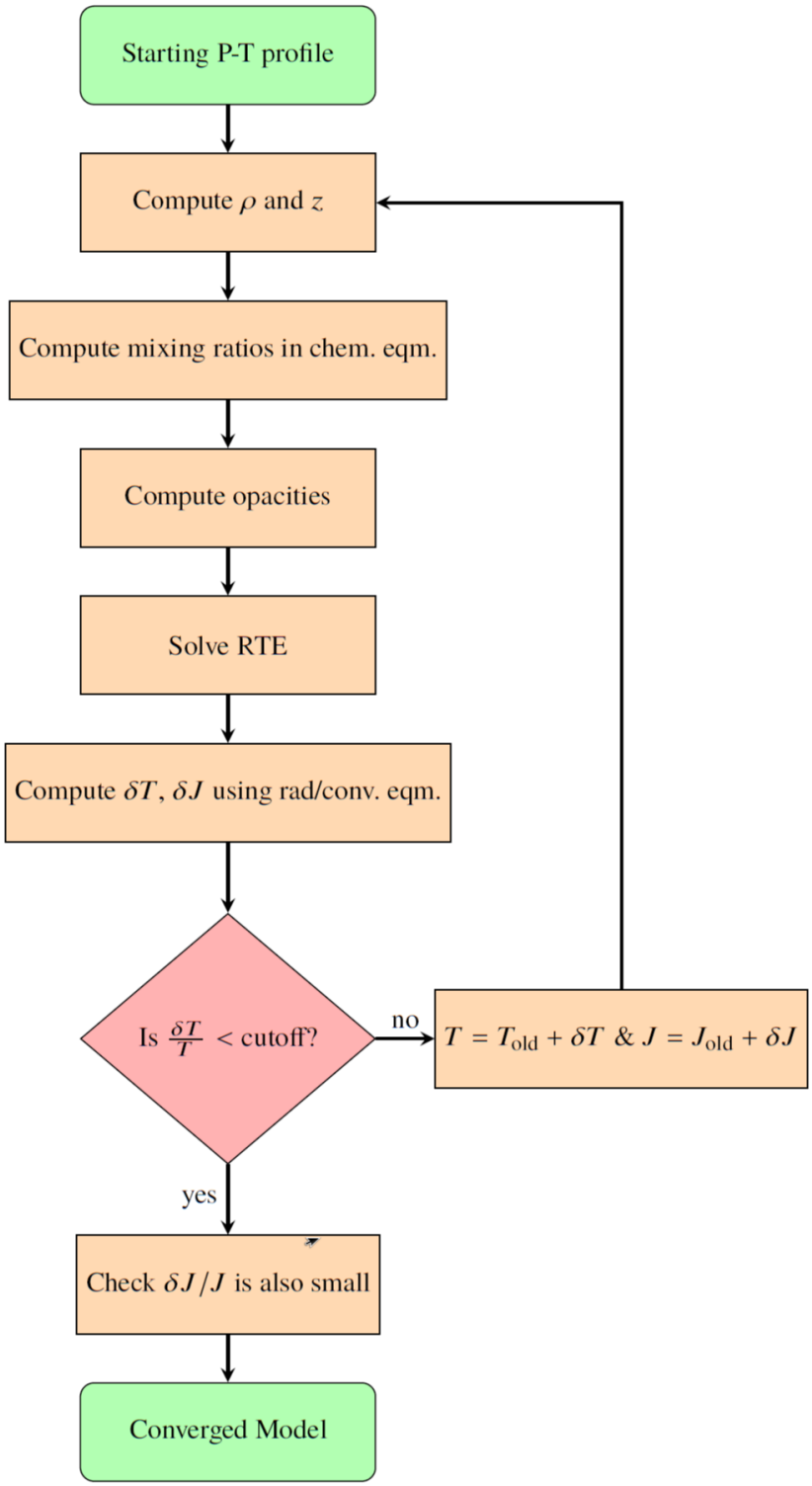

Fig. 3.1 The GENESIS Modelling Framework. The flowchart shows the key components of the model and the steps followed to converge to radiative-convective equilibrium. The description of each step is given in section 3.3.2.

Inputs					**Key Features**
Stellar Properties:	$R_{\rm star}$	$\log(g_{\rm star})$	$T_{\rm eff,star}$	$Z_{\rm star}$	RTE using Feautrier Method
Planet Properties:	$R_{\rm planet}$	$\log(g_{\rm planet})$	$T_{\rm int,planet}$	$a_{\rm planet}$	Rybicki's method for temperature iterator
	d	$f_{\rm r}$	Mixing length l	{X/H}	Chemical Equilibrium option
Outputs					Convection from mixing length theory
Spectrum		Profiles of P, T, ρ, chemical species			Line-by-line opacities
Not yet included:		Clouds			Irradiated and non-irradiated atmospheres

Table 3.2 The inputs, outputs and key features of GENESIS. $R_{\rm star}$, $\log(g_{\rm star})$, $T_{\rm eff,star}$ and $Z_{\rm star}$ are the radius, log(gravity), metallicity, and effective temperature of the planet hosting star. $R_{\rm planet}$, $\log(g_{\rm planet})$, $T_{\rm int,planet}$ and $a_{\rm planet}$ are the radius, log(gravity), internal temperature, and the orbital separation of the planet. d is the distance to the system. The stellar redistribution factor $f_{\rm r}$ denotes the fraction of the insolation received by the dayside atmosphere, accounting for spherical geometry, day-night energy redistribution, etc. The mixing length for the convection l (usually taken to be the scale height) and the elemental abundances relative to atomic hydrogen {X/H} are also inputs. The model has the option to either fix the molecular abundances of the main gaseous species at equilibrium values or set them to other specified values for each layer. The outputs are the emergent spectrum, either the planet-star flux ratio or the planet flux alone, the pressure-temperature ($P-T$) profile and the chemical profiles. Clouds/hazes have not been included in the present work.

density, and composition. In the present work, for purposes of demonstrating the model, we focus on cloud-free H_2-dominated atmospheres, i.e. of gas giants. Extension to other planetary types can be easily achieved by incorporating the required chemistry and planetary properties. Here we discuss the different components of the model.

3.3.1 Basic Equations

The main equations governing the model are as follows.

$$\frac{dP}{dz} = -\rho g, \tag{3.1}$$

$$P = \frac{\rho k_b T}{\overline{m}}, \tag{3.2}$$

$$\mu \frac{dI_\nu}{d\tau_\nu} = I_\nu - S_\nu, \tag{3.3}$$

$$d\tau_\nu = -(\kappa_\nu + \sigma_\nu) dz, \tag{3.4}$$

$$\int_0^\infty \kappa_\nu (J_\nu - B_\nu) d\nu = 0. \tag{3.5}$$

The first equation describes the hydrostatic equilibrium for a fluid in one dimension and the second is the ideal gas equation, with the pressure P (Pa), temperature T (K), mean molecular mass $\overline{m}$ (kg), and density ρ (kgm^{-3}) in a layer of the atmosphere at a distance z (m) in the vertical direction. The third is the Radiative Transfer Equation (RTE) describing the transfer of photons through an optical depth τ_ν at an angle cosine $\mu = \cos(\theta)$ relative to the vertical, with a specific intensity I_ν and a source function S_ν (WSr^{-1}Hz^{-1}). τ_ν depends on the extinction coefficient, which is the sum of the absorption coefficient κ_ν (m^{-1}) and scattering coefficient σ_ν (equation 3.4). κ_ν is the cumulative absorption from all the species. The final equation is the balance of energy entering and leaving a given layer of the atmosphere, the radiative equilibrium equation, with the mean intensity of radiation J_ν and Planck function B_ν (WSr^{-1}m^{-2}Hz^{-1}). We note that this equation is corrected for the convective flux where the atmosphere is unstable against convection, as discussed in section 3.3.4. An overview of the methods is described below, followed by the sections explaining in detail how the methods are implemented.

3.3.2 Overview of the Methods

Figure 3.1 shows a flowchart of the GENESIS model components. Here we give a brief overview of the modelling scheme and elaborate on the details in subsequent sections below. For a fixed pressure grid in the atmosphere, the five unknowns z, T, ρ, I_ν and τ_ν are fully determined by solving the above five equations. We first begin with a trial pressure-temperature ($P-T$) profile. The assumption of hydrostatic equilibrium and the ideal gas equation of state are solved to obtain the profiles of ρ and z at each pressure level. The quantities P, T, and ρ, along with the elemental abundances, are then used in a chemical equilibrium module to derive mixing ratios of the major chemical species in the atmosphere. At the same time, P and T are also used to derive the absorption cross sections of the corresponding chemical species. The mixing ratios and the absorption cross sections, along with any scattering, together determine the opacity, and hence the optical depth τ_ν, in the atmosphere. Then we solve the radiative transfer equation at each sampled frequency to determine the radiation field denoted by the specific intensity I_ν.

The derived I_ν for the initial trial P-T profile will not necessarily satisfy the radiative-convective equilibrium. Therefore, an adjustment to the $P-T$ profile and the mean intensity is determined using a temperature correction scheme. This procedure is repeated until the temperature is accurate to within a certain tolerance level, which

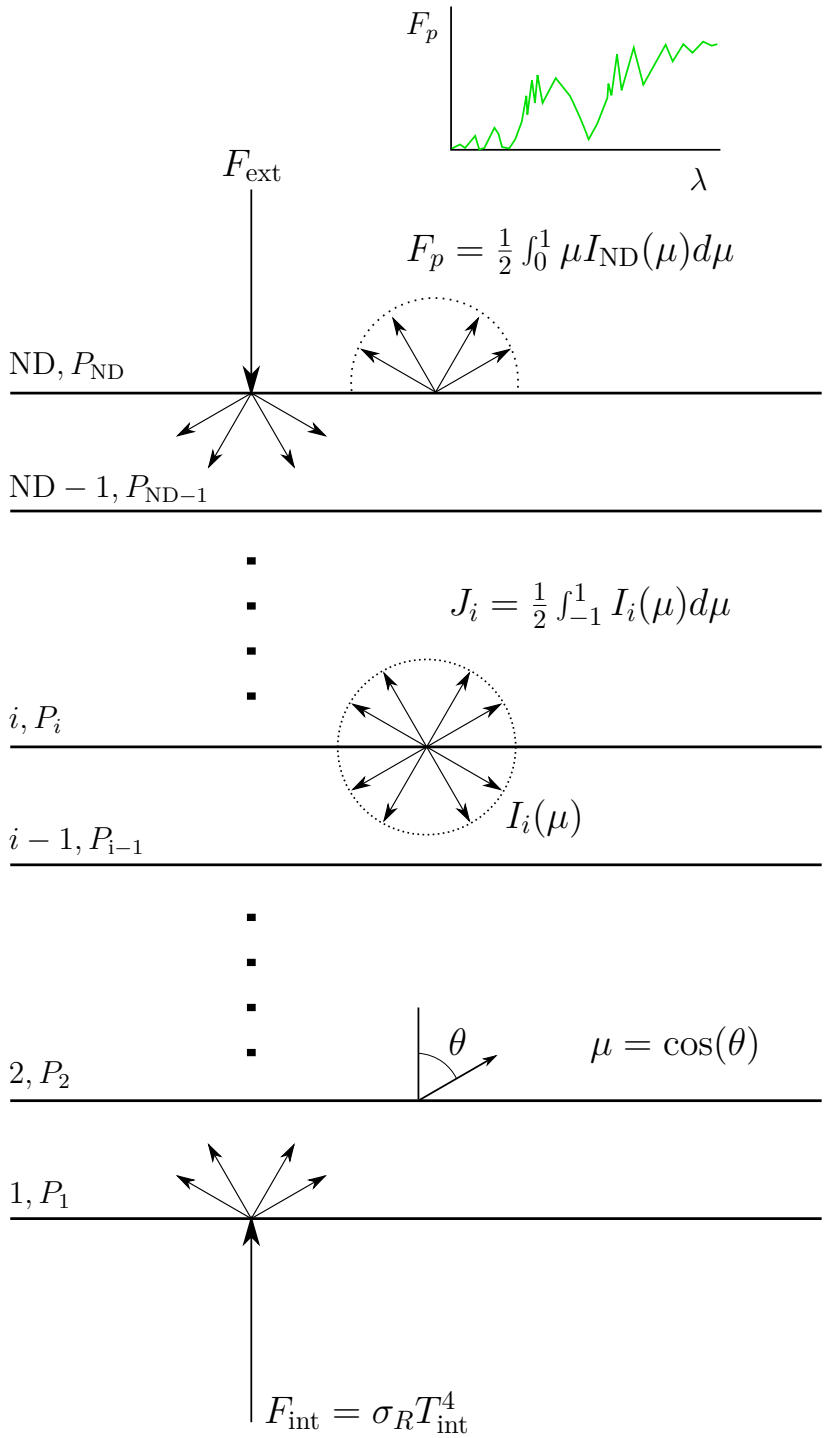

Fig. 3.2 Schematic of the model atmosphere. The plane-parallel model comprises of ND layers, with the stellar flux incident at the top ($F_{\rm ext}$) and the internal heat flux at the bottom denoted by $F_{\rm int}$, corresponding to temperature $T_{\rm int}$. The specific intensity is I, J is the mean intensity, and F_p is the emergent flux from the top of the atmosphere.

we take to be 10^{-4}. Once convergence is achieved, the corresponding solution provides the emergent spectrum and the atmospheric profiles.

The model, therefore, comprises of four key components: (a) Radiative Transfer, (b) Radiative-Convective Equilibrium, (c) Chemical Equilibrium, and (d) Opacities. In what follows, we describe each component of the model in detail. We begin by elaborating on how we solve the radiative transfer equation for a fixed $P-T$ profile (the formal solver) using the Feautrier method, followed by energy transport and how we ensure radiative-convective equilibrium using the Rybicki procedure. We then present the chemical module to determine the chemical abundances, and finally the methods used to determine the opacity, including calculating the absorption cross sections. Finally, we discuss how we account for the stellar flux incident on the planet.

3.3.3 Radiative Transfer

To obtain a solution to the RTE for a given $P-T$ profile, we use the Feautrier method described in Mihalas (1978). It is second order accurate, and many angle points can be used without excessive computational expense. It can be modified to exactly solve the transfer equation as well, an advantage in the case of strong scattering (no iterative solving of the RTE is required). The full details of this method and others are explored in detail in Hubeny and Mihalas (2014), and for convenience we adopt the notation used in it. The first 3 moments of the specific intensity of radiation I are given by

$$J_\nu = \frac{1}{2}\int_{-1}^{1} I(\mu)d\mu, \tag{3.6}$$

$$H_\nu = \frac{1}{2}\int_{-1}^{1} \mu I(\mu)d\mu, \tag{3.7}$$

$$K_\nu = \frac{1}{2}\int_{-1}^{1} \mu^2 I(\mu)d\mu. \tag{3.8}$$

The J term is also known as the mean intensity of radiation. We also define f_ν and g_ν for future convenience

$$f_\nu \equiv K_\nu/J_\nu = \frac{\int_{-1}^{1} I(\mu)\mu^2 d\mu}{\int_{-1}^{1} I(\mu)d\mu}, \tag{3.9}$$

$$g_\nu \equiv \frac{H_\nu(\tau=0)}{J_\nu(\tau=0)} = \frac{\int_{0}^{1} I(\mu,\tau=0)\mu d\mu}{\int_{-1}^{1} I(\mu,\tau=0)d\mu}. \tag{3.10}$$

The source function in the RTE is

$$S_\nu = \frac{\kappa_\nu B_\nu + \sigma_\nu J_\nu}{\kappa_\nu + \sigma_\nu}. \tag{3.11}$$

$$B(T,\nu) = \frac{2h\nu^3}{c^2}\frac{1}{e^{\frac{h\nu}{k_b T}} - 1}, \tag{3.12}$$

is the Planck function that describes the spectral radiance of a body at a temperature T and frequency ν. Now consider 2 beams of radiation travelling in the direction $\pm\mu$. The radiative transfer equations for these are

$$\mu\frac{\partial I_\nu(\mu)}{\partial \tau_\nu} = I_\nu(\mu) - S_\nu(\mu), \tag{3.13}$$

$$\begin{aligned} -\mu\frac{\partial I_\nu(-\mu)}{\partial \tau_\nu} &= I_\nu(-\mu) - S_\nu(-\mu), \\ &= I_\nu(-\mu) - S_\nu(\mu), \end{aligned} \tag{3.14}$$

where for the last line we assume that the source function is symmetric in μ. Defining the new quantities

$$j_{\mu,\nu} = \frac{1}{2}(I_\nu(\mu) + I_\nu(-\mu)), \tag{3.15}$$

$$h_{\mu,\nu} = \frac{1}{2}(I_\nu(\mu) - I_\nu(-\mu)), \tag{3.16}$$

then equation 3.13 and 3.14 can be combined into a second order equation in $j_{\mu,\nu}$.

$$\mu^2\frac{\partial^2 j_{\mu,\nu}}{\partial \tau_\nu^2} = j_{\mu,\nu} - S_\nu, . \tag{3.17}$$

For a given source function S_ν, we can numerically solve for $j_{\mu,\nu}$ to derive the mean intensity J_ν. Any $S(\mu)$ can be used, as long as it satisfies $S(\mu) = S(-\mu)$. The RTE can also be expressed by an integration over μ to

$$\frac{\partial^2(f_\nu J_\nu)}{\partial \tau_\nu^2} = J_\nu - S_\nu = \frac{\kappa_\nu(J_\nu - B_\nu)}{\kappa_\nu + \sigma_\nu}. \tag{3.18}$$

The boundary conditions at the top and bottom of the atmosphere are

$$\left.\frac{\partial(f_\nu J_\nu)}{\partial \tau_\nu}\right|_{\tau=0} = g_\nu J_\nu(0) - H_{\rm ext}, \tag{3.19}$$

$$\left.\frac{\partial(f_\nu J_\nu)}{\partial \tau_\nu}\right|_{\tau=\tau_{max}} = \frac{1}{2}(B_\nu - J_\nu) + \frac{1}{3}\frac{\partial B_\nu}{\partial \tau_\nu}. \tag{3.20}$$

equation 3.19 is a flux conservation condition with external stellar irradiation $H_{\rm ext} = F_{\rm ext}/(4\pi)$ incident at the top of the atmosphere. The condition at the bottom of the atmosphere (equation 3.20) is known as the diffusion approximation where the atmosphere can be considered to be optically thick due to the strong opacity and gas density, hence photons are diffusive and not ballistic. The current method is unsuitable for strong scattering; iteration of the radiative transfer equation will be required for a fixed $P-T$ profile to converge onto the radiation field if scattering is significant compared to the absorption. In future work the method will be modified to take into account strong scattering and anisotropic scattering due to clouds. The computational method for implementing the solution of the RTE, equation 3.17, is described in appendix A.1.

3.3.4 Radiative-Convective Equilibrium

The temperature profile in the atmosphere is governed by the energy budget in each layer of the atmosphere. In equilibrium, the temperature profile is required to be such that no net energy accumulates in any layer. In regions of the atmosphere where radiation is the efficient means of energy transport pure radiative equilibrium is satisfied. On the other hand, when the atmosphere is unstable against convection, an additional convective flux needs to be accounted for. Here we discuss the methods we use to ensure radiative-convective equilibrium in our model atmosphere to find a converged temperature profile.

Radiative Equilibrium

The energy flowing into a layer of the atmosphere must equal the energy flowing out if it is in equilibrium. For an initial $P-T$ profile that we begin with, this will not necessarily be the case. To correct the temperature and bring it into equilibrium, we need to know the amount of energy or flux flowing into and out of a layer. Local energy balance between each layer of the atmosphere determines the temperature profile and ensures total global energy conservation. The radiative equilibrium condition in a

single layer of the atmosphere can be written as either

$$\int_0^\infty \kappa_\nu (J_\nu - B_\nu) d\nu = 0, \text{or} \tag{3.21}$$

$$\int_0^\infty \frac{d(f_\nu J_\nu)}{d\tau_\nu} d\nu = \frac{\sigma_R}{4\pi} T_{\text{int}}^4. \tag{3.22}$$

Here, T_{int} is referred to as the temperature corresponding to the internal heat flux that emanates from the planet's convective core. Stellar contexts often refer to this as T_{eff}, but we reserve this notation for the effective temperature of the host star. Equation 3.21 is an energy match condition, and equation 3.22 represents conservation of the total flux entering/leaving in a given layer. Indeed, it may be shown by differentiating equation 3.22 with respect to τ and using equation 3.18 that equation 3.21 is identical. The reason why both forms are given is that numerically they both behave differently. Near the top of the atmosphere, equation 3.21 is a better constraint to use as the $d\tau$ in equation 3.22 is a small quantity, whereas near the bottom equation 3.21 runs into difficulty as numerical instabilities occur when κ is large. We apply a switch around the $\sim$1 bar level in the atmosphere to keep the constraint numerically stable.

We use equations 3.21 and 3.22 to determine the self-consistent $P - T$ solution iteratively. For a given $P - T$ profile, the equations for hydrostatic equilibrium, the ideal gas equation and the radiative transfer equation are used to give the radiation field. A correction to the temperature is calculated using Rybicki's method by complete linearisation, as we demonstrate at the end of this section. This brings the atmosphere into radiative equilibrium.

Radiative equilibrium may also be enforced using the equation of energy conservation including the full 3-D velocity field of the atmosphere (Vallis, 2006). 1-D models, including ours, generally set the velocity field to be zero and derive a time independent solution. Full General circulation models can use the 3D energy conservation condition that accounts for the velocity field. Both approaches are equivalent.

Convection

Some regions of the atmosphere can be unstable to convection. Convection needs to be considered since this will almost always dominate the energy transport mechanism over radiative transport deeper in the atmosphere. Here the optical depth can be high and the radiative flux can be low and inefficient to transport energy. In order to account for convection, the region where the atmosphere is convective needs to be determined and the appropriate flux needs to be calculated.

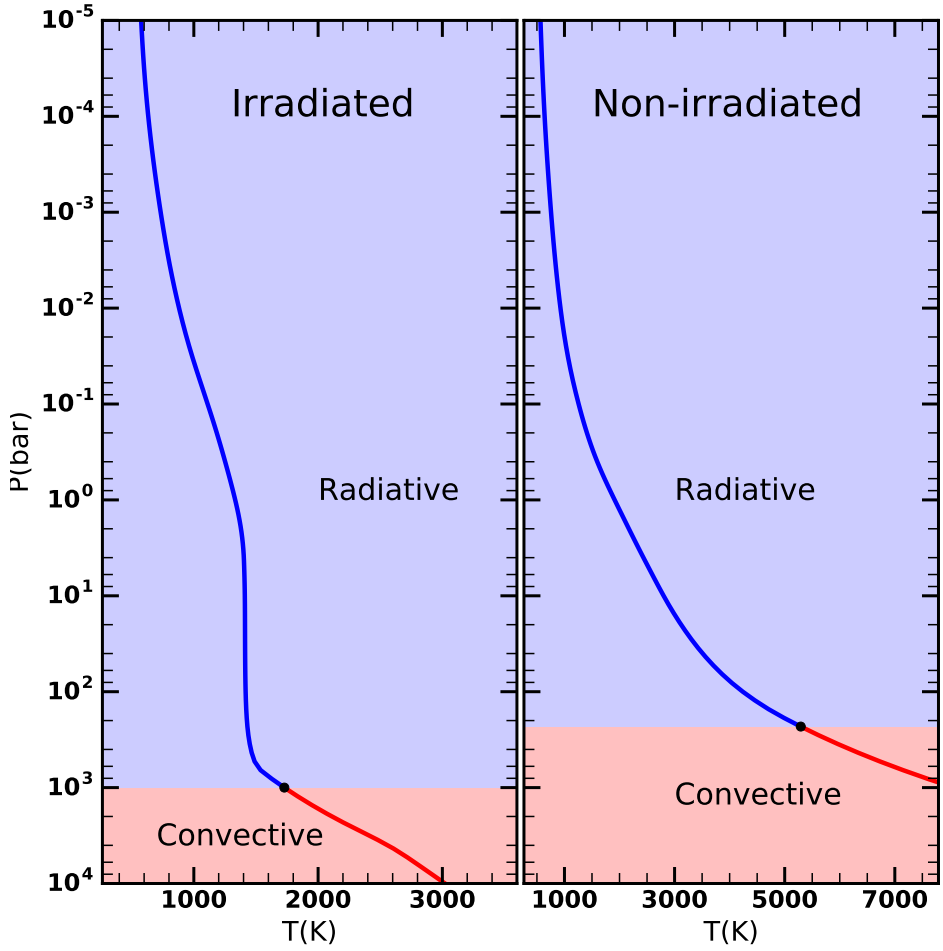

Fig. 3.3 Demonstration of the radiative and convective zones in atmospheres of irradiated vs non-irradiated giant planets. A Jupiter-sized planet is considered with solar elemental abundances in chemical and radiative-convective equilibrium. The irradiated planet has an equilibrium temperature of 1000 K (left) and the one with no irradiation has an internal flux corresponding to 1000 K (right). The solid lines are the converged pressure-temperature profiles, the blue shaded region represents the radiative zone, and the red region near the bottom of the atmosphere is the convective zone, with the transition point shown by the black circle.

Convection is treated in the model using the Mixing Length Theory (Kippenhahn *et al.*, 2012). We can assume adiabatic cooling for a parcel of gas that rises up in the atmosphere (the time scale for the gas to be in thermal equilibrium with the surroundings is negligible compared to the time it takes to rise in the atmosphere for most cases). Considering gas giant atmospheres consist mainly of diatomic hydrogen and the temperature is usually such that the 2 rotational modes are active, so $\gamma \equiv C_p/C_V = 7/5$. The third rotational mode (with the axis along the line of the molecule) has too small a moment of inertia and thus is not active. We additionally assume that the vibrational mode is suppressed, given the temperature is not sufficient to activate this. However, this is easy to modify if required. The adiabat is $PV^\gamma = \text{cst}$, so we have $(d\ln T/d\ln P)|_{\text{ad}} = 2/7$ from the ideal gas equation. If the temperature gradient exceeds the adiabatic gradient (or dry lapse rate) then the parcel of gas will be warmer than the surroundings and thus will rise. The temperature gradient thus determines which regions of the atmosphere, if any, will be unstable to convection. If the Schwarzschild condition for convective instability holds,

$$\nabla > \nabla_{\text{ad}}, \tag{3.23}$$

where $\nabla \equiv d\ln T/d\ln P$. The radiative equilibrium conditions 3.21 and 3.22 now include another flux where the atmosphere is unstable to convection.

$$\int_0^\infty \kappa_\nu (J_\nu - B_\nu) d\nu + \frac{\rho g}{4\pi}\frac{dF_{\text{conv}}}{dP} = 0, \tag{3.24}$$

$$\int_0^\infty \frac{d(f_\nu J_\nu)}{d\tau_\nu} d\nu + \frac{F_{\text{conv}}}{4\pi} = \frac{\sigma_R}{4\pi} T_{\text{int}}^4, \tag{3.25}$$

with the convective flux F_{conv} given by mixing length theory (full details of the derivations can be found in Kippenhahn *et al.* (2012)).

$$\begin{aligned} F_{\text{conv}}(\nabla, T, P) &= \left(\frac{gQH_P}{32}\right)^{1/2} \rho c_P T (\nabla - \nabla_{\text{el}})^{3/2} (l/H_P)^2, \\ &\equiv F_0 (\nabla - \nabla_{\text{el}})^{3/2}, \end{aligned} \tag{3.26}$$

$$\nabla - \nabla_{\text{el}} = \frac{1}{2}B^2 + (\nabla - \nabla_{\text{ad}}) - B\left(\frac{1}{4}B^2 + (\nabla - \nabla_{\text{ad}})\right)^{1/2}, \tag{3.27}$$

$$B \equiv \frac{16\sqrt{2}\sigma_R T^3}{\rho c_P (gQH_P)^{1/2}(l/H_P)} \frac{\tau_{el}}{1 + \frac{1}{2}\tau_{el}^2}, \tag{3.28}$$

where c_p is the heat capacity at constant pressure and $Q \equiv -(d\ln\rho/d\ln T)_P$, which is equal to 1 for an ideal gas. $\tau_{\text{el}} = l\chi_R$ is the optical depth of a small parcel of gas of

size l, which is a free parameter usually taken to be $\approx H_P$, the scale height of the atmosphere. The choice of l has minimal effect on the observed flux for hot Jupiters as convective regions are generally deep below the observable atmosphere as discussed in section 3.4. χ_R is the Rosseland mean opacity and $\nabla_{\rm el}$ is the elemental logarithmic temperature gradient, which satisfies

$$\nabla_{\rm el} - \nabla_{\rm ad} = B\sqrt{\nabla - \nabla_{\rm el}}. \tag{3.29}$$

By adding ∇ to both sides and rearranging, $\nabla - \nabla_{\rm el}$ can be calculated from the resultant quadratic in $\sqrt{\nabla - \nabla_{\rm el}}$.

$$\nabla - \nabla_{\rm ad} = \nabla - \nabla_{\rm el} + B\sqrt{\nabla - \nabla_{\rm el}}. \tag{3.30}$$

If convection is present in the atmosphere, the convective flux terms are also linearised by Rybicki's method described below.

Rybicki's Method and Linearisation

We perturb the temperature profile iteratively to converge to radiative-convective equilibrium using Rybicki's Method and Linearisation. Using the Feautrier method described in section 3.3.3 above the solution to the radiative transfer equation is obtained for a given temperature. To proceed and find a correction to the $P - T$ profile the equations above (equations 3.18, 3.19, 3.20, 3.24 and 3.25) are linearised with respect to temperature. To implement Rybicki's correction procedure (Rybicki, 1971), all elements (J, T, $\Delta\tau$, κ and σ, B etc.) are replaced with perturbed values with respect to J_k (where applicable for a given frequency k) and T (e.g J_k to $J_k + \delta J_k$, T to $T + \delta T$, $\Delta\tau$ to $\Delta\tau + \frac{\delta\Delta\tau}{\delta T}dT$, B to $B + \frac{\delta B}{\delta T}dT$ etc.). The linearised absorption coefficient is

$$\delta\kappa = \frac{\delta\kappa}{\delta T}dT = \left(\frac{\partial\kappa}{\partial T} + \frac{\partial\kappa}{\partial P}\frac{dP}{dT}\right)dT, \tag{3.31}$$

and similarly for the scattering coefficient. The full details of the linearisation of all coefficients can be found in Hubeny and Mihalas (2014), but is essentially a Newton-Raphson procedure. It is described in more detail in appendix A.2. Introducing the vector $\delta\mathbf{J_k} = (\delta J_{1,k}, \delta J_{2,k}, \cdots, \delta J_{ND,k})$ one obtains the set of matrix equations for J_k

and T

$$\mathbf{U}_k \delta\mathbf{J}_k + \mathbf{V}_k \delta\mathbf{T} = \mathbf{E}_k, \tag{3.32}$$

$$\sum_{k=1}^{NF} \mathbf{X}_k \delta\mathbf{J}_k + \mathbf{A}\delta\mathbf{T} = \mathbf{F}, \tag{3.33}$$

where NF is the total number of frequency grid points. $\mathbf{U}$ and $\mathbf{V}$ are the tridiagonal matrices obtained from linearisation of RTE, and $\mathbf{X}$ and $\mathbf{A}$ are the bidiagonal matrices from linearisation of radiative equilibrium. equation 3.32 represents the linearised form of the radiative transfer equation for every frequency k, and equation 3.33 is the constraint of radiative-convective equilibrium (either form). Combining each of the equations 3.32 (i.e., for every frequency) and equation 3.33 together yields the matrix equation

$$\begin{pmatrix} \mathbf{U_1} & 0 & \cdots & \cdots & 0 & \mathbf{V_1} \\ 0 & \mathbf{U_2} & 0 & \cdots & \vdots & \mathbf{V_2} \\ \vdots & 0 & \mathbf{U_3} & 0 & \vdots & \mathbf{V_3} \\ \vdots & \vdots & \vdots & \ddots & \vdots & \vdots \\ 0 & 0 & 0 & \cdots & \mathbf{U_{NF}} & \mathbf{V_{NF}} \\ \mathbf{X_1} & \mathbf{X_2} & \mathbf{X_3} & \cdots & \mathbf{X_{NF}} & \mathbf{A} \end{pmatrix} \begin{pmatrix} \delta\mathbf{J_1} \\ \delta\mathbf{J_2} \\ \delta\mathbf{J_3} \\ \vdots \\ \delta\mathbf{J_{NF}} \\ \delta\mathbf{T} \end{pmatrix} = \begin{pmatrix} \mathbf{E_1} \\ \mathbf{E_2} \\ \mathbf{E_3} \\ \vdots \\ \mathbf{E_{NF}} \\ \mathbf{F} \end{pmatrix} \tag{3.34}$$

The vector $\delta\mathbf{J_k}$ can be written in terms of $\delta\mathbf{T}$ by

$$\delta\mathbf{J_k} = (\mathbf{U_k^{-1}E_k}) - (\mathbf{U_k^{-1}V_k})\delta\mathbf{T}, \tag{3.35}$$

Inversion of the $\mathbf{U_k}$ matrices is only requires a linear number of operations in the number of layers ND, as they are tridiagonal. The bottom line of the matrix equation 3.34 is then given by

$$\sum_{k=1}^{NF} \mathbf{X_k}((\mathbf{U_k^{-1}E_k}) - (\mathbf{U_k^{-1}V_k})\delta\mathbf{T}) + \mathbf{A}\delta\mathbf{T} = \mathbf{F},$$

$$\left(\mathbf{A} - \sum_{k=1}^{NF} \mathbf{X_k}(\mathbf{U_k^{-1}V_k})\right) \delta\mathbf{T} = \left(\mathbf{F} - \sum_{k=1}^{NF} \mathbf{X_k}(\mathbf{U_k^{-1}E_k})\right). \tag{3.36}$$

The inversion of the $ND \times ND$ matrix on the left gives the change in temperature of each layer by yielding $\delta\mathbf{T}$. As the matrix on the left is in general full, this is an $O(ND^3)$ operation. Hence the total computation time $a(ND)(NF) + b(ND^3)$ is highly advantageous as it is linear in the frequencies, and one can have a very large number

and sample many wavelengths without an overly expensive increase in computation time. The new temperature is then found for each layer by applying the correction $\delta\mathbf{T}$ to $\mathbf{T}$. The whole process is then repeated for this new temperature, iteratively until a tolerance of $\delta\mathbf{T}/\mathbf{T} = 10^{-4}$ is reached.

3.3.5 Chemical Composition

The chemical composition centrally governs the opacity in each layer of the atmosphere. The opacity due to any chemical species is given by the product of its absorption cross section and its number density in the given layer. The total opacity is then the sum of contributions from all individual species. In chapter 2, we discuss how we compute the absorption cross sections for the different chemical species. Here we discuss how we compute their abundances.

The abundances of the chemical species in the atmosphere are determined under the assumption of thermochemical equilibrium. In planetary atmospheres the chemical species are mostly molecular with the exception of a few species which can survive in atomic form under specific conditions. The equilibrium abundances of the various chemical species are determined by minimizing the Gibbs free energy of the system for a given temperature, pressure, and elemental abundances. There is an extensive body of literature on the chemical compositions of exoplanetary atmospheres under various conditions (Blecic *et al.*, 2016; Heng and Tsai, 2016; Lodders and Fegley, 2002; Madhusudhan, 2012; Madhusudhan *et al.*, 2016; Moses *et al.*, 2013; Venot *et al.*, 2012). In general, the equilibrium abundances of a large number of species can be determined numerically for any P and T, considering a full list of elements. However, the chemical abundances and opacity in giant exoplanetary atmospheres are dominated by species containing O, C, and N, which are the most abundant elements after H and He. Therefore, in the present initial study, we consider equilibrium abundances of only the dominant chemical species containing O, C, and N. We denote the abundances by volume mixing ratios, i.e. ratios by number density.

In the present work, we focus on giant planet atmospheres. Therefore, the key parameters driving the chemical mixing ratios are P, T, and the elemental abundances of He, O, C, and N, relative to H. Our model atmospheres span a wide range in metallicities (solar to 30× solar), C/O ratios (0.5-1.5), P (10^{-5} - 100 bar), and T (∼400-3000 K). While we can compute the chemical mixing ratios numerically (Madhusudhan, 2012), we currently use the semi-analytical prescriptions of Heng and Tsai (2016) which give accurate estimates for the prominent O, C, and N based molecules of interest over the desired parameter space. These molecules are H_2O, CH_4, NH_3, CO, HCN, CO_2, C_2H_2,

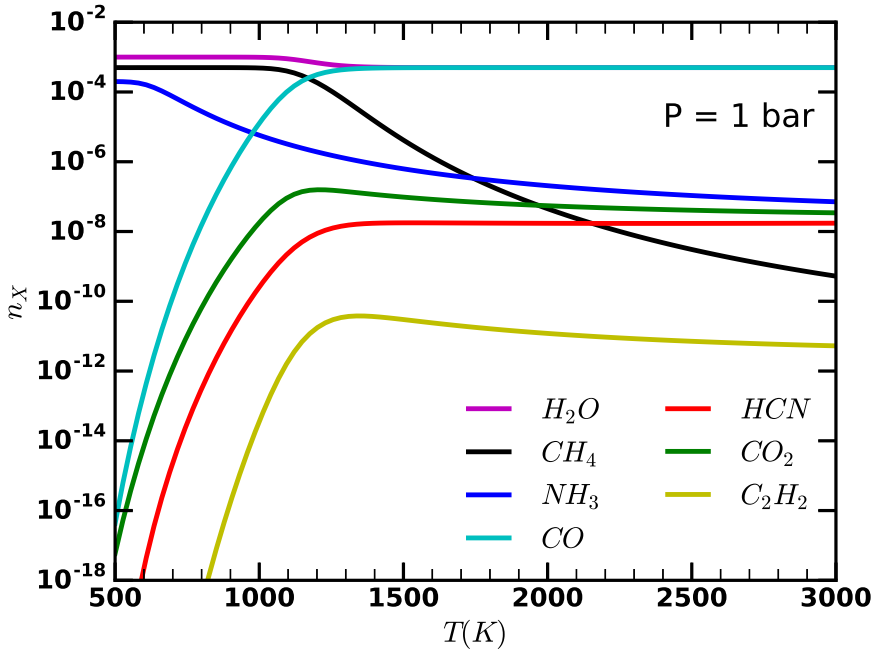

Fig. 3.4 Molecular mixing ratios of prominent molecules in H_2-rich atmospheres in chemical equilibrium. The dependence of the mixing ratios on the temperature is shown for a nominal pressure of 1 bar assuming solar elemental abundances, as discussed in section 3.3.5.

N_2 and C_2H_4. In specific cases, we also consider additional gaseous species such as Na, K, and TiO, to demonstrate particular physical processes, e.g. of strong optical absorption or thermal inversions. Here we briefly discuss the prescriptions we use for the prominent molecules. Figure 3.4 shows a representative calculation of molecular mixing ratios for solar elemental abundances at a nominal pressure of 1 bar and over a wide range of temperatures.

The main 6 reactions that govern the mixing ratios of the O, C, N molecules are (Heng and Tsai, 2016):

$$\begin{aligned} CH_4 + H_2O &\leftrightarrows CO + 3H_2, \\ CO_2 + H_2 &\leftrightarrows CO + H_2O, \\ 2CH_4 &\leftrightarrows C_2H_2 + 3H_2, \\ 2C_2H_4 &\leftrightarrows C_2H_2 + H_2, \\ 2NH_3 &\leftrightarrows N_2 + 3H_2, \\ NH_3 + CH_4 &\leftrightarrows HCN + 3H_2. \end{aligned} \tag{3.37}$$

Taking $n_i = N_i/N_{H_2}$ to be the mixing ratio of species i relative to hydrogen, where N_i is the number density. The particle conservation equations give

$$\begin{aligned} n_{CH_4} + n_{CO} + n_{CO_2} + n_{HCN} + 2n_{C_2H_2} + 2n_{C_2H_4} &= 2n_C, \\ n_{H_2O} + n_{CO} + 2n_{CO_2} &= 2n_O, \\ 2n_{N_2} + n_{NH_3} + n_{HCN} &= 2n_N. \end{aligned}$$

The equilibrium constants are

$$
\begin{aligned}
K_1 &= \frac{n_{\mathrm{CO}}}{n_{\mathrm{CH_4}} n_{\mathrm{H_2O}}} = \left(\frac{P_0}{P}\right)^2 \exp\left(\frac{-\Delta G_{0,1}}{RT}\right), \\
K_2 &= \frac{n_{\mathrm{CO}} n_{\mathrm{H_2O}}}{n_{\mathrm{CO_2}}} = \exp\left(\frac{-\Delta G_{0,2}}{RT}\right), \\
K_3 &= \frac{n_{\mathrm{C_2H_2}}}{n^2_{\mathrm{CH_4}}} = \left(\frac{P_0}{P}\right)^2 \exp\left(\frac{-\Delta G_{0,3}}{RT}\right), \\
K_4 &= \frac{n_{\mathrm{C_2H_2}}}{n_{\mathrm{C_2H_4}}} = \left(\frac{P_0}{P}\right) \exp\left(\frac{-\Delta G_{0,4}}{RT}\right), \\
K_5 &= \frac{n_{\mathrm{N_2}}}{n^2_{\mathrm{NH_3}}} = \left(\frac{P_0}{P}\right)^2 \exp\left(\frac{-\Delta G_{0,5}}{RT}\right), \\
K_6 &= \frac{n_{\mathrm{HCN}}}{n_{\mathrm{NH_3}} n_{\mathrm{CH_4}}} = \left(\frac{P_0}{P}\right)^2 \exp\left(\frac{-\Delta G_{0,6}}{RT}\right).
\end{aligned}
$$

Here, $\Delta G_{0,i}$ is the standard Gibbs free energy for reaction i given in Heng and Lyons (2016). Specifying the ratios C/H = n_{C}, O/H = n_{O} and N/H = n_{N}, the 9 equations can then be solved for the mixing ratios of the 9 species. This is achieved by solving a decic equation knowing each of the equilibrium constants, which are functions of pressure of temperature. The details of the implementation can be found in Heng and Tsai (2016). Thus, given a $P - T$ profile the equilibrium mixing ratios of the 9 molecules can be determined in each layer of the atmosphere. The mixing ratios can then be multiplied by the number density of H_2 to obtain the total number density of gas N_i of each species i. The number density together with the relevant cross sections can then be used to obtain the total absorption and opacity.

3.3.6 Opacities

The various potential sources of opacity in the atmosphere are described in chapter 2. These include the cross sections of the molecular and atomic species which may be present in the atmosphere, as well as collisionally induced absorption from H_2-H_2 and H_2-He interactions and Rayleigh scattering from molecular hydrogen. In this work we have used opacity sampling, and thus GENESIS has the capability to handle arbitrary resolution down to the native resolution of the line list, as the opacity tables are simply computed to the desired resolution. For the current purpose we have chosen a resolution that is appropriate for our applications, as shown in Fig. 3.6 and discussed

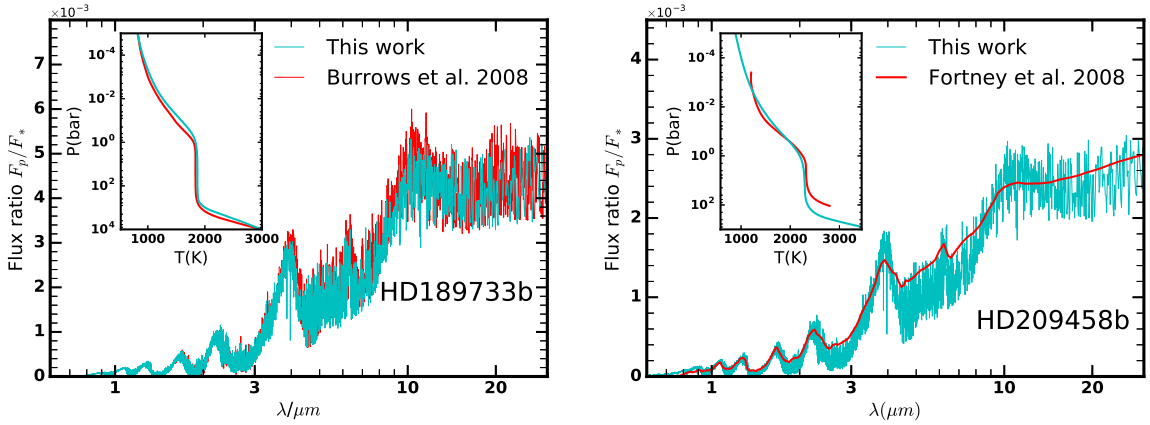

Fig. 3.5 Comparison of GENESIS models with published results. A model of the hot Jupiter HD 189733 b from Fig. 1 and Fig. 4 of Burrows *et al.* (2008) is shown in the left panel, and a model of HD 209458 b from Fig. 12 of Fortney *et al.* (2008) is shown on the right. The planet-star flux ratios and the $P-T$ profiles in the inset show good agreement. The models assume chemical equilibrium with solar elemental abundances.

in section 3.3.8. Any higher resolution beyond R~10^4 has a negligible effect on the spectrum and the equilibrium $P-T$ profile.

3.3.7 Stellar Flux

The incoming stellar flux sets the boundary condition at the top of the atmosphere (equation 3.19). We use a Kurucz model spectrum (Castelli and Kurucz, 2004; Kurucz, 1979) based on the stellar parameters. We linearly interpolate in the effective temperature and log gravity of the Kurucz model grid to determine the theoretical stellar spectrum for the required stellar parameters at the nearest metallicity on the grid. However, with regards to the convergence of the GENESIS models and the observed flux ratio, only minor differences were seen between the stellar model and a Planck function, similar to the findings of Malik *et al.* (2017) with Kurucz and PHOENIX stellar models. The incident flux on the planetary dayside for the different assumptions for stellar flux is given by

$$F_{\text{ext,Planck}} = f_{\text{r}}\ \pi B(T_{\text{eff}}, \nu)\ \frac{R_{\text{star}}^2}{a^2}, \tag{3.38}$$

$$F_{\text{ext,Kurucz}} = f_{\text{r}}\ 4\pi H_{\text{star}}(T_{\text{eff}}, \nu, \log(g_{\text{star}}), Z)\ \frac{R_{\text{star}}^2}{a^2} \tag{3.39}$$

where T_{eff} is the stellar effective temperature, B is the Planck function, and H_{star} is the Eddington Flux at the stellar surface obtained from a Kurucz model. R_{star} and a

are the stellar radius and semi-major axis, respectively. Here, $f_{\rm r}$ is used to account for the average flux incident on the whole day side of the planet, rather than only at the sub-stellar point, and to consider part of the incident flux transported to the night side.

3.3.8 Model Validation

We tested GENESIS extensively for accuracy, convergence, and performance. As discussed in section 3.3, the model comprises of four key modules: (a) line-by-line opacities, (b) equilibrium chemistry, (c) radiative transfer, and (b) temperature correction via radiative-convective equilibrium. Each of these components were tested extensively. Our new line-by-line cross sections for all the molecules were tested against the latest published sources, both our own previous computations (Hedges and Madhusudhan, 2016) as well as other databases (Tennyson *et al.*, 2016), over a wide range of pressures, temperatures and wavelengths, and thermal/pressure broadening. The molecular abundances in chemical equilibrium were validated against those of Heng and Tsai (2016), as discussed in section 3.3.5. The radiative transfer module computes a spectrum for a given $P-T$ profile and composition. This module was extensively tested for various conditions and validated against models from our existing radiative transfer codes. Finally, the radiative-convective equilibrium module which is responsible for the iterative temperature correction procedure was tested extensively for convergence and stability; our current code is convergent to temperature differentials within our desired tolerance level of 10^{-4}. The model is extremely stable, both in the radiative and convective regimes, over the entire range of parameter space considered in the present work.

The GENESIS models were also tested for a range of spatial and spectral resolutions. We explored the effect of varying the number of layers in the atmosphere, ND, and the number of frequency points, NF, and hence the spectral resolution. We perform these tests in order to be able to determine what the most optimal values are for accuracy and computation time. To perform these tests, a representative hot Jupiter with an equilibrium temperature of 1500 K was chosen around a solar type star. Fig. 3.6 reveals some interesting behaviour. Firstly, the choice of ND between 30 and 150 layers has only a marginal effect on the $P-T$ profile, with only the starting layer of the convective zone having any significant effect. This can however be explained by the discrete nature of the grid used; the temperature gradient is fixed between layers, so convective zones can only begin at layer boundaries. This is why the three test cases with $ND = 100$ have the same convective zone transition, but altering ND moves the

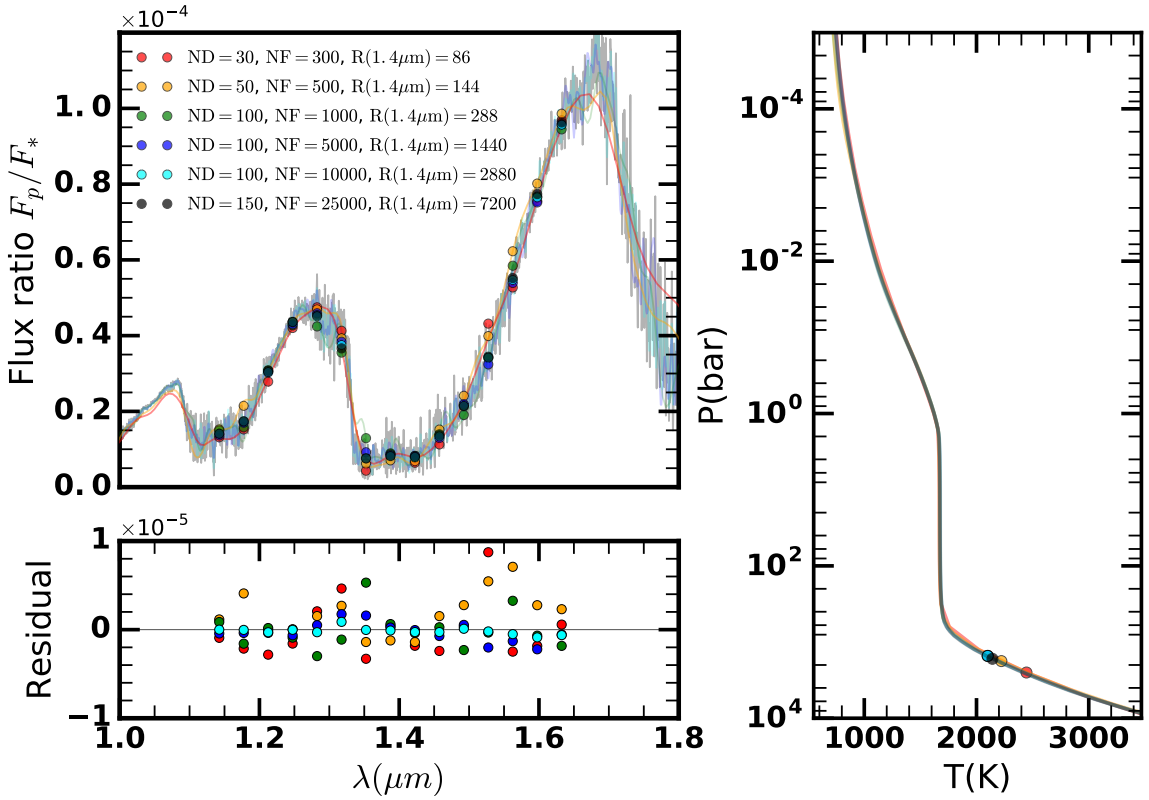

Fig. 3.6 Model spectra and $P-T$ profiles for a hot Jupiter with $T_{\rm eq}$ = 1500 K computed at different spectral and spatial resolutions. ND denotes the number of layers in the model atmosphere and NF denotes the number of frequency points with the corresponding spectral resolution R = $\nu/d\nu$ given at 1.4 μm, near the centre of a strong H_2O band as well as of the HST WFC3 G141 spectrograph. Six models are considered with different ND and NF, as discussed in section 3.3.8. The left hand side (top) shows the flux ratio overlaid with circles indicating binned model points in the HST WFC3 bandpass. The bottom figure on the left shows the differences in the binned points for each model relative to the highest resolution model. The right hand plot shows the corresponding $P-T$ profiles, with the radiative-convective boundary for each model marked with a circle of the corresponding colour.

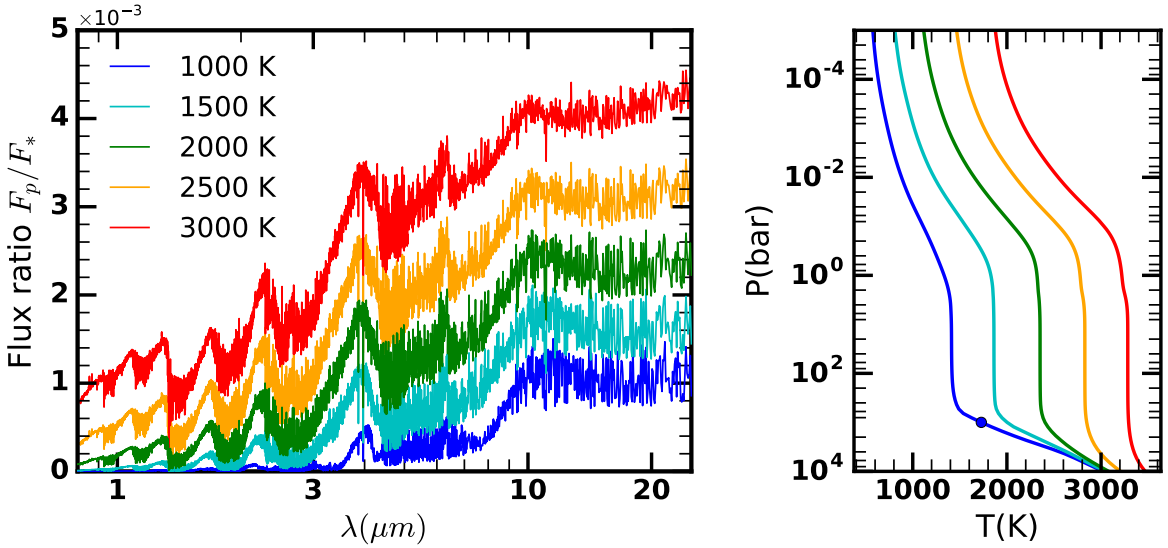

Fig. 3.7 Self-consistent model spectra and $P-T$ profiles of hot Jupiters with different levels of irradiation, represented by the equilibrium temperatures. The left plot shows the planet-star flux ratio as a function of wavelength for equilibrium temperatures of $T_{\rm eq} = 1000$ K (blue) to $T_{\rm eq} = 3000$ K (red). The right panel shows the converged $P-T$ profiles. The mass and radius of this test planet are taken to be that of Jupiter, and the host star and the overall atmospheric metallicity is modelled as solar. The onset of convection is represented by a circle, and is only visible in the figure for the lowest equilibrium temperature; higher temperatures suppress convective regions to higher pressures due to the incident irradiation.

transition. The top left panel of Fig. 3.6 shows the planet-star flux ratio and binned model points in the HST WFC3 bandpass (as circles) and the bottom panel shows the differences relative to the highest resolution model. An increase in the number of frequency points used alters the binned points quite significantly until $NF = 5,000$ (R= 1440 at 1.4 μm), where the binned data begin to lie very close to each other (~2 ppm); the $NF = 10,000$ (R= 2880) and $NF = 25,000$ (R= 7200) models have data points almost completely indistinguishable. Hence in the next section, all of our models were run with $NF = 10,000$ and $ND = 100$, as any higher resolution would be longer to run computationally but would not alter the converged $P-T$ and flux profile significantly, as the run time scales as $\sim(NF)(ND) + \text{const.}(ND^3)$.

We have also compared our full model against some published self-consistent models and found good agreement. For this purpose, we considered models of two well known hot Jupiters HD 189733b and HD 209458b. We compared our model of HD189733b with a previous cloud free model by Burrows *et al.* (2008), shown in Fig. 3.5. The planetary parameters were adopted from Burrows *et al.* (2008) to enable an accurate

comparison. We computed the molecular abundances assuming solar abundances and chemical equilibrium, and the Na and K abundances in our model increase linearly with the pressure until they reach solar values at 100 bar, to simulate their depletion at low T and P in the upper atmosphere in chemical equilibrium. The resulting converged $P-T$ profile and planet-star flux ratio spectrum are shown in blue in Fig. 3.5, which provide a good match to those of Burrows *et al.* (2008) (Fig. 1 and 4 in their paper). In both cases, the convective zone starts ~100 bar, and the isotherm temperatures agree to within $\sim$ 15 K. The $P-T$ profile and flux are most strongly influenced by water and carbon monoxide, the only gases present in any significant quantities at these pressures and temperatures. Any slight differences are likely due to the opacities in our model being from a newer line list, or our equilibrium mixing fractions differing because of the different methods used to calculate them.

We also compared our cloud free model of HD209458b with the dayside profile from Fortney *et al.* (2008) without a thermal inversion in Fig. 3.5. The planetary parameters used were once again taken from Fortney *et al.* (2008). The $P-T$ profile is matched quite well in the region where their profile was available. The model spectra also match quite well, though our model is at a higher resolution than theirs and computed with the latest opacities which are likely more complete compared to what they used. Additionally, there are significant differences in the model implementation. Our model involves line-by-line radiative transfer with the Feautrier method whereas theirs involves using the two-stream source function with the correlated-k approximation, implemented at a lower resolution which gives the smoother spectrum seen in Fig. 3.5. Similarly the temperature correction scheme is also different as discussed in section 3.1. Nevertheless, the good agreement between the two models both in the $P-T$ profile and the spectrum is noteworthy, particularly given the development of more complete line lists for molecules over the recent years (see chapter 2).

3.4 Results

We now use the methods discussed above to generate models of exoplanetary atmospheres over a range in parameter space. We assume some nominal values for the system parameters for our baseline model and explore variations thereof for our model grid. The model input parameters are shown in Table 3.2. Firstly, except for our models of known exoplanets, we generally assume the planetary mass and radius, and hence gravity, to be Jovian-like and the stellar properties to be solar. Secondly, while our model is generally applicable to any composition, we explore only H_2-dominated

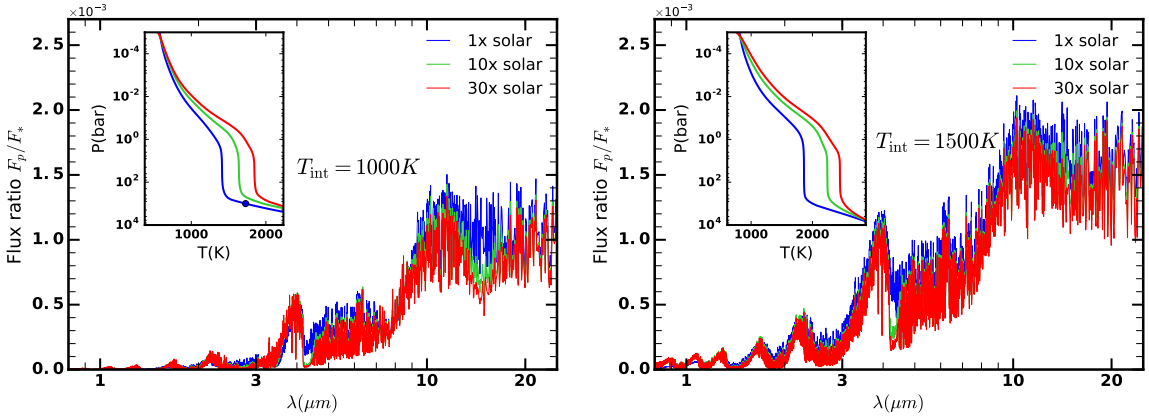

Fig. 3.8 Effect of metallicity on the planet-star flux ratio and $P-T$ profile of a hot Jupiter. The metallicity is explored between 1-30× solar, with the left panel showing models with equilibrium temperature of 1000 K and the right showing 1500 K. The inset plots show the converged $P-T$ profiles.

atmospheres, i.e., such as atmospheres of gas giants and ice giants. Thus, our baseline model has a solar elemental composition and we explore variations thereof in metallicities and C/O ratios for other models. The key sources of opacity are the prominent molecules expected in thermochemical equilibrium for the given elemental abundances, collision-induced absorption from H_2-H_2 and H_2-He, and Rayleigh scattering from H_2. For the incident stellar flux, in the cases of planets with strong irradiation, we assume that half the incident flux is redistributed to the night side, i.e. f_r of 0.5. For the isolated planets we assume an internal heat flux corresponding to a blackbody with $T_{\rm int} = 1500$ K, and for the irradiated planets we assume $T_{\rm int} = 75$ K.

For each GENESIS model, we report the emergent spectrum and the atmospheric pressure-temperature ($P-T$) profile as a function of a chosen parameter. All the models are computed over a wavelength range of 0.4-30 μm wavelength, with $NF = 10,000$ evenly spaced points in frequency, and $ND = 100$ layers in the atmosphere evenly spaced in log P. We explore a wide range of atmospheric models in two regimes of importance for currently known exoplanets: (a) highly irradiated close-in exoplanets which dominate the transiting planet population, and (b) planets with negligible irradiation dominated by internal flux, as relevant for directly imaged exoplanets on wide orbital separations. We also generate model spectra and temperature profiles of several irradiated hot Jupiters over a wide temperature range, and compare our models of two well studied hot Jupiters to some of those reported in the literature.

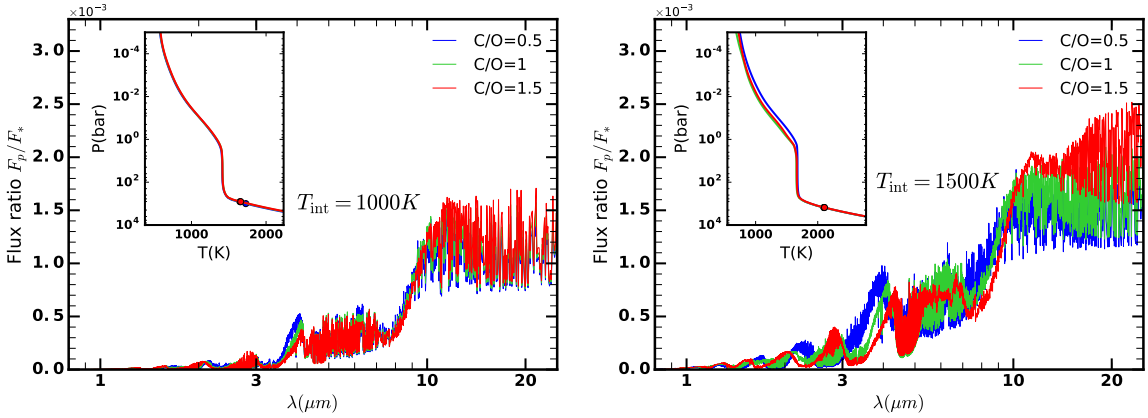

Fig. 3.9 Effect of C/O ratio on the planet-star flux ratio and $P-T$ profile of a hot Jupiter. Two models are considered, with equilibrium temperatures of 1000 K (left) and 1500 K (right). The O/H is fixed at solar value and the C/H is varied to obtain the required C/O ratio; the solar C/O ratio is 0.5.

3.4.1 Irradiated Atmospheres

We first investigate atmospheric models of highly irradiated giant planets, particularly hot Jupiters, which are the most studied class of exoplanetary atmospheres. Unless specified otherwise we assume a Jovian-like planet, in mass and size, orbiting a sun-like star. We explore the dependance of emergent spectra and temperature profiles on the degree of irradiation, metallicity and C/O ratio, and the presence of optical absorbers which dominate the absorption of incident starlight and can cause thermal inversions. For the spectra, we report the planet-star flux ratio as a function of wavelength as typically measured for transiting hot Jupiters (see e.g. Madhusudhan *et al.*, 2014a). We assume a Kurucz model spectrum for the star.

Effect of Stellar Irradiation

We begin with the test case of a hot Jupiter around a sun-like star and investigate models with varying degrees of irradiation, represented by the equilibrium temperature $T_{\rm eq}$. Altering the semi-major axis, and hence the incident irradiation, causes the equilibrium temperature to vary according to $T_{\rm eq} = T_{\rm eff}\sqrt{R_{\rm star}/2a}$, assuming efficient energy redistribution between the day and night sides. We consider models with $T_{\rm eq}$ between 1000 K and 3000 K (in steps of 500 K), representing the temperature range of currently known hot Jupiters. The chemical composition is fixed by thermochemical equilibrium assuming solar elemental abundances and considering only prominent C-N-O chemistry, as discussed in section 3.3.5. Depending on the particular temperature,

the key sources of opacity are the prominent O and C bearing species such as H_2O, CO, CH_4, and CO_2 which contribute significant molecular absorption primarily in the infrared. We also included Na and K as sources of visible opacity with abundances as discussed in section 3.3.8.

The model spectra and temperature profiles are shown in Fig. 3.7. The general behaviour of the temperature profiles are consistent with expectations for strongly irradiated H_2-rich atmospheres, as also reported in previous studies (e.g., Burrows *et al.*, 2008; Mollière *et al.*, 2015). An isotherm occurs for all of these systems at pressures above ∼1 bar. Below the isothermal layer is the convective zone, the transition to which is marked with a circle for each $P - T$ profile in Fig. 3.7. The convective energy transport is due to the heat emanating from the planetary interior, taken to be at a temperature of 75 K for this demonstration. Above the isothermal layer the temperature decreases monotonically outward and ultimately approaches isotherms again in the very low optical depth regime, and as expected, the temperature profiles become consistently hotter with increasing irradiation. The equilibrium chemistry beyond $\approx$ 1500 K is similar, dominated by CO and H_2O (see Fig. 3.4) due to which the profiles do not show much variation in the gradient. The atmosphere is entirely radiative down to $\sim 10^3$ bar, with the radiative-convective boundary appearing in the region marked with a circle. This can only be seen for the lowest equilibrium temperature of 1000 K. Higher stellar fluxes increase the depth of the radiative zone owing to the strength of the incoming radiation, driving the convection zone deeper into the atmosphere. Eventually all of the $P - T$ profiles converge onto the same adiabat at great depth, which is determined most strongly by the internal heat flux and the opacity. Lack of strong visible opacity can also be responsible for suppressing the convective regions to lower in the atmosphere (for instance see Fig. 3.10), and this is discussed in more detail in 3.4.1.

The planet-star flux ratios reveal the interplay between the temperature profiles and chemistry. A negative temperature gradient in the temperature profile results in strong absorption features in the emergent spectrum as shown in Fig. 3.7. Again, the general behaviour of these spectra is as expected and extensively discussed in the literature (see e.g., Burrows *et al.*, 2008; Madhusudhan and Seager, 2010). The stellar spectrum peaks in the visible whereas the planetary spectra for these temperatures peak in the near-infrared, implying that the planet-star flux ratio increases with wavelength in the infrared until eventually becoming constant in the mid-far infrared in the Rayleigh-Jeans limit. Naturally, the spectrum is brighter for hotter planets. The locations and amplitudes of the features in the spectra are driven by the temperature gradient and

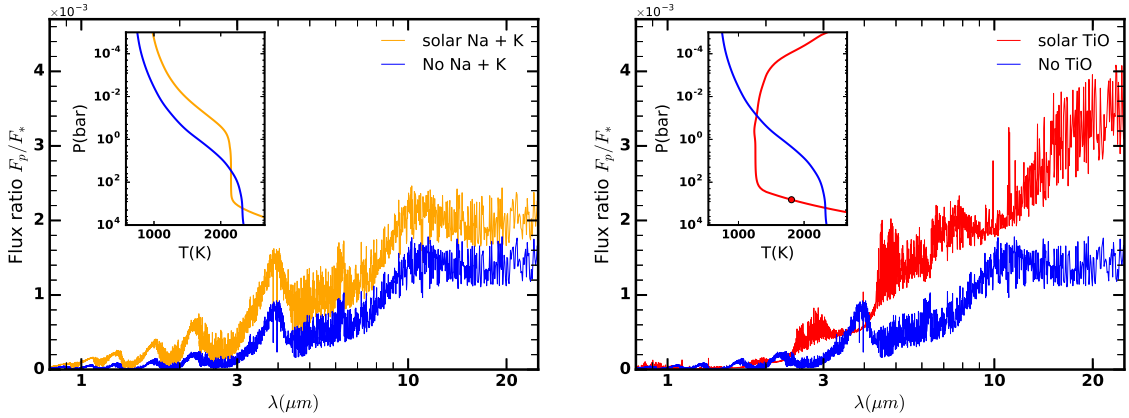

Fig. 3.10 Effect of Na/K and TiO visible opacity on the emergent spectrum and $P-T$ profile of a hot Jupiter. The left plot shows a hot Jupiter without sodium or potassium (blue) and with sodium+potassium included at solar abundances (yellow). The right hand side shows the same blue curve (without any visible absorbers) and the red curve with TiO at solar abundances. In each case the equilibrium temperature was 1500 K, with an identical incident stellar flux for all the cases shown. The inset shows the converged radiative-convective equilibrium $P-T$ profiles. The transition to the convective zone for the red curve is marked on the plot with a circle.

the abundances of absorbing molecules. As alluded to above, the temperature profiles with negative gradients give rise to the observed absorption features at wavelengths where the the abundance molecules absorb. The peaks in the spectrum probe deeper regions of the atmosphere where as the troughs probe regions higher up. In the current temperature range for H_2-rich atmospheres in chemical equilibrium, the prominent molecular opacity is provided by H_2O in most of the observed features, followed by CO in the 4-6 μm region. Additional features can be contributed by other species such as CH_4 and CO_2 depending on the temperature, metallicity, C/O ratio, etc. While the troughs in the spectra correspond to the absorption features, the peaks correspond to windows in molecular opacity where the temperature in the isothermal deep atmosphere is probed (deeper than ~1 bar). On the other hand, the presence of a thermal inversion reverses this symmetry whereby the peaks would correspond to molecular emission features, as discussed in section 3.4.1, and also discussed in previous works (e.g., Burrows *et al.*, 2008; Madhusudhan and Seager, 2010).

Effect of Metallicity and C/O Ratio

Here we investigate the effect of chemical composition on the model spectra and $P-T$ profiles. We explore the dependence of the spectra on the elemental abundances via

two key parameters, the overall metallicity and the C/O ratio, which are expected to govern the dominant molecular composition in hot Jupiter atmospheres (Heng and Lyons, 2016; Lodders and Fegley, 2002; Madhusudhan, 2012; Moses *et al.*, 2013). The molecular abundances are determined from the elemental abundances of O, C, and N under the assumption of thermochemical equilibrium as discussed in section 3.3.5; the baseline model assumes solar abundances with a C/O = 0.5. In hot Jupiter atmospheres in the 1000-3000 K temperature range the prominent molecules expected are typically H_2O, CO, CH_4, CO_2, and a few other trace species. The relative abundances of these molecules depend on the particular temperature and C/O ratio (Madhusudhan, 2012; Moses *et al.*, 2013). For solar abundances, H_2O and CH_4 are the dominant molecules at $T \lesssim 1300$ K where as H_2O and CO dominate at higher temperatures. Increasing the metallicity of all the elements uniformly, i.e. keeping the C/O constant, increases all these molecular abundances almost linearly but with slightly higher enhancement of CO_2 (Madhusudhan and Seager, 2011). As the C/O ratio is increased the carbon-based molecules become more abundant at all temperatures. A particularly non-linear effect arises at high temperatures ($\gtrsim$1300 K) for which as the C/O approaches 1 the H_2O abundance drops substantially. Therefore, the C/O ratio is expected to have a particularly high effect on high-temperature atmospheres (Madhusudhan, 2012). Therefore, in what follows we assess the effect of metallicity and C/O on the models for two different temperatures, 1000 K and 1500 K.

We discuss here models for three representative metallicities of solar, 10× solar, and 30× solar, assuming a C/O ratio of 0.5. And, in each case we investigate two representative temperatures of 1000 K and 1500 K. The results are shown in Fig. 3.8. Increasing the metallicity uniformly across all the elements effectively amounts to a nearly linear increase in the opacity via the increased molecular mixing ratios. For a given irradiation, or $T_{\rm eq}$, the higher opacity increases the atmospheric absorption and causes the temperature profiles to be systematically hotter and their gradients to be steeper. Additionally, due to the increased opacity the onset of the isotherm in the lower atmosphere also happens earlier (i.e. at lower pressures or higher altitudes). All these effects are even stronger for higher $T_{\rm eq}$. The higher temperatures also suppress convective regions deeper in the atmosphere, and so the atmospheres are mostly radiative at the pressures modelled (only the solar 1000 K $P-T$ profile shows the radiative-convective boundary in Fig. 3.8). The consequent effect on the spectra is deeper spectral features for higher metallicities caused by not only the hotter and steeper $P-T$ profiles but also the increased abundances of the molecules causing the absorption. The differences in the spectra between the $T_{\rm eq}$ of 1000 K and 1500 K is

due to the differences in molecular abundances as a function of temperature, with CO being more abundant in the higher temperature case causing the features in the 4-6 μm region, whereas CH_4 and CO_2 being more abundant in the lower temperature case causing the spectral features in the 3-5 μm and $\sim$15 μm regions. Overall, however, the effect on the spectra over this metallicity range is relatively modest (also see Mollière *et al.*, 2015), as the H_2O absorption troughs which dominate the spectra are nearly saturated.

The spectra are more strongly affected by changes in the C/O ratio than by the overall metallicity, particularly for high temperature atmospheres. As discussed above, the changes in C/O ratio mainly influence the composition by increasing the C-based molecules relative to the O-based molecules. The effect is only marginal for $T_{\rm eq}$ of 1000 K as at such low temperatures most of the C is in CH_4 and most of the O is in H_2O, irrespective of the C/O ratio. On the other hand, for higher temperatures the H_2O abundances can be over 100$\times$ lower for C/O $\gtrsim$ 1 relative to solar C/O ratio. The corresponding effect on the spectrum is quite clear, as shown in Fig. 3.9. In the $T_{\rm eq}$ = 1500 K case, it is important to note the substantial differences in the spectra despite the marginal differences in the temperature profiles, which indicates that the differences are predominantly due to the change in chemistry. The temperature profile for the C/O = 0.5 case is marginally hotter than the high C/O cases because of higher opacity in the former due to the high H_2O opacity; this effect is similar to the high metallicity cases discussed above. The differences in the spectra are most prominent in the H_2O absorption bands across the spectral range.

Visible Absorbers and Thermal Inversions

Here we investigate the effect of visible opacity on the spectra and $P-T$ profiles. In the previous sections we investigated the effect of infrared opacity due to prominent C and O molecules on the atmospheric structure and spectra. However, several species are expected to be prevalent in hot Jupiter atmospheres that can provide strong visible opacity, e.g. the alkali atoms Na and K, and metal oxides (TiO, VO, etc.). While the Na and K absorption is primarily due to strong doublet resonance lines centred at $\sim$0.59 μm and $\sim$0.77 μm, respectively, and appropriately broadened, the absorption due to TiO, VO, etc., are very strong and broad bands spanning almost the entire optical spectrum and hence contributing much stronger opacity. On the other hand, TiO is not expected to be as abundant in gas phase as Na/K due to the significantly lower abundance of Ti, much higher condensation temperature, and much more prone to settling and C/O ratios (e.g. Knutson *et al.*, 2010; Madhusudhan *et al.*, 2011a;

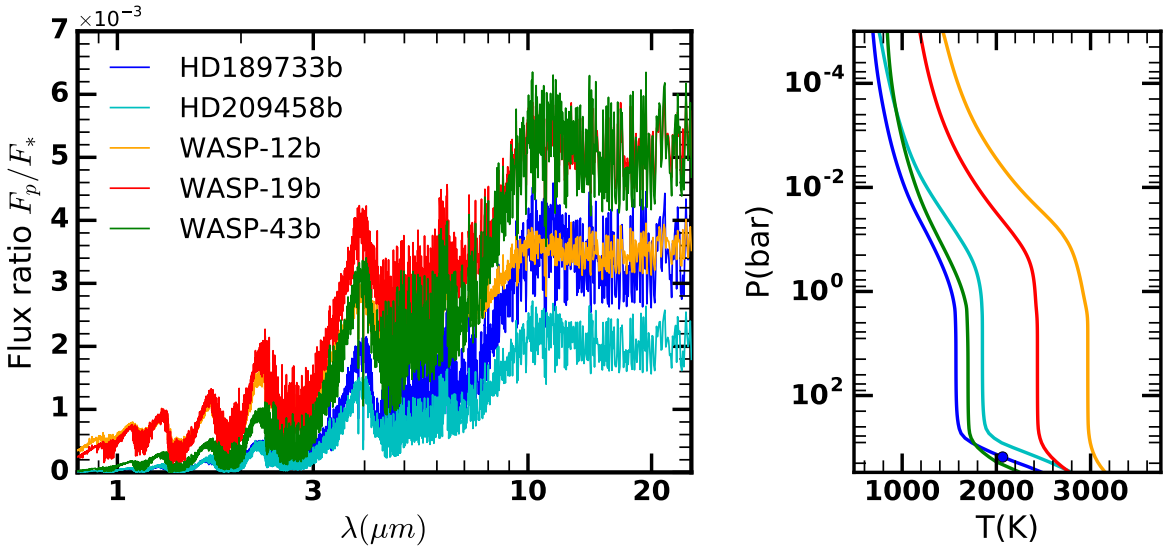

Fig. 3.11 Model spectra and $P-T$ profiles for several known hot Jupiters. The planetary and stellar parameters are given in Table 3.3. The models are discussed in section 3.4.2.

Spiegel *et al.*, 2009). Nevertheless, TiO has been suggested as a potential candidate to cause thermal inversions in the hottest of hot Jupiters (Fortney *et al.*, 2008; Hubeny *et al.*, 2003) and has also been suggested in 2 systems (Evans *et al.*, 2016; Haynes *et al.*, 2015). Therefore, we explore the dependence of spectra and $P-T$ profiles on both Na/K and TiO.

Considering Na and K in the atmosphere (Burrows and Volobuyev, 2003) at solar abundances (at pressures greater than 0.1 bar) increases the opacity in the visible part of the spectrum, near the peak of the stellar flux. The left panel in Fig. 3.10 shows the comparison between models with and without Na/K absorption. The increased visible opacity leads to greater absorption of the incident star light in the upper layers of the atmosphere making the upper temperature profile hotter. It also means that less of the stellar flux penetrates deeper down thereby causing the lower isothermal layer to start higher up in the atmosphere and so does the radiative-convective boundary. Even small quantities of sodium and potassium at solar abundances are adequate to significantly influence the $P-T$ profile, as shown in Fig. 3.10, and the resultant flux is substantially increased as well.

Now we consider a model planet which has only TiO as the visible absorber. As it is only present as a gas at the very highest temperatures that exoplanets can be, we decided to model WASP-12b, with an equilibrium temperature of almost 3000 K (see table. 3.3). If TiO is present at solar abundance instead of sodium or potassium

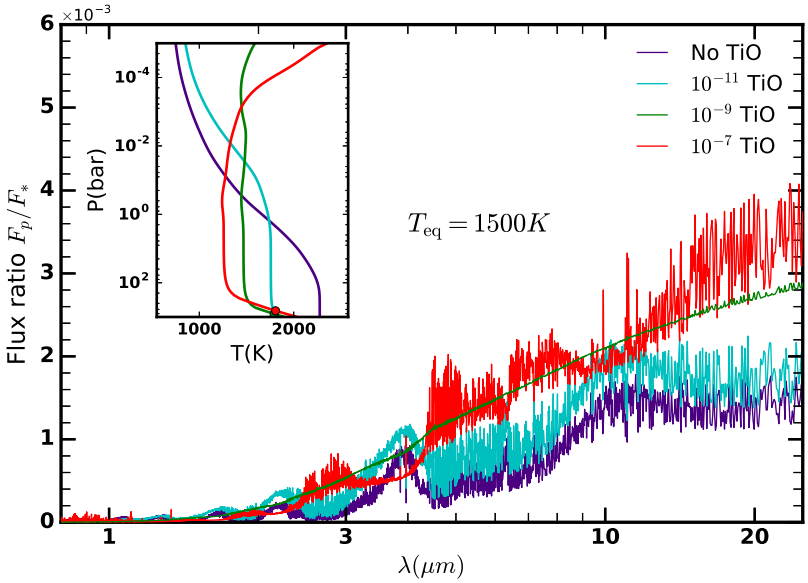

Fig. 3.12 Effect of TiO absorption on the spectrum and $P-T$ profile of a hot Jupiter. A model with equilibrium temperature of 1500 K is considered with varying levels of TiO in the atmosphere with the mixing ratio ranging from zero to 10^{-7}.

(see fig. 3.10), a temperature inversion occurs at the top of the atmosphere and totally transforms the $P-T$ profile and flux ratio. The very strong TiO opacity means more of the stellar flux is absorbed near the top of the atmosphere. This causes the top of the atmosphere to heat up, and keeps the lower layers cooler by preventing the peak stellar flux penetrating down. The increase in opacity leads the convective region to move up higher into the atmosphere as well. TiO is very effective at absorbing the incident stellar flux in the visible, and is able to influence the atmospheric temperature profile significantly despite being present in much smaller quantities than other prominent volatiles species (Fortney *et al.*, 2008; Madhusudhan, 2012). The inversion created means that absorption features in the infrared now become emission features, coming from the hotter regions higher up. An inverted profile is an indication of very strong opacity in the visible near the top of the atmosphere, and indeed only a few data points are needed to verify this (Diamond-Lowe *et al.*, 2014; Madhusudhan and Seager, 2010).

The effect of TiO on the temperature profile and spectrum can be seen in Fig. 3.12. As the TiO abundance is gradually increased the $P-T$ profile transitions from having no inversion to having a strong inversion, for a nominal hot Jupiter with an equilibrium temperature of 1500 K. The upper layers become hotter as more TiO is added, and the lower layers have a reduced flux incident upon them and hence are cooler. The

green line is the transition point at which absorption features become emission features, resulting from the inversion.

3.4.2 Models of Known Irradiated Planets - Effect of System Properties

We use GENESIS to generate models of several known hot Jupiters to investigate the effect of system parameters, particularly the stellar properties. We consider five well studied hot Jupiters spanning a wide range in temperature ($T_{\rm eq}$ ∼1200 - 2600 K): HD 189733b (1200 K), WASP-43b (1375 K), HD 209458b (1450 K), WASP-19b (2065 K), and WASP-12b (2580 K). The system parameters are shown in Table 3.3 and the model spectra and temperature profiles are shown in Fig. 3.11. We generate fiducial models assuming solar values for the elemental abundances, and consider only the prominent O, C, and N based molecular species. We also include Na and K absorption and collision induced opacity due to H_2-H_2 and H_2-He. In each case, the stellar flux was modelled using the Kurucz spectrum for the corresponding stellar properties shown in Table 3.3.

As expected, both the incident irradiation at the planet and the stellar spectrum have a palpable effect on the atmospheric temperature profile. A greater irradiation, represented by $T_{\rm eq}$, causes a hotter temperature profile for the same chemical composition, as can be seen in Fig. 3.11. Consequently, the $P-T$ profiles of HD 189733b and WASP-12b are the coolest and hottest in our sample. On the other hand, despite the $T_{\rm eq}$ for WASP-43b and HD 209458b being similar, the $P-T$ profiles have different gradients. This is due to the difference in the stellar spectra. WASP-43 is a cooler star (see table 3.3), implying that the peak of its spectrum is at a longer wavelength, due to which the incident radiation penetrates deeper down causing a steeper temperature gradient. These models, along with the results in section 3.4.1, demonstrate that the temperature gradient in a highly irradiated atmosphere is influenced by several factors including the incident irradiation, the stellar spectrum, and the chemical composition, both of visible and infrared absorbers.

The stellar properties also have a significant effect on the observed planet-star flux ratio. Generally, for a given host star, hotter and larger planets have higher emergent fluxes. However, for transiting exoplanets the key observable quantity is the planet-star flux ratio. This implies for the same planetary properties a cooler and/or smaller star would lead to larger planet-star flux ratio. Fig. 3.11 demonstrates this natural expectation. At the cooler end, the planets HD 189733b, WASP-43b, and HD 209458b

Planet	$Z_{\rm star}$	$T_{\rm eff}$ (K)	$R_{\rm star}$ ($R_{\rm sun}$)	$\log(g_{\rm star})$ (c.g.s)	a (A.U.)	$T_{\rm eq}$ (K)	R_p (R_J)	$\log(g_{\rm pl})$ (c.g.s)	dist. (pc)
HD189733b	-0.03	5040	0.756	4.587	0.0310	1200	1.14	3.34	19.5
HD209458b	0.00	6065	1.155	4.361	0.0472	1450	1.359	2.97	49.6
WASP-12b	0.30	6300	1.63	4.38	0.0225	2580	1.79	2.99	267.0
WASP-19b	0.02	5500	0.99	4.5	0.0163	2065	1.39	3.17	250.0
WASP-43b	-0.05	4400	0.598	4.65	0.0142	1375	0.930	3.71	80.0

Table 3.3 System parameters of known hot Jupiters modelled in section 3.4.2 and Fig. 3.11. $Z_{\rm star}$ is the stellar metallicity, $T_{\rm eff}$ is the effective temperature of the star and $T_{\rm eq}$ is the equilibrium temperature of the planet. The equilibrium temperature is calculated assuming the albedo is 0, and complete redistribution of flux over the planet, $T_{\rm eq} = T_{\rm eff}\sqrt{R_{\rm star}/(2a)}$. The system parameters are obtained from exoplanets.org.

have similar equilibrium temperatures (1200-1450 K), with HD 209458b being the hottest. However, WASP-43b has over twice the planet-star flux ratio compared to HD 209458b, with HD 189733b being in between, owing to the the host star WASP-43 being the coolest star in our sample. Similarly, at the hotter end WASP-19b and WASP-12b have similar $T_{\rm eq}$ but the flux ratio for WASP-19b is significantly higher than WASP-12b, again owing to its smaller and cooler star. As an extreme case, WASP-12b has nearly twice the $T_{\rm eq}$ of WASP-43b but still lower flux ratio than the latter. Thus, the stellar parameters play a key role in determining the observability of emergent spectra of exoplanets, which justifies the numerous current exoplanet searches around cooler and smaller stars.

3.4.3 Non-irradiated Atmospheres

GENESIS has the capability to simultaneously and self-consistently consider both external stellar irradiation and internal flux from within the planet. We now turn to models of non-irradiated atmospheres which are relevant for planets on large orbital separations or free floating planets and brown dwarfs. Such models are particularly useful for directly-imaged sub-stellar objects, young giant exoplanets (Barman *et al.*, 2015; Bonnefoy *et al.*, 2014; Macintosh *et al.*, 2015; Marois *et al.*, 2010) and brown dwarfs (Apai *et al.*, 2013; Burgasser, 2014) detected via direct imaging and for which high quality spectra are becoming available. Several conventional models of non-irradiated objects exist in the literature (e.g. Barman *et al.*, 2015; Madhusudhan *et al.*, 2011c; Marley *et al.*, 2012) and include cloud-free as well as cloudy models, unlike self-consistent models of irradiated hot Jupiters which are generally cloud free (e.g.

Burrows *et al.*, 2008; Fortney *et al.*, 2008). In the present work, we explore only cloud-free models of non-irradiated objects and will consider cloudy models in future work.

For our present exploration, we will again model a Jovian-like planet but now with an increased internal temperature that is much greater than the 75 K we considered for irradiated planets; $T_{\rm int}$ is now 1500 K unless otherwise specified and the stellar irradiation is negligible. We nominally consider a solar-type star with the orbital separation of the planet at 10 AU. In direct imaging the observable is the emergent spectrum directly from the planet and not the planet-star flux ratio. We assume the distance to the system to be 10 parsecs. The chemical composition, again, is determined via chemical equilibrium with solar elemental abundances. In what follows, we first compare the differences in the emergent spectrum and $P-T$ profile for irradiated and non-irradiated planets with matching equilibrium and internal temperatures. We then explore how the internal flux and metallicity influences the profile and spectrum for non-irradiated planets.

Non-irradiated vs. Irradiated Planets

The differences in the observed spectra for planets with strong external versus internal flux are shown in Fig. 3.13. The fluxes set the top/bottom boundary conditions for the irradiated and non-irradiated atmospheres, respectively. For the irradiated planet we consider a $T_{\rm eq}$ =1500 K and $T_{\rm int}$ = 75 K whereas for the non-irradiated planet we consider negligible irradiated and $T_{\rm int}$ = 1500 K. The strong external flux applied at the top of the atmosphere for the irradiated planet leads to a hotter region near the top. However, the internal flux for the non-irradiated planet causes the deep layer temperature to be hotter. Strong external irradiation suppresses the convective region of the atmosphere to deeper in the atmosphere, below the pressure range in the inset figure, and the temperature tends to an isotherm in the lower atmosphere as seen in the previous sections. On the other hand, the radiative-convective boundary can be seen for the non-irradiated planet.

The spectrum has greater emission for the irradiated planet in the infrared, as the temperature in the regions where the emission occurs is greater, i.e. higher up in the atmosphere above the $\sim$1 bar level. The non-irradiated planet has the higher emission at $\sim 1\,\mu$m where there is little opacity at these wavelengths and hence deeper regions below the $\sim$1 bar level are probed, where the internal flux dominates. The absorption features for the non-irradiated planet are also much more pronounced, and show greater flux differences. This is owing to the greater temperature gradient for the

non-irradiated atmosphere. Fig. 3.13 thus shows a clear difference between the spectra and $P-T$ profiles of highly irradiated planets observed using transit spectroscopy and weakly irradiated planets observed by direct imaging.

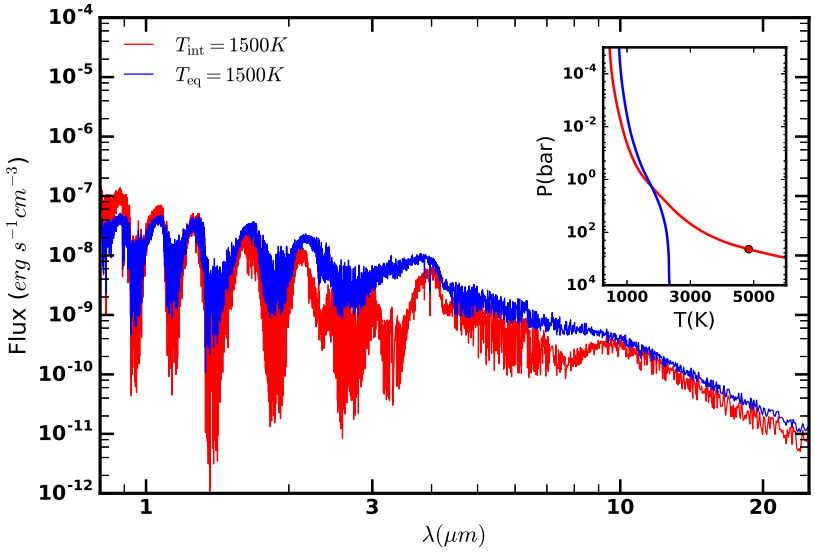

Fig. 3.13 Comparison between an irradiated and a non-irradiated giant planet. The two models show the emergent spectra and $P-T$ profiles for an irradiated hot Jupiter with an equilibrium temperature of 1500 K (blue) and a non-irradiated Jupiter with an internal temperature of 1500 K (red), as discussed in section 3.4.3. Both the planets are assumed to be 10 pc away from the observer. The circle in the $P-T$ profile indicates the radiative-convective boundary.

Effect of Internal Flux

We explore models of our fiducial non-irradiated planet described above with the internal flux, represented by an effective internal temperature $T_{\rm int}$, varied between 1000 K to 2000 K. The elemental abundances are kept fixed at solar values and thermochemical equilibrium is assumed; the molecular composition however may change depending on the temperature structure. The emergent spectra and $P-T$ profiles are shown in Fig. 3.14. Naturally, higher internal flux leads to hotter temperature profiles in the atmosphere. In particular the deeper regions are warmer as higher flux is transported upwards from within the planet. The radiative-convective boundary is also shifted upwards and to a higher temperature as well; the increase in internal flux drives a greater convective flux. Considering the lowest pressures, the external irradiation is now negligible, and so the atmospheres all tend to the same isotherm, one where the

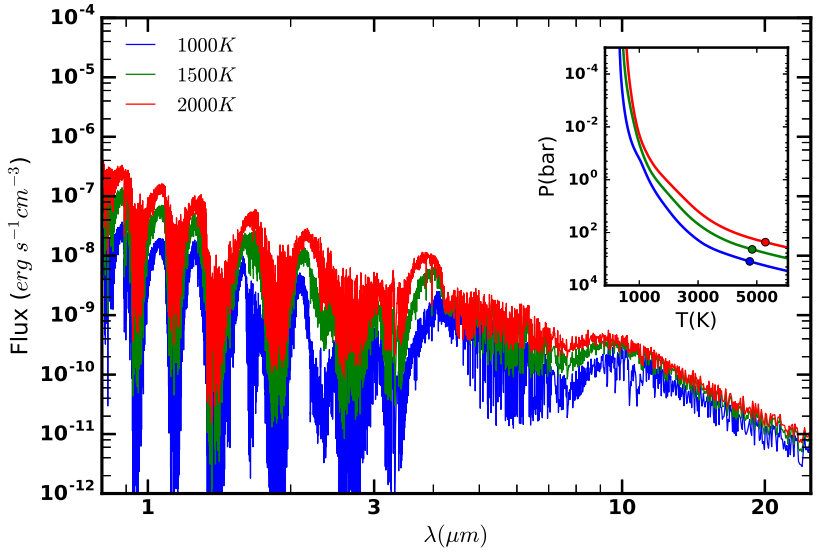

Fig. 3.14 Effect of internal heat on emergent spectra and $P-T$ profiles of non-irradiated planets. A Jupiter placed at 10 A.U. is modelled with different internal heat fluxes represented by $T_{\rm int}$. The emergent flux is shown for the source at 10 pc from the observer. The corresponding $P-T$ profiles are shown in the inset. The circles denote the radiative-convective boundary.

escaping heat balances the heat from the core. The internal heat has a very weak influence on the top layers of the atmosphere, as the optical depth and hence absorption of the flux is low. There are slight differences in the $P-T$ gradient arising from varying chemistry, and vice versa, particularly at $\sim$ 1000 K where the abundances (therefore the optical depth and absorption) are the most sensitive to temperature. The emergent spectra show greater emission for the planets with greater internal temperature for every wavelength, perhaps unsurprisingly as every point of the atmosphere is hotter. The figure shows clearly that the internal heat flux, although often considered deep inside the planet, strongly influences the observed spectrum, with amplitudes of spectral features of even several orders of magnitude when considering some of the absorption features.

Effect of Metallicity and C/O ratio

We also report models over a range of metallicities, as shown in Fig. 3.15. The metallicities of C, O, and N considered were solar, 10$\times$ solar, and 30$\times$ solar, with the internal temperature now fixed at 1500 K, analogous to Fig. 3.8 for irradiated planets. Note that now the resultant $P-T$ profile is not as different, with only a

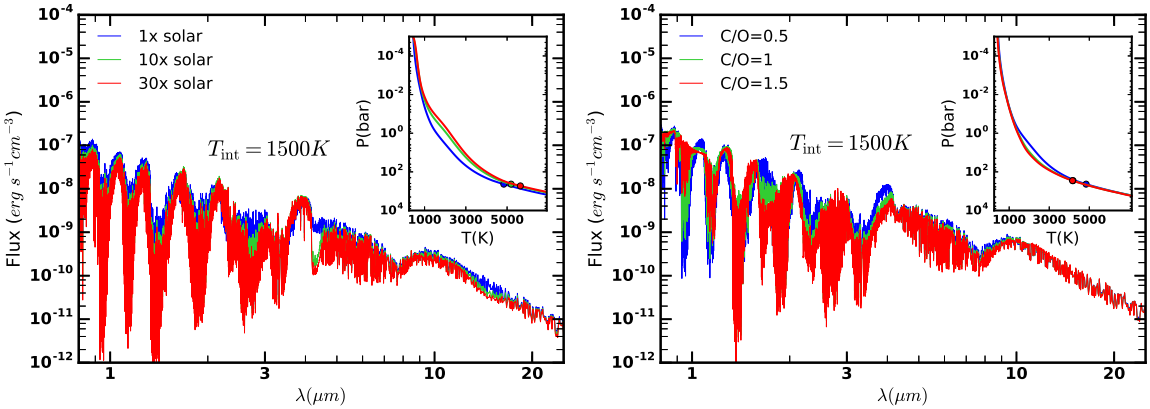

Fig. 3.15 Effect of metallicity and C/O ratio on emergent spectra and $P-T$ profiles for non-irradiated planets. A jupiter-sized planet with an internal temperature of 1500 K is considered. The metallicity is explored between 1-30 ×solar and the C/O ratio spans 0.5-1.5.

slightly greater temperature seen for the highest metallicities. The radiative-convective boundary is also not dissimilar, occurring near similar temperatures (~5000 K) and pressures (~1000 bar) for each case.

The flux spectrum does show nominal differences between the different metallicities, with the higher flux observed for the solar metallicity due to lower absorption. The strong opacity for the green and red curves mean the emission occurs from lower pressures, where it is cooler. The features in the flux plot are more pronounced for the highest metallicity due to the greater molecular abundance leading to greater absorption in the molecular bands. Furthermore, the strong feature in the 4-5 μm region in the higher metallicity and higher temperature models is due to the higher abundance of CO and CO_2. Altering the C/O ratio does alter the received flux more significantly, as increased C/O ratios beyond 1 reduce the water abundance by orders of magnitude (especially at temperatures exceeding 1000 K, here the oxygen is taken up in the CO). This reduces the spectral features of H_2O, and hence even though the $P-T$ profile is largely unaffected, the chemistry and therefore the flux has observable differences.

We have explored models of non-irradiated planets over a range in metallicity, C/O ratio and internal flux. The $P-T$ profiles and emergent spectra show clear differences compared to those of irradiated planets, as expected and found in previous works. In the future, more models exploring the parameter space in greater detail would be beneficial, particularly with the inclusion of clouds that are inferred for several

substellar objects (Barman *et al.*, 2015; Madhusudhan *et al.*, 2011c; Marley *et al.*, 2012) and brown dwarfs (Apai *et al.*, 2013; Burgasser, 2014).

3.5 Summary and Discussion

We introduce a new code GENESIS for modelling exoplanetary atmospheres. Our effort is driven by current and upcoming high-resolution and high-precision spectra of exoplanets and brown dwarfs. Current observations of exoplanetary spectra span a variety of methods, ranging from transit spectroscopy and direct imaging to very high resolution Doppler spectroscopy with $R \sim 10^5$. On the other hand, observational inferences and theoretical studies are suggesting that exoplanetary and brown dwarf atmospheres can span a wide range of physicochemical conditions, e.g., incident irradiation, metallicities, C/O ratios, and internal fluxes. Consequently, there is a growing need in the field for high-fidelity self-consistent models of exoplanetary spectra that span over all these parameters and a wide range in spectral resolution. Several self-consistent models exist in the field, mostly derived from pre-existing codes e.g., from stellar or solar-system applications, with varied degrees of complexity and applicability to these requirements but also suggesting the need for a new generation of models, as discussed in section 3.1.

The GENESIS code is custom-built for self-consistent, line-by-line, plane-parallel modelling of exoplanetary atmospheres with a high degree of robustness and applicability. The code can be used to model exoplanetary atmospheres over a wide range in incident irradiation, metallicity, C/O ratio, internal fluxes, etc., and can be used to model irradiated as well as non-irradiated atmospheres. The code uses well-tested robust and accurate methods for each component of the model. The radiative transfer is solved line-by-line using the Feautrier method which allows for treatment of full angular dependance of the intensity and is second order accurate. The code ensures radiative-convective equilibrium using the Rybicki's method with complete linearisation to find the temperature correction. The radiative and convective regions of the atmosphere are solved simultaneously and self-consistently, treating the external irradiation and internal flux as the top and bottom boundary conditions, respectively. The line-by-line absorption cross sections of the chemical species are derived from the latest high temperature line lists, including the effect of thermal and pressure broadening. The atmosphere is assumed to be in chemical equilibrium with the temperature profile and, given the elemental abundances, the main constituent gas mixing fractions are found using established methods.

In the present work, we demonstrate our code for modelling giant exoplanetary atmospheres, both irradiated and non-irradiated, which are currently the most studied objects in the field. The code is tested extensively for consistency and robustness and against published models of some known hot Jupiters generated using existing codes. We generate grids of models in the parameter space for both irradiated and non-irradiated objects. For irradiated planets, we explore the effects of $T_{\rm eq}$, metallicity and C/O ratio on the $P-T$ profile and emergent spectrum, and find trends consistent with previous studies. We note how the C/O ratio has a significant effect on the spectrum, particularly at high temperatures. We also discuss the effects of visible opacity, e.g. of Na/K and TiO, and, particularly, the formation of thermal inversions in hot Jupiters atmospheres as a function of TiO abundance. Finally, we investigate model of several known hot Jupiters are discuss the effect of the stellar properties on the observable atmospheric properties. We also investigate models for non-irradiated planets observing how the $P-T$ profile and emergent flux vary with the internal flux and metallicity, and demonstrate the significant differences between the spectra and $P-T$ profiles of irradiated and non-irradiated atmospheres. This provides a good demonstration of the robustness and diversity of the model in its ability to model across the parameter space accurately.

In the present code we make some basic assumptions that are common to all self-consistent equilibrium models of exoplanetary atmospheres. The main basis of the model is a plane-parallel geometry, though our radiative transfer scheme does take into account the angular dependence of the specific intensity in each layer of the atmosphere. We assume general equilibrium conditions, i.e., local thermodynamic equilibrium (LTE), hydrostatic equilibrium, radiative-convective equilibrium, and chemical equilibrium. Even though the code is generic for any chemical composition, we currently focus on giant exoplanetary atmospheres. As such, we assume the atmosphere to be H_2-rich. Furthermore, here we only focus on the dominant chemical compositions expected in such atmospheres, namely considering only the prominent molecular species with C-O-N chemistry in chemical equilibrium. However, the extension to include other molecules is straightforward using a full equilibrium chemistry code (e.g. Madhusudhan, 2012; Seager *et al.*, 2005). We also consider additional species such as Na/K and TiO to demonstrate some cases with strong visible opacity. We have assumed that the scattering is only due to H_2 Rayleigh scattering and that the atmosphere is cloud-free. Any non-equilibrium phenomena, e.g. photochemical or dynamical effects, have been ignored.

The code can be further developed to incorporate new processes that depart from the present equilibrium assumptions. While our current cloud-free models may be applicable to a range of irradiated hot Jupiters as well as to some brown dwarfs (e.g. T Dwarfs), observations and theoretical studies suggest that clouds/hazes can exist in several of these atmospheres (Barman *et al.*, 2015; Helling *et al.*, 2008; Madhusudhan *et al.*, 2011c; Marley *et al.*, 2012). Therefore, we anticipate including clouds/hazes in our model in the future. While some previous models have pursued it in the two-stream approximation (Marley *et al.*, 2012), in our case the radiative transfer solver which currently uses the matrix Feautrier method would need to be modified to handle anisotropic scattering, e.g., using the Discontinuous Finite Elements (DFE) method with Accelerated Lambda Iteration (Hubeny and Mihalas, 2014; Sudarsky *et al.*, 2003). Additionally, our model currently does not include any prescription to self-consistently transport energy to the night side, e.g., due to winds, etc. We do indirectly account for that effect by adjusting the incident stellar flux with a parametric factor ($f_{\rm star}$), as also pursued by (Fortney *et al.*, 2008). This can be improved in the future by adding an energy sink on the dayside and self-consistently ensuring radiative equilibrium (e.g., Burrows *et al.*, 2008). We could also incorporate prescriptions in our code to consider non-equilibrium chemical processes. Finally, the chemical and opacity database used in the present model can be expanded significantly beyond the species currently considered. The models can also be easily extended to considering lower mass planets with significantly different compositions from the H_2-rich atmospheres explored in our current work.

The GENESIS models are aimed to be a valuable resource to the community[1]. We provide self-consistent models of emergent spectra and pressure-temperature-density profiles over a grid in parameter space of giant exoplanetary atmospheres. Additionally, we also provide models of several known hot Jupiters based on their system parameters. In the future our models could be computed at very high resolution. In particular, this is highly desirable for atmospheric detections using high dispersion spectroscopy where accurate high-resolution (R$\sim 10^5$) models are cross-correlated with an observed spectrum to detect a molecule (e.g., Brogi *et al.*, 2012). Since the models can simulate both irradiated and non-irradiated atmospheres they are applicable to a wide range of objects, spanning the entire range of irradiated hot Jupiters (1000-3000 K) and non-irradiated giant planets and also brown dwarfs. Given its high computational efficiency, our code can also be integrated into radiative transfer components of higher dimensional models. For example, it can be integrated with minimal adaptation into detailed non-

[1]The models are made publicly available at https://github.com/exo-worlds/genesis

equilibrium chemistry codes (Moses *et al.*, 2013) to compute the chemical and $P-T$ profiles self-consistently, and similarly into general circulation models (Showman *et al.*, 2009). As such, the GENESIS models would be valuable both in the planning and interpretation of observations as well as in detailed theoretical understanding of the physical and chemical processes of exoplanetary atmospheres. This is all the more timely given the impending renaissance in atmospheric characterisation of exoplanets with upcoming observations from current and large facilities on the horizon, e.g. HST, VLT, JWST, E-ELT, etc.

Chapter 4

New Avenues for Thermal Inversions in hot Jupiters

"As with most of life's problems, this one can be solved by a box of pure radiation."
- Mark Watney, The Martian, A. Weir

This chapter uses the GENESIS code to explore thermal inversions on hot Jupiters. I have modelled these inversions with the inclusion of several new molecular species, namely AlO, CaO, MgH and NaH. I have also explored the effect of varying the infrared opacity and investigated how the thermal inversions vary as the atmospheric C/O ratio is increased for each of the four new species as well as TiO and VO. This work has been published in Gandhi and Madhusudhan (2019).

4.1 Introduction to Thermal Inversions

One of the major areas of research through thermal emission spectroscopy has been the study of thermal inversions in highly irradiated exoplanets, particularly hot Jupiters. Thermal inversions (or stratospheres) are regions of the atmosphere where the temperature increases with altitude, similar to the stratosphere on Earth. This is caused by entrapment of the incident stellar irradiation due to the presence of strong UV/visible absorption, such as O_3 for Earth's stratosphere. In hot Jupiters, molecules such as TiO and VO have been suggested to play a similar role (Fortney *et al.*, 2008; Hubeny *et al.*, 2003). The larger and hotter extrasolar giant planets have been thus far the most studied thanks to their strong spectral signatures. Initial observational inferences of thermal inversions, were based mostly on photometric data (Burrows *et al.*, 2007, 2008; Knutson *et al.*, 2008, 2009; Madhusudhan and Seager, 2010), several of which have

Table 4.1 Summary of developments in the theory of thermal inversions in strongly irradiated giant planets.

Study	**Investigation into Thermal Inversions on hot Jupiters**
Hubeny *et al.* (2003)	Proposed *TiO* and *VO* as a candidate for thermal inversions in hot Jupiters.
Fortney *et al.* (2008)	Introduced a two-class system for classifying hot Jupiters dependant on the atmospheric temperature.
Spiegel *et al.* (2009)	Investigated depletion of *TiO* and *VO* in hot Jupiter atmospheres due to gravitational settling.
Zahnle *et al.* (2009)	Proposed *HS* and S_2 as candidates for thermal inversions at intermediate temperatures ($\sim$1000-2000 K).
Knutson *et al.* (2010)	Investigated effect of stellar activity and concluded inversions are more likely with lower UV flux.
Madhusudhan *et al.* (2011b)	Investigated dependence of *TiO* and *VO* on C/O ratio.
Mollière *et al.* (2015)	Suggested atomic *Na* and *K* are capable of leading to thermal inversions for a C/O ratio near 1.
Beatty *et al.* (2017a)	Proposed that higher log(g) suppresses inversions due to cold-trap processes.
Lothringer *et al.* (2018)	Proposed *Fe*, *Mg*, *SiO* and metal hydrides as candidates for inversions on planets with $T_{\rm eq}$>2500 K.
This work	Propose four species, *AlO*, *CaO*, *NaH* and *MgH* for causing thermal inversions. Investigated the effect of the infrared opacity on thermal inversions.

since been revised (Diamond-Lowe *et al.*, 2014). More recently, inferences of thermal inversions have been possible with Hubble Space Telescope's Wide Field Camera 3 (HST WFC3) observations (Evans *et al.*, 2017; Haynes *et al.*, 2015; Sheppard *et al.*, 2017). These planets are of great interest as only a handful of species have been suggested to be capable of leading to a thermal inversion in such atmospheres. Their strong effect on the temperature profile results in significant observable consequences in the thermal emission spectra of exoplanets. A review on thermal inversions can be seen in Madhusudhan *et al.* (2014a).

The first theoretical work on thermal inversions on hot Jupiter atmospheres was by Hubeny *et al.* (2003). Here they proposed two molecules, TiO and VO, which both had sufficiently strong absorption in the visible that they should be capable of causing thermal inversions at or near their expected solar abundances on hot Jupiters. These species are only expected to exist in the atmospheres of planets with temperatures exceeding 2000 K, but a significant number of irradiated giant planets so far discovered exceed this temperature on their dayside (e.g WASP-33b, WASP-12b, WASP-18b). This work was built upon by Fortney *et al.* (2008), who also modelled atmospheres with TiO and VO to calculate radiative-convective equilibrium P-T profiles of the atmospheres of several known hot Jupiters. They propose a two-class hot Jupiter classification, dependant on the equilibrium temperature being above or below ∼1500 K. Below ∼1500 K, planets were expected to be too cool to host TiO or VO in their gaseous state. Therefore only planets above this temperature are expected to have the TiO/VO in sufficient abundances to lead to thermal inversions.

Subsequent studies investigated other factors that influence the possibility of thermal inversions on hot Jupiters. A detailed investigation of the effect of TiO across a number of hot Jupiters was carried out by Spiegel *et al.* (2009). In this study, the vertical upwelling in the atmosphere and the day-night redistribution were also considered. They proposed that when gravitational settling was considered, an atmospheric temperature higher than ∼1800 K was required for TiO to be abundant enough in the observable atmosphere to cause thermal inversions. Therefore, they proposed that only the hottest exoplanets were capable of thermal inversions. They also determined that VO is less likely to play a significant role in thermal inversions on hot Jupiters due to its weaker cross section and lower equilibrium solar abundance compared to TiO.

Zahnle *et al.* (2009) proposed that sulphur species, such as HS and S_2, may be responsible for thermal inversions in the stratospheres for planets with intermediate temperatures, ranging from ∼1000-2000 K. Both of these species possess significant UV absorption (in particular HS) and thus can lead to radiative heating rates that are

significant enough to lead to thermal inversions. Knutson *et al.* (2010) investigated the effect of the star's UV flux, and whether spectrally active species would remain stable on such exoplanets. The most active stars with the strongest UV fluxes were the least likely to support thermal inversions in the planets given that visible absorbers would most likely be dissociated by the incident UV irradiation. Therefore they predicted that thermal inversions would be more likely on hot Jupiters if the incident UV flux was low enough for inversion-causing species to exist. Inversions have also been suggested to be caused by thermal instabilities in the presence of ohmic dissipation in highly irradiated atmospheres from general circulation models (Menou, 2012).

Madhusudhan *et al.* (2011b) investigated the equilibrium abundances of TiO and VO as the C/O ratio varied. They found that a C/O ratio of 1 reduced the abundance of these species by a factor of ∼100, thereby reducing the visible opacity of the atmosphere. Madhusudhan (2012) proposed a 2D classification scheme, depending on the atmospheric temperature and the C/O ratio for hot Jupiters. When the C/O ratio exceeds unity, the available oxygen preferentially binds to carbon to form carbon monoxide. The atmosphere is thus depleted of oxygen to form species such as H_2O, TiO and VO. Mollière *et al.* (2015) on the other hand found that a C/O ratio near 1 also resulted in thermal inversions from the gaseous atomic species Na and K. They discovered that with an atmospheric temperature over 2000 K, thermal inversions were seen in the model atmospheres with F5, G5 and K5 stars at pressures of ∼0.1-0.01 bar. This results from the atomic line wings, which result in significant absorption of the visible flux and therefore emulate the role of TiO or VO to lead to a thermal inversion. More recently, Beatty *et al.* (2017b) analysed the spectrum of an irradiated brown dwarf and hypothesised that the lack of a thermal inversion seen was due to the high surface gravity. The higher log(g) would likely enhance cold-trap processes which prevent TiO/VO from circulating up into the photosphere and therefore reasoned that this may prevent thermal inversions from forming on more massive exoplanets.

More recent work suggesting the thermal dissociation of H_2O in ultra hot Jupiters ($T \gtrsim 2500$ K) has shown that thermal inversions may also form more readily on such planets (Arcangeli *et al.*, 2018; Lothringer *et al.*, 2018; Parmentier *et al.*, 2018). The inversions are driven by the lack of H_2O, which causes the photospheric cooling to be more inefficient (Mollière *et al.*, 2015). Thus thermal inversions can form due to species such as TiO and VO in such atmospheres. The dayside emission spectra from such dissociated atmospheres are expected to have weak HST WFC3 spectral features due to the weaker H_2O absorption but have strong CO features in the Spitzer 4.5μm bandpass as this does not readily dissociate. This mechanism of thermal dissociation

has thus been proposed to explain the lack of significant WFC3 spectral features seen in several ultra hot Jupiters with an equilibrium temperature in excess of 2000 K(e.g. Kreidberg *et al.*, 2018; Parmentier *et al.*, 2018). Lothringer *et al.* (2018) have also explored equilibrium models of hot Jupiters such as KELT-9b, with $T_{eq} \sim 4500$ K, when species such as TiO/VO begin to thermally dissociate and proposed several candidate species for inversions in the atmospheres of such extremely hot planets (see table 4.1). These species, such as Fe, Mg and SiO, remain thermally stable over a much wider range of temperatures. On the other hand, several ultra hot Jupiters do show strong H_2O absorption which remains a conundrum (Parmentier *et al.*, 2018).

At the same time as equilibrium models, retrievals of hot Jupiter emission spectra has enabled atmospheric characterisation and abundance analyses from observations. Focus of research has recently moved into investigating the candidate species for thermal inversions. It has only been very recently that we have been able to obtain spectra of sufficient quality so as to infer such species in exoplanets. Haynes *et al.* (2015) reported signs of a thermal inversion from an emission spectrum of WASP-33b. Retrievals of WASP-33b revealed that this stratosphere was likely the effect of TiO in the atmosphere. Nugroho *et al.* (2017) also detected TiO in WASP-33b using high resolution spectroscopy. Evans *et al.* (2016) obtained transmission spectra of WASP-121b with visible and near-infrared WFC3 observations and hypothesised that the spectrum was best fit with TiO or VO present in the atmosphere. This is plausible given that the equilibrium temperature for this planet is ∼2400 K and further supported by the presence of a thermal inversion on the dayside (Evans *et al.*, 2017) found in their subsequent study. Sheppard *et al.* (2017) have also studied the dayside atmosphere of WASP-18b and found a thermal inversion in the infrared emission spectrum, also confirmed by Arcangeli *et al.* (2018). Thus there is a growing number of exoplanets which possess thermal inversions and we are now beginning to place constraints on TiO and VO through such observations. More recently, Sedaghati *et al.* (2017) reported a detection of TiO through the ground based transmission spectrum of the planet WASP-19b using VLT. A subsequent attempt to detect the same using GMT proved unsuccessful (Espinoza *et al.*, 2019). With new advances in instrumentation, it is likely that detections of such species becomes commonplace in exoplanets. Therefore a theoretical understanding of how thermal inversions occur in exoplanets and due to which chemical species is of paramount importance.

In this chapter we report three key aspects of thermal inversions on hot Jupiters. Firstly, using semi-analytic models, we explore the required atmospheric abundance for species with strong visible cross sections in order for a thermal inversion to occur in

the atmosphere. These analytic models form the basis for predictions we will use and provide a good insight into the relevant radiative processes occurring in the atmosphere. We also test how well the semi-analytic prediction holds for a real atmosphere by testing against full radiative-convective equilibrium models of the atmosphere using line-by-line radiative transfer.

Secondly, we explore species beyond TiO and VO which possess strong visible opacity and thus may be capable of leading to thermal inversions. Here, we find 4 species, AlO, CaO, NaH and MgH which if present at sufficient abundances are capable of forming thermal inversions in hot Jupiters. This is done through our self-consistent radiative-convective equilibrium code GENESIS (chapter 3). Key to this new find has been the molecular cross sections generated from the latest and most accurate line lists available (Hill *et al.*, 2013; McKemmish *et al.*, 2016; Patrascu *et al.*, 2015; Rivlin *et al.*, 2015; Yadin *et al.*, 2012; Yurchenko *et al.*, 2016).

Thirdly, we explore the effect of the infrared opacity on thermal inversions. It is well known that it is the ratio of the visible to infrared opacity that governs the formation of thermal inversions (Guillot, T., 2010; Hansen, 2008; Hubeny *et al.*, 2003). Thus far, only variation of the visible opacity has been considered through species such as TiO and VO. However, we show that the infrared opacity is just as significant for causing inversions as previously suggested by Mollière *et al.* (2015). We vary the infrared opacity through the C/O ratio of the atmosphere. The abundance of the volatile species (e.g H_2O, CH_4, NH_3, CO, HCN, CO_2, C_2H_2) is closely tied to the C/O ratio and altering this can change the abundance of these species by several orders of magnitude (Moses *et al.*, 2013). This can thus alter the overall infrared opacity of the atmosphere and therefore the required visible opacity for an inversion. We demonstrate that with a C/O ratio near unity species such as TiO can be at sub-solar abundance and still lead to thermal inversions. However, in this work we do not explore the variation of the metallic species with equilibrium temperature, which has shown to also deplete as the C/O ratio nears unity (Madhusudhan *et al.*, 2011b). We follow on to model WASP-121b, a hot Jupiter known to possess a thermal inversion (Evans *et al.*, 2017). We explore the required abundance of each of the metallic species to cause a thermal inversion in its atmosphere for both C/O=0.5 (solar) and C/O=1 for the planet.

In what follows, section 4.2 introduces the theory and the conditions required for a thermal inversion in the atmosphere of a hot Jupiter. Section 4.3 describes the effect of the visible opacity and the new species which can lead to stratospheres in these atmospheres. Section 4.4 discusses the importance of the infrared opacity in

determining the conditions for a thermal inversion through the effect of the C/O ratio. We explore the thermal inversion in a known system, WASP-121b, in section 4.5 with comparisons between models with various inversion-causing species against the observations. Finally, the conclusion and implications of the work are discussed in section 4.6.

4.2 Theory of Thermal Inversions

Thermal inversions or 'stratospheres' on exoplanets require specific atmospheric conditions, but leave strong signatures on the emergent spectra. The spectral signatures allow us to study stratospheres from observations of exoplanet spectra and explore the chemical species which may be responsible. In this section we will explore the theory of thermal inversions in hot Jupiters from prominent species which can cause inversions to the influence of volatile species such as H_2O. On Earth, the thermal inversion is achieved through ozone, which absorbs the strong UV radiation incident from the Sun, thus heating the upper layers of the atmosphere. Hot Jupiters can exhibit thermal inversions with quite different chemistry thanks to their high temperature and extreme irradiation. In both cases however, the method through which thermal inversions are achieved is the same, strong absorption of the incident flux at shorter wavelengths of light, typically UV/visible ($\sim$0.4-1μm). The flux from the star is greatest in the visible part of the spectrum, and any absorber with a strong visible cross section that is present in significant quantities will heat the upper atmosphere. This thermal inversion effects the thermal emission spectrum received from the dayside atmosphere. Outlined below is the effect of these stratospheres on the observed spectra. We then explore semi-analytic and full line-by-line radiative-convective equilibrium models and their importance in predicting and modelling inversions on exoplanet atmospheres.

4.2.1 Signatures of Thermal Inversions in Emission Spectra

Despite the relatively modest spectral coverage, recent observations have been able to reveal stratospheres in a number of hot Jupiters (Evans *et al.*, 2017; Haynes *et al.*, 2015; Sheppard *et al.*, 2017). These dayside emission spectra are well suited to characterise the pressure-temperature (P-T) profile, and in particular determine whether the atmosphere possesses a thermal inversion as the spectra are very strongly dependant on the thermal gradient in the photosphere. The strong influence on the observed spectrum means

that through instruments such as the HST WFC3 spectrograph, tight constraints have been obtained for the temperature gradient in the photosphere.

4.2.2 Analytic Model

Semi-analytic models of atmospheres can provide important insights into the atmospheric processes that occur. In particular they can help understand the underlying principles of thermal inversions in what are often complex atmospheres, with a number of chemical species each with its own frequency dependant spectral features. To begin, we will consider the analytic model by Guillot, T. (2010). This allows us to understand the dominant physics that determines thermal inversions on exoplanets. From then, we can consider self-consistent equilibrium models to complete the picture and compare to the simple analytic model.

The analytic temperature profile at an optical depth τ, for a planet with internal temperature $\mathrm{T_{int}}$ and irradiation temperature $\mathrm{T_{irr}}$ is given by (Guillot, T., 2010),

$$T^4 = \frac{3}{4}\mathrm{T_{int}}^4(\frac{2}{3}+\tau) + \frac{3}{4}\mathrm{T_{irr}}^4\mu(\frac{2}{3}+\frac{\mu}{\gamma}+(\frac{\gamma}{3\mu}-\frac{\mu}{\gamma})e^{-\gamma\tau/\mu}), \tag{4.1}$$

where $\gamma = \kappa_{\mathrm{vis}}/\kappa_{\mathrm{ir}}$ denotes the ratio of visible to infrared opacity. Here, τ refers to the monochromatic optical depth of the atmosphere. $\mu^2 = K_{\mathrm{vis}}/J_{\mathrm{vis}}$ is defined by the ratio of moments of the specific intensity in the visible $I_{\mathrm{vis},\mu}$,

$$J_{\mathrm{vis}} = \frac{1}{2}\int_{-1}^{1} I_{\mathrm{vis},\mu}d\mu, \tag{4.2}$$

$$K_{\mathrm{vis}} = \frac{1}{2}\int_{-1}^{1} \mu^2 I_{\mathrm{vis},\mu}d\mu. \tag{4.3}$$

For strongly irradiated planets, we can assume that the internal temperature is negligible compared to the irradiation temperature, $\mathrm{T_{int}} \ll \mathrm{T_{irr}}$. For there to be an inversion in the atmosphere, the temperature at small optical depth must exceed that at high optical depth,

$$f \equiv \frac{T(\tau=0)^4}{T(\tau\gg 1)^4} \approx \frac{\frac{2}{3}+\frac{\gamma}{3\mu}}{\frac{2}{3}+\frac{\mu}{\gamma}} > 1. \tag{4.4}$$

The denominator is determined at a high optical depth ($\tau >> 1$) but also below the penetration depth ($\tau < \tau_{\mathrm{pen}}$), where the internal heat flux of the planet dominates over the incident radiation flux. This typically occurs at $P_{\mathrm{pen}} \gtrsim 100 - 10^3$ bar (see chapter

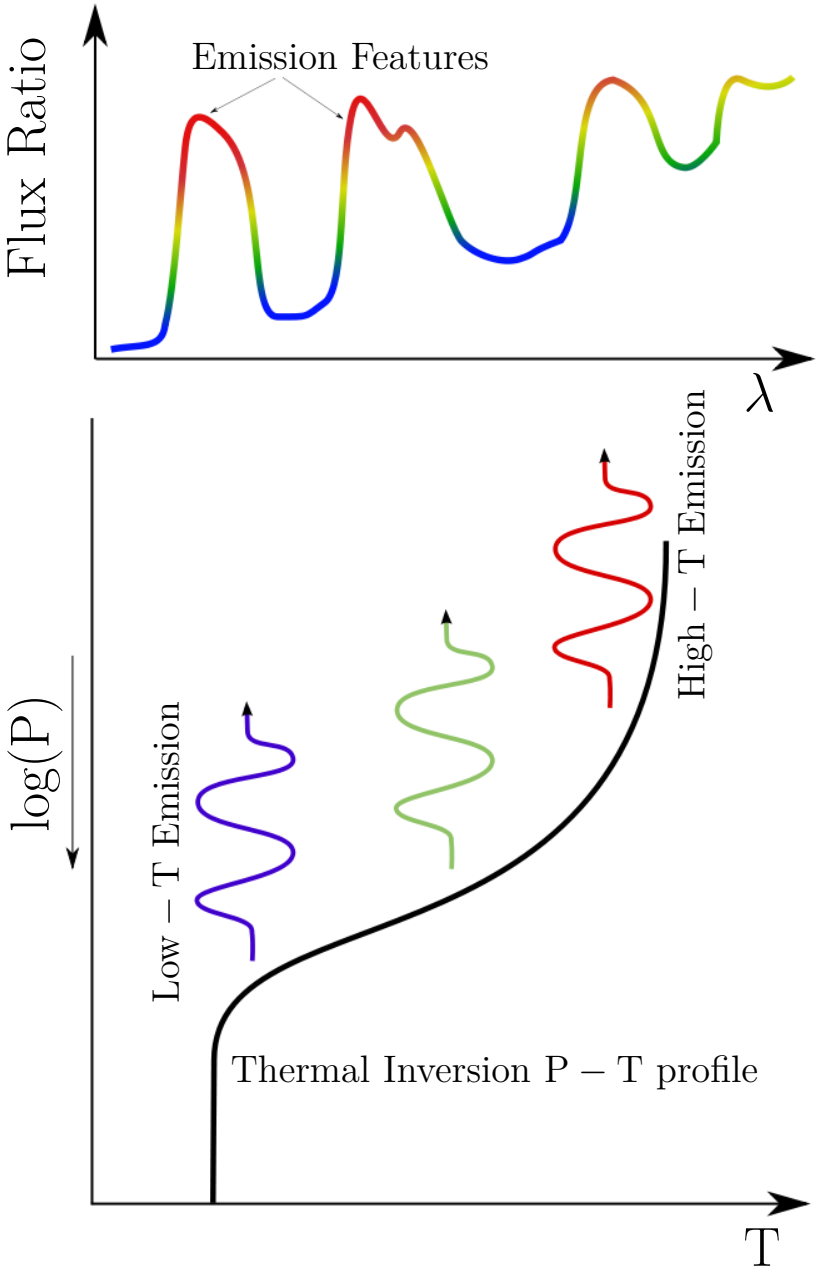

Fig. 4.1 Schematic showing the effect of a thermal inversion on the observed planet/star flux ratio. Lower regions in the atmosphere, where the temperature is cooler, are probed in opacity windows, i.e. wavelengths with low opacity. At wavelengths where molecular absorption is stronger, emission features occur due to the flux being emitted from higher up in the atmosphere where temperature is higher in the case of a thermal inversion (see section 4.2.1).

3). Rearranging gives us a quadratic in γ. Hence the condition on the atmospheric opacity ratio γ is

$$\frac{\gamma^2}{3\mu} - \frac{2}{3}(f-1)\gamma - \mu = 0, \tag{4.5}$$

$$\gamma = \kappa_{\rm vis}/\kappa_{\rm ir} = \mu(f-1) + \mu\sqrt{(f-1)^2+3}. \tag{4.6}$$

Thus for a thermal inversion to take place (i.e $f > 1$), $\gamma > \mu\sqrt{3}$. Under the assumption of isotropic incoming and outgoing radiation, where $\mu \approx 1/\sqrt{3}$ (Hubeny and Mihalas, 2014), this becomes

$$\gamma = \kappa_{\rm vis}/\kappa_{\rm ir} \gtrsim 1. \tag{4.7}$$

Hence the visible opacity must exceed the infrared opacity in order for a thermal inversion to occur in the atmosphere. Higher infrared opacity thus requires a greater visible opacity in order to cause an inversion. The assumptions that have gone into this analytic model should be emphasised here, namely that the incident stellar flux is negligible in the infrared and that the planet's own emission occurs primarily in the infrared. The analytic model also assumes an outgoing and an incident beam of radiation, the two-stream approximation, and that the opacity is not a function of wavelength in the visible and the infrared. However, these results do match well with full radiative-convective equilibrium models with layer-by-layer opacity calculations as discussed in section 4.2.3 below.

4.2.3 Self-Consistent Models

The semi-analytic grey model will now be compared against our self-consistent atmospheric model GENESIS discussed in chapter 3. This model includes full line-by-line frequency dependent radiative transfer with radiative-convective equilibrium. We will test how well the condition for a thermal inversion from the analytic model holds given a more complex atmosphere. The algorithm used to run the equilibrium models uses the Feautrier radiative transfer method with Rybicki's linearisation scheme for temperature correction, the full details of which can be found in chapter 3 and in the work by Hubeny (2017). This model calculates the radiative-convective equilibrium atmospheric profile which we can compare against the analytic model to determine how much the frequency dependant molecular opacity affects the P-T profile. For this work we have assumed the bottom boundary condition to be the diffusion approximation. We investigated pressures of 100, 10^3 and 10^4 bar for the bottom of the atmosphere, but

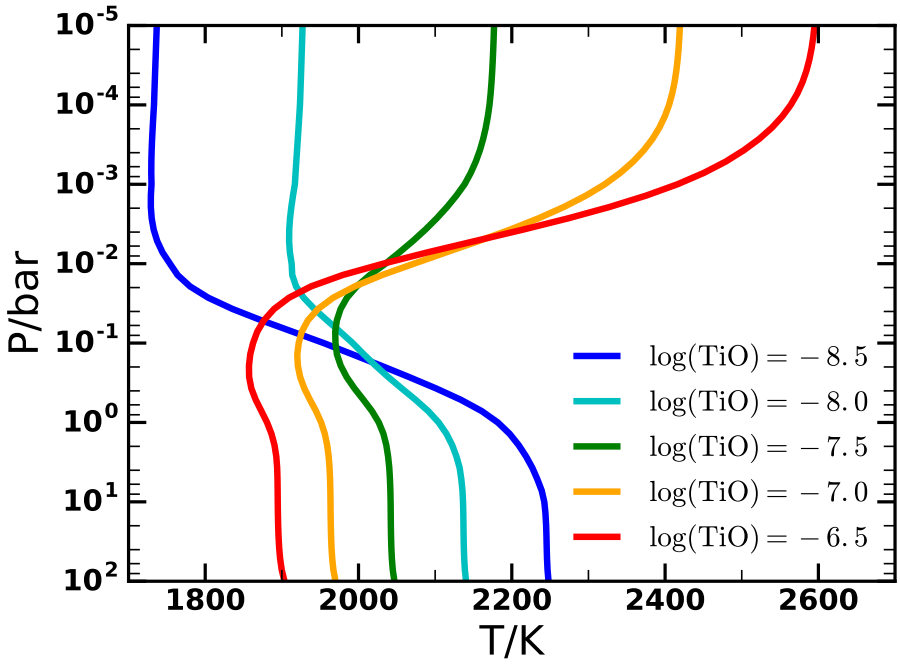

Fig. 4.2 Effect of varying the TiO abundance on the equilibrium P-T profile of a hot Jupiter. The P-T profiles are generated with the GENESIS model of a hot Jupiter with equilibrium temperature of 2000 K and solar equilibrium abundances for the volatile species. In this model we assume TiO is the sole source of the visible opacity.

found no significant differences in the resultant equilibrium P-T profile and emergent spectrum. This is because these pressures are significantly below the photosphere and the internal heat flux from the planet is significantly weaker than ambient flux due to irradiation.

For illustration, we consider a hot Jupiter around a Sun-like star, with an equilibrium temperature of 2000 K and a cloud-free atmosphere. We assume the infrared opacity to be contributed by the seven prominent volatile species, H_2O, CH_4, NH_3, CO, CO_2, HCN and C_2H_2 which are considered to be in chemical equilibrium (see chapter 3.3.5). The visible opacity is assumed to arise from TiO only. The choice of this is two-fold: TiO has been observed in the visible under transmission spectroscopy (Sedaghati *et al.*, 2017) and has been suggested as a candidate for thermal inversion in the atmosphere of hot Jupiters because of its very strong visible cross-section (Fortney *et al.*, 2008; Hubeny *et al.*, 2003). The TiO is assumed to be uniformly mixed throughout the atmosphere and the atmospheric volume mixing fraction is varied to alter the visible opacity as needed.

For the analytic model, we first need to obtain an estimate of the infrared and visible opacity of the atmosphere, $\kappa_{\rm ir}$ and $\kappa_{\rm vis}$. This is done by summing the molecular cross-sections of each of the chemical species, weighted by their mixing fractions, and then integrating over frequency following Hubeny *et al.* (2003). The opacity from a species i is given by

$$\kappa_{\nu,i} = \frac{P}{k_b T}\sigma_i(\nu), \tag{4.8}$$

where $\sigma_i(\nu)$ is the molecular cross section as a function of frequency ν and k_b is the Boltzmann constant. The molecular cross sections are computed over a broad spectral range between 0.4-50μm. A representative temperature and pressure ($T_p = 2000$ K and $P = 0.1$ bar) were chosen to match the conditions of the photosphere. The overall opacity in the infrared is estimated through the Planck mean opacity which for a species i is given by

$$\kappa_{\rm IR,i} = \frac{\int_0^\infty \kappa_{\nu,i} B_\nu(T_p){\rm d}\nu}{\int_0^\infty B_\nu(T_p){\rm d}\nu}. \tag{4.9}$$

Here, the Planck function effectively weights the opacity $\kappa_{\nu,i}$ according to the emergent radiation to determine the overall infrared opacity. To determine the visible opacity for a species j we use the absorption mean opacity for a solar type star ($T_s = 5700$ K),

$$\kappa_{\rm vis,j} = \frac{\int_0^\infty \kappa_{\nu,j} B_\nu(T_s){\rm d}\nu}{\int_0^\infty B_\nu(T_s){\rm d}\nu}. \tag{4.10}$$

The absorption mean weights the opacity with the stellar Planck function to determine the effective absorption from species with strong visible cross-sections which absorb the incident star light which peaks in the visible. A further discussion of the absorption mean and Planck mean opacities can be found in Hubeny *et al.* (2003). By equating $\kappa_{\rm ir}$ to $\kappa_{\rm vis}$, we find the minimum required mixing fraction of TiO for which an inversion occurs as

$$X_{\rm TiO} = \frac{\sum_i \kappa_{{\rm IR},i} X_i}{\kappa_{\rm vis,TiO}}. \tag{4.11}$$

We calculate the mixing fractions X_i for each of the 7 volatile species at 2000 K and 0.1 bar pressure in chemical equilibrium assuming solar abundances. The $\kappa_{\rm vis,TiO}$ term denotes the absorption mean opacity of TiO weighted with a black body at $T_s = 5700$ K. We then find $\log(\rm X_{TiO}) \approx -7.0$ for our model atmosphere. For a general

species j with strong absorption in the visible, the abundance required for a certain P-T profile with a fixed $\gamma \equiv \kappa_{\rm vis}/\kappa_{\rm ir}$ is given by

$$X_{\rm vis,j} = \gamma \frac{\sum_i \kappa_{{\rm IR},i} X_i}{\kappa_{\rm vis,j}}. \tag{4.12}$$

Figure 4.2 shows the effect on the P-T profile of varying TiO throughout the atmosphere in the self-consistent equilibrium model. The abundance is increased from $\log(\mathrm{X_{TiO}}) = -8.5$ to -6.5, keeping the chemical composition of the volatile species fixed at solar composition. The figure shows the P-T profile inverting as expected for a TiO abundance remarkably close to $\log(\mathrm{X_{TiO}}) = -7.0$. This confirms that the analytic model gives a good estimate of the opacity required for an inversion. We have also tested this against the required abundance for a thermal inversion from the semi-analytic model for a number of species and have also found good agreement with GENESIS. Hence, we use the analytic model to provide a good guide to estimate the required abundance of species in order for thermal inversions to occur (see table 4.2).

Figure 4.2 shows that the temperature at pressures $\lesssim 0.1$ bar increases as the abundance of TiO increases from $\log(\mathrm{X_{TiO}}) = -8.5$ to -6.5. This is due to increased absorption of the incident radiation in the upper atmosphere. Consequently, a smaller fraction of the stellar flux penetrates down into the deeper layers of the atmosphere, hence why the atmosphere at P$\gtrsim 1$ bar is cooler as the TiO abundance is increased. Eventually at a TiO abundance of -6.5, the P-T profile is dominated by the strong visible opacity, and ≈ 700 K inversion is seen between the top and bottom of the atmosphere. Throughout all of the variation of TiO abundance however, the region of the atmosphere near P~ 0.1 bar remains at a similar temperature. This is the photosphere where much of the emission occurs. Therefore, the temperature gradient in the photosphere is strongly affected by the abundance of the TiO, even though the temperature here may not vary too significantly at 0.1 bar.

The solar abundance of Ti is $\log(\mathrm{Ti_{solar}}) \approx -7.1$, similar to that required for TiO to result in a thermal inversion. If we assume that most of the Ti will be in the form of its oxide, then the atmospheric abundance is sufficient at solar abundance to result in an inversion. However, we observe a spread in hot Jupiters with thermal inversions, which may be due to the differences in the chemical compositions of these planets. Other factors such as cold-trap process (Beatty *et al.*, 2017a) may also prevent thermal inversions occurring. Rain-out of TiO at temperatures below ~ 2000 K is also another important consideration (Spiegel *et al.*, 2009). TiO will only be in its gaseous form on the very hottest of exoplanets, and may be a contributing factor as to why some of the

Table 4.2 Table showing the solar atomic log mixing ratio and the required molecular log mixing ratios of each metallic species in order to form a thermal inversion for various C/O ratios. The solar atomic abundances were obtained from Asplund *et al.* (2009). The required volume mixing ratios were determined from eqn. 4.12 and thermochemical equilibrium of the volatile infrared species at 2000K and 0.1 bar. In each model the species with strong visible opacity was included by itself with no other visible absorbers present.

		Required log(Vol. Mixing Ratio)		
Species	Solar	C/O = 0.5	C/O = 1	C/O = 1.5
TiO	-7.1	-7.0	-9.2	-7.5
VO	-8.0	-6.5	-8.7	-7.1
AlO	-5.6	-5.9	-8.2	-6.5
CaO	-5.7	-6.5	-8.8	-7.1
NaH	-5.8	-6.2	-8.5	-6.9
MgH	-4.5	-6.6	-8.9	-7.2

cooler hot Jupiters such as WASP-43b (Kreidberg *et al.*, 2014) and HD209458b (Line *et al.*, 2016) show non-inverted atmospheric temperature profiles.

4.3 Effect of Visible Opacity on Inversions

We will now investigate species other than the commonly hypothesised TiO which may lead to stratospheres. Fig. 2.1 shows the molecular cross sections at 2000 K and 0.1 bar for a number of metallic species. These cross sections were computed using the line lists obtained from EXOMOL (Tennyson *et al.*, 2016) with the pressure broadening coefficients derived using the method in Sharp and Burrows (2007). Fig. 2.1 shows the species which have strong visible cross sections and are therefore able to affect the equilibrium P-T profile of the atmosphere even at trace mixing ratios. As we have already seen in the previous sections, TiO at solar abundance is sufficient for a thermal inversion, even lower than this amount is sufficient in some cases (see section 4.4). Therefore these species with strong visible opacity are important in determining the P-T profile and hence the emergent emission spectrum from the dayside atmosphere.

VO is another candidate often considered for a thermal inversion (Fortney *et al.*, 2008; Spiegel *et al.*, 2009). Like TiO, VO is predicted to only be gaseous in hot Jupiter atmospheres at temperatures exceeding ∼1800 K. Table 4.2 shows the required abundances for VO to result in a thermal inversion and the solar abundance of V (Asplund *et al.*, 2009). Only slightly super-solar abundance of VO is sufficient to satisfy

equation 4.7 and thus result in stratosphere. However, any species shown in the table with strong visible absorption is capable of causing thermal inversions on hot Jupiters if their abundance is significant enough.

4.3.1 Other Sources of Visible Opacity

By carefully studying molecular cross sections, we are able to explore several new species that can cause thermal inversions. As well as the well explored TiO and VO, AlO, CaO, NaH and MgH all possess strong molecular spectral features in the visible region of the spectrum as shown in fig. 2.1. These cross sections have been derived from the latest line lists of each of these species (Patrascu *et al.*, 2015; Rivlin *et al.*, 2015; Yadin *et al.*, 2012; Yurchenko *et al.*, 2016). They all have distinct cross sections, but over the visible spectrum they provide similar strong opacity. We now model the effect of each of these new species on the model atmosphere. As previously we will assume a planet with an equilibrium temperature of 2000 K and equilibrium abundances of volatile species such as H_2O, CH_4, NH_3, CO, HCN, CO_2 and C_2H_2. We determine the abundances required for each of the species in table 4.2 to lead to an inversion for a range of model atmospheres.

4.3.2 Effects on Equilibrium Profile

We determined the required abundance for each of the prominent species capable of causing thermal inversions. This was done by first calculating the absorption mean opacities for the known metallic species with strong visible cross-sections to determine $\kappa_{\rm vis}$. We calculated the infrared opacity assuming equilibrium chemistry for the 7 volatile species. We then equated the infrared and visible opacity to determine the required mixing fraction for an inversion, analogously with TiO in eqn. 4.11. Table 4.2 shows the required abundances of each species to satisfy $\gamma = 1$ from the semi-analytic model as well as their solar atomic abundances. If we assume that all of the atomic species are present in the form of their relevant molecule (i.e., that the atom is bound only to the relevant molecule), all four of the new species, AlO, CaO, NaH and MgH are at or near the abundance required for an inversion at solar abundance. This is because despite the overall lower mean molecular cross sections compared to TiO and VO, all of their respective atomic abundances are higher than Ti or V.

Fig. 4.3 shows the effect of the metallic species on the equilibrium P-T profile of the atmosphere. The models were run with our GENESIS self-consistent radiative-convective equilibrium model, assuming equilibrium chemical compositions for the

volatile species at a C/O ratio of 0.5 (solar value). As seen in the previous section, TiO results in an inversion at 0.1 bar of ∼500 K between the top and bottom of the atmosphere at solar composition (left panel fig. 4.3). At solar abundance, VO is not present in sufficient quantities to lead to a thermal inversion, as per the prediction from the analytic models (see table 4.2).

Of the new species at solar composition, AlO is at just the abundance required for an inversion and thus we can see the onset of the temperature inversion at pressures lower than 10 mbar on the left panel in figure 4.3. CaO shows a similar trend to TiO, with a similar P-T profile for the atmosphere and an inversion of ∼400 K. The similar P-T profiles for these two species is likely due to the similar molecular cross sections, which show broad coverage over all of the visible spectrum (see fig. 2.1). NaH only shows very weak signs of a thermal inversion at 1 bar, and the temperature profile is monotonically decreasing with height. The molecular abundance at solar composition is not quite sufficient to produce a significant inversion as it is very near the critical abundance required. MgH on the other hand does show a strong molecular cross section only up to 0.8μm in fig. 2.1 and therefore displays a significantly different P-T profile to TiO, VO or CaO. MgH thus allow some of the stellar flux to penetrate down to the deeper layers due to its lack of strong opacity over all of the peak stellar flux range.

The right panel of fig. 4.3 shows the effect of altering the mixing fraction of each of the metallic species through equation 4.12. The abundance of each of the species was adjusted accordingly to maintain $\gamma \equiv \kappa_{\rm vis}/\kappa_{\rm ir} = 10$ and therefore result in a thermal inversion of similar extent for all of the species. We now see similar equilibrium P-T profiles from all of the species, however, the non-grey nature of the opacity results in some differences. AlO and MgH show the inversion occurring higher in the atmosphere (P $\sim 10^{-2}$ bar) and the deepest layers being hotter than with the other species. This can be traced to the molecular cross sections of these species in fig. 2.1. Both MgH and AlO display strong cross sections in the wavelength region near 0.5μm which drop away significantly nearer to the infrared. AlO displays a lower cross section near 0.6μm and the cross section of MgH becomes almost completely negligible above 0.8μm. This means that unlike the other metallic species, there are opacity windows in which the stellar irradiation is able to penetrate down to the higher pressures. This in turn causes the deeper layers of the atmosphere to heat up, hence why the temperature of the deep atmosphere is the highest with these two species. This also shifts the thermal inversion to higher in the atmosphere. The other metallic species (TiO, VO, CaO and NaH) display strong cross sections throughout the visible region (<1μm) due to which the deepest layers of these model atmosphere are left relatively cool.

Some equilibrium P-T profiles in fig. 4.3 also show small non-inverted profiles near ~ 1 bar before the inversion at P$\lesssim 0.1$ bar in the atmosphere, particularly for species such as AlO. This dip in the P-T profile is contributed by the variation in the value of $\gamma \equiv \kappa_{\rm vis}/\kappa_{\rm ir}$ as a function of pressure. We found that the overall value of γ decreases for pressures greater than 1 bar. This is primarily dominated by the broadening of the molecular features, which result in a change in the overall opacity. The broadening of the lighter volatile species with pressure is greater than those of the much more massive metallic species such as TiO and VO. Thus at P~ 1 bar the $\kappa_{\rm ir}$ is often dominant over the visible opacity. At lower pressures, however, the metallic species dominates the opacity, and thus $\gamma > 1$ at higher altitudes, resulting in an inversion at pressures below 0.1 bar. In addition, species such as MgH and AlO have significant opacity windows (see fig. 2.1) where radiation flux can penetrate deeper in the atmosphere (as discussed above) to heat these layers just below the photosphere.

All of these species are capable of causing thermal inversions in hot Jupiters. At solar elemental abundance most of the species are at or near the abundances required to form inversions. It is quite likely that multiple such species may contribute to the visible opacity and thus require lower abundances of each for an inversion. How much we expect of such species in the atmospheres of hot Jupiters is an unknown, given that as well as the chemical equilibrium, disequilibrium effects may act to enhance/diminish the abundance. Another assumption here is that all of the nuclei of the relevant metal are bonded to the given molecule, which may not be the case depending on the temperature and pressure dependant chemical equilibrium of the atmosphere. For instance, the Mg may partially form Magnesium silicate clouds in the atmosphere instead of MgH, thus reducing the overall atmospheric abundance. Mixing from the night side and/or upwelling from deeper in the atmosphere may also alter the abundance. However, what we have been able to demonstrate here is that as well as TiO and VO, other species are also capable of forming thermal inversions on the very hottest extrasolar giant planets. We have also demonstrated the effect of the individual species on the equilibrium P-T profile, and how there is variation with the molecular cross section of each species compared to the simple analytic model seen in section 4.2.2. Our whole focus so far has been on the visible opacity, $\kappa_{\rm vis}$, but in section 4.4 we will explore how the infrared opacity from the 7 volatile species can also alter the P-T profile.

4.3.3 Inversions on Very Hot Planets

The temperature on hot Jupiters for these newer species to exist in the gaseous phase is however very high, $\sim$2500 K (Burrows, 2009; Sharp and Burrows, 2007), and only the

most strongly irradiated exoplanets are going to have conditions sufficient for them to remain in their gaseous form. Temperatures such as this have been observed for several systems, e.g WASP-33b and WASP-18b. We do observe thermal inversions in both of these systems (Haynes *et al.*, 2015; Sheppard *et al.*, 2017). Recent observations of thermal emission from other very hot Jupiters equilibrium temperatures greater than 2000 K) has revealed some surprising insights into the atmospheric temperature profile. Many of these extremely hot planets studied with WFC3 data show very few spectral features. This indicates that the temperature may be close to isothermal in these atmospheres. If this is the case it would mean that the infrared opacity does equal the visible opacity. This would be an important observation for hot Jupiter atmospheres as it shows the visible opacity is significant for these exoplanets. Photodissociation of H_2O has also been proposed at these high temperatures (Parmentier *et al.*, 2018). This would reduce the strength of spectral features in the infrared due to the loss of H_2O. In addition, the formation of H- in the atmosphere may result in strong visible opacity due to its cross section. This would act to increase the strength and possibility of an inversion as it would increase the overall visible to infrared opacity ratio (Lothringer *et al.*, 2018; Parmentier *et al.*, 2018). Lothringer *et al.* (2018) has proposed various candidate species (e.g. Fe, Mg and SiO) which may provide sufficient visible opacity in order to form thermal inversions in atmospheres of planets such as KELT-9b, with an equilibrium temperature exceeding 4000 K.

4.3.4 Inversions on Cooler Planets

Cooler hot Jupiters with equilibrium temperatures between 1000-2000 K are less likely to have a thermal inversion from the metallic species considered above. None of the species considered here remain gaseous at these comparatively low temperatures and therefore $\kappa_{\rm vis}$ remains lower than $\kappa_{\rm ir}$, preventing an inversion from occurring. However, other species have been proposed which exist in the gaseous phase at temperatures below 2000 K and which may have strong visible cross sections. Zahnle *et al.* (2009) showed that at these intermediate temperatures absorption from species such as HS or S_2 is sufficient to produce thermal inversions thanks to their strong UV absorption. These species may however photo-dissociate under strong irradiation (Knutson *et al.*, 2010). Further exploration of the disequilibrium chemistry may suggest the feasibility of thermal inversions by these sulphur bearing species. Other proposed species capable of thermal inversions at these intermediate temperatures include atomic Na and K (Mollière *et al.*, 2015).

4.4 Effect of Infrared Opacity

Variation of the infrared opacity, $\kappa_{\rm ir}$, can also alter γ such that we can satisfy the inequality in equation 4.7. This is an area that has not been explored in great detail, but the infrared opacity is just as significant in determining the conditions for thermal inversions as the visible. If $\kappa_{\rm ir}$ is reduced whilst holding $\kappa_{\rm vis}$ fixed, the visible opacity will eventually exceed the infrared opacity. This will lead to thermal inversions in the photosphere without the need for high abundances for species with strong visible cross sections. We will vary the infrared opacity in the atmosphere through the atmospheric C/O ratio. The motivation for this was two-fold. Firstly, we may explore the variation in the infrared opacity using a single parameter and whilst maintaining chemical equilibrium for the volatile molecular species (see fig. 4.4). This allows us to explore the more complex parameter space of these species and their chemical reactions without having to use unphysical atmospheric parameters. Secondly, the variation of the C/O ratio results in a very large variation in the overall infrared opacity of the atmosphere, especially due to the low H_2O abundance at C/O>1. Up to 3 orders of magnitude difference can be achieved by varying the C/O ratio by only a factor of $\sim$2 due to the very sharp change in equilibrium chemistry near C/O$\sim$1 (see fig. 4.4). Therefore we are able to significantly alter γ and thereby lead to inversions with only relatively small changes in the atomic abundances.

4.4.1 Chemical Equilibrium of Volatile Species

The equilibrium chemical abundance of the volatile species can vary by many orders of magnitude as the C/O ratio is altered. Fig. 4.4 shows the equilibrium abundance of H_2O, CH_4, NH_3, CO, CO_2, HCN and C_2H_2 as a function of the C/O ratio at a temperature of 2000 K and 0.1 bar pressure following Madhusudhan (2012). Low C/O ratios such as solar values ($\sim$0.54) are dominated by water vapour and CO. The remaining species are only present in very small quantities, with the exception being N_2, not shown in fig. 4.4 as it has no significant spectroscopic signature. Increasing the C/O ratio towards 1 increases the CO abundance linearly until C/O>1, where it levels off given that its abundance is now limited by the available oxygen. As there is now a dearth of O, oxygen bearing species such as H_2O and CO_2 are greatly depleted in the atmosphere. On the other hand, carbon rich species such as CH_4 and C_2H_2 are now enhanced in the atmosphere, as well as HCN. This change in the abundance by several orders of magnitude results in a significant change to the opacity.

The infrared opacity is most strongly influenced by H_2O. The cross section for H_2O is stronger than the other species and therefore the atmospheric H_2O abundance effects the $\kappa_{\rm ir}$ the most strongly. Therefore, as the C/O ratio is increased towards 1, the H_2O and thus the total infrared opacity decreases as shown in fig. 4.4. This has previously been explored in the work by Mollière *et al.* (2015). At a C/O ratio of 1, the most abundant species is CO. This therefore greatly reduces the $\kappa_{\rm vis}$ required for a thermal inversion in the atmosphere, i.e to satisfy equation 4.7. With C/O>1, the volume mixing ratio of the carbon rich species now increases and therefore $\kappa_{\rm ir}$ increases accordingly. We explore the required abundances of the metallic species with a strong visible opacity to cause thermal inversions in the atmosphere as a function of the C/O ratio.

4.4.2 Thermal Inversions with Super-Solar C/O Ratio

As the C/O ratio is increased towards 1, the required visible opacity in order to produce a thermal inversion decreases. As a result, the required abundance for the species with strong visible cross sections for thermally inverted photospheres is reduced as shown in fig. 4.5. The lower infrared opacity means a lower visible opacity is needed to satisfy equation 4.7. As expected, TiO possesses the strongest opacity and therefore the required abundance for an inversion is the least compared to the other species we consider in our study. The 4 new species, AlO, CaO, NaH and MgH all require ∼1.5-2 orders of magnitude higher abundance than the TiO due to their weaker opacity.

What is uncertain however is the abundances of the metallic species as the C/O ratio increases. As oxygen is most likely in the CO, it is unclear whether the oxygen bearing species such as TiO, VO, AlO and CaO would be present in sufficient quantities. Equilibrium calculations have shown that with a C/O ratio of 1, the abundances of TiO and VO reduce by a factor of ∼100-1000 (Madhusudhan *et al.*, 2011b). However, these species would not need to be at solar abundances to lead to inversions when the C/O ratio is 1. Fig. 4.5 and table 4.2 show the required molecular mixing fraction of each species in order to invert the P-T profile as a function of the C/O ratio. To match the infrared opacity, these species can be sub-solar and still lead to a thermal inversion. Even though the TiO and VO are depleted they may still be capable of leading to thermal inversion on carbon rich planets. In this work, however, we do not explore the variation of these species with C/O ratio, only the required abundances for inversions with C/O ratio. With a C/O ratio of 1 even atomic species such as Na/K are capable of producing thermal inversions in the photosphere of hot Jupiters around some stars. A discussion of the Na/K opacity and its effect at C/O= 1 can be found

in Mollière *et al.* (2015). The required mixing fraction of all of the metallic species has dropped by a similar quantity thanks to the lower infrared opacity.

Fig. 4.6 shows the effect of solar abundances and $\kappa_{\rm vis}/\kappa_{\rm ir} = 10$ on the P-T profile when the C/O ratio equals 1. The volatile molecular species are taken to be in chemical equilibrium in each layer of the atmosphere. Now, in contrast to fig. 4.3, all of the metallic species are abundant enough at solar composition to lead to strong thermal inversions in the photosphere (left side if fig. 4.6). This can be seen from both fig. 4.5 and table 4.2. The visible opacity in the left panel is the same as fig. 4.3, but the infrared opacity has now decreased for a C/O ratio of unity. The overall $\kappa_{\rm ir}$ has dropped as the H_2O, which is the dominant source of opacity in the infrared, is now at a lower mixing fraction. With such little infrared opacity, solar composition of species such as TiO can lead to an inversion with ΔT of over 1000 K. Therefore, should it be the case that high C/O atmospheres still have some visible opacity sources, we may expect that thermal inversions are more likely at C/O$\sim$1. The condition $\kappa_{\rm vis}/\kappa_{\rm ir} = 10$ requires ~ 2 dex lower mixing fraction for all of the metallic species than solar, such is the weakness of $\kappa_{\rm ir}$ when C/O=1. The profiles agree well with each other here, with the temperature in the deeper atmosphere (> 0.1bar) very similar for all of the metallic species. Once again though the AlO leads to an inversion at a higher point in the atmosphere than the other species, most likely caused by its lower visible cross section.

As the C/O ratio is increased to 1.5 the infrared opacity remains relatively low. Table 4.2 and figure 4.5 show that the required abundance for a thermal inversion has increased but is still well below that for a solar C/O ratio. The dominant source of the infrared opacity is now species such as CH_4 and C_2H_2 which can be highly abundant in such carbon-rich atmospheres (Madhusudhan, 2012), as shown in fig. 4.4. All of the species at solar abundance are still capable of leading to thermal inversions in the left hand panel of fig. 4.7. All of the species are within 1 dex of the mixing fraction required to satisfy $\kappa_{\rm vis}/\kappa_{\rm ir} = 10$, therefore both sides of fig. 4.7 shows similar P-T profiles. It is interesting to note that despite varying the C/O ratios which leads to $\kappa_{\rm ir}$ varying by many orders of magnitude, thermal inversions always form in the photosphere near P= 0.1 bar. It should also be noted that when the C/O ratio exceeds 1, other larger hydrocarbon molecules not included here may also form in the atmosphere with significant opacity both in the infrared and possibly the visible and thus affect the inversions. With these detailed atmospheric models we will now model a planet with a known thermal inversion, WASP-121b (Evans *et al.*, 2017).

4.5 Case Study: Hot Jupiter WASP-121b

WASP-121b is a hot Jupiter with a radius of $\sim$1.7R_J orbiting an F6 star with an equilibrium temperature of $\sim$2300 K. Emission spectroscopy of this planet has shown the presence of a thermal inversion from HST WFC3 observations (Evans *et al.*, 2017). Transmission and emission spectra have also shown evidence for TiO/VO in the atmosphere of this planet (Evans *et al.*, 2016; Evans *et al.*, 2017). This makes the exoplanet a good candidate to study thermal inversions and investigate the species responsible. We model WASP-121b for a C/O ratio of 0.5 and 1 with all of the 6 species we have considered thus far that are capable of leading to a thermal inversion. The abundances are set such that the thermal emission spectra most closely resemble the observations.

Fig. 4.8 shows the equilibrium P-T profiles for a range of metallic species for each C/O ratio for WASP-121b. The presence of the inversion affects the corresponding spectra in fig. 4.9 as evident in the emission features. These are clearly visible with all of the species considered, as discussed in section 4.2.1. The required abundances to match the observed spectrum are within $\lesssim$1 dex of solar for all of the species for the C/O=0.5 case (see left panel of fig. 4.8 and fig. 4.9). A C/O ratio of 0.5 also requires a higher abundance of metallic species thanks to the greater infrared opacity due to the H_2O content of the atmosphere. As was the case previously, a C/O ratio of 1 reduces the abundances needed for each of the metallic species and therefore sub-solar abundances are sufficient to produce the observed thermal inversion. The required mixing fraction in order to cause an inversion has dropped by $\sim$1.5 dex below that required for a solar C/O ratio. With the C/O ratio of 1, the lack of water vapour or any other strongly IR active species means a lower $\kappa_{\rm ir}$ and therefore a lower $\kappa_{\rm vis}$ is required for a thermal inversion.

The features of H_2O are more prominent on the left panel of fig. 4.9 and thus provide a stronger spectral feature in the HST WFC3 range compared to the right panel with C/O=1. The spectra follow the observations closer with a C/O ratio of 0.5 than the C/O=1 case, as the H_2O emission features are clearly seen in the WFC3 observations. Nevertheless, regardless of the C/O ratio of the atmosphere, we are still able to produce an inversion over both the C/O ratios considered here that matches the observed emission spectrum.

We are able to model the thermal inversion on WASP-121b with 4 new species, AlO, CaO, NaH and MgH along with the well studied TiO and VO. From the GENESIS model we have been able to reproduce the observed emission spectrum for all of the species in radiative-convective equilibrium (fig. 4.9). As we have no observations beyond

the near infrared, we are unable to further constrain the refractory species responsible for this inversion. Transmission spectroscopy in the optical can further investigate which metallic species are likely to be present in the atmosphere given that they all have strong and unique spectral features below 1μm.

4.6 Discussion and Conclusion

The goal of our work is to characterise the nature of thermal inversions in hot Jupiters and the molecular species which allow thermal inversions to occur. We explored semi-analytic and line-by-line radiative equilibrium models with a number of species thus far not explored and determined 4 new species which are capable of leading to thermal inversions in hot Jupiter atmospheres. We also explored the effect of varying the infrared opacity through the C/O ratio and found that a C/O ratio of 1 results in inversions with the lowest required abundance of metallic species. With this exploration of the parameter space for thermal inversions we compared our findings with WASP-121b, a planet known to have a thermal inversion and which shows evidence for TiO and/or VO (Evans *et al.*, 2016; Evans *et al.*, 2017).

As well as the well established TiO and VO (Fortney *et al.*, 2008; Spiegel *et al.*, 2009), we found that AlO, CaO, NaH and MgH may also be present in significant enough quantities in order to cause thermal inversions in extrasolar giant planets. Each of these species is capable of causing thermal inversions at or near their solar atomic abundance. We explored the effects of varying their abundance from solar composition (Asplund *et al.*, 2009) to $\kappa_{\rm vis}/\kappa_{\rm ir} = 10$ for a number of different C/O ratios. For each of the metallic species we also obtain the required mixing fraction in order to produce a thermal inversion on a hot Jupiter with an equilibrium temperature of 2000 K. These new molecules open up a new avenue to explain thermal inversions in hot Jupiter atmospheres.

Whilst many of these species are capable of causing thermal inversions, there are some caveats and simplifications in our models which we should emphasise. Given their refractory nature, these new species AlO, CaO, NaH and MgH require very high temperatures (>2000 K) to be present in the gas phase (Sharp and Burrows, 2007; Woitke *et al.*, 2018). Therefore, very strongly irradiated atmospheres are required for these species to be present in significant quantities to cause thermal inversions. Such temperatures have been seen for a handful of exoplanets (Beatty *et al.*, 2017a; Cartier *et al.*, 2017; Evans *et al.*, 2017; Haynes *et al.*, 2015; Sheppard *et al.*, 2017), but many hot Jupiters may be too cool for these species (Crouzet *et al.*, 2014; Kreidberg *et al.*, 2014;

Line *et al.*, 2016). This is also consistent with the fact that thermal inversions have been inferred in only the hottest of hot Jupiters (Evans *et al.*, 2017; Haynes *et al.*, 2015; Sheppard *et al.*, 2017). Photodissociation of species such as H_2O (Parmentier *et al.*, 2018) has not been included here, and this may play an important role in determining the overall $\kappa_{\rm ir}$ on such high temperature planets. Another important consideration is that we have not explored how equilibrium chemistry affects these metallic species. We assume that the atomic abundance of each of these metallic species is equal to the molecular abundance (i.e. that all of the atoms are bound to the relevant species) but this can be significantly lower for some molecules. Species such as Na have already been observed in hot Jupiters, and thus NaH may not be present at or near its solar atomic abundance in the atmosphere. However, observations of these systems may be able to constrain some of the species to determine how well each is able to cause an inversion.

Optical transmission spectra of such hot Jupiters may provide key insights into the possible metallic species which result in thermal inversions and their atmospheric abundances. Each of these metallic species has a strong opacity at visible wavelengths, with a unique molecular cross section, as shown in fig. 2.1. As such these species are observable with optical transmission spectra. We now have high precision and resolution transmission spectra for a number of planets (Chen *et al.*, 2018; Nikolov *et al.*, 2014; Wyttenbach *et al.*, 2015), with some even showing evidence for TiO (Sedaghati *et al.*, 2017). With future instruments such as JWST we will be able to obtain even higher precision data down to a wavelength of 0.6μm, where all of these species possess a strong cross section.

We have also explored variation in the infrared opacity, $\kappa_{\rm ir}$, through the C/O ratio. This has been largely ignored until now, but the influence of the infrared active species on thermal inversions is a key step towards understanding the physical processes and emergent spectra. The change in the C/O ratio can result in significant changes in the atmospheric abundance of the volatile species (e.g. Madhusudhan, 2012; Moses *et al.*, 2013) and thus $\kappa_{\rm ir}$. We found that the required mixing fraction for a thermal inversion for all of the relevant metallic species decreased as we increased the C/O ratio. The lowest infrared opacity and thus the lowest required mixing fraction of a metal species for a thermal inversion was when the C/O ratio was close to unity. At these C/O ratios, the infrared opacity is dominated at such high temperatures by CO, which has only a small molecular cross section. The H_2O abundance is low when C/O=1 ($\log(H_2O) < 10^{-5}$), and thus there is no significant opacity from water vapour, which possesses the dominant molecular cross section of all of the infrared volatile

species. This means that in order to satisfy $\kappa_{\rm vis} > \kappa_{\rm ir}$ we require a lower visible opacity compared to the C/O = 0.5 case.

The C/O ratio is likely to strongly affect the abundance of the metallic species, and we should expect the atmosphere to be greatly depleted particularly of oxygen rich species such as TiO, VO, AlO and CaO. For instance, TiO and VO have their abundance reduced by between 2-3 orders of magnitude when the C/O ratio is 1 compared to their solar abundance (Madhusudhan *et al.*, 2011b). However, the H_2O abundance and thus the overall infrared opacity falls by a similar amount. Therefore the required molecular abundance for an inversion-causing metallic species also drops by over 2 orders of magnitude from its solar abundance. It is therefore unclear whether atmospheres of C/O ratio near unity are capable of thermal inversions as both of these species are depleted by a similar amount. Here we only explore the required abundance for each of the species. It may also be the case that multiple of these species act together to increase the overall visible opacity and lead to an inversion. The weaker infrared opacity even means that now weaker visible absorbers such as Na and K can also affect the inversion (Mollière *et al.*, 2015).

We modelled the thermal inversions on WASP-121b (Evans *et al.*, 2017), a hot Jupiter observed to have a thermal inversion in the retrieved emission spectrum. We modelled all of the metallic species that are capable of leading to thermal inversions and found the abundances that are required to produce a thermal inversion for both C/O=0.5 and C/O=1. We found that we are able to match the observed emission spectrum with every species over both C/O ratios, as shown in figs. 4.8 and 4.9.

Inversions on planetary systems throughout the solar system are common despite the compositional range of the planets that are present, and strongly irradiated hot Jupiters are ideal laboratories to study such inversions. They have strong spectral signatures, and even with current facilities we can obtain high resolution and high precision spectra from their dayside. Studying how and why these planets possess thermal inversions can not only tell us about the landscape of the hot Jupiter systems and their chemistry, but also provide key insights into the formation mechanisms of such planets. This is particularly so given the strong effect the C/O ratio has on the overall infrared opacity and thus the likelihood for an inversion. With current and future instrumentation such as the VLT and JWST we can probe in even more detail the chemical structure and temperature profile of such atmospheres and learn more about the processes that occur on such systems.

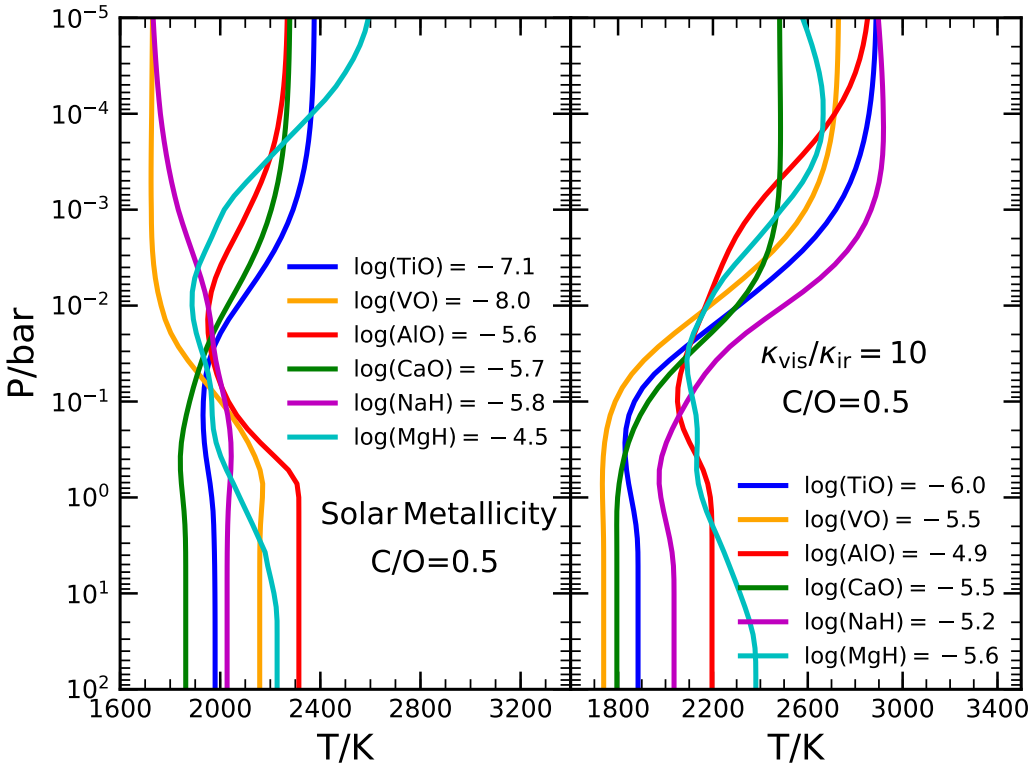

Fig. 4.3 Radiative equilibrium P-T profiles of model atmospheres with varying abundances of metallic species. The model assumes a hot Jupiter with an equilibrium temperature of 2000 K and a solar C/O ratio of 0.5. The left panel shows the effect of solar mixing fractions for the inversion-causing refractory species. In the right panel, the abundances of the inversion-causing species are such that the ratio of visible to infrared opacity was 10. The volatile species were assumed to be in chemical equilibrium with solar abundances, and in each model the species was included in the atmosphere by itself with no other visible absorbers.

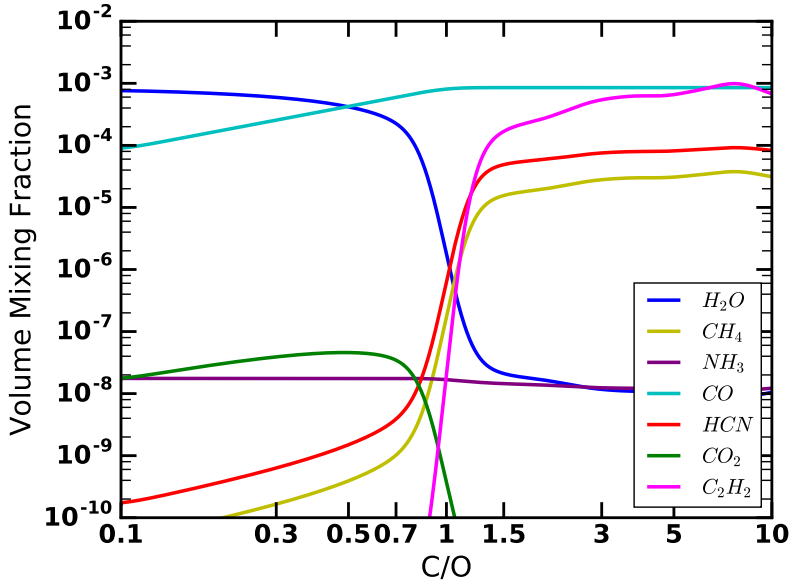

Fig. 4.4 Equilibrium mixing ratios for the 7 volatile species which have significant absorption in the infrared as a function of the C/O ratio. This was calculated at a temperature of 2000 K and 0.1 bar pressure.

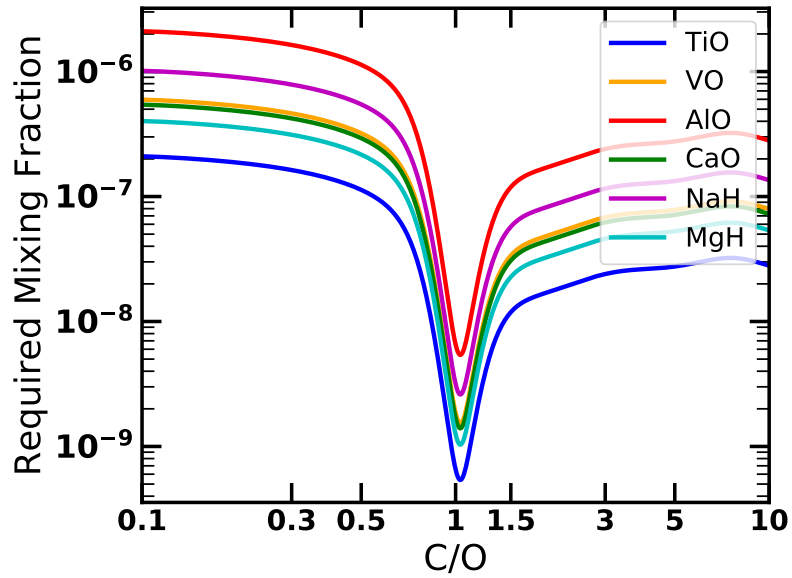

Fig. 4.5 Required molecular abundance for a thermal inversion for each of the metallic species as a function of the C/O ratio. These were calculated assuming the analytic model such that the visible opacity equals the infrared opacity. The model atmosphere was assumed to have an equilibrium temperature of 2000 K.

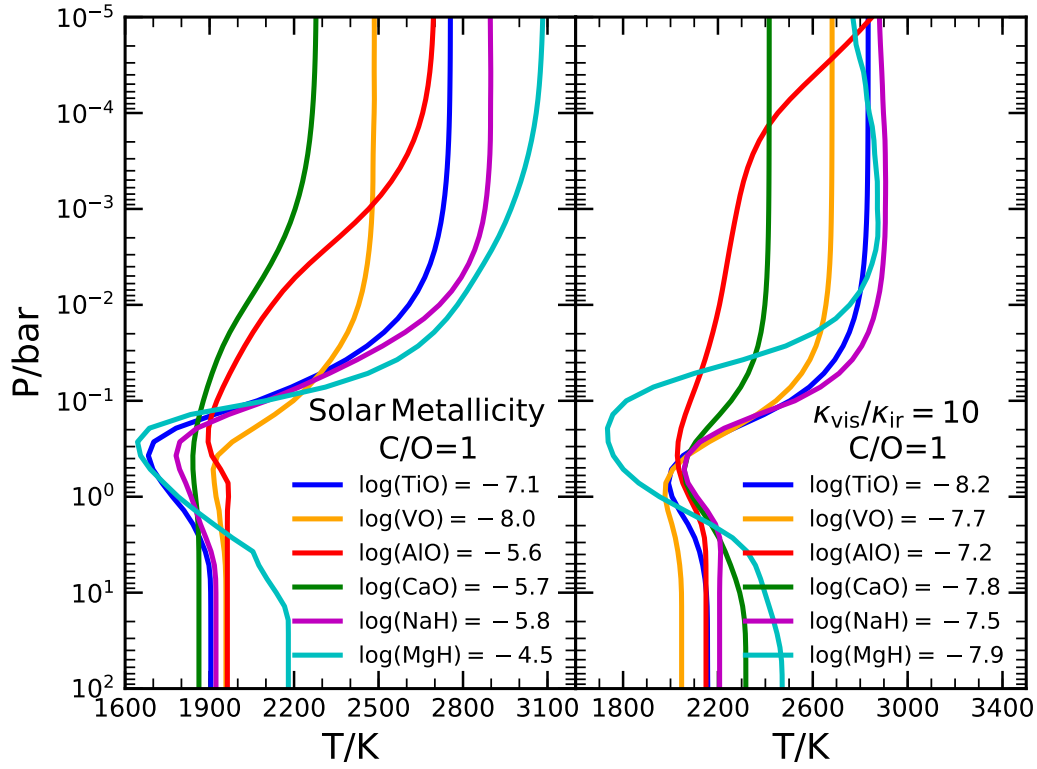

Fig. 4.6 Radiative equilibrium P-T profiles of model atmospheres with varying abundances of metallic species for C/O = 1. The model assumes a hot Jupiter with an equilibrium temperature of 2000 K. The left panel shows the effect of solar mixing fractions of the metallic species, and the right panel shows the abundances such that the ratio of visible to infrared opacity was 10. The volatile species were assumed to be in chemical equilibrium at C/O = 1, and in each model the species was included in the atmosphere by itself with no other visible absorbers.

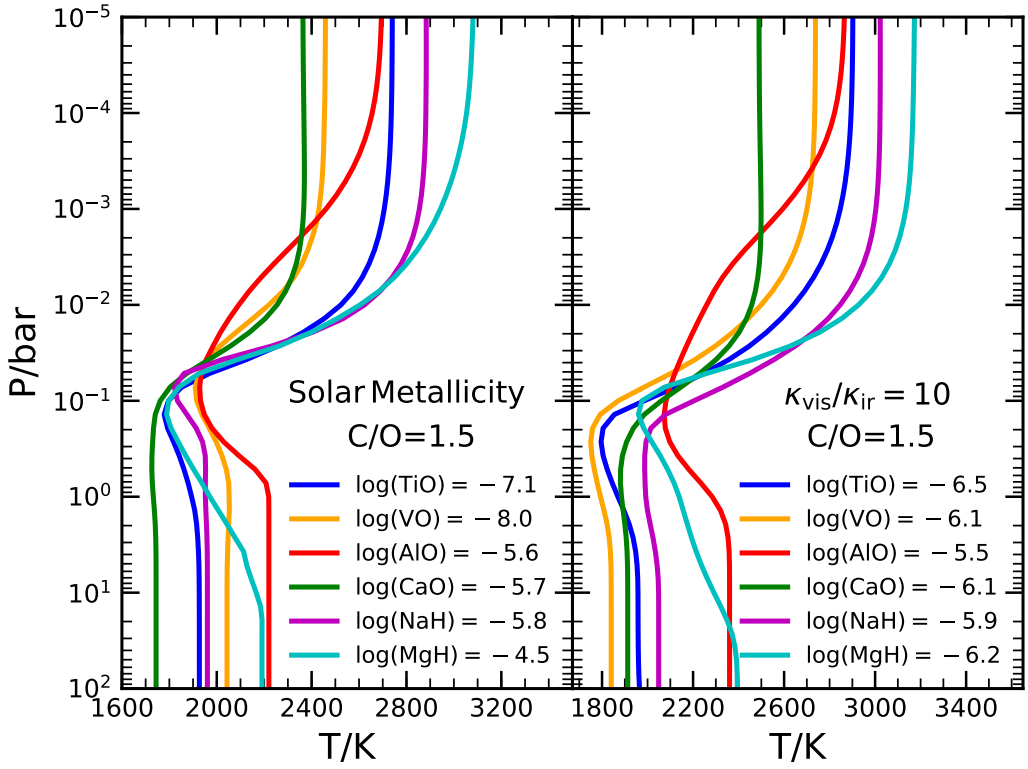

Fig. 4.7 Radiative equilibrium P-T profiles of model atmospheres with varying abundances of metallic species for C/O = 1.5. The model assumes a hot Jupiter with an equilibrium temperature of 2000 K. The left panel shows the effect of solar mixing fractions of the metallic species, and the right panel shows the abundances such that the ratio of visible to infrared opacity was 10. The volatile species were assumed to be in chemical equilibrium at C/O = 1.5, and in each model the species was included in the atmosphere by itself with no other visible absorbers.

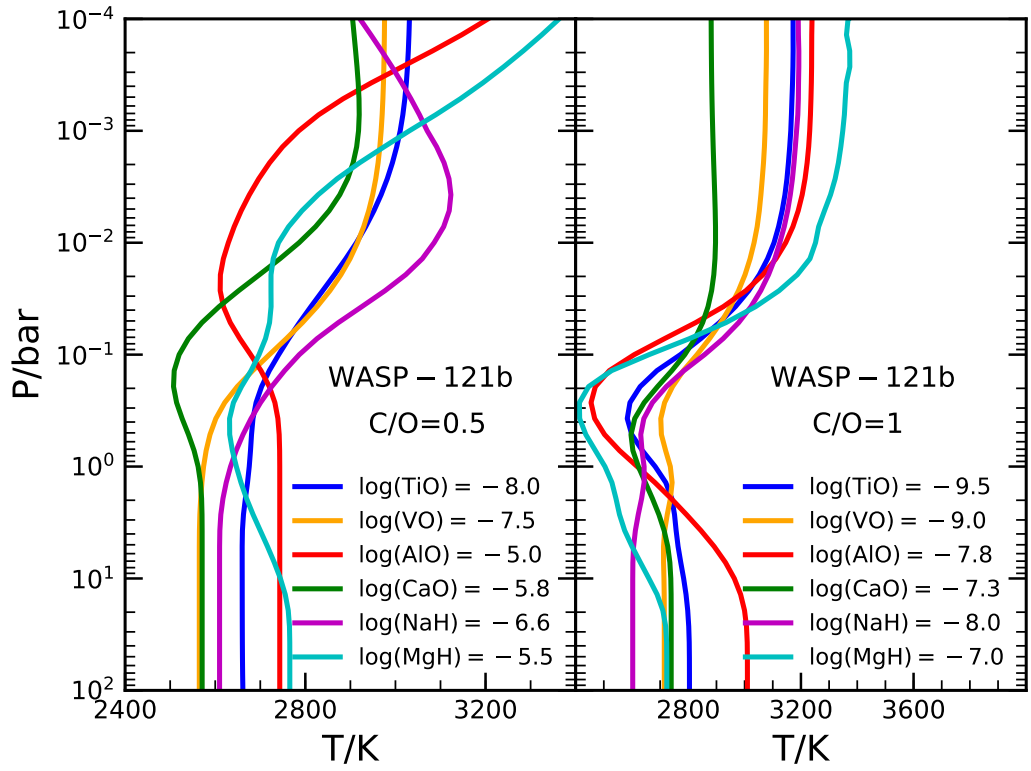

Fig. 4.8 Radiative-convective equilibrium P-T profiles for the planet WASP-121b for a C/O ratio of 0.5 (left) and 1 (right) that most closely match the observed spectrum. In each model the species was included in the atmosphere by itself with no other visible absorbers.

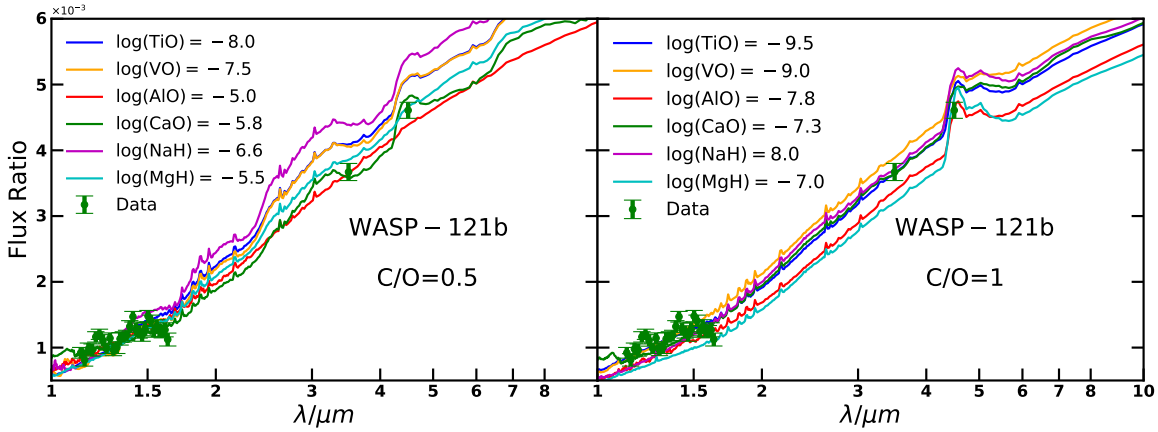

Fig. 4.9 Planet/star flux ratios for the radiative-convective equilibrium models of WASP-121b for a C/O ratio of 0.5 (left) and 1 (right). The green points indicate the Hubble WFC3 and Spitzer photometric observations. The corresponding P-T profiles are shown in fig. 4.8.

Chapter 5

Retrieval of Exoplanet Emission Spectra with HyDRA

"In this house we obey the laws of thermodynamics!"
- H. Simpson, M. Groening et al.

This chapter discusses the HyDRA model for retrievals of thermal emission spectra that I have developed. The HyDRA framework also allows constraints on disequilibrium processes in the retrieved atmospheres. This work has been published in Gandhi and Madhusudhan (2018). I describe the retrieval model, which constrains the model parameters for a given dataset. I then use these retrieved parameters to test the physical plausibility of the retrieved solutions through comparisons with the GENESIS equilibrium model. The HyDRA framework is also used in chapters 6 and 7 to carry out retrievals for a number of hot Jupiter emission spectra. In addition to emission retrievals, I have helped adapt my HyDRA retrieval code to perform retrievals of transmission spectra through the AURA code, as discussed in Pinhas *et al.* (2019). These transmission spectra have been used for a homogeneous study of chemical abundances in ten giant exoplanets as well as for other applications in our group.

5.1 Background

Two distinct methodologies exist for atmospheric modelling of exoplanets, that of self-consistent or "forward" models and retrievals. Self-consistent models, as discussed in chapter 3, have been used for many years to predict and interpret spectra of hot Jupiter atmospheres (e.g. Barman *et al.*, 2005; Fortney *et al.*, 2008; Hubeny *et al.*, 2003; Seager *et al.*, 2005). On the other hand, retrievals have been a recent development

over the past decade (Madhusudhan and Seager, 2009). It is important to distinguish the parametric models used in retrievals to self-consistent equilibrium models such as GENESIS (chapter 3). The latter models compute the $P-T$ profile, molecular composition, and the spectrum, of an atmosphere ab initio based on assumptions of thermochemical and radiative-convective equilibrium given the macroscopic system parameters (see e.g. Madhusudhan *et al.*, 2014a, for a comparison between retrieval and equilibrium models).

On the other hand, retrieval methods are inverse modelling techniques which formally fit models to spectral data to derive statistically robust constraints on the atmospheric properties through the constrained model parameters. Several studies have conducted atmospheric retrieval of thermal emission spectra of transiting exoplanets (Evans *et al.*, 2017; Lee *et al.*, 2012; Line *et al.*, 2012; Madhusudhan and Seager, 2009; Madhusudhan *et al.*, 2014b; Oreshenko *et al.*, 2017). The methods generally involve a parametric model, with the pressure-temperature (P-T) profile and abundances of chemical species as free parameters, with no prior assumptions about chemical or radiative equilibrium. The model is coupled to a statistical inference algorithm to explore the model space and estimate the parameters. A variety of statistical methods have been used in the literature with varying levels of sophistication and have resulted in constraints on thermal inversions and chemical abundances in several exoplanets (Evans *et al.*, 2017; Haynes *et al.*, 2015; Line *et al.*, 2014; Madhusudhan *et al.*, 2014b).

What is ultimately desirable is a self-consistent equilibrium model that can work in tandem with a retrieval. The primary advantage of retrieval methods is the ability to estimate the composition and the $P-T$ profiles from spectral data without any a priori assumptions, e.g of chemical/radiative equilibrium. Conversely, retrievals can in principle also be used to constrain deviations of the retrieved thermal/chemical properties from equilibrium expectations, thereby allowing constraints on non-equilibrium processes. Some studies in the past have explored this avenue to constrain disequilibrium chemistry in exoplanetary atmospheres. Early retrievals used a chemical parametrisation which directly retrieved deviations from equilibrium chemistry (Madhusudhan and Seager, 2009). More recently, retrievals typically use parametric mixing ratios, assumed to be uniform in the atmosphere, and assess for deviation from chemical equilibrium a posteriori (Madhusudhan *et al.*, 2011b; Stevenson *et al.*, 2010). On the other hand, some studies have considered enforcing chemical equilibrium to narrow down the solution space in retrievals, referred to as "chemically consistent" retrievals (Line *et al.*, 2016). However, statistical constraints on deviations from chemical equilibrium are not a routine feature in most retrievals.

As for compositional disequilibrium, retrievals in principle should also be able to constrain deviations of the retrieved $P-T$ profiles from radiative-convective equilibrium if any. To date this aspect has not been explored, arguably due to computational challenges in the past. Most notably, self-consistent versus retrieval modelling codes often employ different frameworks owing to their contrasting functionalities and their development by independent groups. Thusly compatibility between the models is often difficult. The computational time is also a consideration, as self-consistent models are typically significantly slower per model evaluation than parametric models used in retrievals. This work aims to bring together both forward and retrieval methods into a common framework in order to facilitate simultaneous constraints on chemical and radiative disequilibrium.

Here we introduce HyDRA, an integrated atmospheric retrieval framework for thermal emission spectroscopy of transiting exoplanets. In addition to retrieving chemical compositions and P-T profiles, HyDRA allows constraints on layer-by-layer deviations of the retrieved atmosphere from chemical and radiative-convective equilibrium. This is pursued by integrating the retrieval model with GENESIS (chapter 3). Both the retrieval and equilibrium codes share the same structure, language, and underlying input data (e.g. opacity database, stellar flux, system parameters, etc.). This means that differences between our retrieved parameters and our equilibrium model will be down to the atmospheric processes at play, and not any differences between the modelling schemes. We study the disequilibrium for our test case of WASP-43b, with one of the most precise spectra available to date. We are able to show using HyDRA that WASP-43b is consistent with both chemical and radiative-convective equilibrium.

In what follows, we describe our modelling and retrieval methodology in section 5.2. We validate the HyDRA retrieval framework using a synthetic data set in section 5.3. We then use HyDRA to retrieve the dayside atmospheric properties of the hot Jupiter WASP-43b in section 5.4, followed by a summary and discussion in section 5.5.

5.2 Methods

HyDRA is a custom-built atmospheric retrieval framework for application to emission spectra of exoplanets. The framework comprises of three key components: (1) a parametric atmosphere model, (2) a Bayesian statistical inference algorithm, and (3) a disequilibrium module for constraining deviations as seen from equilibrium. The parametric model computes an atmospheric thermal emission spectrum given the parametric composition and temperature structure. Given a dataset, the Bayesian

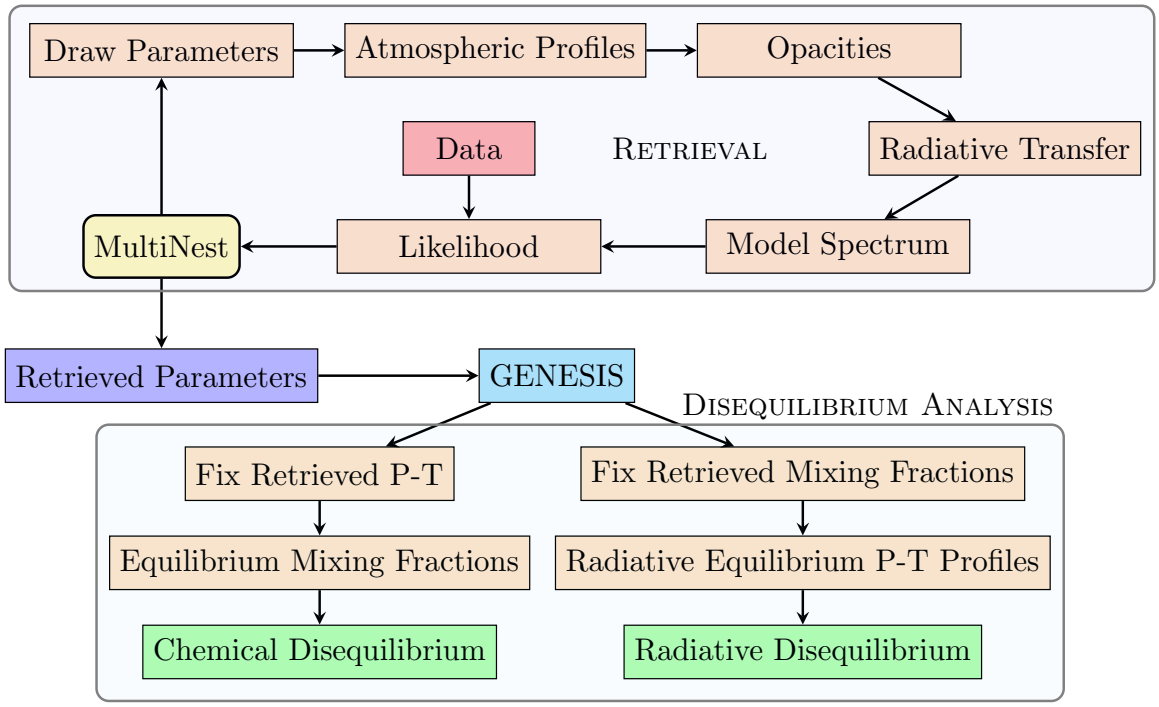

Fig. 5.1 The HyDRA modelling and retrieval framework. The model parameters, discussed in section 5.2.2, are used to compute the atmospheric structure (see section 5.2.2 and 5.2.2), the opacities (section 5.2.3) and the emergent spectrum for a model atmosphere (section 5.2.4 and 5.2.6). The likelihood is computed using the data and the model spectrum binned to the resolution of the data. The statistical inference, including parameter estimation and model selection, is conducted using the nested sampling algorithm implemented using the MultiNest package, as discussed in section 5.2.7. Once the retrieval is completed the retrieved $P-T$ profile and chemical compositions are used in tandem with the GENESIS self-consistent equilibrium model to compute deviations from radiative-convective equilibrium and chemical equilibrium, as discussed in section 5.2.8.

inference involves estimating the model parameters and detection significances. The disequilibrium module constrains the deviations of the retrieved atmospheric properties from chemical and radiative-convective equilibrium. In the following sections, we discuss each of the above aspects of HyDRA. The modelling and retrieval architecture of HyDRA is shown in fig. 5.1.

5.2.1 Geometry

We focus on emission spectra of transiting exoplanets as observed at secondary eclipse. Immediately prior to secondary eclipse, emission is observed both from the star as well as the dayside of the planet combined. When the planet is in secondary eclipse only the stellar flux is observed, which when subtracted from the combined emission gives the planetary spectrum. Dividing the two quantities yields the planet-star flux ratio that is independent of the distance to the system. The observed planet-star flux ratio can be expressed as

$$\frac{\mathrm{F_p}(\nu)}{\mathrm{F_{star}}(\nu)} \approx \frac{\mathrm{R_p^2 B}(\mathrm{T_{p,\nu}}, \nu)}{\mathrm{R_{star}^2 B}(\mathrm{T_{star,\nu}}, \nu)}. \tag{5.1}$$

Here, $\mathrm{T_{p,\nu}}$ and $\mathrm{T_{star,\nu}}$ refer to the planetary and stellar brightness temperatures at the frequency ν, and R_p and R_star are their corresponding radii. $B(T, \nu)$ is the Planck function corresponding to the brightness temperature T, ν at a frequency ν. $\mathrm{T_{p,\nu}}$ is a representative temperature corresponding to the $\tau_\nu \approx 1$ surface (the "photosphere") at frequency ν. The exact calculation of the emergent spectrum from the planetary atmosphere is described in section 5.2.4.

The flux ratio has wavelength dependant emission which occurs from different pressure levels in the atmosphere depending on the opacity and hence atmospheric chemistry. The emission spectrum therefore provides constraints on the temperature profile, chemical composition, and energy transport in the dayside atmosphere. Hot Jupiter atmospheres are particularly conducive to observations of thermal emission due to their large radii and high temperatures.

Figure 5.2 shows a schematic of the emission occurring from a planet, with the pressure-temperature (henceforth $P - T$) profile shown. The region of the atmosphere where the optical depth is of order unity is where the emission will occur from. This will also be a function of the wavelength and of the constituent molecular species (i.e their cross-section). Where the emission occurs from cooler parts of the atmosphere, a smaller thermal signal is generated. Absorption features thus result from the temperature decreasing with altitude, and vice versa for thermal inversions (where the temperature

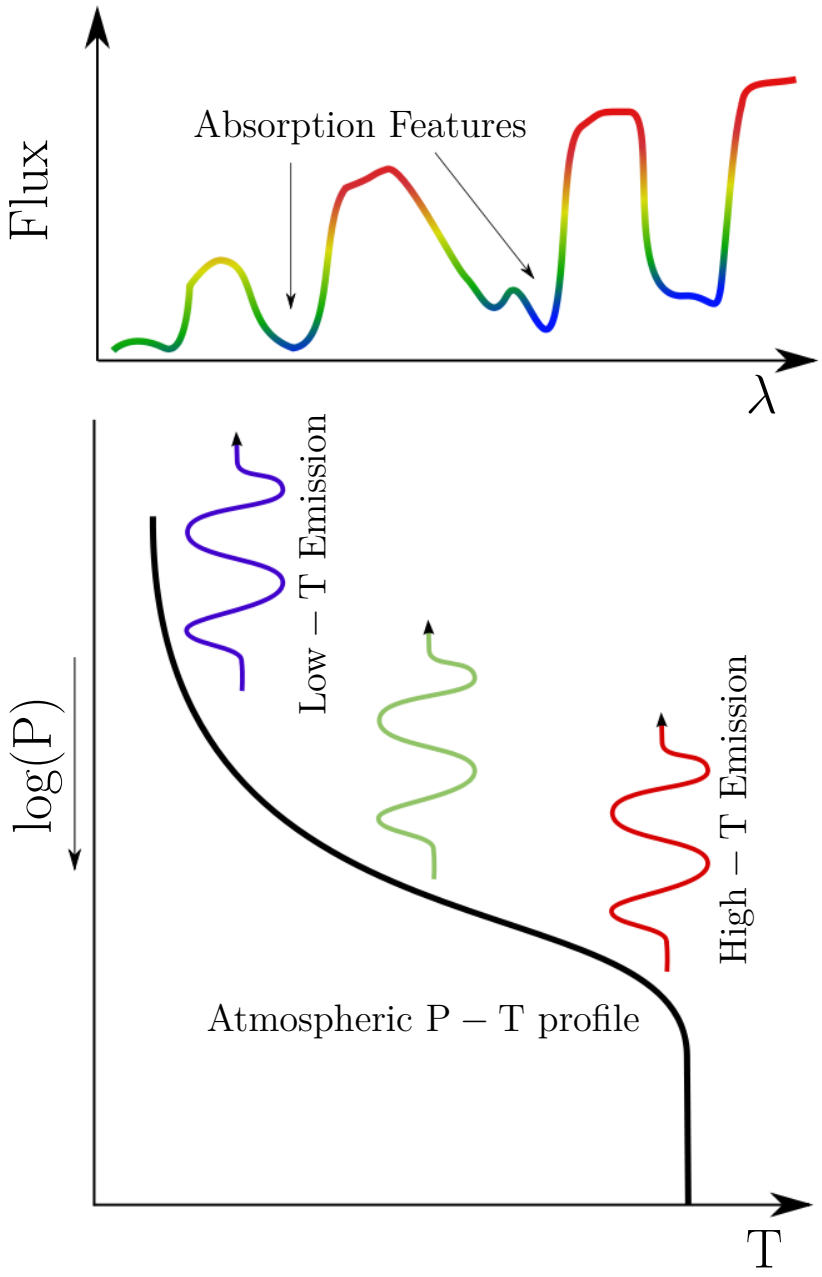

Fig. 5.2 Schematic of thermal emission from an atmosphere. The lower diagram shows a model pressure-temperature profile and the upper diagram shows the corresponding observed spectrum. If the emission occurs from lower in the atmosphere (where the temperature is greater) the emitted flux is greater (red regions) and vice versa for cooler (blue) regions. Thus, features in molecular bands where the opacity is greater appear as absorption features in the flux spectrum if the temperature decreases with height and originate higher up in the atmosphere.

Table 5.1 The set of parameters we choose in order to test our model. These were chosen so as to explore the model in the region of the parameter space in which we would expect the results to lie and taken from a self-consistent equilibrium profile. The first 7 values are the mixing fractions of the molecular species (section 5.2.2) and the total absorption coefficient calculation is given in section 5.2.3. The final six generate the $P-T$ profile described in section 5.2.2. As the original $P-T$ profile to generate the data set is from the self-consistent model, the analytic profile parameters are the closest fit.

Mixing Fraction						
X_{H_2O}	X_{CH_4}	X_{NH_3}	X_{CO}	X_{HCN}	X_{CO_2}	$X_{C_2H_2}$
5×10^{-4}	10^{-4}	10^{-4}	10^{-4}	10^{-4}	10^{-4}	10^{-4}

$P-T$ Profile					
T_{100mb}/K	$\alpha_1/K^{-\frac{1}{2}}$	$\alpha_2/K^{-\frac{1}{2}}$	P_1/bar	P_2/bar	P_3/bar
1725	0.42	0.6	0.2	2×10^{-4}	0.3

increases with height). This allows us to probe the $P-T$ profile of the planet by studying the spectrum and the absorption from spectrally active species. In the retrieval algorithm, we will need to model the atmosphere for a wide range of $P-T$ profiles and chemistry that is possible for such exoplanets to explore the parameter space.

In our model we take a grid of 4000 evenly spaced wavelength points in the Hubble WFC3 and Spitzer IRAC 1 and 2 bandpasses between 1 and 5.5 μm, and 100 atmospheric layers evenly spaced in log(P) ranging from $10^2 - 10^{-5}$ bar. The temperature profile is used to determine the density of gas under the ideal gas assumption, taking the atmosphere to be in hydrostatic equilibrium.

5.2.2 Model Parameters

$P-T$ Profile Parametrisation

Atmospheric temperature profiles can have strong dependence with pressure. Being able to model P-T profiles effectively with a minimal number of free parameters is critical, particularly in emission spectroscopy where the spectrum is quite sensitive to the temperature gradient (see fig. 5.7). We adopt the parametric P-T profile of Madhusudhan and Seager (2009) which is known to be effective in capturing a wide range of P-T profiles (Burningham *et al.*, 2017; Madhusudhan *et al.*, 2014b). Line *et al.* (2013) explored alternate parametrisation of the $P-T$ profile, either an analytic profile (Guillot, T., 2010) for grey atmospheres or a level-by-level approach, where the atmosphere is subdivided into several regions and the temperature in each of these

layers left as a retrieval parameter. Retrievals with HyDRA were checked with both of these temperature profiles as well to ensure minimal effect of the $P-T$ parametrisation on the derived atmospheric structure, as was seen in Line *et al.* (2016).

In this work we adopt the profile from Madhusudhan and Seager (2009), the atmosphere is divided into 3 broad regions with the boundaries between them given by $P_0 \leqslant$ layer 1 $< P_1$, $P_1 \leqslant$ layer 2 $< P_3$ and $P_3 \leqslant$ layer 3. P_2 represents the base pressure of the thermal inversion, only present in the atmosphere if $P_1 < P_2$. The temperature profile in each layer is given by

$$P = P_0 e^{\alpha_1 (T-T_0)^{\beta_1}} \text{ in layer 1,} \tag{5.2}$$

$$P = P_2 e^{\alpha_2 (T-T_2)^{\beta_2}} \text{ in layer 2,} \tag{5.3}$$

$$T = T_3 \text{ in layer 3.} \tag{5.4}$$

with the free parameters α_1, α_2, β_1 and β_2 determining the gradient of the $P-T$ profile, and T_i representing the temperature at pressure P_i. We set $\beta_1 = \beta_2 = 0.5$ as per the reasoning in Madhusudhan and Seager (2009), and fix the top of the atmosphere $P_0 = 10^{-5}$ bar; pressures below this do not significantly affect the observed emission spectrum due to lack of any significant opacity. These conditions, along with the continuity of the temperature between each layer, result in 6 free parameters to fully specify the temperature at any pressure, which for convenience we take to be T_0, α_1, α_2, P_1, P_2 and P_3.

The parameters that we retrieve are shown in table 5.1. In the retrieval itself, we choose to parametrise the temperature at 100 mbar pressure $T_{100\text{mb}}$ instead of T_0. This is convenient as it offers the value of the temperature near the photosphere, and not simply the top of the model atmosphere which would be quite poorly constrained anyway and dependant on the choice of the model (the lowest pressure modelled). It also provides tighter constraints on the other parameters, given that the spectrum is most sensitive to the temperature at this pressure. The measurement at 0.1 bar can also be more easily compared to the planet's equilibrium temperature, and any conclusions we can draw from the observed temperature.

Chemical Mixing Ratios

As well as the $P-T$ structure of the atmosphere, we also wish to determine the abundances of the spectroscopically active species. Molecular species have been discovered in both transmission and emission spectroscopy, most notably H_2O, in several transiting exoplanets. As typically considered in retrievals (Line *et al.*, 2016; MacDonald

and Madhusudhan, 2017; Madhusudhan *et al.*, 2014b) we include molecular species that are expected to be most dominant in H_2-rich atmospheres at high temperatures (Heng and Lyons, 2016; Madhusudhan, 2012; Moses *et al.*, 2013): H_2O, CH_4, NH_3, CO, CO_2, HCN and C_2H_2 (see table 5.1).

The molecular mixing ratio of species i is given by $X_i = n_i/n_{\rm tot}$, where n_i is the number density of the species and $n_{\rm tot}$ is the total number density of all species. The mixing ratio X_i can be left as a free parameter to be retrieved or fixed to a specific value. The helium fraction $X_{\rm he}$ is fixed to be 0.15 (the He:H_2 ratio is 0.17), i.e solar composition. The hydrogen mixing ratio is calculated from $X_{H_2} = 1 - \sum_i X_i$ (only for hydrogen dominated atmospheres), in order to ensure that the sum of the mixing ratios equals unity. Our model takes as input the volume mixing ratios of the molecular species; to convert from the mixing fraction of a species to its ratio relative to H_2 it can be multiplied by 1.17.

We consider the atmosphere to be in hydrostatic equilibrium, and the mean molecular weight of the atmosphere $\overline{m}$ is calculated self-consistently using the ideal gas law, taking into account the relative molecular masses of each of the gaseous species m_i and the corresponding abundance X_i. The density ρ and number density n are given by

$$\overline{m} = \sum_i X_i m_i, \tag{5.5}$$

$$P = \frac{\rho k_b T}{\overline{m}}, \tag{5.6}$$

$$n = \frac{\rho}{\overline{m}}. \tag{5.7}$$

5.2.3 Opacities

Spectroscopically active species present can absorb and emit photons in the atmosphere, dependent on the relevant cross-section. These wavelength dependent molecular absorption bands determine the emergent spectrum. The molecular cross-sections are computed for the gaseous species considered, along with the collisionally induced absorption from the dominant H_2 and He gases. The sum of these, the total opacity, is required to calculate the flux ratio from the forward model (section 5.2.4). The full details of the computation carried out to compute the cross-sections can be found in chapter 2.

Once the molecular cross section, $\kappa_i(\mathrm{P}, \mathrm{T}, \nu)$ is computed for each $P - T$ point of the atmosphere, we simply sum the cross sections of all of the species, weighted by their mixing fractions X_i (see section 5.2.2). This gives the total absorption coefficient

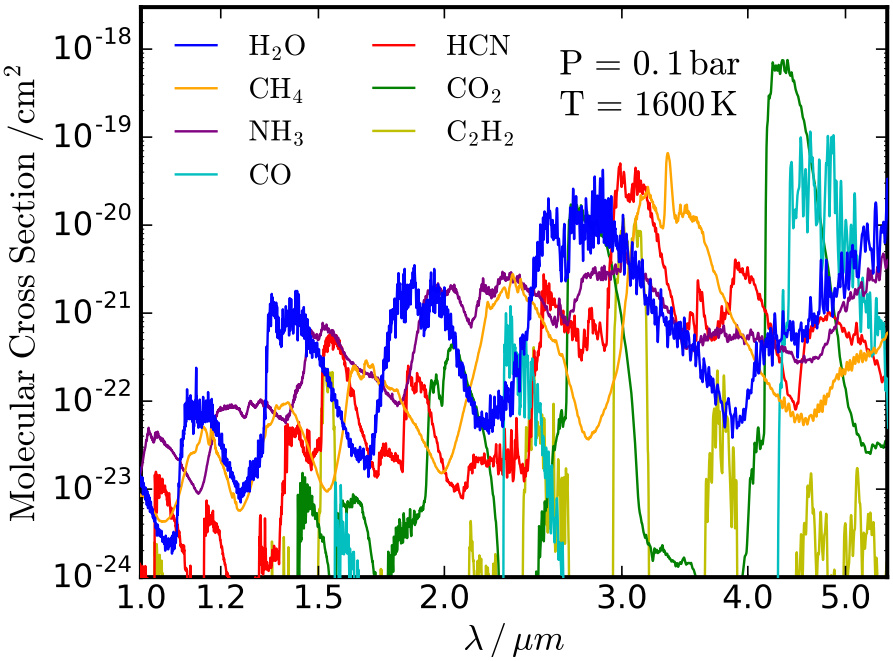

Fig. 5.3 Molecular absorption cross sections for the 7 volatile species considered in our retrievals. These are shown at 1600K, approximately WASP-43b's expected temperature, and at a pressure of 0.1 bar, where most of the emission from the planet originates. The cross sections have been gaussian smoothed in the figure for clarity.

κ_ν and the optical depth τ_ν as a function of pressure, temperature and frequency

$$\kappa(\mathrm{P},\mathrm{T},\nu) = n(\mathrm{P},\mathrm{T}) \sum_i \mathrm{X}_i \, \sigma_\mathrm{i}(\mathrm{P},\mathrm{T},\nu) + \sigma_{\mathrm{CIA}}(\mathrm{P},\mathrm{T},\nu), \tag{5.8}$$

$$\mathrm{d}\tau(\mathrm{P},\mathrm{T},\nu) = (\kappa(\mathrm{P},\mathrm{T},\nu) + \sigma_{\mathrm{H_2}}(\mathrm{P},\mathrm{T},\nu))\mathrm{d}z, \tag{5.9}$$

where $\sigma_{\mathrm{H_2}}$ and σ_{CIA} refer to the loss from the beam due to Rayleigh scattering of molecular hydrogen and collisionally induced absorption respectively. Further details on the calculation of the absorption and scattering coefficients can be found in chapter 2 Fig. 5.3 shows the molecular cross sections for the 7 molecules considered at 1600K temperature and 0.1 bar pressure, representative of the typical conditions expected in WASP-43b's photosphere. Strong absorption from these prominent species can be seen in the WFC3 range between 1.1-1.7 μm, particularly for H_2O.

5.2.4 Radiative Transfer

Once the total opacity contribution from each species has been summed, we require calculation of the emergent flux out of the model atmosphere. The radiative transfer method to obtain the emergent planetary spectrum is discussed here. We only consider radiative transfer models in the pure absorption limit, where the scattering into the beam of radiation is assumed to be negligible. Therefore the source function of radiation is taken to simply be the Planck function, B_ν. The radiative transfer equation 3.3 is thus reduced to

$$\mu \frac{\partial I_{\mu,\nu}}{\partial \tau_\nu} = I_{\mu,\nu} - B_\nu, \tag{5.10}$$

where μ refers to the angle cosine relative to the vertical ($\mu = \cos\theta$). However, this approximation begins to deviate from the full solution (i.e ones that account for scattering into the beam) once the wavelength is below $\sim 1\mu$m (i.e where scattering can no longer be assumed small). Various methods exist to compute the emergent intensity of radiation, with varying levels of sophistication, but a simple forward model is needed for the retrieval. This is so as to be computationally fast whilst also capturing the relevant physics, as typically retrievals evaluate millions of models to map the parameter space. For this purpose we tested several approaches in order to determine which would be the most favourable in terms of accuracy and time.

Consider a slab of optical thickness τ and temperature T, with a radiation intensity I_0 emergent from underneath at an angle θ to the normal, with $\cos(\theta) = \mu$. The radiation emergent out of the slab as a function of frequency ν and angle cosine μ is

given by (Seager, 2010)

$$I_1(\nu,\mu) = I_0(\nu,\mu)e^{-\tau/\mu} + B(T,\nu)(1-e^{-\tau/\mu}), \tag{5.11}$$

for a Planck function $B(T,\nu)$ at temperature T and frequency ν. For a model atmosphere with ND layers, we simply compute the contributions of each slab by integrating upwards through the atmosphere along a ray to find the emergent intensity $I_{\rm top}$. The flux exiting the top of the atmosphere is then given by

$$F_{\rm top}(\nu) = \int_0^{2\pi}\int_0^1 \mu I_{\rm top}(\nu,\mu)d\mu d\phi = 2\pi\int_0^1 \mu I_{\rm top}(\nu,\mu)d\mu, \tag{5.12}$$

where the integral over the azimuth ϕ is assumed to be trivial assuming axial symmetry. If the distance to the system is d, the observed flux at the observer is then

$$F_{\rm p}(\nu) = F_{\rm top}(\nu)\frac{R_{p,\nu}^2}{d^2}. \tag{5.13}$$

Here $\mathrm{R}_{p,\nu}$ is the radius of the planetary photosphere (where $\tau_\nu = 1$) at the frequency ν. The mean radius of the planet, required to calculate the temperature profile, is taken to be the observed radius set at a pressure of 0.1 bar which represents the mean pressure of the $\tau_\nu = 1$ surface.

Our model computes flux from radiation exiting the atmosphere accounting for the loss from the beam due to absorption and scattering. There are multiple approaches to calculate the flux. We experimented with the case where only one ray was considered for the emergent intensity, at $\mu = 0$ (vertical), to calculate the flux. We found significant differences ($>$ 30ppm) between this and the 6 angle dependent radiative transfer using the Feautrier method as described in chapter 3 (see fig. 5.4). This single ray approach is the method used in Line *et al.* (2013) and Madhusudhan and Seager (2009), and has been reasonable given previous observational data. It is computationally fast, requiring only one ray's exiting radiation field to be calculated. Perhaps a more representative angle could have been used for single ray calculations, e.g $\mu = 1/\sqrt{3}$. However, given the high accuracy on the WASP-43b dataset, we chose to explore other methods in order to calculate the flux to a greater accuracy. This is achieved by integrating over multiple angles. Trapezium rule integration over μ with 6 evenly spaced values of μ ranging between 0 and 1 significantly improves the result, as the variation of the intensity with angle is considered. In this latter case, the difference from the full Feautrier calculation is below 10 ppm as shown in fig. 5.4. However, just two or three angles with Gaussian quadrature provided excellent match to the full solution (see

Table 5.2 Weights and angles (μ) used for each integration scheme. The angles for the integration with the Feautrier method can be found in chapter 3 and are the same as triple ray quadrature.

Method	Weights	μ
Single Ray	1	1
Trapezium Rule	0.1, 0.2, 0.2, 0.2, 0.2, 0.1	0, 0.2, 0.4, 0.6, 0.8, 1
Double Ray	0.5, 0.5	$\frac{1}{2} - \frac{1}{2}\sqrt{\frac{1}{3}}$, $\frac{1}{2} + \frac{1}{2}\sqrt{\frac{1}{3}}$
Triple Ray	5/18, 4/9, 5/18	$\frac{1}{2} - \frac{1}{2}\sqrt{\frac{3}{5}}$, $\frac{1}{2}$, $\frac{1}{2} + \frac{1}{2}\sqrt{\frac{3}{5}}$

table. 5.2). Increasing the number of angles further did not result in major differences in the spectra, but did increase the computation time significantly (time per model scales with the number of μ values). It is for this reason that we adopt two angles with Gaussian quadrature in our model. The two angle integration is able to account for the variation in the radiation intensity as a function of μ (see equation 5.11) without affecting the computation time too significantly. For comparison, the precision of the WASP-43b data in secondary eclipse considered here is $\sim$ 35ppm, and so the present accuracy in our radiative transfer more than suffices for our purpose. In future, however, with higher quality data sets it would be imperative to use as accurate a solution as possible to ensure accurate constraints.

5.2.5 Stellar Spectrum

The data sets presented in emission spectroscopy of transiting hot Jupiters are given in terms of the ratio of the planetary to stellar flux (e.g see fig. 5.4). It is therefore vital that in order to obtain an accurate spectrum that we compute the flux of the host star. We calculate this using the available properties of the star and the Kurucz model grid of spectra (Castelli and Kurucz, 2004; Kurucz, 1979). The effective temperature of the star, the surface gravity, log(g), and metallicity are interpolated on the model grid to obtain the flux $F_{\rm top,star}$ at the top of the stellar atmosphere (see chapter 3.3.7. The observed flux at earth is then given by

$$F_{\rm star}(\nu) = F_{\rm top,star}(\nu)\frac{R_{\rm star}^2}{d^2}. \tag{5.14}$$

We then use this flux along with $F_{\rm p}$ from section 5.2.4 to calculate the theoretical data points for such a model below. We also checked against a simple Planck function for the star's flux, and did see some small differences where the stellar spectrum had absorption features or varied significantly from the Planck function. This was as expected and

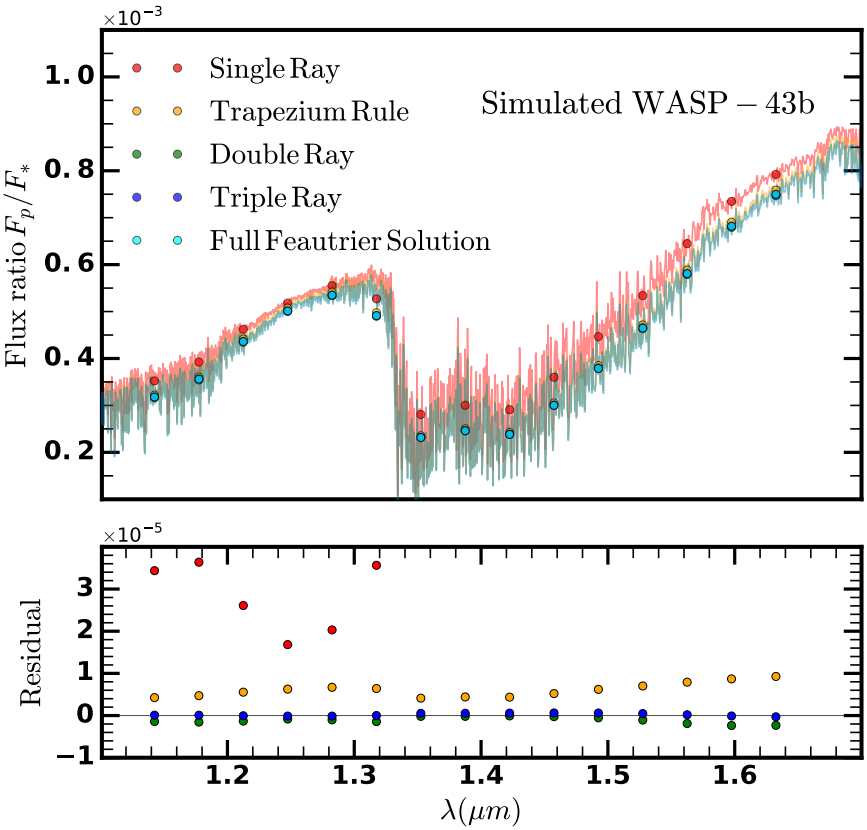

Fig. 5.4 Theoretical emergent flux spectra (top) and residuals (bottom) for various choices of the radiative transfer model shown compared to the full Feautrier radiative transfer solver in chapter 3. The markers indicate the binned WFC3 spectrum at the resolution of the WASP-43b data. 2000 wavelength points between 1.1 and 1.7 μm were used to generate the spectra with 100 atmospheric layers. The choice of model parameters are given in table 5.1.

when the noise constraints on the data set was greater than 20 ppm in the WFC3 bandpass as in our case the differences were negligible. It is however noteworthy that the quality of the stellar spectrum will be important to interpret exoplanetary spectra with very high precision.

5.2.6 Generating Model Data

The spectroscopic instruments used to obtain the model data points for a given spectrum (e.g Hubble's WFC3 and Spitzer's IRAC) have their own transmission properties which must be taken into account when generating the model data points. All of the instruments have their own sensitivity as a function of wavelength; the

Hubble WFC3 bandpass also has multiple grisms that results in the received flux being convolved with an instrument point spread function (PSF) before it is binned (in our case only the G141 grism requires this). Hence, to accurately determine where the spectral points for our model spectrum lie, a given theoretical flux F is firstly convolved where necessary to give

$$F_{\rm conv}(\lambda) = \int_{-\infty}^{\infty} F(\lambda')PSF(\lambda - \lambda')d\lambda'. \tag{5.15}$$

Conversion from frequency space, $F(\nu)$, to wavelength space, $F(\lambda)$, is easily given by

$$F(\lambda) = F(\nu) \mid \frac{d\nu}{d\lambda} \mid = F(\nu)\frac{c}{\lambda^2}. \tag{5.16}$$

The convolved spectrum $F_{\rm conv}$ is then multiplied by the instrument sensitivity function $S(\lambda)$ and normalised to obtain the binned flux,

$$F_{\rm binned} = \frac{\int_{\lambda_{\rm min}}^{\lambda_{\rm max}} F_{\rm conv}(\lambda)S(\lambda)d\lambda}{\int_{\lambda_{\rm min}}^{\lambda_{\rm max}} S(\lambda)d\lambda}, \tag{5.17}$$

with the bin edges having a minimum and maximum wavelength $\lambda_{\rm min}$ and $\lambda_{\rm max}$ respectively. The model spectrum needs to be convolved with the PSF only for the HST WFC3 spectrograph and not for the Spitzer photometric bands. These steps are carried out for the stellar and the planetary fluxes $F_{\rm star}$ and $F_{\rm p}$ and the final model points (given as a flux ratio) are

$$y_{\rm model,n} = \frac{F_{\rm p,binned,n}}{F_{\rm star,binned,n}}, \tag{5.18}$$

for every bin n that is considered.

5.2.7 Parameter Estimation and Statistical Inference

In atmospheric retrieval, a parametric forward model is coupled to a statistical inference algorithm to estimate the model parameters given the data and to perform model comparisons. Contemporary retrieval codes routinely use rigorous Bayesian statistical inference methods such as MCMC (Line *et al.*, 2013; Madhusudhan, 2012) and nested sampling (Benneke and Seager, 2013; Lavie *et al.*, 2017; Line *et al.*, 2016; MacDonald and Madhusudhan, 2017). We utilise nested sampling (Skilling, 2004), which is advantageous in that it allows for calculation of the Bayesian evidence and hence model comparisons.

In our work, we employ the multimodal nested sampling algorithm MultiNest (Feroz and Hobson, 2008; Feroz *et al.*, 2009, 2013), using the python package PyMultiNest developed by Buchner *et al.* (2014). The full details of the statistical methods and the priors used for the analysis can be found in MacDonald and Madhusudhan (2017). We briefly summarise the approach below for convenience. We begin with the statistical techniques used to ascertain how well the model describes observations, and proceed afterwards onto the Bayes factor calculations to compare different models.

Bayesian Evidence

Given a set of parameters θ that describe some forward models M_k, we have a set of a priori expectations on the values through a prior probability density function $\pi(\theta, M_k)$. $p(\theta|y_{\rm obs}, M_k)$ is the prior posterior probability distribution. With the observations and spectral data points $\mathbf{y}_{\rm obs}$ and $\mathbf{y}_{\rm k}$ respectively, this can be rewritten (Trotta, 2008) utilising Bayes theorem to

$$p(\theta|y_{\rm obs}, M_k) = \frac{\mathcal{L}(y_{\rm obs}|\theta, M_k)\pi(\theta, M_k)}{\mathcal{Z}(y_{\rm obs}|M_k)}, \tag{5.19}$$

where we have defined the likelihood function, prior and the Bayesian evidence as $\mathcal{L}$, π and $\mathcal{Z}$ respectively. We will take the likelihood function to be

$$\mathcal{L}(y_{\mathbf{obs}}|\theta, M_k) = \prod_i^{N_{\rm obs}} \frac{1}{\sqrt{2\pi}\sigma_i} \exp\left(\frac{-(y_{\rm obs,i} - y_{\rm k,i})^2}{2\sigma_i^2}\right). \tag{5.20}$$

This is a measure of how likely the choice of spectrum produces the observed data points, a higher likelihood indicates that the set of parameters is favoured. Eqn. 5.20 assumes that the error is independently gaussian distributed for each data point. To avoid bias, uniform priors are often used. The Bayesian evidence $\mathcal{Z}_{\rm k}$ for a spectrum k is simply a normalisation factor and is given by an integral over all parameter space

$$\mathcal{Z}_{\rm k} = \int_\theta \mathcal{L}(y_{\rm obs}|\theta, M_k)\pi(\theta, M_k)d\theta \tag{5.21}$$

The Bayesian evidence is simply a "figure of merit" that assesses the ability of a given model to descrive the data and can hence be used for model comparisons (see below).

Bayes Factor

Whilst comparing two models M_0 and M_1, we require the Bayes factor

$$B_{01} \equiv \frac{\mathcal{Z}(y_{\rm obs}|M_0)}{\mathcal{Z}(y_{\rm obs}|M_1)}. \tag{5.22}$$

This describes how one model performs relative to another in explaining the observations. If $B_{01} > 1$, model M_0 is favoured over M_1 given the observed data (its Bayesian evidence is greater). This allows us to demonstrate quantitatively whether a more complex model or a simple one is required. For instance, if we wish to calculate the significance of a detection of a molecule, we can find the Bayes factor B_{01} for a model with the molecule (M_0) and one with the same parameters but with this molecule removed (M_1). This then establishes the evidence for such a molecule. Bayes factors greater than 3, 12 and 150 are often quoted as weak, moderate and strong detections. The larger the Bayes factor, the more evidence there is to support model M_0, i.e the better the explanation of the data with the relevant parameter. This can then also be converted into a detection significance. For further details on Bayesian analysis, we refer the reader to Trotta (2008). The detection significances can tell us not only about the species that is present but given equilibrium models also provide constraints on disequilibrium phenomena.

5.2.8 Constraints on Disequilibrium

One of the key functionalities of HyDRA is to constrain the deviations of the retrieved compositions and *P-T* profiles from chemical and radiative-convective equilibrium. This is achieved by operating the retrieval code in tandem with our GENESIS self-consistent equilibrium model for exoplanetary atmospheres. As modules from both the retrieval and equilibrium models are shared, any deviations between retrieved and equilibrium properties are unlikely to be due to the intrinsic model differences but rather to non-equilibrium atmospheric processes at play.

Radiative-Convective Disequilibrium

We constrain radiative-convective disequilibrium by investigating deviations of retrieved *P-T* profiles from equilibrium *P-T* profiles with the same retrieved compositions. This is done by considering the posterior distributions of the retrieved *P-T* profiles, and their corresponding compositions, and computing the equilibrium *P-T* profiles using GENESIS by keeping the compositions fixed to the retrieved values. The resultant

equilibrium *P-T* profiles are used to compute the temperature differential (ΔT) between the equilibrium and retrieved profiles as a function of altitude (or pressure). The profile of ΔT and its statistical uncertainties provides a measure of the deviation from radiative-convective equilibrium.

The GENESIS model (chapter 3) determines the atmospheric $P-T$ profile in equilibrium, such that the incoming and outgoing radiation from each layer in the atmosphere is equal. The integral form of radiative-convective equilibrium in each layer is given by

$$\int_0^\infty \kappa_\nu (J_\nu - B_\nu) d\nu + \frac{\rho g}{4\pi} \frac{dF_{\rm conv}}{dP} = 0. \tag{5.23}$$

Here, κ_ν refers to the absorption coefficient, J_ν is the mean radiation intensity and B_ν is the Planck function at a frequency ν, and the convective flux $F_{\rm conv}$ is applied where convective regions occur in the atmosphere. Whereas the retrieval's $P-T$ profile is parametrised, the GENESIS model calculates the temperature for every pressure layer in the model atmosphere. The opacity and stellar flux calculations are identical to the retrieval algorithm, and the full radiative transfer scheme shows negligible differences as explored in section 5.2.4.

As we hold the chemistry fixed to a range of the retrieved values, we know that any deviation that arises can be attributed to effects not accounted for. These differences can provide key insights into atmospheric energy transport, and about the validity of 1-D models. It also provides clues to the next steps in our modelling approaches in order to match observations and incorporate new physics, e.g atmospheric dynamics, into 1-D models used in retrievals.

Chemical Disequilibrium

We constrain chemical disequilibrium in the atmosphere by considering deviations of the retrieved compositions from those computed assuming chemical equilibrium for the same retrieved *P-T* profiles. Given the posterior distributions of the retrieved parameters, we choose a representative statistical sample of compositions and their corresponding *P-T* profiles. These *P-T* profiles are then used to compute equilibrium abundances of all the chemical species and the corresponding uncertainties. The differences between the retrieved and equilibrium abundance provide constraints on the deviations from chemical equilibrium. The chemical species considered here include H_2O, CH_4, NH_3, CO, HCN, CO_2, C_2H_2, C_2H_4 and N_2.

To determine the equilibrium mixing fractions for a species at a given pressure and temperature, we utilise the semi-analytic calculations in chapter 3.3.5. The main chemical equations that govern the mixing ratios in a hydrogen dominated atmosphere are shown in equation 3.37. Given the elemental abundances relative to atomic hydrogen for carbon, oxygen and nitrogen (which we take as solar, a reasonable assumption given that the retrieved water abundance is consistent with solar, see section 5.4), the abundances of each of the species in the set of chemical equations above can be determined. Therefore, for a fixed $P-T$ profile we can determine the mixing ratios for our hydrogen dominated atmosphere. For the purpose of this work, we ignore N_2 as it offers no spectral signature, as well as C_2H_4 as it is present only in very small quantities and thus does not significantly affect the spectra and cannot be retrieved to any certainty for our spectral range.

5.3 Retrievals with Simulated Data

We now proceed to validate the HyDRA retrieval framework. The aim of this exercise is to demonstrate the effectiveness of HyDRA for atmospheric retrieval with emission spectra and to explore any degeneracies that may be present in the model parameter space given a dataset. We apply the code to synthetic data to demonstrate its effectiveness in extracting parameter values that are known a priori. Each component of HyDRA, i.e the $P-T$ parametrisation, the opacity calculations and the simplified radiative transfer module were also checked against a fully self-consistent radiative-convective equilibrium model (see fig. 5.4) to ensure a common modelling framework.

We apply HyDRA to a simulated thermal emission spectrum of the hot Jupiter WASP-43b. The choice of this system was driven by the quality of data available and its conduciveness for thermal emission observations. WASP-43b is a hot Jupiter with a mass of $\sim$2 M_J and radius of 0.93 R_J and orbits a K7 dwarf (Hellier *et al.*, 2011). The relatively small and cool star leads to a high planet-star flux ratio making the planet a prime target for thermal emission observations. Consequently, WASP-43b is the most observed transiting planet in thermal emission with high S/N observations using HST WFC3 (Stevenson *et al.*, 2014) and Spitzer (Blecic *et al.*, 2014). The synthetic emission spectrum was generated using a theoretical spectrum computed using our GENESIS self-consistent radiative-convective equilibrium model (chapter 3). The compositions for the volatile atmospheric molecules shown in table 5.1. The model atmosphere is in radiative-convective but not thermochemical equilibrium, to demonstrate the retrieval's

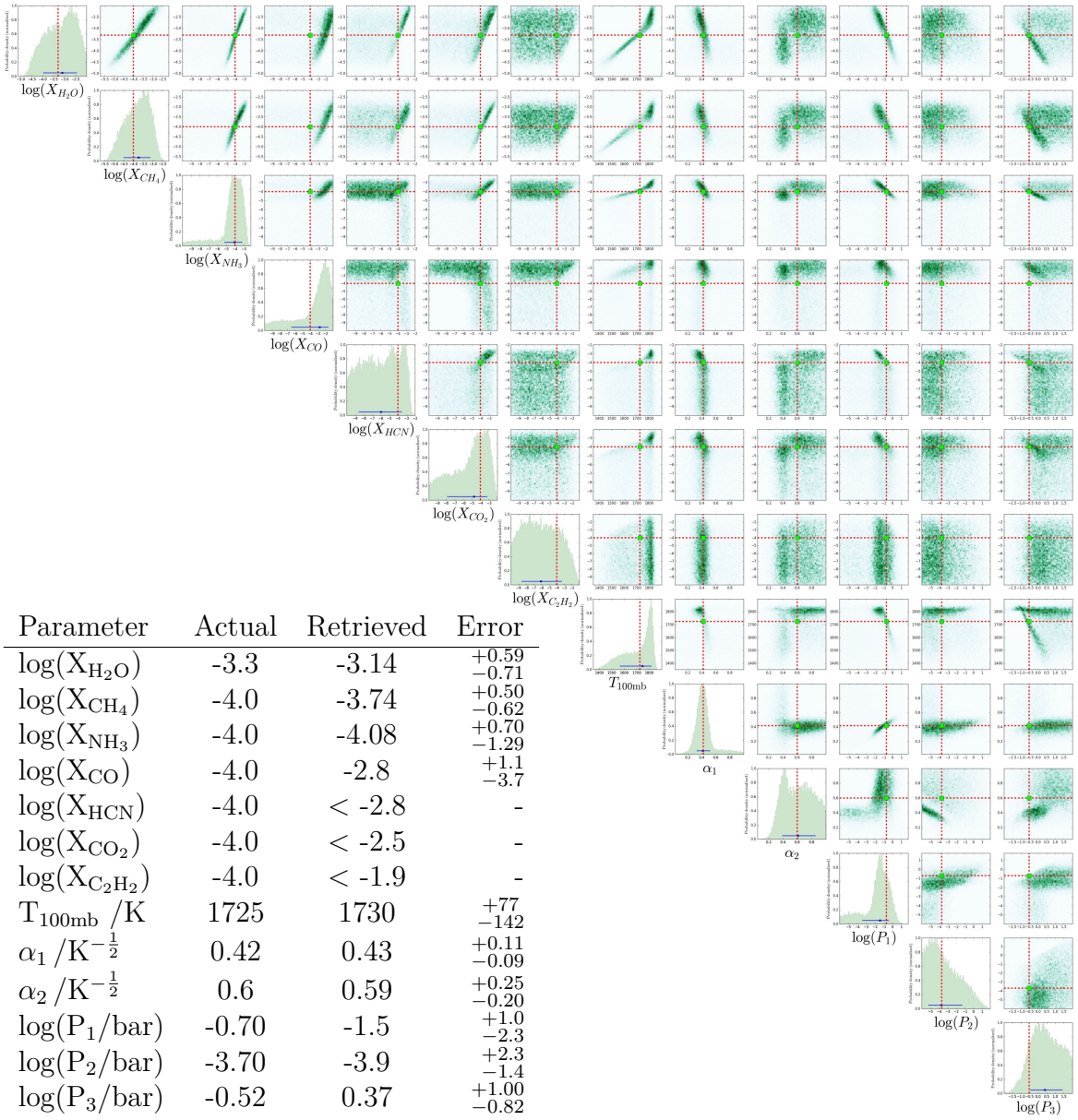

Parameter	Actual	Retrieved	Error
$\log(X_{H_2O})$	-3.3	-3.14	$^{+0.59}_{-0.71}$
$\log(X_{CH_4})$	-4.0	-3.74	$^{+0.50}_{-0.62}$
$\log(X_{NH_3})$	-4.0	-4.08	$^{+0.70}_{-1.29}$
$\log(X_{CO})$	-4.0	-2.8	$^{+1.1}_{-3.7}$
$\log(X_{HCN})$	-4.0	< -2.8	-
$\log(X_{CO_2})$	-4.0	< -2.5	-
$\log(X_{C_2H_2})$	-4.0	< -1.9	-
T_{100mb} /K	1725	1730	$^{+77}_{-142}$
α_1 /K$^{-\frac{1}{2}}$	0.42	0.43	$^{+0.11}_{-0.09}$
α_2 /K$^{-\frac{1}{2}}$	0.6	0.59	$^{+0.25}_{-0.20}$
$\log(P_1/\text{bar})$	-0.70	-1.5	$^{+1.0}_{-2.3}$
$\log(P_2/\text{bar})$	-3.70	-3.9	$^{+2.3}_{-1.4}$
$\log(P_3/\text{bar})$	-0.52	0.37	$^{+1.00}_{-0.82}$

Fig. 5.5 Marginalised posterior distribution for the synthetic retrieval on the emergent dayside spectrum of WASP-43b, with the simulated spectrum taken from our self-consistent model GENESIS (chapter 3) so as to be in radiative equilibrium. The red lines indicate the actual value of each parameter in the posterior corner plot and the histograms show the retrieved values and their error. The blue error bars indicate the median and 1σ error bars. Over 10^6 models were run with 4000 live samples and 4000 wavelength points between 1 and 5.5 μm, with the model atmosphere consisting of 100 atmospheric layers. The table on the left shows the actual and retrieved parameters along with their associated uncertainty. The $P-T$ profile parameters are described in section 5.2.2 and the abundances and opacity calculations are described in section 5.2.3.

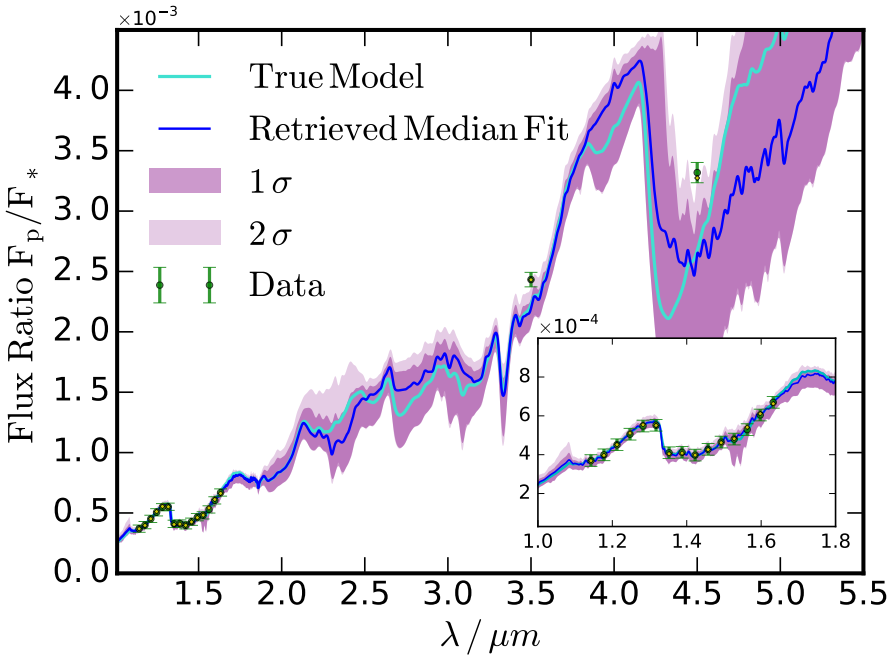

Fig. 5.6 Retrieved emergent spectrum from the simulated data of WASP-43b. The spectrum used for our retrieval was taken from the self-consistent model shown in cyan. The best-fitting model is shown in blue along with its binned data points as yellow diamonds. The dark and light purple contours show the 1σ and 2σ spread of 4000 parameter combinations from the posterior. The green markers indicate the spectral data points for the WFC3 (see inset) and Spitzer 3.6 μm and 4.5 μm channels and their associated error. The noise on the data is identical to the actual spectrum for the planet.

ability to constrain the chemical species when they are out of chemical equilibrium. Many of the modules between the models are shared (see section 5.2.8).

We have performed consistency and sensitivity analyses of our modelling framework over a range of fixed parameters and adopt the most optimal values. The model spectrum is binned to obtain simulated data points with the same precision and resolution as those obtained from real observations in the WFC3 and Spitzer IRAC bandpasses (Blecic *et al.*, 2014; Kreidberg *et al.*, 2014). The parameters of the synthetic model are shown in table 5.1, with the chemical abundance fixed for all pressures for consistency with the retrieval framework. The uncertainties in the simulated spectrum are taken to be exactly the same as those of the observed spectrum discussed above and added as random gaussian noise on the synthetic model. The parameters in the retrieval include abundances of the seven prominent volatile species expected in hot Jupiters (H_2O, CH_4, NH_3, CO, HCN, CO_2 and C_2H_2) and six parameters that

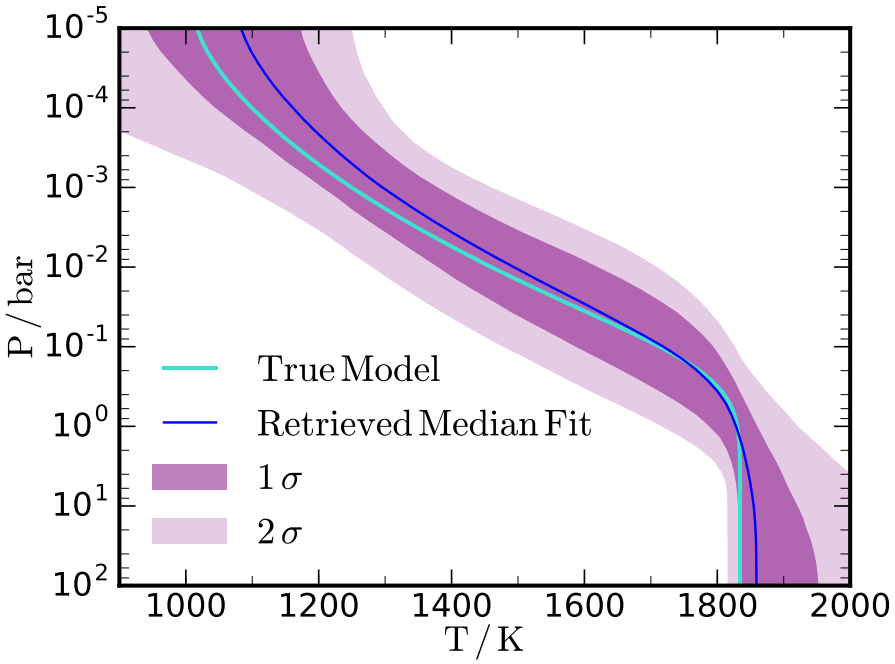

Fig. 5.7 Retrieved dayside $P-T$ profile from the simulated spectrum of WASP-43b, with the actual $P-T$ profile used to generate the simulated data shown in cyan. The blue line indicates the median fit and the dark and light purple contours show the 1σ and 2σ spread in the results drawn from the posterior.

describe the $P-T$ profile. The spectral resolution of the model was set to contain 4000 points uniformly spaced between 1-5.5 μm, for both the self-consistent model as well as retrievals. The retrievals were carried out using the nested sampling algorithm with 4000 live sample points. We have considered a range of spectral resolutions, number of live sample points in nested sampling, variation in pressure grid in the P-T profiles, etc, and have adopted the most conservative values for each. We also tested the radiative transfer with a simple single ray $\mu = 0$ case against integration over multiple angles (see section 5.2.4) and have adopted the optimal two-angle quadrature. In what follows, we discuss the results of our retrievals with the simulated data, given in table 5.1.

5.3.1 Retrieved Abundances

The retrieved abundances show very good agreement with the true abundances of the synthetic model. Figure 5.5 shows the posterior distributions for the retrieved chemical species along with their estimated and true values. We find that the true values lie within the 1-σ uncertainties for all the species. The best retrieved molecule is H_2O with the median value only 0.16 dex away from the true value and an average

uncertainty of 0.65 dex. Other molecules retrieved at similar precision include CH_4 and NH_3. The detection significances of H_2O, CH_4, and NH_3 obtained from nested model comparisons are 6.7σ, 5.6σ, and 2.1σ, respectively. The reason behind the well constrained abundances of these three molecules is a combination of their high abundances used in the synthetic model as well as their relatively strong spectral features mainly in the WFC3 bandpass; H_2O being the strongest and NH_3 the weakest of the three. The lower significance of NH_3 is also due to degeneracies with HCN in the WFC3 bandpass as discussed below (also see MacDonald and Madhusudhan, 2017).

The other molecules only have weak constraints, largely owing to the lack of significant unique features in the observed spectral range. The spectral features of the molecules in the observed wavelength range are shown in fig. 5.3. HCN has a minor feature at $\sim 1.55\mu$m, mostly overwhelmed by the NH_3 and H_2O (MacDonald and Madhusudhan, 2017) and as such allows for only an upper-limit of $X_{HCN} < 10^{-2.8}$ that is still consistent with the true value. The C_2H_2 has very weak features so there is almost no constraint on its abundance $X_{C_2H_2} < 10^{-2}$. In principle, CO and CO_2 have strong features in the Spitzer 4.5 μm IRAC bandpass but are degenerate with each other for the same reason, as discussed below. As such their abundances are also relatively unconstrained. Finally, the spectral resolution and precision of the data also limit the capability of the retrieval in constraining the abundances.

CO_2 Degeneracy

As alluded to above we find CO and CO_2 to be degenerate given the single IRAC 4.5 μm band with significant features. The CO and CO_2 abundances show an "L"-shaped correlation, as also seen in previous studies Line *et al.* (2016); Madhusudhan *et al.* (2011a). The absorption in the 4.5 μm band can be explained by either a high CO and low CO_2 or vice versa or a combination of both, leading to the L-shaped behaviour. The weak constraints on the species are also contributed by the large uncertainty in the 4.5 μm Spitzer IRAC data point. The detection significance of CO or CO_2 individually is weak, but the joint detection significance of having either one of CO or CO_2 is over 10σ. With our chemical equilibrium model (chapter 3) and full equilibrium calculations for similar planets (Moses *et al.*, 2011; Moses *et al.*, 2013), we find that the H_2O abundance always exceeds the CO_2 abundance, regardless of the C/O ratio and metallicity. Hence, when considering hot Jupiter retrievals, we impose the constraint that the H_2O abundance must exceed the CO_2 abundance, as suggested in previous studies (Heng and Lyons, 2016; Madhusudhan, 2012). This partially breaks the degeneracy and allows for more chemically realistic mixing fractions. It should be

noted that this assumption can only be made when considering H_2 rich atmospheres. This allows for tighter constraints on the other species, and the temperature can be retrieved more accurately.

Abundance-T_{100mb} Degeneracy

The molecular abundances are generally correlated with the retrieved temperature (see fig. 5.5). A higher abundance raises the opacity, and hence emission is seen to occur from higher in the atmosphere. This increase in the chemical abundance can be compensated by a subsequent alteration in the temperature profile, as long as the temperature at which the emission occurs in the atmosphere remains the same. Given the observational uncertainties in our dataset, we find the abundances and T_{100mb} to lie on a line of degeneracy (see fig. 5.5). We see from fig. 5.6 that in the WFC3 bandpass there is no significant deviation between the retrieved and true models. However, as the spectrum proceeds away from the WFC3 spectral range the uncertainty in the retrieved flux ratio increases due to the lack of high precision data. Observations at other wavelengths in future with instruments such as JWST may be able to better constrain the flux ratio and hence the atmospheric properties more effectively. The Spitzer IRAC photometric points at 4.5, 5.8 and 8 μm channels may also be used to address the problem, however, these points often come with larger associated errors and difficult systematics (Diamond-Lowe *et al.*, 2014) making it difficult to do so.

5.3.2 Retrieved $P-T$ Profile

Similar to the chemical abundances the parameters of the P-T profile are also retrieved at high accuracy. The retrieved posterior distributions of the parameters and their estimated values are shown in fig. 5.5. The true values of all the parameters are recovered to within the 1-σ uncertainties. The retrieved temperature profile along with the confidence limits is shown in fig. 5.7, and is in agreement with the true profile within 1σ for almost all pressures. The fit is particularly good at $\simeq$1 mbar-1 bar, with an error of only $\lesssim$50 K on average between the median profile and the true value. The photospheric temperature is also well constrained with an average uncertainty on T_{100mb} to be $\sim$110 K. The retrieval captures the temperature gradient near the photosphere accurately, unsurprising as this is where the bulk of the spectrum is generated. Naturally, the constraints on the temperature are weaker in the lowest and highest regions of the atmosphere that are inaccessible to the observations.

5.3.3 Radiative-Convective Disequilibrium

We now use the retrieved posterior distributions of the P-T profiles to constrain deviations from radiative-convective equilibrium. This is done by considering the chemical compositions corresponding to the retrieved P-T profiles and deriving the corresponding P-T profiles in radiative-convective equilibrium using the GENESIS self-consistent model. This provides a test of our model's ability to infer disequilibrium in the temperature, as the simulated data set used for the retrieval was in thermal equilibrium. The GENESIS model was run for 1000 randomly sampled retrieved chemical abundances from the posterior, and calculating the equilibrium $P-T$ profile this chemistry.

Fig. 5.8 shows both the retrieved and the radiative-equilibrium $P-T$ profiles, along with the actual $P-T$ profile of the simulated data. All lie within 1σ of each other, particularly in the vicinity of $\tau_\nu = 1$. Hence with the combination of our self-consistent and our retrieval algorithm we can conclude that our simulated planet is in equilibrium at all modelled pressures. This is quite a significant result, as this allows one to investigate whether a retrieved profile is consistent with 1-D radiative-convective equilibrium throughout the atmosphere, and if not, quantify where in the atmosphere the temperature deviates.

5.3.4 Chemical Disequilibrium

The deviation of the retrieved model atmosphere from chemical equilibrium was calculated by holding the temperature profiles fixed from the retrieval and determining the equilibrium chemical abundances. Chemical deviation provides a handle on the mixing at play in the atmosphere, e.g. from winds to vertical mixing, and perhaps even the photo-dissociation for some species. 1000 randomly sampled retrieved values were used, and the theoretical equilibrium mixing fractions calculated as a function of the pressure for 100 layers, evenly spaced in log(P) ranging from 100-10^{-5} bar.

Fig. 5.9 shows the mixing fractions used to generate the spectrum and the retrieved chemical abundances on the simulated data set. We find that all of our retrieved values are consistent with the black line used to generate the model spectrum. The chemical equilibrium values are also shown in fig. 5.9 for the retrieved $P-T$ profiles, and gives us a handle to the disequilibrium present on a planet. We chose our simulated atmosphere to be out of chemical equilibrium (but in radiative equilibrium) given that equilibrium abundances were too low for many of the species in order for them to be constrained effectively. The higher abundances also highlight any degeneracies

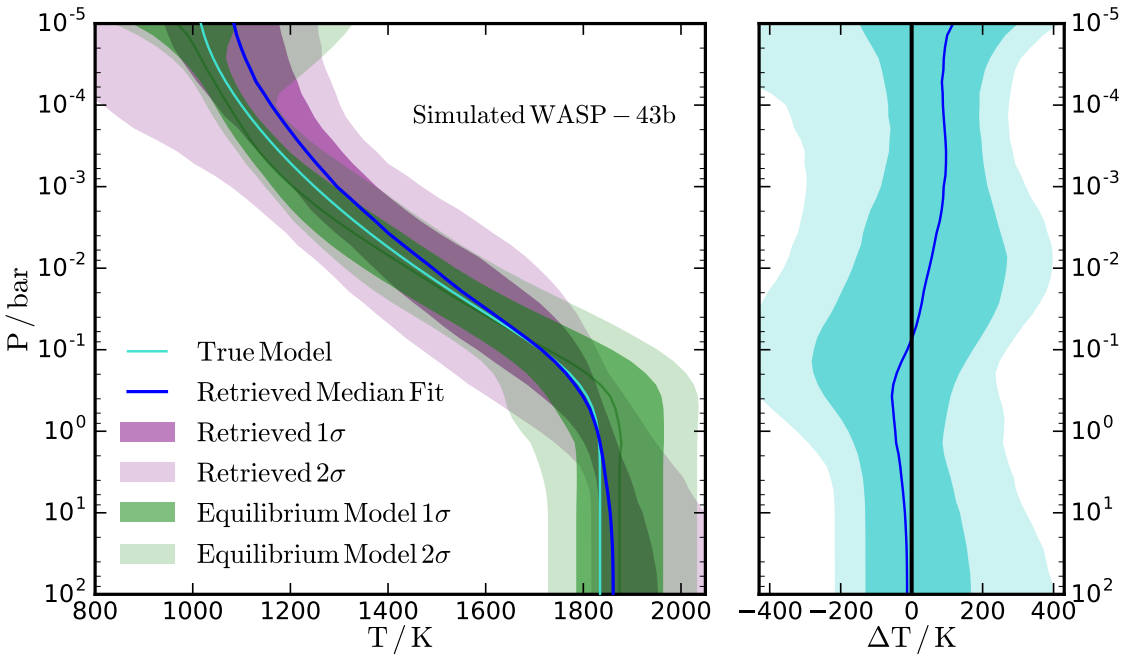

Fig. 5.8 Retrieved $P-T$ profiles (purple) and theoretical radiative equilibrium calculations performed with GENESIS (in green) for the dayside of WASP-43b shown on the left. The cyan line indicates the $P-T$ profile of the simulated data. The right hand side shows the temperature difference between the median retrieved and equilibrium models, and the associated 1 and 2 σ confidence contours. The retrieval's solution was used to run the equilibrium model with retrieved chemistry, to determine the radiative-convective profile and hence the equilibrium profile. The spread in the equilibrium model's $P-T$ profile is due to the chemical variations in the retrieval's solution. The sodium and potassium abundances were set to solar compositions for the equilibrium calculations.

that may be present between molecules in the retrieval and demonstrate HyDRA's effectiveness in determining chemical disequilibrium. The predicted CH_4, NH_3 and HCN abundances decrease with height in the atmosphere, whereas the CO_2 mixing fraction remained reasonably constant. It was however at all points less than the H_2O abundance, justifying our assumption that the CO_2 abundance should not exceed H_2O. We can clearly see from the simulated retrieval that the model planet's spectrum is not in equilibrium.

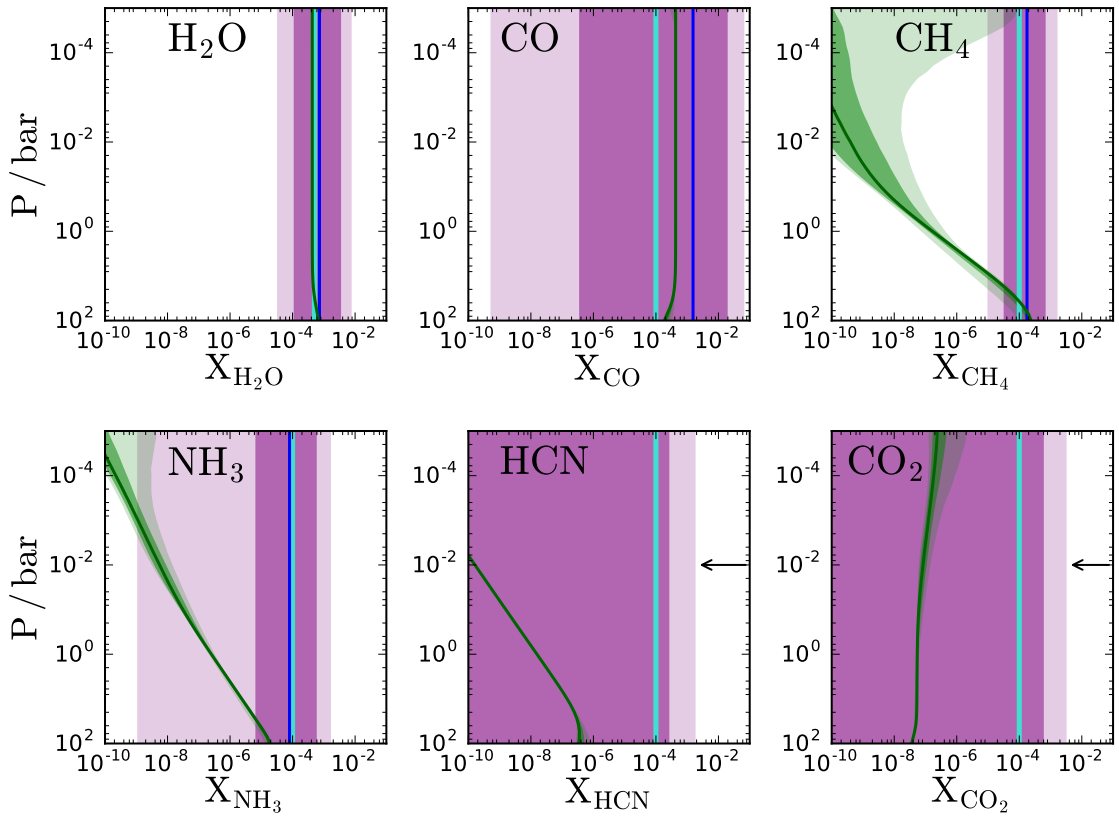

Fig. 5.9 Comparison of retrieved chemical abundances and theoretical chemical equilibrium models for simulated data. The cyan line indicates the actual mixing ratio used to generate the spectrum that was retrieved, the dark and light purple contours show the 1 and 2σ errors for the retrieval respectively, and the dark and light green the corresponding equilibrium mixing fractions for each species. Where a molecule was detected in the retrieval, the median fit value is also plotted in blue, and where no abundance could be constrained, the 2σ upper bound is shown with an arrow. 1000 randomly sampled retrieval points were used, and 100 layers taken for the model atmosphere. The $P-T$ profile was fixed for each random sample from the posterior.

5.4 Results

We now apply HyDRA to retrieve the dayside atmospheric properties of WASP-43b using observed spectra. Kreidberg *et al.* (2014) and Stevenson *et al.* (2014) reported detailed retrieval analyses for WASP-43b and reported constraints on its H_2O abundance, *P-T* profile, and day-night energy circulation. In the present work, we use the observed thermal emission spectra from these previous works and revisit the constraints on the atmospheric properties using HyDRA. In addition to previous constraints we specifically investigate the deviations of the derived compositions and *P-T* profile from chemical and radiative-convective equilibrium. We take the radius of the planet to be 0.93 R_J, with a semi-major axis of 0.014 A.U. and a log(g) = 3.7 (taken from exoplanets.org).

Following previous works we consider high-precision HST and Spitzer data for the present analysis. The WFC3 data, in the 1.1-1.7 μm range, were obtained from Kreidberg *et al.* (2014) and two Spitzer IRAC photometric points, at 3.6 μm and 4.5 μm were obtained from Blecic *et al.* (2014). The model parameters, as described in section 5.2, include mixing ratios of the prominent chemical species (H_2O, CH_4, NH_3, CO, HCN, CO_2 and C_2H_2) and the parameters of the *P-T* profile. The retrievals, carried out using the nested sampling algorithm, used 4000 live samples and included over 10^6 model evaluations per retrieval. The detection significances for the chemical species were carried out using nested model comparisons (see e.g. MacDonald and Madhusudhan, 2017), resulting in $\sim 10^7$ model evaluations overall. Section 5.2.7 has further information on the Bayesian model comparisons and describes how we evaluated the detection significance of a species given the evidence $\mathcal{Z}$ for each model with and without the relevant species. The results of the retrieval are shown in figs. 5.10 and 5.11 with deviations from equilibrium given in figs. 5.12 and 5.13.

5.4.1 Constraints on Chemical Abundances

We report strong constraints on the abundance of H_2O which is detected at 8-σ significance. The constraints on the chemical abundances of all species considered are shown in fig. 5.10. The volume mixing ratio of H_2O is retrieved to be $\log X_{H_2O} = -3.54^{+0.82}_{-0.52}$ is consistent with that of Kreidberg *et al.* (2014) within 1-σ, and is consistent with expectations from a solar abundance atmosphere at the temperature of WASP-43b. We also note the H_2O-T_{100mb} degeneracy in fig. 5.10 as seen for our simulated data and discussed in section 5.3.1. The corresponding spectral fit is shown in fig. 5.11. The

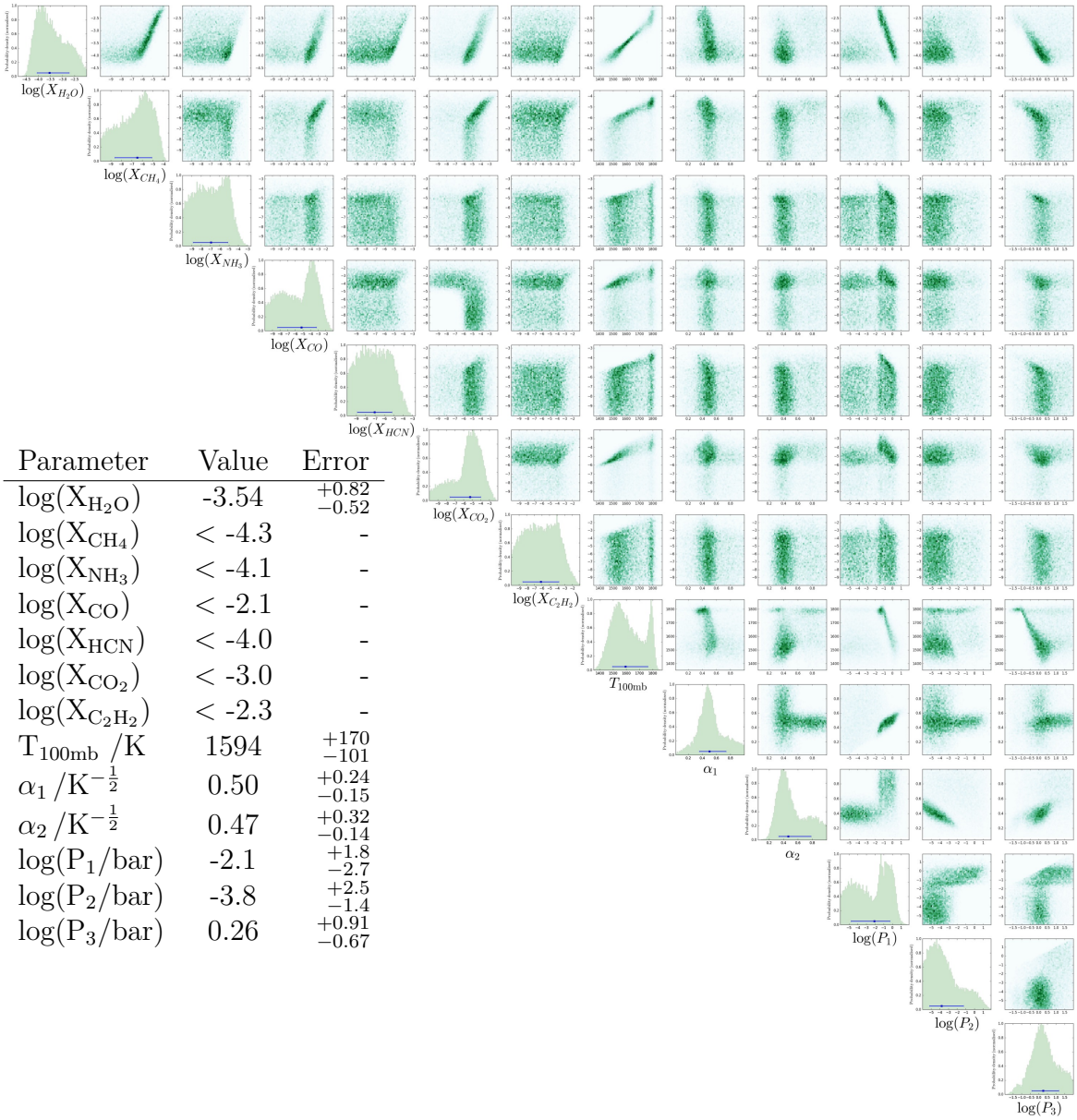

Parameter	Value	Error
$\log(X_{H_2O})$	-3.54	$^{+0.82}_{-0.52}$
$\log(X_{CH_4})$	$<$ -4.3	-
$\log(X_{NH_3})$	$<$ -4.1	-
$\log(X_{CO})$	$<$ -2.1	-
$\log(X_{HCN})$	$<$ -4.0	-
$\log(X_{CO_2})$	$<$ -3.0	-
$\log(X_{C_2H_2})$	$<$ -2.3	-
T_{100mb} /K	1594	$^{+170}_{-101}$
α_1 /K$^{-\frac{1}{2}}$	0.50	$^{+0.24}_{-0.15}$
α_2 /K$^{-\frac{1}{2}}$	0.47	$^{+0.32}_{-0.14}$
$\log(P_1/bar)$	-2.1	$^{+1.8}_{-2.7}$
$\log(P_2/bar)$	-3.8	$^{+2.5}_{-1.4}$
$\log(P_3/bar)$	0.26	$^{+0.91}_{-0.67}$

Fig. 5.10 Marginalised posterior distribution of WASP-43b's atmosphere under emission spectroscopy. The data set used for the retrieval was obtained from Kreidberg *et al.* (2014) and considers the Hubble WFC3 and Spitzer 3.6 μm and 4.5 μm channels. We considered 7 molecular volatile species and six parameters describing the $P-T$ profile of the atmosphere. 4000 evenly spaced points in wavelength were used to generate spectra between 1 μm and 5.5 μm, with 4000 live points used for the nested sampling and 100 atmospheric layers, with over 10^6 models run in total. The histograms and relative correlations between the retrieval parameters is shown on the top right hand side. The table shows the retrieved values and their associated 1σ error bars. The upper limits where shown are 2σ upper bounds.

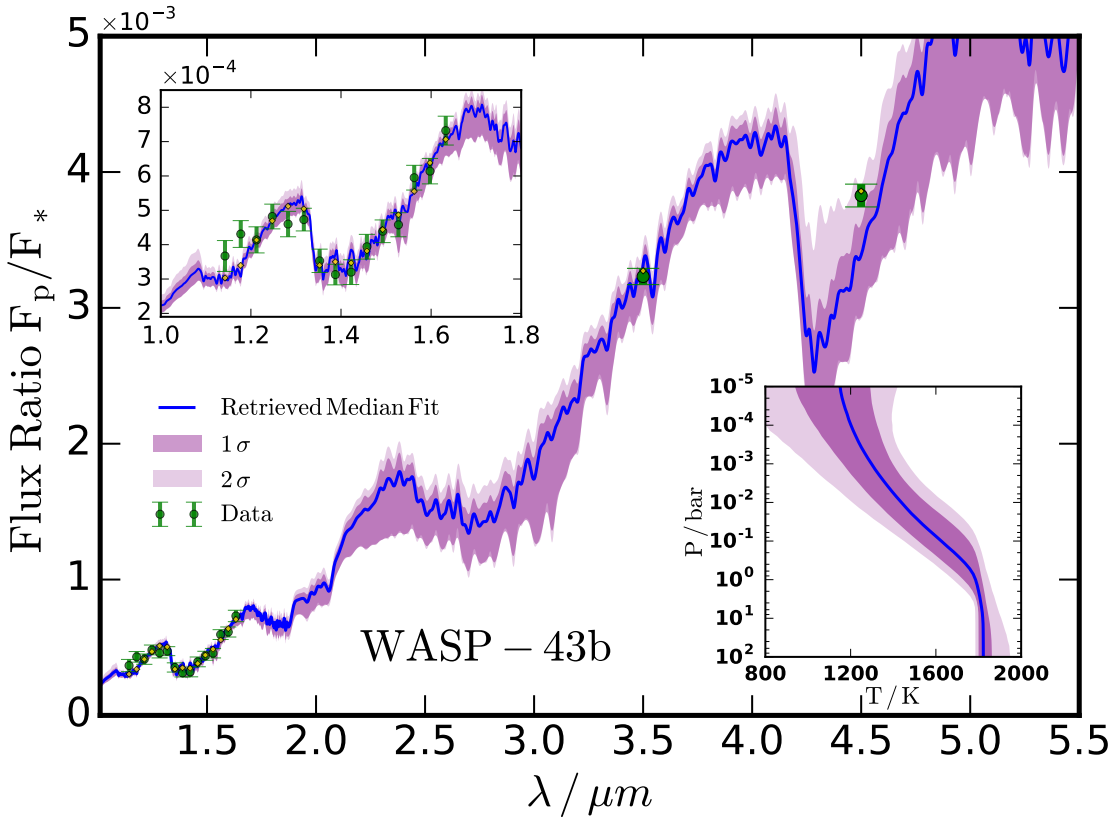

Fig. 5.11 Retrieved emission spectrum of WASP-43b, showing the median fit spectrum and the 1 and 2σ uncertainty. The green markers indicate the data set and the corresponding error bars, and the yellow diamonds the binned median model. The top left inset shows the WFC3 bandpass and the corresponding data points and spectral fit. The bottom right inset shows the retrieved $P-T$ profile and the corresponding retrieved error on the temperature.

strong constraint on the H_2O abundance is made possible by the strong H_2O features in the WFC3 bandpass.

We also report a joint detection of CO or CO_2 in the atmosphere. The constraint on these two species arise from the strong features of both species in the Spitzer 4.5 μm bandpass. This also leads to a degeneracy between the two molecules due to a lack of strong features from either molecule elsewhere in the observed spectral range. The degeneracy is apparent in the "L"-shaped feature in the CO-CO_2 correlation plot in fig.5.10. Neither CO nor CO_2 have individual significant detection evidences (1.3 and 2.1 σ, respectively), however we do find that the combined significance CO/CO_2 is 7.9σ. This amounts to a strong detection of carbon chemistry in WASP-43b.

We do not find conclusive evidence for any of the remaining species considered with only upper-limits retrieved. CH_4, NH_3 and HCN are constrained to be less than $\sim 10^{-4}$ at 2-σ confidence; they are ostensibly present in smaller quantities than can be retrieved with the current data. As discussed below, equilibrium calculations would also predict low abundances of these species given the temperature. Therefore, their non-detections are perhaps unsurprising. No meaningful constraint is obtained for C_2H_2, as its cross-section is too weak or has very low abundance and hence is dominated by other species in the WFC3 and Spitzer bandpasses.

5.4.2 Retrieved $P-T$ Profile

The observed spectrum provides robust constraints on the P-T profile of the dayside atmosphere. The retrieved $P-T$ profile along with confidence contours is shown on the inset in fig. 5.11. The results show the clear absence of a temperature inversion in the observable dayside atmosphere, in agreement with Kreidberg *et al.* (2014) and Stevenson *et al.* (2014). The strong absorption features observed in the spectrum, both in the WFC3 and Spitzer 4.5 μm bands, constrain the temperature profile to be monotonically decreasing outward in the observable atmosphere. The derived profile also shows an isothermal temperature structure below the photosphere which is characteristic of irradiated hot Jupiters (e.g. Burrows *et al.*, 2008; Fortney *et al.*, 2008).

The data also provide a strong constraint on the photospheric temperature. The temperature at 100 mbar is constrained to be 1594^{+170}_{-101} K, which is in nearly exact agreement with Kreidberg *et al.* (2014). The derived photospheric temperature is also consistent with the equilibrium temperature without efficient redistribution ($\sim$1635 K), which is also indicated by thermal phase curve observations (Stevenson *et al.*, 2014) as discussed below. The most stringent constraint on the temperature is at $\sim$1 bar, near to where the photosphere ($\tau_\nu \sim 1$) is located. The uncertainty on the temperature

increases away from the photosphere on either side and is highest on the two ends of the profile at pressures which are inaccessible to observations as expected.

5.4.3 Radiative-Convective Disequilibrium

Using HyDRA we are able to constrain the layer-by-layer deviation of the temperature profile from radiative equilibrium. For hot Jupiters, the observable atmosphere in equilibrium is dominated by radiative energy transport. However, non-equilibrium processes such as those caused by atmospheric dynamics (e.g. winds) could drive the atmosphere out of radiative equilibrium. As discussed in section 5.2 one of the primarily capabilities of HyDRA is to constrain the effects of such properties on the layer-by-layer temperature profile. This is achieved by comparing the retrieved distribution of *P-T* profiles with those obtained in radiative-convective equilibrium for the same chemical compositions obtained from the retrieval. As discussed in section 5.2 the self-consistent models are computed using GENESIS code (chapter 3) which has been developed in the same framework as the retrieval code. The constraints on the temperature differentials (ΔT) are evaluated based on 1000 randomly sampled points from the posterior distributions of the retrieved *P-T* profiles and their corresponding compositions.

We report the dayside atmosphere of WASP-43b to be in radiative equilibrium with low day-night energy redistribution. Figure 5.12 shows the constraints on ΔT as a function of pressure and the distributions of both the retrieved and equilibrium *P-T* profiles showing excellent agreement. At all points in the atmosphere the ΔT is consistent to zero within 1-σ, implying concordance between the retrieved and equilibrium *P-T* profiles. Additionally, the observed agreement is achieved with a low day-night energy redistribution in the equilibrium models. This is also consistent with the inefficient redistribution suggested by Stevenson *et al.* (2014) based on the large day-night temperature contrast observed with thermal phase curves of the planet. The transition to the isotherm in the lower atmosphere occurs at $\sim$ 1bar, in agreement with what would be expected in equilibrium. This is the region of the atmosphere where the optical depth exceeds 1 and hence the photons become diffusive, which leads to a profile that does not vary with the pressure. This isothermal structure in the lower atmosphere is consistent with predictions from self-consistent equilibrium models of highly irradiated hot Jupiters (Burrows *et al.*, 2008; Fortney *et al.*, 2008). As shown in these studies, the transition from the isothermal radiative structure to a convective adiabat occurs much deeper in the atmosphere, at pressures of $\gtrsim$100 bar, which are well below the observable atmosphere. As such, for our equilibrium model we assumed

the internal flux of the planet to be negligible as it only effects the deep adiabat which is not accessible to current observations.

Future observations in other spectral regions will be able to further constrain the temperature profile and deviations from radiative equilibrium. We also assume that the sodium/potassium abundance is solar, and that no other visible absorbers are present in any significant quantities. Visible absorbers such as TiO are likely to be present only in small quantities, as otherwise thermal inversions would occur in the photosphere at ∼0.1-0.01 bar (see chapter 4). These models also assume solar composition Na/K, given that the retrieved H_2O abundance was consistent with solar. Future compositional estimates on visible absorbers can provide more definitive inputs to the equilibrium models.

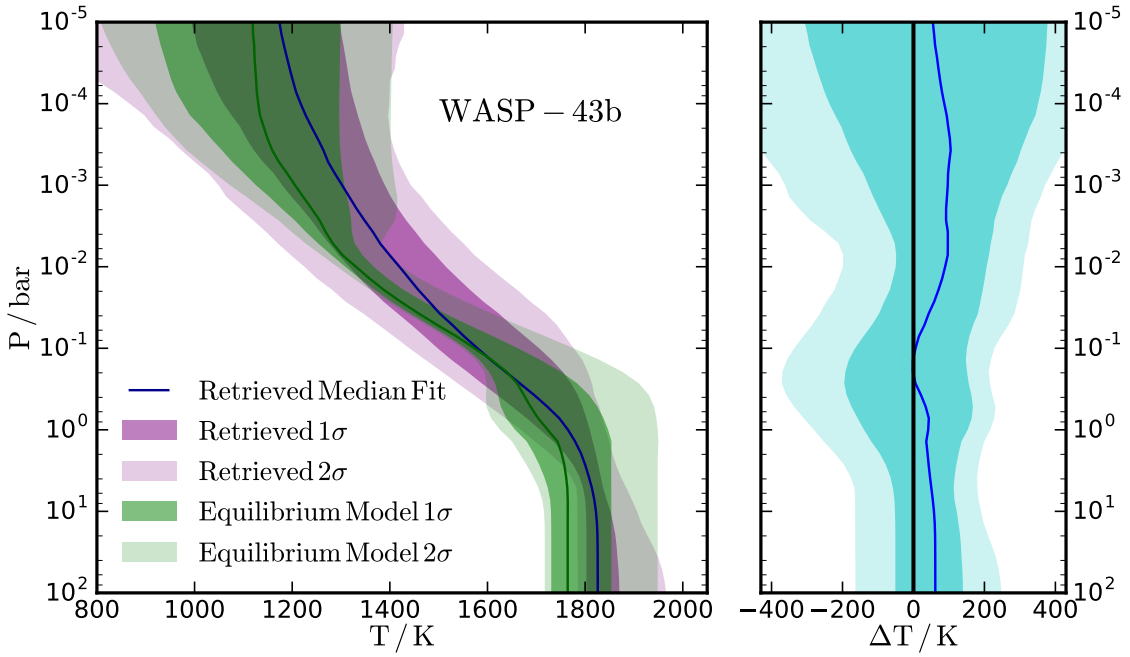

Fig. 5.12 Deviation from 1-D radiative-convective equilibrium present on WASP-43b. The left hand side shows the retrieved $P-T$ profiles in purple and theoretical radiative equilibrium calculations performed with GENESIS in green, with the chemistry fixed to the retrieved values. The right hand side shows the difference between the retrieved and the equilibrium temperatures, with the darker and lighter shade representing the 1 and 2σ uncertainties respectively. 1000 randomly sampled points from the retrieval were used to generate the equilibrium models and the sodium and potassium abundances (not retrieved) were set to solar compositions.

5.4.4 Chemical Disequilibrium

Here we investigate the possible deviation of the retrieved chemical abundances from thermochemical equilibrium. To do so, we compare the retrieved distributions of the chemical abundances, with their corresponding *P-T* profiles, against those obtained assuming chemical equilibrium for the same *P-T* profiles. The approach is discussed in section 5.2. The retrieved and equilibrium mixing ratios for the prominent chemical species are shown in fig. 5.13. The retrieved H_2O abundance is consistent with that obtained in thermochemical equilibrium with the assumption of solar composition. It is important to note that even in chemical equilibrium the H_2O abundance is expected to be relatively uniform with depth, as assumed in the retrievals, unlike some other species. This is owing to the fact that at high temperatures, with a solar abundance C/O ratio of 0.5, H_2O is expected to be the dominant carrier of oxygen throughout the observable atmosphere (Madhusudhan, 2012; Moses *et al.*, 2013).

While only upper-limits are available for molecules besides H_2O we nevertheless find the constraints to be consistent with equilibrium expectations. Furthermore, with the exception of H_2O and CO, the remaining species are also expected to be present in small quantities in equilibrium. For example, the CH_4 abundance in equilibrium decreases outward in the atmosphere with decreasing pressure and is well below the observed upper-limit in the photosphere. In principle, strong vertical mixing could dredge up a higher abundance of CH_4 from deeper layers of the atmosphere (e.g. Moses *et al.*, 2013). However, out current upper-limit on CH_4 suggests that the corresponding quench pressure level from where such dredge up might occur could not be greater than $\sim$10 bar. Generally, the retrieved CH_4 abundance $\lesssim 10^{-5}$, is in agreement with our chemical equilibrium predictions. Equilibrium chemistry suggests that the NH_3 and HCN should be present in significant amounts only in the deeper layers of the atmosphere, greater than 1 bar in the atmosphere, below which the atmosphere is opaque to radiation ($\tau_\nu >> 1$). They can also be dredged up from the vertical mixing into the photosphere (MacDonald and Madhusudhan, 2017; Moses *et al.*, 2013) though no strong evidence for the same is seen here.

5.5 Discussion and Summary

In this study we introduce HyDRA, a new atmospheric retrieval framework for emission spectroscopy of exoplanets. In addition to the functionalities of existing retrieval codes, HyDRA is geared towards constraining deviations of retrieved solutions from chemical and radiative equilibrium. Emission spectroscopy allows probing the temperature

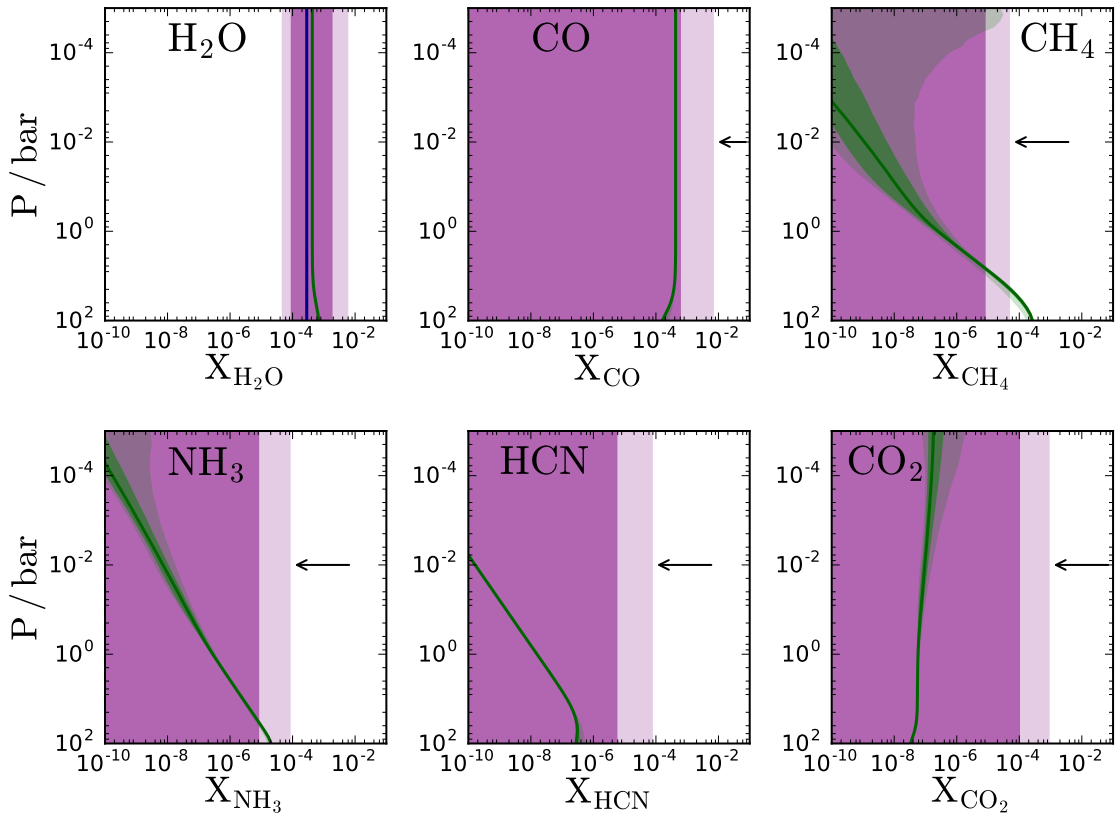

Fig. 5.13 Retrieved chemical abundances and theoretical chemical equilibrium calculations performed with GENESIS. The dark and light purple contours show the 1 and 2σ errors for the retrieval respectively, and the dark and light green the corresponding thermochemical equilibrium mixing fractions with the $P-T$ profile fixed to the retrieved values. Where a molecule was detected using our Bayesian analysis, the median fit value is also plotted in blue, and where there was no significant detection, the 2σ upper bound is shown by an arrow. 1000 randomly sampled retrieval points were used, and 100 layers taken for the model atmosphere. The atomic abundances were kept at solar values for C, O and N during the equilibrium calculations.

structure and chemical composition of the dayside atmospheres of transiting exoplanets. In the present work, we develop a common framework to operate a state-of-the-art retrieval algorithm in tandem with self-consistent equilibrium models of thermal emission from exoplanets.

We test HyDRA using simulated data of the hot Jupiter WASP-43b and demonstrate accurate retrieval of the abundances and temperature structure, along with deviations from equilibrium. Consistently with previous work in the literature, we find degeneracies between the retrieved abundances of carbon monoxide and carbon dioxide given the limited observations currently available. This degeneracy was partially broken by imposing the constraint that the H_2O abundance must exceed the CO_2 abundance, as this is always the case for H_2-rich atmospheres (Heng and Lyons, 2016; Moses *et al.*, 2011), but the retrieved abundance is still degenerate with CO. We also see a degeneracy between abundances and the photosphere temperature, where we parametrise the temperature as $T_{100\mathrm{mb}}$. This degeneracy may be broken with sufficient spectral coverage, particularly data in regions where the continuum opacity is probed (e.g 2-2.5 μm). With the future development of instruments that do so, this should be resolved to give us the tightest constraints on the chemistry present on exoplanets.

Whilst previous work has already been done in this field, our model combines several modules from our 1-D self-consistent forward model, GENESIS (chapter 3), such as a similar radiative transfer scheme (which has been tested against the self-consistent solution in section 5.2.4) and identical molecular cross-section calculations. The Kurucz stellar model and the line lists for the opacity calculations are also shared. All of this means that we are able to compare quantitatively the difference between retrieved and equilibrium models for a given data set of a planet, and constrain the chemical and radiative-convective disequilibrium. The latter in particular is novel and allows for the precise determination of the deviation in the temperature profile from what is expected for a 1-D model. This opens up many avenues to expand upon our current understanding, and improve our modelling techniques.

We demonstrate our retrieval algorithm on the emission spectrum of WASP-43b, with one of the most precise observations of exoplanets under emission to date (Kreidberg *et al.*, 2014), as a demonstration of our code. We find that the temperature structure of WASP-43b shows agreement with our radiative-convective and chemical equilibrium model. By taking the chemistry to be that which was retrieved, we are able to conclude that this planet's temperature profile is consistent with our forward model. In running our model we assume there is little stellar flux redistribution over to the nightside, and find results in agreement with Stevenson *et al.* (2017).

The volatile abundances obtained reveals that the planet is most likely close to solar composition water and provides some constraints on the CO abundance. The C/O ratio is likely to be less than 1, particularly given the high water abundance observed and our chemical equilibrium calculations in section 5.4. The other species have not been detected to any high significance. The $P-T$ profile indicates that there is no thermal inversion present in the region of $\tau \sim 1$. The 100 mbar temperature is constrained to be 1594^{+170}_{-101} K, in agreement with the result from Kreidberg *et al.* (2014). The chemical equilibrium analysis indicates that the planet is within chemical equilibrium given the retrieved temperature, albeit with large uncertainties on the results, as lower abundances do not significantly affect the spectrum and hence cannot be retrieved.

HyDRA is a new emission spectroscopy retrieval algorithm that couples a retrieval capability with an equilibrium model to constrain disequilibrium processes. It includes high temperature molecular data along with the most advanced radiative transfer techniques and the latest statistical methods. There is much excitement over the future of the field with new and upcoming observations with VLT, JWST, ELT and many others, and the work presented here prepares us for this new era of atmospheric observations. This will allow for even deeper insights into the structure and composition of exoplanetary atmospheres. HyDRA used for emission spectroscopy retrieval in conjunction with our self-consistent GENESIS model represents a new development in the field and allows constraints on departures from 1-D equilibrium in exoplanetary atmospheres, a vital step towards detailed characterisation of atmospheric processes in exoplanets.

Chapter 6

On the effect of H- in Ultra-hot Jupiters

"All we have to decide is what to do with the time that is given us."
- J. R. R. Tolkien

This chapter describes my recent work on retrievals of ultra-hot Jupiters, with dayside temperatures in excess of 2500 K. I modified the HyDRA retrieval algorithm to be able to retrieve such hot atmospheres through the inclusion of thermal dissociation of a number of species and the addition of H- opacity. This was tested by retrieving the emission spectrum of WASP-18b.

6.1 Introduction

Recent observations of thermal emission spectra of hot Jupiters have yielded some of the most precise data to date. Such data have allowed for constraints on the chemical composition and temperature profile of the dayside atmospheres thanks to instruments such as the Hubble Space Telescope's Wide Field Camera 3 (HST WFC3) spectrograph (Haynes *et al.*, 2015; Stevenson *et al.*, 2014). Through these observations a new class of irradiated giant planets, that of ultra-hot Jupiters, has emerged. These planets have dayside temperatures exceeding $\sim$ 2500 K owing to the strong incident stellar flux and their close in orbit. Observations of such objects have revealed that many of these atmospheres show no significant features in the WFC3 band (Kreidberg *et al.*, 2018; Sheppard *et al.*, 2017). With such featureless spectra constraints on species such as H_2O have been minimal, and only upper limits have been placed. Various theories have been put forward to explain the featureless spectra and thus lack of an H_2O

feature. Madhusudhan (2012) and Moses *et al.* (2013) proposed that a super-solar atmospheric C/O ratio can deplete the atmosphere of H_2O. This is because the oxygen preferentially binds to form CO when C/O $\gtrsim$1 with little left over to form H_2O, thus reducing the overall abundance by many orders of magnitude. This in turn leads to very weak features in the WFC3 spectrum. A high C/O ratio has been used to explain muted H_2O features in many hot Jupiters, both under transmission and emission (e.g. Madhusudhan *et al.*, 2014b; Pinhas *et al.*, 2019; Sheppard *et al.*, 2017).

Recent work on equilibrium models of ultra-hot Jupiters has revealed that the dissociation of species such as H_2O and the formation of H- may play an important role in determining the emergent spectrum (Arcangeli *et al.*, 2018; Lothringer *et al.*, 2018; Parmentier *et al.*, 2018). The latter is in fact the dominant source of opacity in some stars (Bell and Berrington, 1987; Wishart, 1979). The H- possesses a strong and largely featureless cross section in the blue end of the HST WFC3 band (1.1-1.7 μm). This means that the H- opacity may overwhelm the H_2O absorption in the WFC3 band, resulting in muted H_2O features. In addition, thermal dissociation of H_2O would act to further mute the H_2O feature in this band at such high temperatures. Very high temperatures ($\gtrsim$2000 K) are required for this to be significant (Arcangeli *et al.*, 2018; Kreidberg *et al.*, 2018; Lothringer *et al.*, 2018; Parmentier *et al.*, 2018) but planets such as WASP-121b, WASP-18b, WASP-12b, Kepler-13Ab and KELT-9b have equilibrium temperatures in excess of $\sim$2400 K and thus this effect may potentially be important. On the other hand, some ultra-hot Jupiters do show strong H_2O absorption which remains a mystery (Beatty *et al.*, 2017b; Parmentier *et al.*, 2018).

Here we retrieve the spectra of a known ultra-hot Jupiter, WASP-18b, by exploring the above proposed theories. Previous retrievals of WASP-18b have proposed a high C/O ratio as an explanation for the observed spectrum, which does not possess strong H_2O features in the WFC3 band (Arcangeli *et al.*, 2018, 2019; Sheppard *et al.*, 2017). On the other hand equilibrium models of this planet propose H- and dissociation as a potential explanation for this (Arcangeli *et al.*, 2018). General circulation models have also explored the phase curve of WASP-18b (Arcangeli *et al.*, 2019). In this work we retrieve all three previous HST WFC3 datasets for this planet (Arcangeli *et al.*, 2018, 2019; Sheppard *et al.*, 2017) along with the Spitzer photometric observations between $\sim$3-10 μm (Maxted *et al.*, 2013; Nymeyer *et al.*, 2011; Sheppard *et al.*, 2017).

We explore all of the various proposed methods to explain the spectrum of WASP-18b. We constrain the C/O ratio of the atmosphere by retrieving the chemical abundances of the prominent carbon bearing and oxygen bearing species, such as H_2O, CO and CO_2. Our parametric temperature profile explores isothermal as well as

inverted and non-inverted profiles to determine the best fit to the observations. We additionally include the effect of thermal dissociation and H- opacity in our model to explore the effect on the retrieved parameters both separately and in tandem. This presents the first time that H- and dissociation have been included into retrievals and we therefore are able to open up a new class of ultra-hot atmosphere retrievals for further exploration.

In what follows, we describe the methods used to calculate the thermal dissociation of various species and determine the H- cross section. This is followed by the results for each of the retrievals conducted with and without H- and dissociation. We discuss the retrieved parameters and compare and contrast with each retrieval and previous work. Finally we discuss the conclusions and future directions.

6.2 Methods

Here we describe the methods used for the retrieval of the emission spectra of ultra-hot giant planets. We use the HyDRA code (chapter 5) as a basis for the retrieval of WASP-18b, an exoplanet with an equilibrium temperature of ~ 2400 K (assuming full redistribution). The HyDRA retrieval framework has been further extended to model the atmospheres of ultra-hot Jupiters by the inclusion of thermal dissociation and H- opacity. Previous studies (e.g. Lothringer *et al.*, 2018; Parmentier *et al.*, 2018) have shown the importance of these effects at temperatures $\gtrsim$2000 K. We therefore include H- and dissociation to study their importance, and report the first retrievals with H- opacity and dissociation included.

Photospheric thermal inversions manifest as emission features in the emergent spectrum due to absorption from the various species present in the atmosphere. Through these features we are able to constrain the pressure-temperature ($P-T$) profile of the atmosphere. Previous retrievals and self-consistent models of WASP-18b show the presence of a thermal inversion (or stratosphere) in the dayside atmosphere of the planet (Arcangeli *et al.*, 2018; Sheppard *et al.*, 2017). In our retrieval the $P-T$ profile has been parameterised using the method in Madhusudhan and Seager (2009) and chapter 5. The 6 free parameters which parameterise the $P-T$ profile freely allow for inversions in the atmosphere. Through these parameters we are able to explore a wide range of inverted, non-inverted and isothermal profiles to best fit the observations.

In addition, the latest high temperature molecular line lists have been used to generate the molecular opacity from the prominent species. These species include H_2O, CO, CO_2, TiO and VO, which are expected in the atmospheres of such ultra-hot H_2

dominated planets. The line list for each species has been obtained from the HITEMP and EXOMOL databases (Rothman *et al.*, 2010; Tennyson *et al.*, 2016) as discussed in chapter 2. Each molecular line has been spectrally broadened by temperature and pressure resulting in a Voigt profile as a function of wavelength as discussed in chapter 2. The opacity due to the presence of H- has been calculated using the work by John (1988) and Wishart (1979) (see section 6.2.2).

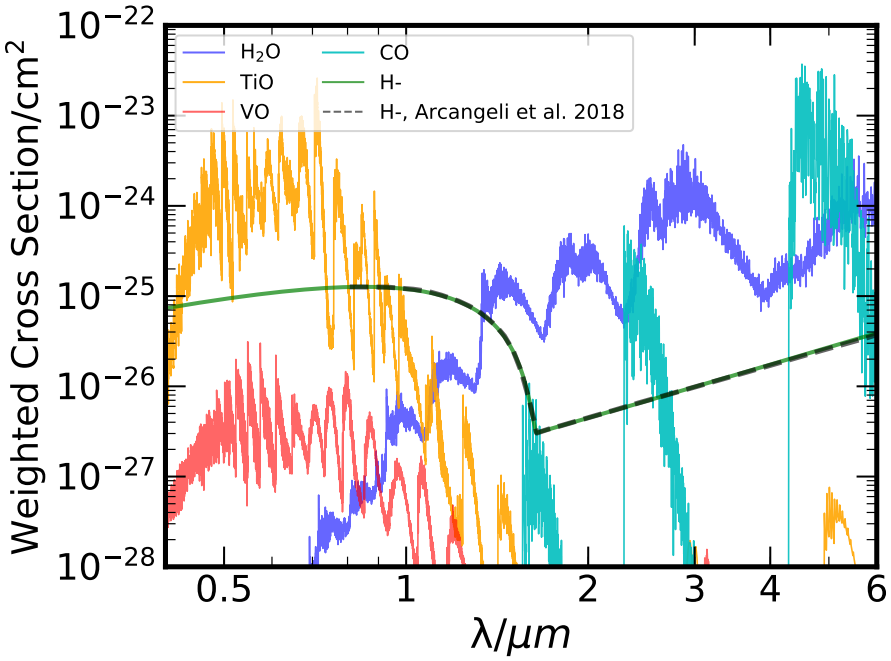

Fig. 6.1 Abundance weighted cross sections for the prominent species in our retrieval at a temperature of 2900K and 0.33 bar pressure. The abundances have been calculated from the dissociation model by Parmentier *et al.* (2018) and the cross sections derived in chapter 2. The H- opacity is calculated in section 6.2.2. We also show the abundance weighted H- cross section from Arcangeli *et al.* (2018).

6.2.1 Thermal dissociation

Ultra-hot giant planets have temperatures in excess of 2500 K, where many molecular species may begin thermally dissociating (Arcangeli *et al.*, 2018; Lothringer *et al.*, 2018; Parmentier *et al.*, 2018). This may result in significant depletion of atmospheric species such as H_2O in the upper atmosphere, which acts to suppress the depth and extent of the $\tau \sim 1$ surface (Parmentier *et al.*, 2018). This can thus reduce the extent of spectral features and therefore significantly alter the emission spectra for such ultra-hot planets. This has been used to explain many of the featureless WFC3 spectra for some of the

hottest systems such as WASP-121b, WASP-18b and WASP-103b (Arcangeli *et al.*, 2018; Kreidberg *et al.*, 2018; Parmentier *et al.*, 2018). We therefore include thermal dissociation for H_2O, TiO, VO and H-, which are expected to be susceptible at such high temperatures.

We calculate the volume mixing fraction of these species as a function of pressure and temperature from the dissociation model developed by Parmentier *et al.* (2018). The volume mixing fraction $A_i(P,T)$ of a species i is given by

$$\frac{1}{A_i^{0.5}} = \frac{1}{A_{0,i}^{0.5}} + \frac{1}{A_{d,i}^{0.5}}. \tag{6.1}$$

$A_{0,i}$ is the deep atmosphere (undissociated) abundance and

$$\log(A_{d,i}) = \alpha_i \log(P) + \beta_i/T - \gamma_i, \tag{6.2}$$

for three parameters α_i, β_i, γ_i and pressure P(bar) and temperature T(K) (Parmentier *et al.*, 2018). These three parameters are provided for H_2O, CO, TiO, VO and some other chemical species in Parmentier *et al.* (2018). Using the deep atmosphere abundance $A_{0,i}$ for each species i we calculate the dissociated volume mixing ratio $A_i(P,T)$ according to the pressure and temperature through equations 6.1 and 6.2. This is done for each layer of the model atmosphere resulting in a volume mixing fraction that is a function of atmospheric depth. In our retrieval the undissociated abundance priors for all of the species span $\log(A_{0,i}) = -15$ and -0.5. This allows us to explore a wide range of atmospheric compositions including thermal dissociation for H_2O, TiO, VO and H-. Thermal dissociation of CO has not been included as it does not readily dissociate at the temperatures seen on WASP-18b and other ultra-hot Jupiters (Moses *et al.*, 2013).

6.2.2 H- opacity

H- may be present in the atmosphere of WASP-18b and can also affect the emergent spectrum due to its strong cross section (see chapter 2.3). Our H- cross section includes both bound-free photo-detachment and free-free transitions. The bound-free transitions possess strong absorption in the WFC3 band with a feature at $\sim$1.64 μm. In the Spitzer photometric bands the free-free transitions from H and e- interactions are the only contributors to the H- opacity. Figure 6.1 shows the abundance weighted cross section at a representative temperature and pressure for WASP-18b. These abundances are calculated from the dissociation model above assuming a solar composition atmosphere. The lower H- abundance is offset by the overall stronger cross section to give a weighted

cross section that is comparable to H_2O in the WFC3 band. We leave the volume mixing ratio of H- as a free parameter in the retrieval to compute the total opacity. We also include thermal dissociation of H- into the retrievals as discussed earlier.

6.2.3 Data and Retrieval Setup

We retrieve both HST WFC3 and Spitzer observations (across the 4 channels ranging between ∼3-10 μm) for WASP-18b for all three available datasets (Arcangeli *et al.*, 2018, 2019; Sheppard *et al.*, 2017). These observations are some of the most precise of ultra-hot Jupiters under emission. Our retrievals for the Sheppard *et al.* (2017) dataset do not include the final three data points in the WFC3 range, as Arcangeli *et al.* (2018) and Arcangeli *et al.* (2019) do not have such data beyond 1.6 μm. This allows us to consistently retrieve each dataset over the same range of observations. The 3.6 μm and 4.5 μm Spitzer data for the Arcangeli *et al.* (2018) and Arcangeli *et al.* (2019) datasets are obtained from Maxted *et al.* (2013) and were re-analysed by Sheppard *et al.* (2017) for their work. For all three sets the eclipse depths in the 5.8 μm and 8 μm channels were obtained from Nymeyer *et al.* (2011). For each retrieval we use 4000 evenly spaced wavelength points between 1.1-10.4 μm for our radiative transfer calculations, encompassing both the WFC3 and Spitzer IRAC observations. We adopt the radius of WASP-18b to be $1.2R_{\rm J}$ which has been obtained along with the stellar parameters from Shporer *et al.* (2019). To generate the stellar spectrum we use the Kurucz model grid (Castelli and Kurucz, 2004; Kurucz, 1979).

Each retrieval contains 6 free parameters for the $P-T$ profile and 5 for the volume mixing fraction of H_2O, CO, CO_2, TiO and VO. An additional free parameter for the H- abundance is also included in the retrievals with H-. The retrieval without H- or dissociation is similar to previous work (Sheppard *et al.*, 2017). In order to accurately retrieve the parameters and provide Bayesian evidences we deploy the Nested Sampling algorithm (Buchner *et al.*, 2014; Feroz and Hobson, 2008; Feroz *et al.*, 2009, 2013). Further details on the forward model calculations and retrieval framework can be found in chapter 5.

6.3 Results

Here we discuss the results from each of the retrievals of WASP-18b's emission spectrum. We retrieved the WFC3 and Spitzer data with and without H- and dissociation in three combinations to see the effect of each separately and together for each of the

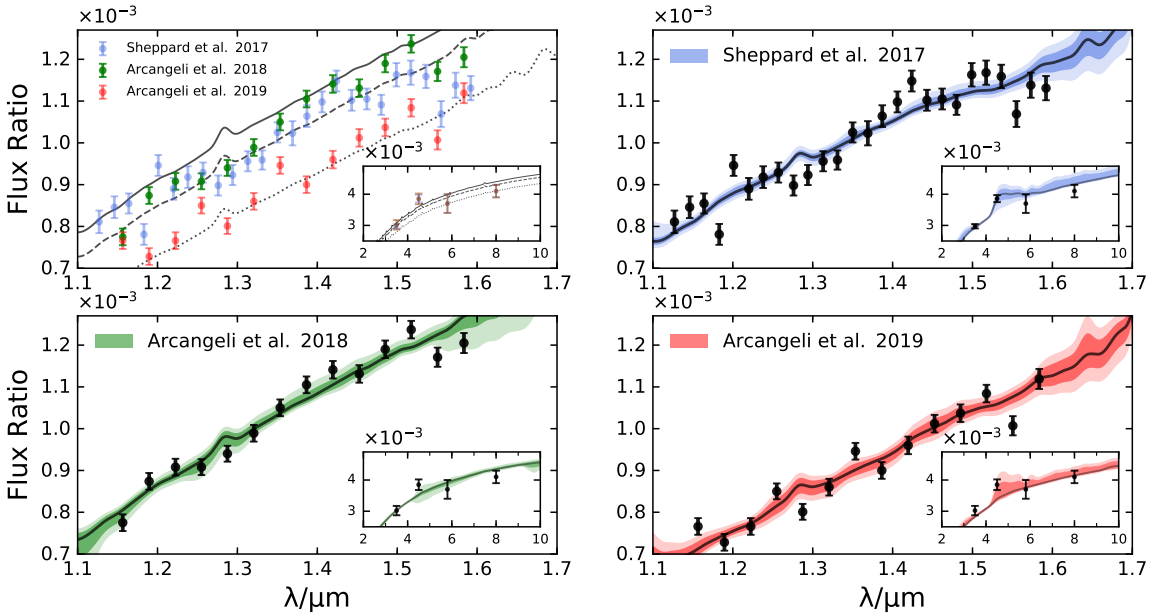

Fig. 6.2 Planet/star flux ratio as a function of wavelength for the WFC3 bandpass for each of the retrievals conducted for the hot Jupiter WASP-18b. The inset in each panel shows the Spitzer IRAC photometric points. The top left panel shows the three datasets together with black body curves at 2800 K (dotted line), 2900 K (dashed line) and 2950 K (solid line). The other three panels show each of the retrievals, with the dark and light colours indicating the 1σ and 2σ uncertainty respectively. The solid line shows the median best fit curve for each. The final three HST WFC3 points for the Sheppard *et al.* (2017) dataset have not been included into our retrievals for comparisons given that the other two do not have data at these wavelengths.

available datasets. Table 6.1 summarises the constraints on the various atmospheric parameters from these datasets, showing the P=100 mbar temperature, H_2O, CO and H- abundances (where retrieved). The spectral fit for the H- and dissociation retrieval is shown for each dataset in figure 6.2. An example of the posterior distribution for the Sheppard *et al.* (2017) dataset with H- and dissociation is shown in fig. 6.4.

Figure 6.2 shows a well fit spectrum for both the WFC3 and Spitzer observations (inset in the figure). The top left panel shows the datasets, along with black body curves for WASP-18b for various temperatures. The HST WFC3 points for all three show a relatively flat spectrum, and thus the constraints on the spectroscopically active species in this spectral range are weak. The Spitzer points on the other hand constrain the CO abundance from the feature in the 4.5 μm Spitzer band as shown in fig. 6.3. The CO_2, TiO and VO abundances are all consistent with solar but we do not observe

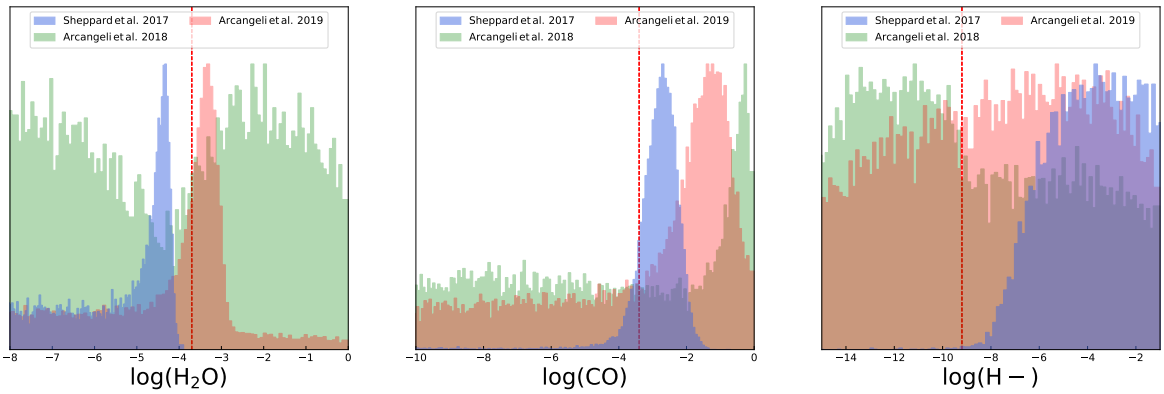

Fig. 6.3 Histogram showing the undissociated H_2O, CO and H- abundance probability distribution functions in the photosphere ($P = 0.1$ bar) for the various retrievals conducted for WASP-18b. In each retrieval the H_2O and H- were thermally dissociated with pressure and temperature according to the model in section 6.2.1. The red dashed line shows the expected abundance assuming solar composition for each of the species (Parmentier *et al.*, 2018).

significant constraints for any of these species from the current observations given their likely trace abundances and weaker features at the wavelengths probed.

The $P-T$ profiles for each of the retrievals also agree well with each other, with the most well constrained temperature for each of the datasets in the photosphere at P∼0.1 bar. This is as we would expect given the similarity of the data. For each dataset we find T_{100mb} between 2800-2900 K as expected from the black body curves in the top left panel of fig. 6.2. These also agree remarkably well with the expected equilibrium temperature of WASP-18b without significant day-night energy redistribution (T≈2850 K). We also see a thermal inversion in the Sheppard *et al.* (2017) dataset due to the stronger Spitzer emission feature and more tightly constrained error bars than the Maxted *et al.* (2013) observations used in the other two datasets. We now discuss some key differences between the retrievals and each datasets along with the implications below.

6.3.1 H_2O abundances

We only retrieve weak constraints for the H_2O abundance, even with the inclusion of H- and dissociation. Figure 6.2 shows the fit to the 1.1-1.7 μm WFC3 data. At these wavelengths the opacity from H_2O, along with perhaps H-, is expected to be dominant over any other. Figure 6.3 shows the retrieved H_2O abundance (undissociated) at

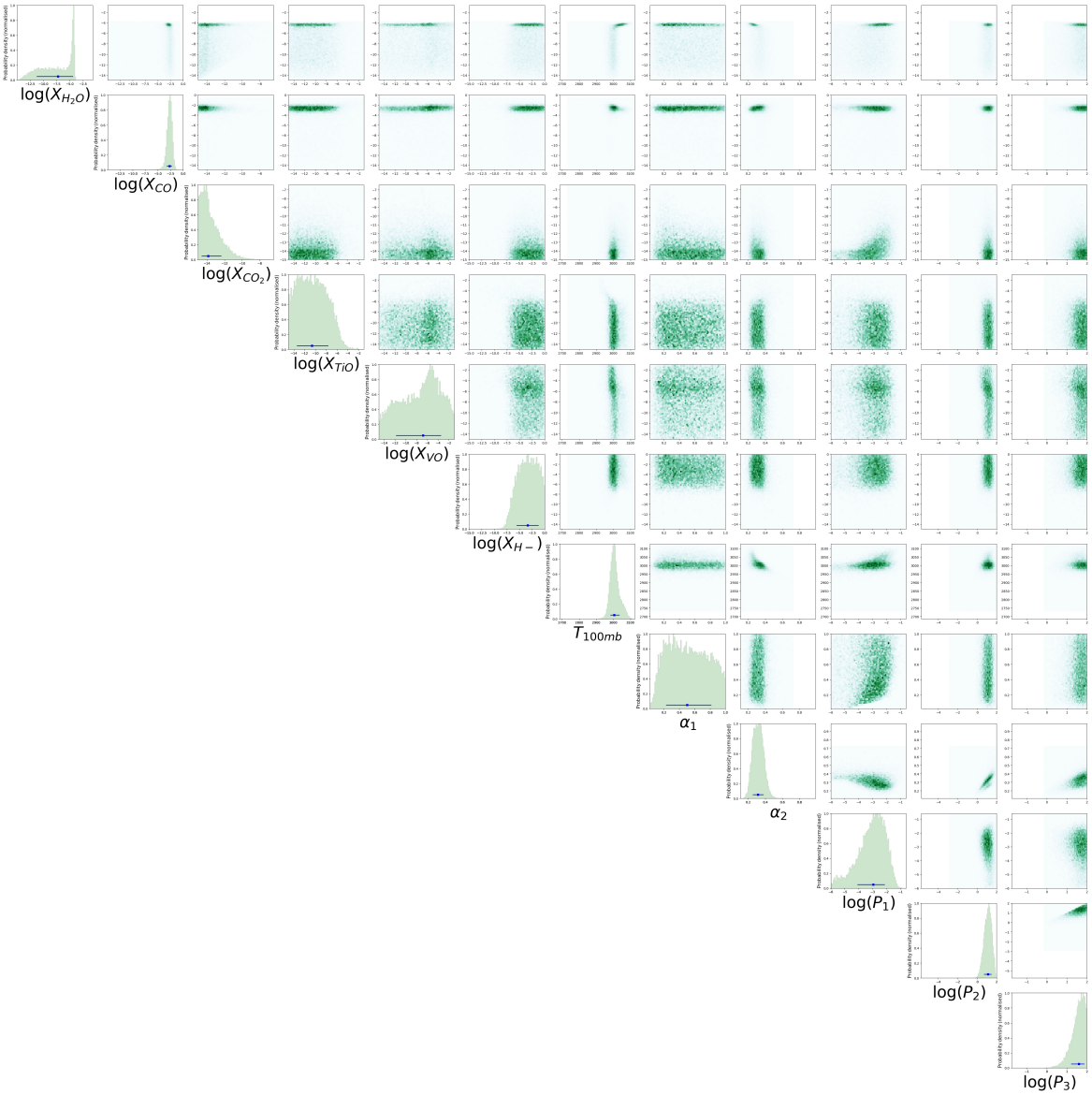

Fig. 6.4 Posterior distribution of WASP-18b's retrieved dayside emission spectrum. The dataset was obtained from Sheppard *et al.* (2017) and considers HST WFC3 and four Spitzer photometric channels between 3.6-8 μm. We retrieved six chemical species, H_2O, CO, CO_2, TiO ,VO and H-, and parametrised the atmospheric temperature profile with six parameters, as discussed in section 5.2.2.

a reference pressure of P=100 mbar. All of the retrievals that were run across all of the datasets do not show strong constraints on H_2O due to the flat spectrum in the WFC3 band (see table 6.1). The inclusion of H- or dissociation into our model does not alter the retrieved H_2O abundance for any of the datasets and all still have wide uncertainties on the abundance. In fact, as a general trend across all of the datasets, the inclusion of H- and dissociation increases the uncertainty on the retrieved abundances slightly due to the extra parameter.

The higher resolution Sheppard *et al.* (2017) data show upper limits on the H_2O at sub-solar abundance, but there is no definitive detection to further constrain this. This is in agreement with retrievals in their work. Our retrievals only show a sub-solar upper limit on the H_2O despite the inclusion of H- and thermal dissociation (see fig. 6.3). Such a sub-solar abundance may have important consequences for the planetary atmosphere (see section 6.4).

Retrievals with Arcangeli *et al.* (2018) data also do not show any constraints on H_2O for all three of the cases run (table 6.1). The H_2O abundance retrieved from the H- and dissociation model is shown in figure 6.3 and indicates no significant peak at any abundance. This is likely due to the isothermal $P-T$ profile retrieved for this dataset (see section 6.3.4). H_2O thus does not have features in the spectrum regardless of its abundance due to the lack of a temperature gradient. Hence the inclusion of H- and dissociation into the model does not help constrain the abundance. In fact, as with the Sheppard *et al.* (2017) dataset, the inclusion of an extra parameter for H- in these retrievals further increases the uncertainty on the H_2O as well as being statistically disfavoured by the Bayesian analysis.

The Arcangeli *et al.* (2019) dataset shows significantly better constraints on the H_2O than the Arcangeli *et al.* (2018) data. The retrieved abundance in fig. 6.3 does seem to peak near the expected solar value, but with a long tail in uncertainty at both low and high abundance meaning that there is no definitive detection. The HST WFC3 data indicate a slightly lower planet/star flux ratio than the other two datasets, with a black body fit closer to 2800 K (fig. 6.2). Thus an inverted $P-T$ profile is retrieved to explain the emission features in the Spitzer data (which remain unchanged to Arcangeli *et al.* (2018)). This thermal inversion is therefore able to constrain the H_2O to a greater degree than Arcangeli *et al.* (2018) and lead to the tighter constraints. Unlike for the other two datasets, the inclusion of H- and dissociation into our models is now favoured, albeit very weakly. The retrieved H_2O abundance however remains relatively unchanged with a wide uncertainty as shown in table 6.1. This indicates

that the H- and dissociation do not play a significant role in determining the H_2O abundance, despite being the favoured models for this dataset.

6.3.2 H- abundances

H- also has strong absorption and a feature in the WFC3 bandpass, but we see no conclusive detection in any dataset. Figure 6.3 shows the H- abundance constrained by each of the three datasets. Despite the strong cross section of H- in the WFC3 range and a spectral feature at $\sim$1.6 μm, the H- cannot be well constrained for any of the datasets due to the relatively flat spectra. The only dataset which shows a peak for the H- is the Sheppard *et al.* (2017) data, which constrains this species from the slight downturn in the red end of the HST WFC3 data where H- has a spectral feature (see fig. 6.1). This retrieval indicates a significantly super-solar abundance with a very broadly constrained abundance. The predicted solar value from the analytic form in Parmentier *et al.* (2018) is $\log(\mathrm{H} - (\mathrm{P} = 0.1 \text{ bar}, \mathrm{T} = 2625 \text{ K})) \approx -9.2$ and our H- constraint is $\log(\mathrm{H}-) = -3.4^{+2.1}_{-2.2}$ as shown in table 6.1. Such an H- abundance, being $\sim 10^6\times$ super-solar, is highly unphysical from chemical models (Parmentier *et al.*, 2018). Therefore the H- abundance does appear to be in tension with equilibrium predictions but without any conclusive detection of H- it is difficult to further quantify this deviation. This H- abundance is also less of a concern with this retrieval given that this case is also statistically disfavoured over one without H- or dissociation.

The other two datasets do not show any constraint whatsoever for H-, as they have more isothermal $P - T$ profiles with weaker temperature gradients. We therefore see no strong evidence for H- in any of the datasets, at odds with previous work (Arcangeli *et al.*, 2018), which indicated a detection of the species and a strong thermal inversion. Our retrievals explored a wide range of temperatures and abundances and found that the flat HST WFC3 spectrum is best explained by an isothermal/low H_2O atmosphere, with only a weak preference for H- and thermal dissociation in the Arcangeli *et al.* (2019) dataset. Further observations of WASP-18b may constrain the H- abundance, but our work is unable to conclusively detect this species in the dayside atmosphere of WASP-18b with any of the observations.

6.3.3 CO abundances

The Spitzer photometric observations show an emission feature at $\sim$4.5 μm for all three datasets (Maxted *et al.*, 2013; Sheppard *et al.*, 2017) as shown in figure 6.2. This is likely due to CO, which which has a strong cross section at $\sim 5\mu$m. The retrieved

CO abundance is shown in figure 6.3. The H- and H_2O opacities are relatively weak compared to CO at such wavelengths, and thus the 4.5 μm Spitzer point can only be well explained by the presence of CO. All three of the datasets constrain CO, with the tightest constraint coming from the Sheppard *et al.* (2017) dataset given their smaller error bars compared to the Arcangeli et al. datasets. The slightly stronger emission feature at 4.5 μm in the re-analysed Sheppard et al. dataset also constrains a stronger thermal inversion in the photosphere due to the emission feature (see figure 6.5). These results do agree well with previous retrievals in Sheppard *et al.* (2017), but we constrain a slightly lower CO abundance by $\sim$1 dex from the inclusion of H- and dissociation, which also increases the CO uncertainty.

On the other hand, the larger uncertainties in the 3.6 μm and 4.5 μm Spitzer points in the Arcangeli *et al.* (2018) and Arcangeli *et al.* (2019) data place weaker constraints on the CO abundance. These do still indicate a CO peak at super-solar abundance ($\log(\mathrm{CO}) \sim -1$) given the 4.5 μm point (see fig. 6.3), but the uncertainty is much greater and the distributions have long tails which go out to low abundances. As with the H_2O, the retrieved CO abundances are largely unaffected by the inclusion of thermal dissociation and H- opacity. This is unsurprising given that CO does not thermally dissociate at such temperatures and given that any H- present would only have weaker free-free absorption in the Spitzer bandpass (see fig. 6.1).

We tested whether the Spitzer data was indeed the source of the CO abundance and thermal inversion constraints by retrieving the each dataset with only the HST WFC3 observations. All except one showed a temperature profile that was isothermal given that the WFC3 spectrum is largely featureless. The Sheppard *et al.* (2017) dataset was the outlier and showed a bi-modal CO constraint due to the slight downturn in the WFC3 spectrum near 1.6 μm. The CO does have weak absorption in the WFC3 range near the H- feature at $\sim$1.6 μm (see fig. 6.1) and therefore it is not unexpected that the dip in the WFC3 points may be explained by either species. In our retrievals we see evidence for either CO or H-, the former of which was claimed in Sheppard *et al.* (2017) given that H- was not included in their work. This constraint on CO is however much weaker than with the inclusion of the Spitzer photometric bands, where CO has a much stronger feature near $\sim$5 μm (see fig. 6.1). The arrival of JWST is therefore likely to place much stronger constraints on the CO abundance with its higher precision and resolution observations available in this CO absorption feature.

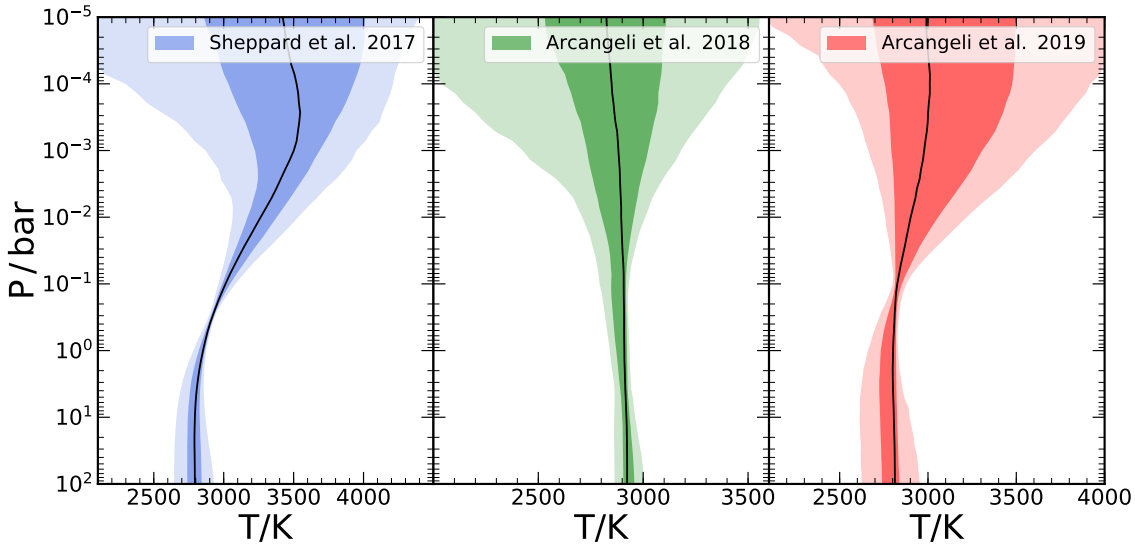

Fig. 6.5 Retrieved pressure-temperature profiles for the retrievals conducted for WASP-18b. In each case the dark and light colours indicate the 1σ and 2σ uncertainty respectively, with the solid black line showing the median best fit.

6.3.4 $P-T$ Profile

Figure 6.5 shows the $P-T$ profiles for each of the retrievals. Our work shows the best constraints on the $P-T$ profile occur in the photosphere probed by the data at P$\sim$0.1 bar. Lower pressures (P$\lesssim 10^{-3}$ bar) show a much less constrained temperature given that they have a negligible effect on the spectrum. This is similar at higher pressures (P$\gtrsim$10 bar) where the onset of the isotherm and the high optical depth limit our ability to constrain the $P-T$ profile here given that the effect on the spectrum is negligible. However, there are some differences in the retrieved $P-T$ profiles which we explore below.

The Sheppard *et al.* (2017) retrievals show a thermal inversion present in the photosphere (P$\sim$100 mbar) with a $T_{100\mathrm{mb}} \approx 3000$ K. This inversion is primarily constrained by the Spitzer photometric data which show a strong CO emission feature at 4.5 μm and thus the inversion is present in every retrieval run for this dataset, with and without H- or dissociation. However, our results for Arcangeli *et al.* (2018) indicate a more isothermal $P-T$ profile. This is caused by the weaker Spitzer constraints from the Maxted *et al.* (2013) observations as well as the featureless WFC3 data. These results were also invariant with the inclusion of H- and dissociation into the retrievals,

still indicating an isotherm over an inversion with H- or thermal dissociation, unlike the study by Arcangeli *et al.* (2018).

The phase resolved spectra of Arcangeli *et al.* (2019) showed an inversion similar to but weaker than Sheppard *et al.* (2017). This is somewhat surprising initially given that the Spitzer observations are identical and the WFC3 spectrum also shows no significant features. However, these differences arise because of the slightly lower planet/star flux ratio in the WFC3, which result in an enhancement of the CO emission feature when compared to the Spitzer data. The photosphere temperature is therefore also slightly cooler at T_{100mb} ∼2800 K due to the lower flux ratio as shown in table 6.1. The difference in the two observations by Arcangeli et al. may be caused by 2019 observations binning the spectrum at phases of 0.4-0.45 and 0.55-0.6, thus averaging over some of the slightly cooler regions of the planet away from the substellar point. However, these differences in the temperature profile are relatively minor. Generally we do see a photosphere temperature that is very close to the expected equilibrium temperature of WASP-18b without significant redistribution for all three of the datasets.

6.3.5 Constraints on other species

Our retrievals are unable to constrain TiO or VO significantly given that these species only have strong cross sections in the visible. Thermal inversions have been predicted from equilibrium models of hot Jupiters due to species such as TiO and VO (Fortney *et al.*, 2008; Spiegel *et al.*, 2009). In our retrievals we only observe very weak constraints for TiO in Arcangeli *et al.* (2018), which show a peak at log(TiO) ~ -6 but with a long-tailed distribution at low and high abundance. The other two datasets do not show any significant peak for TiO or VO across any of the retrievals with and without H- and dissociation. Expectations from solar abundances (Asplund *et al.*, 2009) and equilibrium models of WASP-18b (Lothringer *et al.*, 2018; Parmentier *et al.*, 2018) indicate that these species should be present at log(TiO) ~ -7 and log(VO) ~ -9 (Asplund *et al.*, 2009). At such abundances the atmosphere of WASP-18b may also be more susceptible to thermal inversions from species such as TiO and VO if the H_2O abundance is sub-solar as indicated by the Sheppard *et al.* (2017) data. This is because the presence of strong infrared opacity (such as H_2O) can act to cool the upper atmosphere due to its radiative efficiency and reduce the effectiveness of species such as TiO and VO at causing inversions as discussed in chapter 4.

We do not constrain the CO_2 abundance significantly given that CO_2 possesses a weaker cross section. Previous theoretical studies have also shown CO_2 is rarely dominant over H_2O and CO in hot Jupiter atmospheres (Heng and Tsai, 2016; Moses

et al., 2013). We thus limit our model to have $\log(CO_2) \leq \log(CO)$ and $\log(CO_2) \leq \log(H_2O)$. This also allows us to break the degeneracy between CO and CO_2 in the 4.5 μm Spitzer band, where both of these species have strong absorption (see chapter 5).

6.4 Discussion and Conclusion

We present here the first retrieval model specifically designed for ultra-hot Jupiter atmospheres with equilibrium temperatures in excess of 2000 K. We demonstrate this model by retrieving the dayside atmosphere of WASP-18b, a planet with an equilibrium temperature of $\sim$ 2400 K. The motivation for this work comes from recent work on equilibrium models of ultra-hot Jupiters which show that H- opacity and thermal dissociation of species such as H_2O may be important (Arcangeli *et al.*, 2018; Kreidberg *et al.*, 2018; Lothringer *et al.*, 2018; Parmentier *et al.*, 2018). To achieve this we have extended our recently developed HyDRA model (chapter 5) in order to retrieve the dissociated abundances of each species as well as the H- mixing ratio within the atmosphere. We carry out 3 separate retrievals on each of the three available datasets for WASP-18b (Arcangeli *et al.*, 2018, 2019; Sheppard *et al.*, 2017) to study the effect of H- and dissociation.

We investigated the H_2O abundances for each of the datasets, with and without H-/ dissociation. We saw good agreement between each of these, as shown in table 6.1. We constrain an H_2O abundance that is slightly sub-solar for the Sheppard *et al.* (2017) dataset, even with the inclusion of dissociation and H- opacity. The Arcangeli *et al.* (2019) dataset similarly indicates a peak for H_2O, but closer to solar composition. The Arcangeli *et al.* (2018) data on the other hand do not show significant H_2O constraints given their smaller temperature gradients (see fig. 6.5). However, none of these datasets conclusively detect H_2O in the atmosphere of WASP-18b given the largely featureless WFC3 spectrum (see figure 6.2) with no significant H_2O absorption or emission feature, in agreement with previous retrievals (Sheppard *et al.*, 2017). The relatively large uncertainties on the H_2O abundance thus remained as we included H- and dissociation into the retrievals due to the flat spectra (see fig. 6.3). We therefore conclude that the inclusion of H- and/or thermal dissociation in our retrievals does not help to fully constrain the H_2O abundance. Further observations, perhaps through transmission spectroscopy, may be required to resolve this conundrum.

We additionally place the first constraints on the H- abundance from retrievals through inclusion of its opacity (John, 1988; Wishart, 1979) into the HyDRA retrieval

framework (see chapter 5). We are however unable to detect H- in the atmosphere for any of the retrievals for any of the datasets. The Sheppard *et al.* (2017) dataset did show a peak at $\log(\mathrm{H}-) \sim -3.4$ when dissociation was also included, but this is much too high to be physical given that the expected solar abundance is $\log(\mathrm{H}-) \sim -9$ (Parmentier *et al.*, 2018). This case was also statistically disfavoured through our Bayesian analysis as shown in table 6.1. The other two datasets showed no constraint on H-. The Arcangeli *et al.* (2019) dataset however did favour the inclusion of H- and dissociation, but the significances were weak and there was regardless no H- abundance peak nor any significant differences in the retrieved H_2O or CO abundances. We thus do not see any strong evidence for H- in any of the observations that have been made for the dayside of this planet, counter to that reported in Arcangeli *et al.* (2018).

The CO has been constrained through its influence on the 4.5 μm Spitzer point. All of the CO constraints have been made primarily through the Spitzer observations (Maxted *et al.*, 2013; Nymeyer *et al.*, 2011; Sheppard *et al.*, 2017). Sheppard *et al.* (2017) first reported CO in WASP-18b and our retrievals also show a clear CO signal, but at a slightly lower abundance than reported when H- and dissociation were included into the retrieval. The other two datasets did only show a weak peak at $\log(\mathrm{CO}) \sim -1$ (fig. 6.3). The re-analysed Spitzer data in Sheppard *et al.* (2017) allowed a tighter constraint given the stronger contrast between the 4.5 μm and 3.6 μm bands with smaller error bars.

The stronger 4.5 μm emission feature in the Spitzer observations also constrained a thermal inversion in the Sheppard *et al.* (2017) dataset. The Arcangeli *et al.* (2018) and Arcangeli *et al.* (2019) datasets constrained a much more isothermal temperature profile given that the Spitzer data had larger error bars and given that the HST WFC3 spectra are all largely featureless. All of these do seem to show peaks for CO at solar or super-solar abundance. This result should however be taken with caution as it is largely dependent on only one of the Spitzer data but may indicate a super-solar C/O ratio and/or metallicity if confirmed (Madhusudhan, 2012).

This work represents a crucial step in the characterisation of ultra-hot Jupiters, which have recently come to the fore thanks to high precision observations (Haynes *et al.*, 2015; Kreidberg *et al.*, 2018; Sheppard *et al.*, 2017). With such extreme temperatures our understanding of atmospheric processes has been pushed to the limit. More observations with instruments such as WFC3 and the upcoming JWST will shed light on these physical processes for planets such as WASP-18b and may allow us to finally confirm the presence of H- and/or dissociation in the dayside atmosphere.

Dataset	**Retrieval**	T_{100mb}/K	log(H_2O)	log(CO)	log(H−)	Model Comparison
Sheppard *et al.* (2017)	No H-, No dissoc.	2829^{+36}_{-48}	$-8.8^{+2.0}_{-2.7}$	$-0.58^{+0.24}_{-0.35}$	-	Reference
	H-, No dissoc.	2804^{+47}_{-99}	$-7.7^{+4.8}_{-3.0}$	$-1.10^{+0.60}_{-6.8}$	$-10.3^{+5.7}_{-3.1}$	Disfavoured by 2.6σ
	H-, dissoc.	3005^{+31}_{-23}	$-7.3^{+2.8}_{-4.0}$	$-2.70^{+0.45}_{-0.57}$	$-3.4^{+2.1}_{-2.2}$	Disfavoured by 3.1σ
Arcangeli *et al.* (2018)	No H-, No dissoc.	2849^{+64}_{-46}	$-7.8^{+2.9}_{-3.0}$	$-1.2^{+1.0}_{-7.0}$	-	Reference
	H-, No dissoc.	2868^{+53}_{-54}	$-7.4^{+3.9}_{-3.2}$	$-2.0^{+1.8}_{-6.4}$	$-11.7^{+2.5}_{-2.1}$	Disfavoured by 1.6σ
	H-, dissoc.	2907^{+13}_{-67}	$-6.5^{+4.6}_{-3.9}$	$-5.4^{+4.7}_{-4.7}$	$-9.4^{+5.5}_{-3.7}$	Disfavoured by 1.9σ
Arcangeli *et al.* (2019)	No H-, No dissoc.	2806^{+22}_{-41}	$-4.2^{+2.3}_{-4.8}$	$-4.8^{+3.3}_{-4.5}$	-	Reference
	H-, No dissoc.	2800^{+24}_{-49}	$-3.6^{+2.1}_{-4.9}$	$-4.8^{+3.3}_{-4.3}$	$-10.6^{+3.4}_{-2.8}$	Favoured by 1.2σ
	H-, dissoc.	2822^{+22}_{-12}	$-4.6^{+1.4}_{-5.2}$	$-2.5^{+1.6}_{-6.2}$	$-7.4^{+4.2}_{-4.8}$	Favoured by 1.4σ

Table 6.1 Retrieved parameters for the various runs conducted on the emission spectrum of WASP-18b. In each case the parameter is shown with its 1σ uncertainty. In models with dissociation the dissociated 100 mbar abundance is shown. We also show the Bayesian comparison for each model versus our reference case.

Chapter 7

Homogeneous Retrievals of Exoplanets

"There are more things in heaven and earth, Horatio, than are dreamt of in your philosophy."
- Hamlet, W. Shakespeare

This chapter details the ensemble study of hot Jupiter emission spectra I carried out with the HyDRA retrieval framework. I have also used the HyDRA high temperature retrieval framework discussed in the last chapter to retrieve the spectra for planets with equilibrium temperatures in excess of 2500 K. The retrieved planets include WASP-43b, HD189733b, HD209458b, WASP-121b, WASP-103b, WASP-18b and Kepler-13Ab. I additionally also retrieved previously unpublished data for WASP-19b, obtained with the HST WFC3 spectrograph. The data reduction on the WASP-19b observations was carried out by my collaborators Dr Avi Mandell and Mr Kyle Sheppard at Goddard Space Flight Centre and discussed in section 7.3.

7.1 Introduction

With the influx of recent atmospheric observations for transiting exoplanets (e.g Evans *et al.*, 2017; Kreidberg *et al.*, 2014; Madhusudhan *et al.*, 2014b; Sheppard *et al.*, 2017), we are now entering the era of comparative exoplanetology. Past efforts to study ensembles of planets using emission spectra were confined largely to photometric data, e.g with Spitzer (Line *et al.*, 2014; Madhusudhan, 2012; Madhusudhan and Seager, 2010). However, in recent years, a sizeable sample of planets (N$\sim$10) have been observed in the infrared with both WFC3 and Spitzer space telescopes. Such data allow us to

pursue population studies of exoplanetary atmospheres. Such comparative studies also allow for observations of outliers and an exploration of the most extreme processes that can occur on such planets.

The abundances thus retrieved can also provide clues on various atmospheric processes and formation conditions on exoplanets. For example, we placed constraints on radiative disequilibrium on the dayside of such atmospheres in chapter 5, and Moses *et al.* (2013) investigated non-equilibrium processes such as vertical mixing and photodissociation. Additionally, a measurement of the atmospheric C/O ratio for a hot Jupiter can provide insights into the conditions in the protoplanetary disk where such a planet may have formed (Madhusudhan *et al.*, 2014c). This is of particular importance given that hot Jupiters have no analogue in our own Solar System.

In this chapter we conduct a homogeneous study of the dayside atmospheres of eight hot Jupiters. The emission spectra for each system were obtained from Hubble Space Telescope's Wide Field Camera 3 (HST WFC3) and Spitzer observations. We use HyDRA to retrieve these emission spectra as discussed in chapter 5. For the ultra-hot Jupiters (with temperatures $\gtrsim$2500 K) we retrieve H- and thermal dissociation of H_2O, TiO, VO and H-. However, in this study we primarily focus on exploring the H_2O abundances for each planet, as this offers the most stringent constraints due to the strong spectral signature of H_2O in the WFC3 bandpass (see fig. 5.3). We also determine the temperatures in the photospheres of each planet and investigate the presence of stratospheric thermal inversions.

In what follows, section 7.2 describes the methods and section 7.3 discusses the WASP-19b data analysis. In section 7.4 we describe the results for the retrievals, in particular discussing the H_2O abundances and temperature profiles for each planet. This is followed by section 7.5 where we summarise the work, explore physical processes that occur and discuss future directions.

7.2 Methods

In this section we will describe the retrieval methods and atmospheric parameters we retrieve from the dayside spectra of these hot Jupiters. This is done in accordance with the retrieval model from chapters 5 and 6. The retrieval model uses line-by-line opacities with the latest radiative transfer methods to accurately determine the emergent flux for a given set of atmospheric parameters. We run many millions of models over a wide range of parameter space and employ the Nested Sampling algorithm MultiNest (Buchner *et al.*, 2014; Feroz and Hobson, 2008) for statistical inferences on the data.

We briefly outline our parametrisation, opacity and radiative transfer calculations below.

7.2.1 $P-T$ Profile

The atmospheric $P-T$ profile is parameterised using the method in Madhusudhan and Seager (2009), as discussed in chapter 5.2.2. This has been demonstrated to reproduce the atmospheric temperature profile of many planets covering a wide range of temperatures with minimal free parameters to capture the behaviour of all possible atmospheric profiles, including thermal inversions. We retrieve 6 parameters for the temperature profile: T_{100mb}, α_1, α_2, P_1, P_2 and P_3. With just these parameters we are able to accurately capture the variation in $P-T$ profile of exoplanetary atmospheres.

7.2.2 Molecular Mixing Ratios

We also retrieve the volume mixing ratio for each molecular species present on the dayside atmosphere with a significant spectral signature. For the cooler planets (with temperatures $\lesssim$ 2000 K) we introduce molecular absorption from 7 molecular species, H_2O, CH_4, NH_3, CO, HCN, CO_2 and C_2H_2. For the hottest systems, so-called 'ultra-hot' Jupiters, we retrieve H_2O, CO, CO_2, TiO, VO and H-. These are expected to be the most prominent species on hydrogen dominated atmospheres at such temperatures ($\sim$1000-3000 K) (Moses *et al.*, 2013; Parmentier *et al.*, 2018). Such species have significant spectral features due to their strong molecular opacity in the near infrared. The strength of the spectral feature in the observations of each molecule determines the abundance in the atmosphere, here assumed to be uniformly mixed throughout the atmosphere. For the ultra-hot Jupiters we also include dissociation which introduces a pressure dependent abundance, as discussed in chapter 6.

For each molecular species we determine the contribution to the opacity from the latest rovibrational line lists. These are obtained from the HITEMP (Rothman *et al.*, 2010), HITRAN (Rothman *et al.*, 2013) and EXOMOL (Tennyson *et al.*, 2016) databases (see chapter 2). The H- opacity is calculated from the method in Bell and Berrington (1987) and John (1988). Figures 5.3 and 6.1 show the cross sections for the prominent species in the atmosphere of the hot Jupiters and ultra-hot Jupiters at a representative temperature and pressure. The H_2O cross sections are the strongest out of all of the species, particularly in the HST WFC3 band. Therefore, given its higher expected abundance, the most stringent constraints from dayside emission spectra is often the H_2O due to its strong $\sim 1.4\mu$m absorption feature. Species such as CH_4,

NH_3 and HCN also possess strong cross sections on hot Jupiters, however, we see weaker constraints on these because of their reduced atmospheric abundance and thus reduced spectral signature (see section 7.4.2). On the ultra-hot Jupiters, H- shows strong opacity but the lack of any significant absorption bands can make it difficult to constrain, as shown in chapter 6.

7.2.3 Radiative Transfer

To determine the radiation field in the atmosphere we must first compute the optical depth due to the molecular species in the atmosphere. The change in optical depth from one layer in the atmosphere to another is given by (eqn 5.9),

$$d\tau_\nu = \left(n \sum_i X_i \kappa_i(P,T,\nu) + \alpha(T,\nu)_{\rm CIA} + \sigma(\nu)_{\rm H_2}\right) dz. \tag{7.1}$$

Here, dz is the vertical height difference between layers, n is the number density of gas and X_i and κ_i refer to the molecular mixing ratio and cross section respectively. We have also included the opacity due to CIA ($\alpha_{\rm CIA}$) and Rayleigh scattering from hydrogen ($\sigma_{\rm H_2}$) into the overall optical depth (see chapter 2). This optical depth determines the frequency dependence of the radiation and in particular the spectral absorption and emission features resulting from molecular species through the transfer equation.

After we have obtained the optical depth we solve the radiative transfer equation for the spectral intensity (I_ν) and emergent flux (F_ν) of the atmosphere (as discussed in chapter 5.2.4). The overall emergent flux out of the planet is given by (eqn 5.12)

$$F_\nu = 2\pi \int_0^1 I_{{\rm top},\nu} \mu {\rm d}\mu. \tag{7.2}$$

where $I_{{\rm top},\mu,\nu}$ is the overall emergent intensity of radiation out of the atmosphere. The overall flux ratio is then calculated using the method in chapter 5.2. The stellar spectrum, F_*, is obtained from the Kurucz model grid (see chapter 3.3.7). This flux is binned to the resolution of the data and thus we determine the likelihood for a given model against the observations. By exploring a wide range of parameter space we are able to determine the most likely configuration of the atmosphere and extract the atmospheric properties through the Nested Sampling algorithm MultiNest (Buchner *et al.*, 2014; Feroz and Hobson, 2008; Feroz *et al.*, 2009, 2013), as discussed in chapter 5.

7.2.4 Target Sample

Our goal is to conduct homogeneous atmospheric characterisation of a sizeable number of hot Jupiters across a wide range of temperatures To this end we consider eight hot Jupiters with the most precise infrared observations. We retrieve the atmospheric properties for HD189733b, WASP-43b, HD209458b, WASP-19b, WASP-121b, WASP-18b, WASP-103b and Kepler-13Ab. These planets also encompass a wide range in mass and radius, as shown in table 7.1. They were chosen as they have high precision HST WFC3 and Spitzer photometric observations. These planets are detailed below.

We obtained the spectrum for HD189733b, one of the coolest planets in our study, from Crouzet *et al.* (2014). Due to its low temperature, this is one of the least well constrained spectra from WFC3. On the other hand, hotter planets such as WASP-121b and WASP-18b (Evans *et al.*, 2017; Sheppard *et al.*, 2017) have incredibly well constrained, high-resolution spectra available due to the increased planet/star flux contrast. Many of the planets (e.g. WASP-43b, HD209458b, Kepler-13Ab) show spectral features in the WFC3 band predominantly from H_2O absorption (see fig. 7.3). The absorption and emission features from molecular chemistry in the atmosphere allows us to constrain the temperature profile and atmospheric composition, even with relatively modest spectral coverage. All of the planets we study have HST WFC3 spectra and Spitzer IRAC 1 and 2 photometric band observations. Three of the eight systems, HD189733b, HD209458b and WASP-18b have also been observed with the Spitzer IRAC 3 and 4 bands, which extends the spectral coverage to $\gtrsim$10 μm (Crouzet *et al.*, 2014; Diamond-Lowe *et al.*, 2014; Nymeyer *et al.*, 2011).

In addition to previously available observations, we also present and retrieve the emission spectrum for WASP-19b, with observations from HST WFC3 and Spitzer IRAC 1 and 2 channels. This planet is of particular importance given its equilibrium temperature, $\sim$2100 K. This is near the temperature at which TiO and VO condense out of the atmosphere (Sharp and Burrows, 2007). The presence of species such as TiO and VO is significant given that they have been proposed to lead to thermal inversions in the dayside atmosphere (Fortney *et al.*, 2008; Hubeny *et al.*, 2003; Spiegel *et al.*, 2009). In addition, this is also the temperature at which thermal dissociation has been predicted to become significant (Lothringer *et al.*, 2018; Parmentier *et al.*, 2018). Therefore, for WASP-19b we have run retrievals in our cooler class of retrievals (with CH_4, NH_3, HCN and C_2H_2) as well as the ultra-hot Jupiter retrievals (with dissociation and H-, TiO and VO) to ensure that the retrieved parameters are similar. In the below section, we explain the derivation of the emission spectrum from WFC3 data. The Spitzer IRAC channel 1 and 2 depths are taken from Wong *et al.* (2016).

7.3 WASP-19b WFC3 Data Analysis

In this work we obtained new observations of the hot Jupiter WASP-19b from our collaborators Dr Avi Mandell and Mr Kyle Sheppard. In what follows, I describe the procedure they adopted to obtain the data which I then used in my retrievals.

We used archival WFC3 observations of a secondary eclipse of WASP-19b from the HST program GO-13431 (PI: C. Huitson). WFC3 obtains low-resolution slitless spectroscopy from 1.1 to 1.7 μm using the G141 grism (R= 130). The observation was taken in spatial scan mode (Deming *et al.*, 2013) with a reverse cadence (i.e. scanning downward on the detector).

We extracted the HST "ima" data files and further processed them by removing background flux via difference frames (Deming *et al.*, 2013) and correcting cosmic rays and flat field effects. The data quality extension diagnosed and masked problematic pixels. All corrections are propagated to the flux errors, which are retrieved from the "ima" error extension and intrinsically account for read noise and bias. We determine the wavelength of each column by using the accompanying photometric image, as done in Sheppard *et al.* (2017).

We follow the parametric marginalization and residual subtraction analysis of Sheppard *et al.* (2017) to detrend systematic effects. We use a grid of models comprising a combination of a linear planetary phase correction and up to four powers of HST phase and wavelength shift (Wakeford *et al.*, 2016). The complete model consists of a systematic model multiplied by a BATMAN eclipse model (Kreidberg, 2015). We first fit the broadband light curve using MPFIT (Markwardt, 2009) to determine center-of-eclipse time (t_0) and a/R_* and to capture the structure of any wavelength-independent correlated noise in the residuals. All other system parameters are fixed to literature values (Hebb *et al.*, 2010; Sedaghati *et al.*, 2017; Tregloan-Reed *et al.*, 2013; Wong *et al.*, 2016). The exposures are then separated into wavelength bins six pixels (0.028 μm) in size and fit individually to derive the emission spectrum. Residual scatter from the fit to the band-integrated light curve is included as a scalable parameter, and t_0 and a/R_* are fixed to the whitelight value, as in Mandell *et al.* (2013) and Haynes *et al.* (2015).

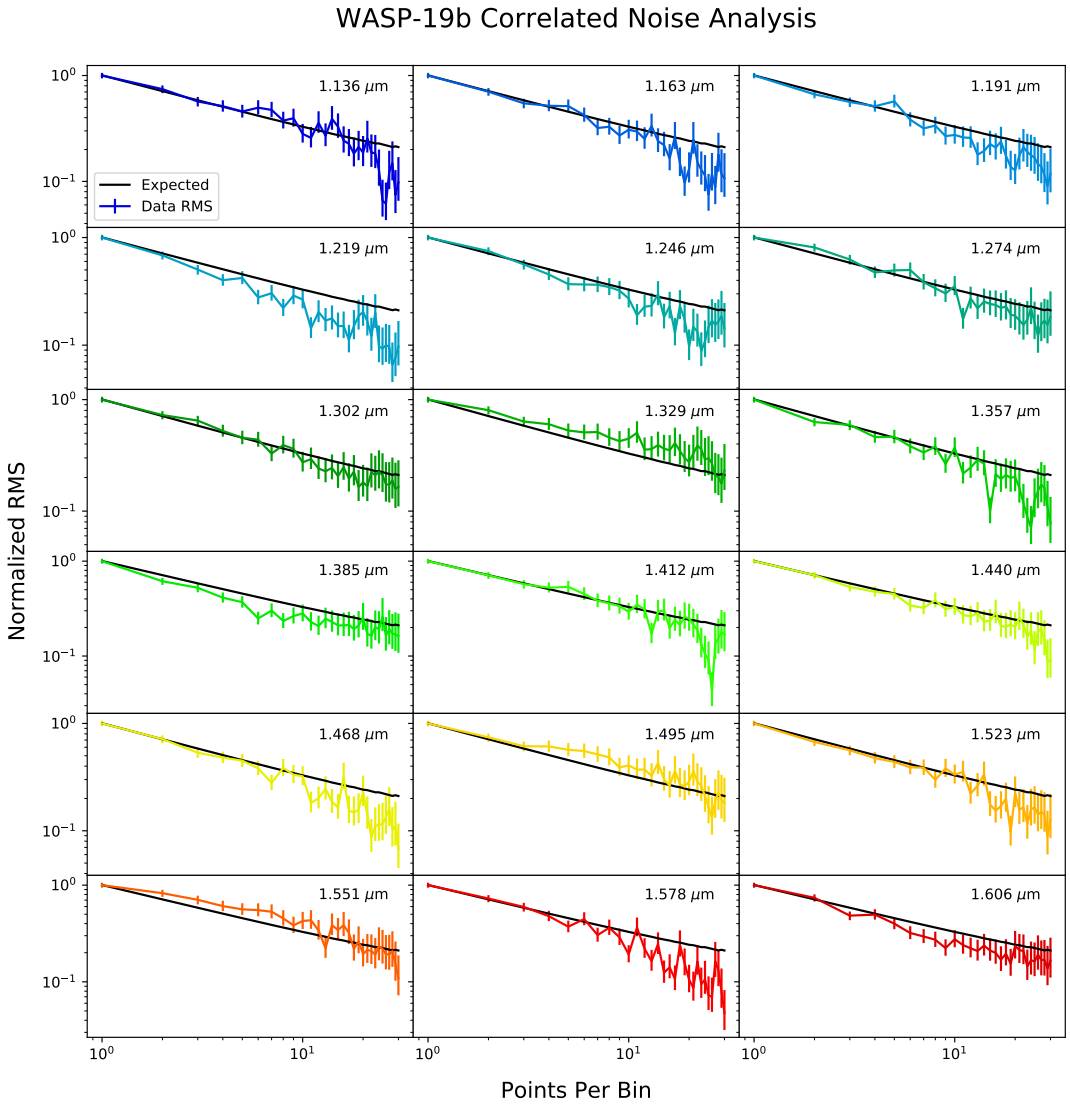

Fig. 7.1 Analysis of the temporal correlated noise in each spectral bin for WASP-19b. The data is binned up in time and the RMS of the light curve residuals is calculated; the results are then normalized by the RMS of the light curve with minimal binning (i.e, one point per bin) and compared with the predicted trend assuming there is no correlation in time ($RMS_0/\sqrt{N}$, where N is the number of exposures per bin). Most light curves show no evidence of correlated noise; only the bin at 1.329 μm) shows any excess noise, but the effect is only seen at large bin sizes.

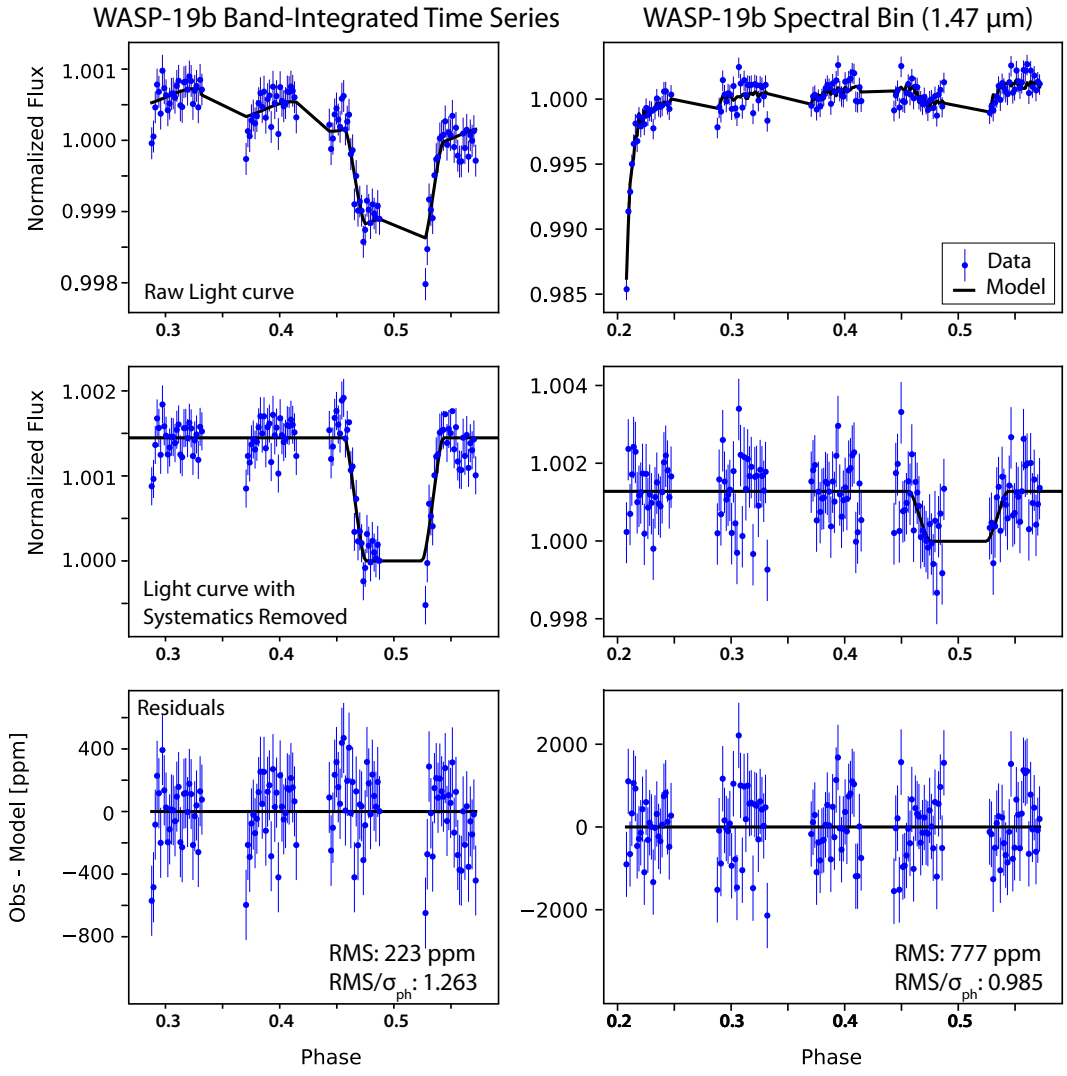

Fig. 7.2 Band-integrated light curve (left) and a sample spectral bin light curve (right) for HST WFC3 observations of WASP-19b. The top panels show the raw data with the best-fit model overplotted, and the middle panels show the light curve and model after detrending systematic effects. The bottom panels show the difference between the observations and the best-fit model at each point in the time series and give the standard deviation of those residuals (RMS).

Planet	R_P/R_J	M_P/M_J	T_{eq}/K	T_{100mb}/K	$\log(X_{H_2O})$	Profile	Ref.
HD189733b	1.1	1.14	1200	1430^{+50}_{-65}	$-3.9^{+1.5}_{-1.9}$	No inversion	Crouzet *et al.* (2014)
WASP-43b	0.93	1.78	1375	1600^{+170}_{-100}	$-3.54^{+0.80}_{-0.52}$	No inversion	Stevenson *et al.* (2014)
HD209458b	1.4	0.69	1450	1500^{+200}_{-70}	$-4.10^{+1.10}_{-0.45}$	No inversion	Diamond-Lowe *et al.* (2014); Line *et al.* (2016)
WASP-19b	1.4	1.13	2100	2550^{+100}_{-140}	$-3.35^{+0.88}_{-0.64}$	No inversion	**This work**
WASP-121b	1.7	1.18	2350	2540^{+25}_{-35}	$-9.6^{+2.3}_{-2.6}$	Inversion	Evans *et al.* (2017)
WASP-18b	1.2	10.2	2400	3005^{+31}_{-22}	$-7.3^{+2.8}_{-4.0}$	Inversion	Sheppard *et al.* (2017)
WASP-103b	1.5	1.49	2500	3000^{+80}_{-25}	$-8.7^{+3.1}_{-3.2}$	Inversion	Kreidberg *et al.* (2018)
Kepler-13Ab	2.0	7.95	2575	3100^{+135}_{-170}	$-3.22^{+1.30}_{-0.61}$	No inversion	Beatty *et al.* (2017a)

Table 7.1 Planet parameters, retrieved properties and data sources for the hot Jupiters we consider in our study. The mass and radius parameters have been obtained from exoplanet.org, and the equilibrium temperature has been calculated assuming full redistribution of the incident flux. The retrieved photospheric temperature temperature and H_2O abundances for each planet were calculated using the retrieval method in chapters 5 and 6 and discussed in section 7.2. The reference for each data source is also shown in the final column.

The RMS of the residuals of the band-integrated light curve is 1.26x the theoretical photon-noise limit, which indicates there is some excess noise present. However, the average and median RMS of the residuals of the spectroscopic light curves are 1.02x and 1.01x the theoretical limit, indicating that no additional noise is present in the binned data after subtracting the band-integrated residuals (see Figure 7.2. An analysis of the RMS of the residuals as a function of binning in time further demonstrates that shot noise is the dominant error source (see Figure 7.1). We emphasize that the emission spectrum is not dependent on methodology: we also fit the light curves using the exponential ramp model from Zhou *et al.* (2017) and found agreement in each bin to well within 1σ.

7.4 Results

We now present the retrieved atmospheric properties of the exoplanet sample in our study. Our goal is to perform homogeneous retrievals with all of the observations using our recently developed retrieval framework as discussed in section 7.2. As discussed above, the planets span a wide range in equilibrium temperature ($\sim$1200-2600 K) and mass ($\sim$0.7-10 M_J). Each of these planets have an HST WFC3 spectrum in the 1.1-1.7 μm range and Spitzer IRAC photometric observations in the $\sim$3-5 μm range. Some systems also have Spitzer IRAC 3 and 4 observations up to $\gtrsim 10\mu$m as well (HD209458b, HD189733b and WASP-18b) (Crouzet *et al.*, 2014; Diamond-Lowe *et al.*, 2014; Nymeyer *et al.*, 2011). We determine the posterior distribution for all of the atmospheric parameters retrieved in our sample. As an example of this, we show the posterior distribution for HD209458b in figure 7.5. An example of the posterior distribution for the ultra-hot planets is shown in fig. 7.6 for Kepler-13Ab. Several studies have performed retrievals on individual planets with these observations (e.g. Evans *et al.*, 2017; Kreidberg *et al.*, 2014; Line *et al.*, 2016; Sheppard *et al.*, 2017) and we will compare these studies to our retrieval.

We standardise the retrieval setup for each system in order to perform a homogeneous retrieval analysis. The statistical analysis is performed using the MultiNest algorithm (Buchner *et al.*, 2014; Feroz and Hobson, 2008; Feroz *et al.*, 2009, 2013), using 4000 live points, as discussed in chapter 5. For each of these planets over 10^6 models were run. Six parameters were used for the temperature profile, T_{100mb}, α_1, α_2, P_1, P_2 and P_3, as described in section 7.2.1 and detailed in Madhusudhan and Seager (2009). For the planets with a temperature of $\lesssim$2000 K we have seven additional free parameters for the atmospheric volume mixing ratios for the volatile species with strong infrared

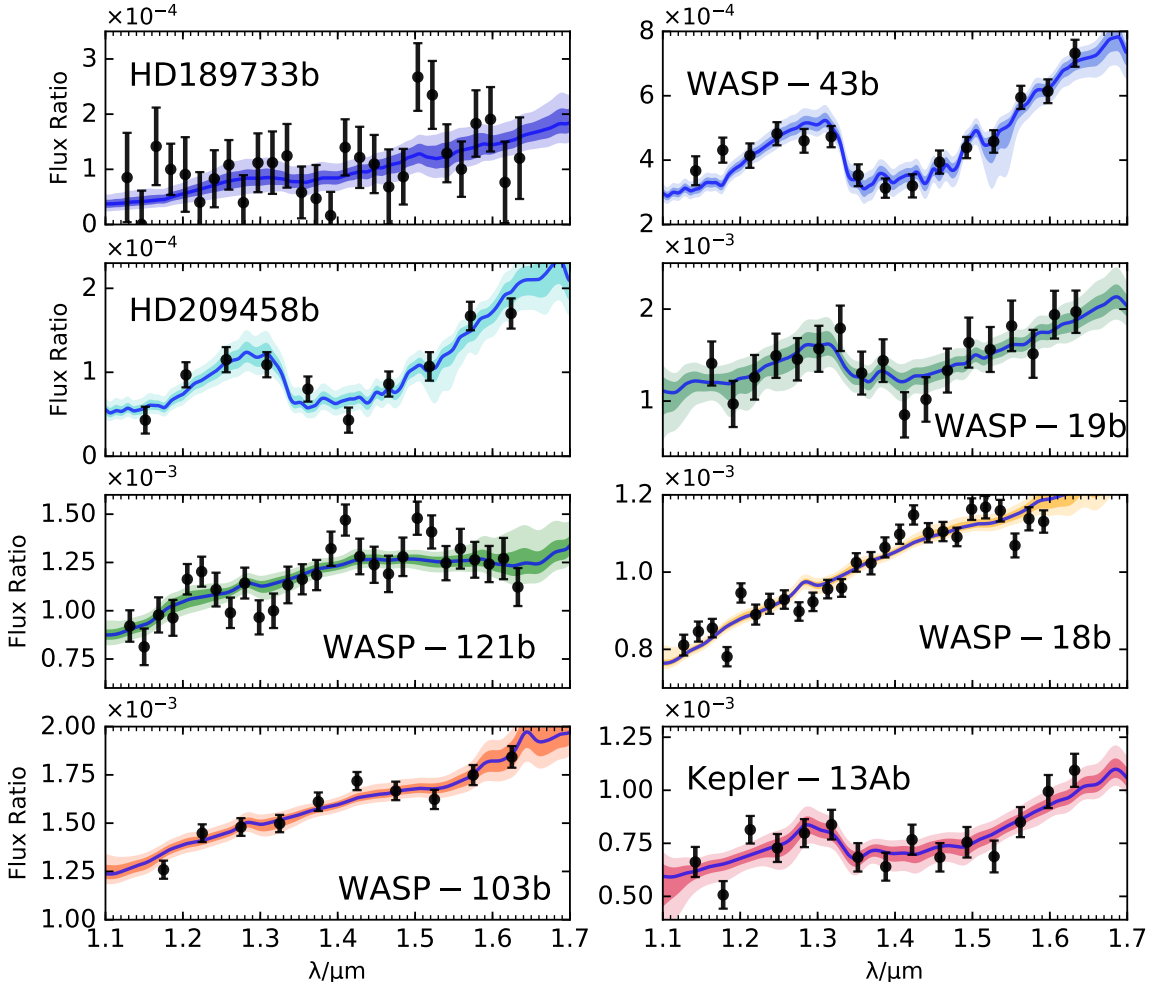

Fig. 7.3 Retrieved spectral fits and HST WFC3 data for each system. The flux ratio is shown against the wavelength in the 1.1-1.7 μm range. The data and its associated error is shown in black and the median fit to the data is shown with the blue curve. The dark and light shaded regions represent the 1 and 2σ uncertainty in the retrieved flux ratio for each planet.

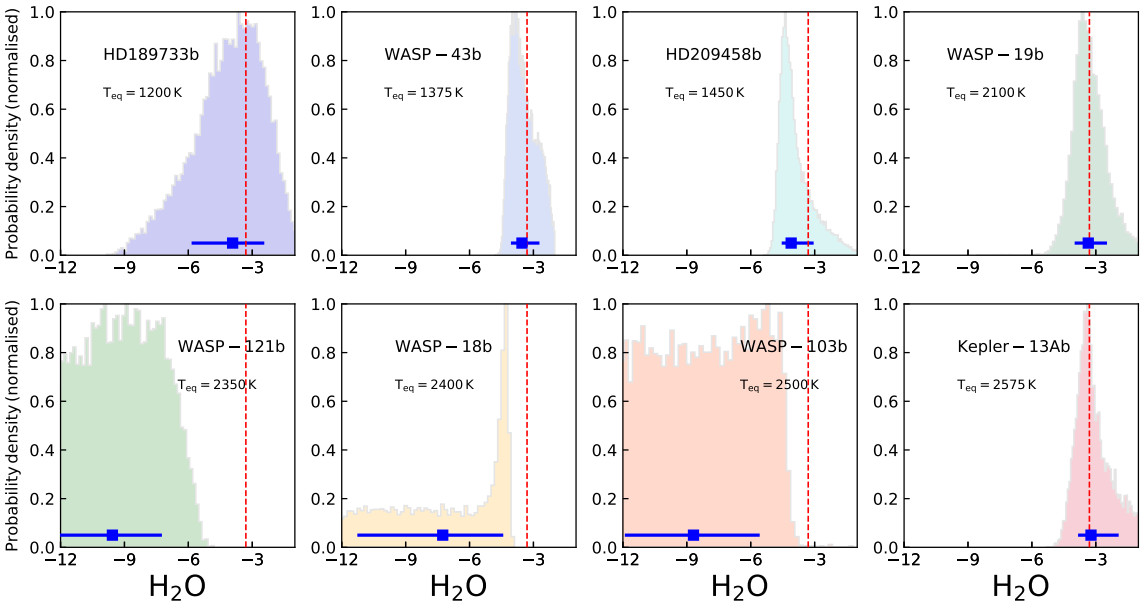

Fig. 7.4 Retrieved H_2O abundances for each planet in our study, coloured according to their equilibrium temperature. Each plot shows the undissociated abundance, and the pressure and temperature dependent H_2O abundance has been calculated from the dissociation model discussed in chapter 6.2.1. The shaded regions show the probability density distribution and the blue error bar represents its median value along with its associated 1σ uncertainty. Also shown on the red dashed line is the solar value of H_2O at the planet equilibrium temperature and 0.1 bar pressure.

spectral signatures, H_2O, CH_4, NH_3, CO, HCN, CO_2 and C_2H_2. For the ultra-hot Jupiters we do not expect many of these species to be present in the atmosphere, and for other effects such as thermal dissociation to be significant. We thus retrieve the H_2O, CO, CO_2, TiO, VO and H- abundance, all with thermal dissociation modelled from Parmentier *et al.* (2018).

The planet properties for each system is shown in table 7.1. In this study we are most interested in the H_2O abundance and temperature profile, given that these are the best constrained parameters given current observations. These are shown in the table along with their 1σ uncertainty. In what follows we describe the spectral fit, molecular abundances and temperatures profiles for each system.

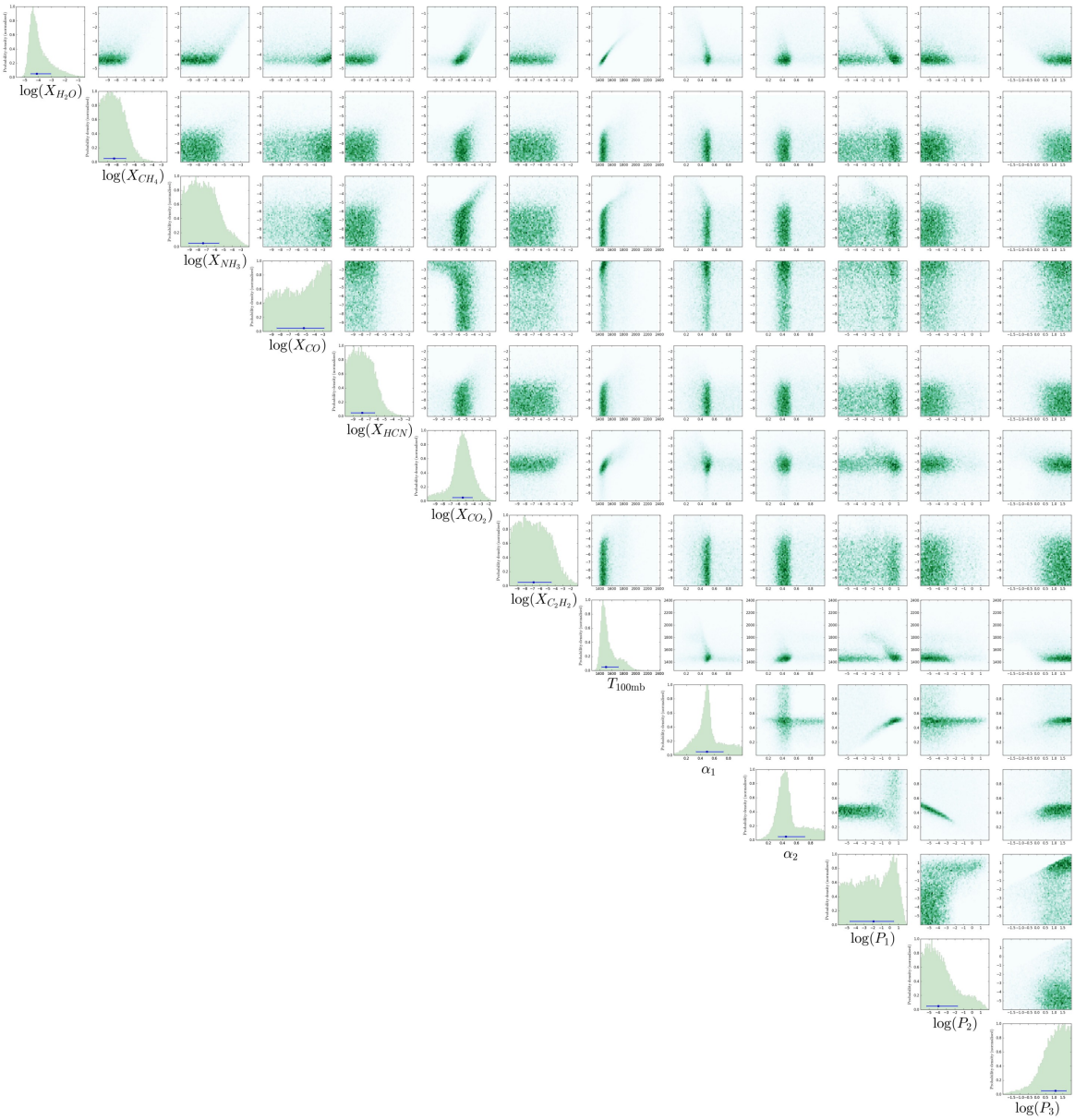

Fig. 7.5 Posterior distribution of HD209458b's retrieved dayside emission spectrum. The dataset was obtained from Line *et al.* (2016) and considers HST WFC3 and four Spitzer photometric channels between 3.6-8 μm. We retrieved seven volatile chemical species, H_2O, CH_4, NH_3, CO, HCN, CO_2 and C_2H_2, and parametrised the atmospheric temperature profile with six parameters, as discussed in section 5.2.2.

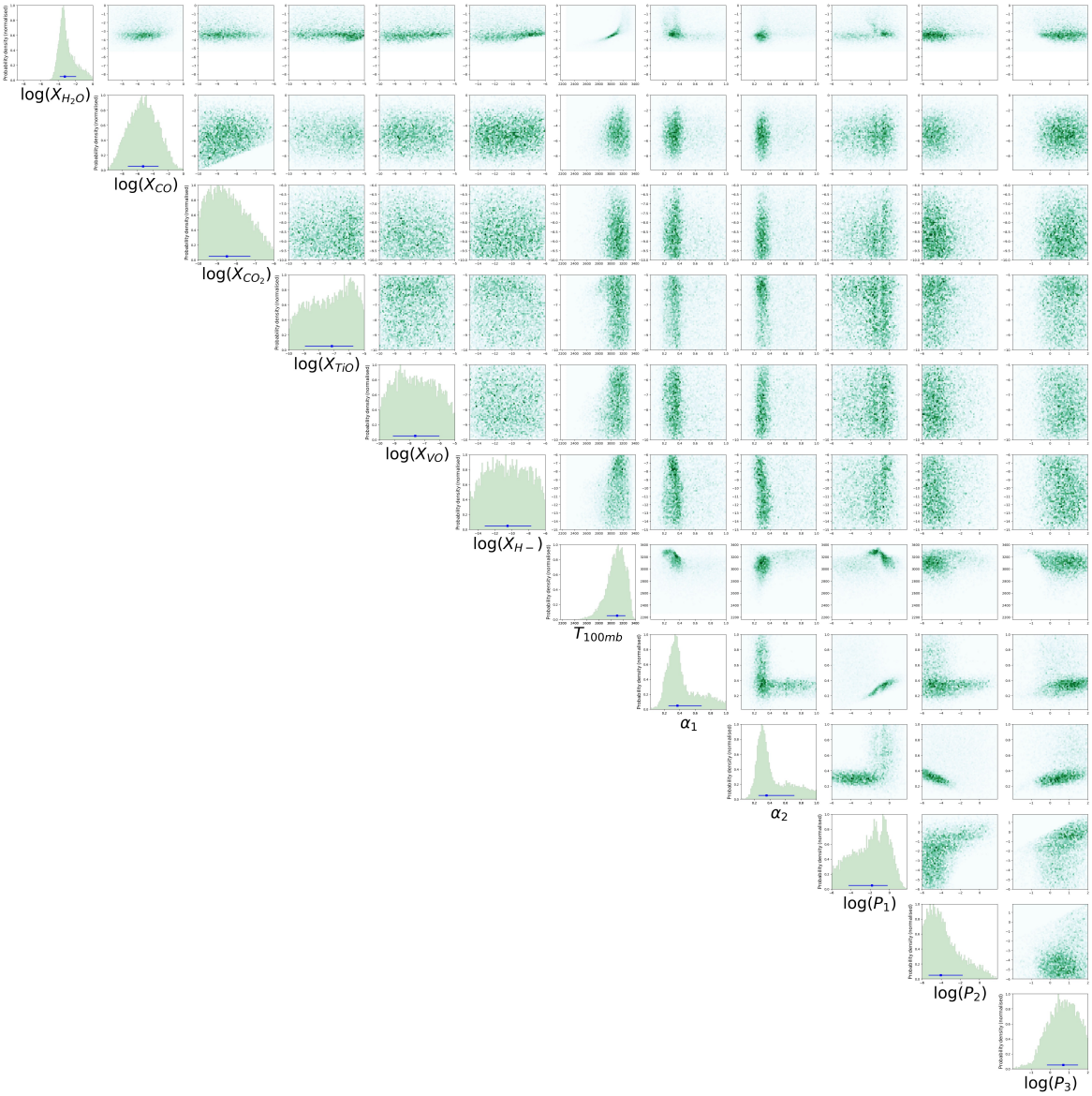

Fig. 7.6 Posterior distribution of Kepler-13Ab's retrieved dayside emission spectrum. The dataset was obtained from Beatty *et al.* (2017a) and considers HST WFC3 and two Spitzer photometric channels between ∼3.6-5 μm. We retrieved six chemical species, H_2O, CO, CO_2, TiO ,VO and H-, and parametrised the atmospheric temperature profile with six parameters, as discussed in section 5.2.2.

7.4.1 Spectral Fits

The retrieved spectral fits to the observations are shown in figure 7.3 for the HST WFC3 1.1-1.7 μm range. We show the 1 and 2σ error on the spectrum from the retrievals of each planet along with the data. The constraints obtained on the spectral fits vary according to each planet. Hot Jupiters such as WASP-43b and HD209458b clearly show tighter constraints on the model parameters due to the higher precision data available. On the other hand HD189733b shows one of the weakest fits with the lowest precision observations. A significant number of the planets, e.g. WASP-43b, HD209458b and Kepler-13Ab, show strong absorption features at $\sim$1.4 μm. These can be attributed to absorption of radiation due to H_2O opacity, as it is the strongest in this spectral range (see fig. 5.3). On the other hand the spectra for WASP-121b, WASP-103b and WASP-18b are largely featureless and therefore we constrain a lower H_2O abundance in the photospheres of these planets. We also constrain a more isothermal/inverted $P-T$ profile for these planets.

The retrieved parameters corresponding to the spectral fits are discussed below. Generally we see good agreement with retrievals performed by previous groups on the datasets. The derived H_2O abundances and their associated errors show the tightest constraints for the observations with the greatest precision. Similarly, the derived photospheric temperature (T_{100mb}) is similar to the expected equilibrium temperature for all of the planets in the sample.

7.4.2 Molecular Abundance Inferences

H_2O Mixing Ratios

The retrieved H_2O abundance for the sample of planets is shown in fig. 7.4. The cooler planets, especially WASP-43b and HD209458b, have good H_2O constraints given their strong H_2O absorption feature seen in fig. 7.3. These two planets also have high precision observations, thus enabling stringent constraints on the atmospheric H_2O abundances. These constraints on the H_2O do agree well with previous retrievals performed for WASP-43b and HD209458b (Kreidberg *et al.*, 2014; Line *et al.*, 2016). The general trend we observe as the equilibrium temperature of the planet is increased is that the H_2O features in the spectra are weaker and the retrieved abundance has a higher uncertainty. For instance, the planets with an equilibrium temperature $\lesssim$2000 K have the most precisely retrieved H_2O abundances compared to hotter planets (see fig. 7.4). This may be caused by a reduced H_2O abundance (e.g. through thermal dissociation or a super-solar C/O ratio) on the hotter planets (WASP-121b, WASP-18b

and WASP-103b), thus reducing the strength of spectral features in the WFC3 band. Planets such as Kepler-13Ab however do show absorption features occurring from H_2O in the atmosphere. Our results are consistent to within 1σ with the previous retrieval analyses for the datasets (Evans *et al.*, 2017; Kreidberg *et al.*, 2014; Line *et al.*, 2016; Sheppard *et al.*, 2017) with only slight differences in the estimated values.

Many of the planets have retrieved H_2O abundances consistent with the solar value of $\log(H_2O) \approx -3.3$ (Madhusudhan, 2012), particularly for the cooler planets but the uncertainties allow for sub-solar as well as super-solar values. At these high temperatures the equilibrium atmospheric chemistry is not expected to vary too significantly, and the H_2O abundance of the photosphere (0.1 bar) in chemical equilibrium is expected to be $\sim 5 \times 10^{-4}$ between ∼1200-2000 K (Madhusudhan, 2012; Moses *et al.*, 2013). At higher temperatures however thermal dissociation may play an important role in reducing the H_2O abundance (see chapter 6). WASP-18b does show sub-solar H_2O in the atmosphere. This is similar to the retrieved abundances of WASP-103b and WASP-121b as shown in table 7.1. All of these retrievals were run with thermal dissociation and their undissociated photosphere abundance is shown in fig. 7.4 which remain inconsistent with and lower than the expected undissociated solar value of $\log(H_2O) \approx -3.3$. Our results for WASP-121b are at odds with previous retrievals (Evans *et al.*, 2017), however, the low H_2O seen for our retrievals is most likely explained by the inclusion of H- opacity (see section 7.4.2). For the other planets the uncertainties allow for sub-solar as well as super-solar abundances. The different pathways for H_2O depletion in hot Jupiter atmospheres are detailed in section 7.5.

Fig. 7.7 shows the 100 mbar temperature and the H_2O abundance for each planet versus the equilibrium temperature, normalised relative to the metallicity of the host star. This normalisation removes variation in the metallicity between host stars and ensures that we consider the metallicity against a Sun-like star. Overall there is a greater abundance variation in our retrieved H_2O mixing ratios for the planets with a higher temperature, particularly those which also possess a thermal inversion. We also show the H_2O abundances computed from an equilibrium chemical model (chapter 3.3.5) at the photospheric pressure for various C/O ratios by the solid curves in fig. 7.7. A planet with a super-solar C/O ratio leads to depletion of H_2O in a chemical equilibrium atmosphere at sufficiently high temperature (Madhusudhan, 2012). At these high temperatures, CO is the most stable chemical species, and therefore a $C/O \gtrsim 1$ depletes the atmosphere of oxygen required to form H_2O as it is bound in CO (Moses *et al.*, 2013). Therefore at temperatures above ∼2000 K H_2O becomes significantly reduced by over two orders of magnitude with a C/O∼1 (see fig. 7.7).

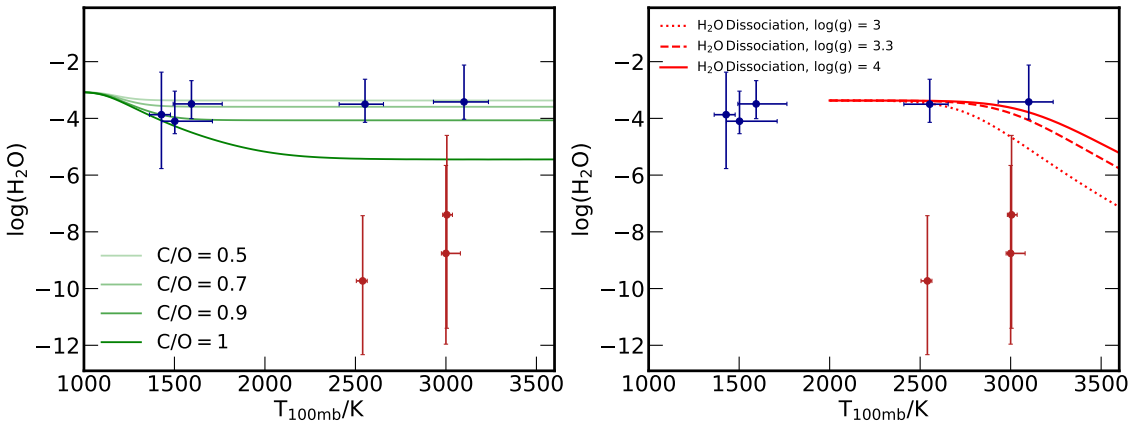

Fig. 7.7 H_2O abundance versus temperature at 100 mbar. These abundances are normalised relative to the metallicity of the host star. These are shown with their 1σ uncertainty. The five hottest planets show the dissociated H_2O abundances. Planets with a thermal inversion have been shown in red and ones without are blue. The left panel also shows the equilibrium chemical abundances for a range of C/O ratios at a pressure of 100 mbar as a function of the temperature (see chapter 3.3.5). The right panel shows the H_2O abundance in the photosphere as a function of temperature from thermal dissociation (Parmentier *et al.*, 2018). These are shown at planetary gravity ranging from $\log(g) = 3 - 4$ (cgs).

The right panel of figure 7.7 shows the predicted H_2O abundances as a function of temperature considering thermal dissociation of H_2O (Parmentier *et al.*, 2018). In the photospheres (P$\sim$0.1 bar) of hot Jupiters with temperatures $\sim$2500-3000 K the H_2O abundance may be reduced by dissociation. For these temperatures and pressures, dissociation can play a significant role in depleting the H_2O and thus result in spectra with significantly reduced features (Arcangeli *et al.*, 2018; Lothringer *et al.*, 2018; Parmentier *et al.*, 2018). Higher $\log(g)$ can also affect the location of the photosphere in the atmosphere. The photospheric pressure is proportional to the surface gravity of an atmosphere, as discussed in Parmentier *et al.* (2018). A lower planetary gravity will increase the scale height of the atmosphere and therefore move the photosphere to lower pressures, where dissociation is more effective. Planets with a low surface gravity such as WASP-121b may therefore be strongly affected by dissociation (Parmentier *et al.*, 2018). With a $\log(g) \sim 3$ (cgs), even temperatures as low as $\sim$2500 K can begin to deplete H_2O in the photosphere and thus reduce the strength of spectral features.

Five of the planets in our study, WASP-19b, WASP-121b, WASP-18b, WASP-103b and Kepler-13Ab, have temperatures in their photospheres high enough for dissociation to significantly affect the H_2O abundance in the dayside atmosphere. We have therefore included dissociation into our retrieval models for these planets. We have also run additional retrievals of WASP-19b without dissociation and H- to ensure agreement between results. WASP-19b and Kepler-13Ab do show a strong H_2O feature in their spectra. Our retrievals on these planets show that with thermal dissociation the abundance of H_2O is consistent with solar expectations. On the other hand, WASP-18b, WASP-121b and WASP-103b show a low H_2O abundance, despite accounting for the loss due to dissociation (e.g. see chapter 6). The uncertainty on the H_2O abundance in the retrieved dayside emission spectra do not allow us to significantly constrain the dissociation of H_2O as the dominant mechanism given that no lower limit is placed on the H_2O abundance. This is due to the much weaker spectral features in the HST WFC3 spectra. Further high precision observations will be key to exploring this further.

Other Species

Constraints on other species are much weaker given the current observational data for these hot Jupiters. Most of the other species are expected to be at a lower abundance for such atmospheres (Madhusudhan, 2012), and thus they possess weaker opacity (as depicted in figs. 5.3 and 6.1). Hence constraints on such species has been minimal.

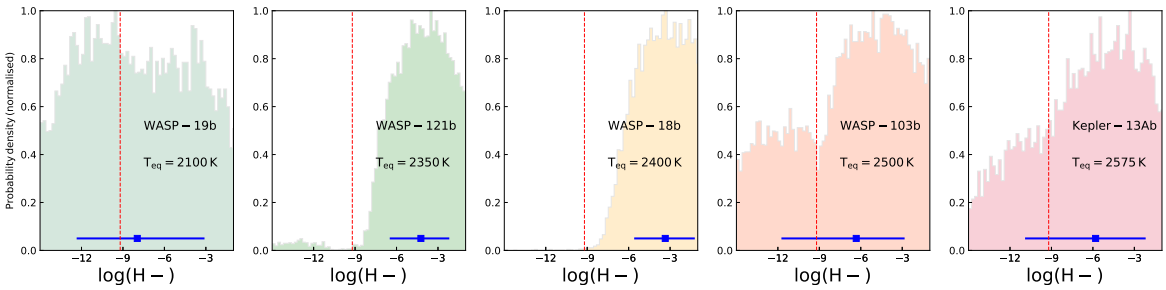

Fig. 7.8 Retrieved H- abundances for the ultra-hot Jupiters in our study, coloured according to their equilibrium temperature. Each plot shows the undissociated abundance, and the pressure and temperature dependent abundance has been calculated from the dissociation model discussed in chapter 6.2.1. The shaded regions show the probability density distribution and the blue error bar represents its median value along with its associated 1σ uncertainty. Also shown on the red dashed line is the solar value of H- at the planet equilibrium temperature and 0.1 bar pressure.

The CO is likely to be present at a significant abundance, but has almost no spectral feature in the 1.1-1.7 μm range. The CO does show features in the Spitzer 4.5 μm bandpass (Burrows *et al.*, 2008; Madhusudhan and Seager, 2010), however we are still unable to extract a significant abundance constraint for most systems. We do constrain the CO abundance on WASP-18b due to the strong emission feature from CO in the 4.5 μm band (see chapter 6). We are also able to constrain CO on WASP-103b from the emission feature in the Spitzer band. We find an abundance of $\log(\mathrm{CO}) = -1.86^{+0.47}_{-0.79}$, super-solar compared to the expected value of $\log(\mathrm{CO}) \sim -3.4$ (Moses *et al.*, 2013). This in fact also constrains our O/H ratio in section 7.5.3 given the lower H_2O abundance. In addition, we retrieve either CO or CO_2 on WASP-43b as discussed further in chapter 5, but are unable to confirm either species due to the degeneracies between the two molecules in the 4.5 μm Spitzer IRAC photometric band.

We investigated the other molecular species and found upper limits for most at $\log(\mathrm{X}) \approx -4$. These species were not well constrained because of their weak spectral signature in the WFC3 bandpass. However we were able to see a potential VO detection for WASP-121b, similar to that seen from Evans *et al.* (2017). The retrievals point to an abundance of $\log(\mathrm{VO}) = -6.9^{+0.8}_{-5.2}$, with the solar value being $\log(\mathrm{VO}) \approx -8$ (see chapter 4). It may be the case however that the abundance cannot be well constrained because of its dependence on a few data points and relatively weak spectral signature in the WFC3 bandpass. Greater spectral coverage in the near infrared with telescopes such as JWST will enable us to further constrain and refine our retrieved abundances, as well as investigate the abundance of other trace species such as CH_4, NH_3 and HCN.

The ionic species H- can also form in the atmospheres of the ultra-hot Jupiters which have temperatures in excess of 2500 K (see chapter 6). We include the H- abundance as a free parameter in our retrievals of these systems, namely WASP-19b, WASP-121b, WASP-103b, WASP-18b and Kepler-13Ab. The retrieved H- abundances are shown in fig. 7.8. We see no constraint for H- in WASP-103b, WASP-19b and Kepler-13Ab, given the current data quality of the WFC3 observations. WASP-121b and WASP-18b have higher precision and spectral resolution and we do see some constraints on H-. However, the abundance is unphysical. The constrained abundance for WASP-121b is $\log(\mathrm{H}-) = -4.2^{+2.1}_{-2.3}$ and WASP-18b is similar at $\log(\mathrm{H}-) = -3.4^{+2.1}_{-2.2}$. These values are inconsistent with the expected solar abundance of $\log(\mathrm{H}-) \sim -8.5$ (Arcangeli *et al.*, 2018). These abundances are constrained by the dip in the handful of WFC3 data points near 1.64 μm in both datasets, where H- has a spectral feature (see figure 6.1). In previous work (Evans *et al.*, 2017) the dip in the WFC3 data at 1.6 μm was best fit with H_2O absorption, but with the inclusion of H- into our model this is now the preferred species to exoplain the spectral feature. To confirm that the H- constraints do indeed come from these data points we have carried out retrievals with the WASP-18b dataset without the dip by eliminating the final 6 data points in the WFC3 band observations. With this we obtain no strong constraints on any chemical species, and only weak constraints on CO and thermal inversion from the Spitzer observations, consistent with that found from Sheppard *et al.* (2017). We have additionally retrieved the emission spectrum of WASP-18b with the data by Arcangeli *et al.* (2018) and Arcangeli *et al.* (2019), but neither of the retrievals run with these datasets showed any constraints on H- as discussed in chapter 6. This shows that H- constraints are weak and highly sensitive to a few data points, thus making H- elusive to detect given current observations, contrary to that seen from equilibrium models (Arcangeli *et al.*, 2018).

7.4.3 $P - T$ Profile

The retrieved atmospheric pressure-temperature ($P - T$) profiles along with their associated uncertainties are shown in fig. 7.9. All of the planets show the most stringent temperature constraints in the photosphere, near ∼0.1 bar pressure. This is unsurprising given that the bulk of the spectrum is generated in this region of the atmosphere. Away from the photosphere the uncertainties increase given that the generated spectrum is less sensitive to the temperature. The most precise constraints are once again obtained from highest precision data for planets such as WASP-43b, HD189733b and WASP-18b. Three planets, WASP-121b, WASP-103b and WASP-18b

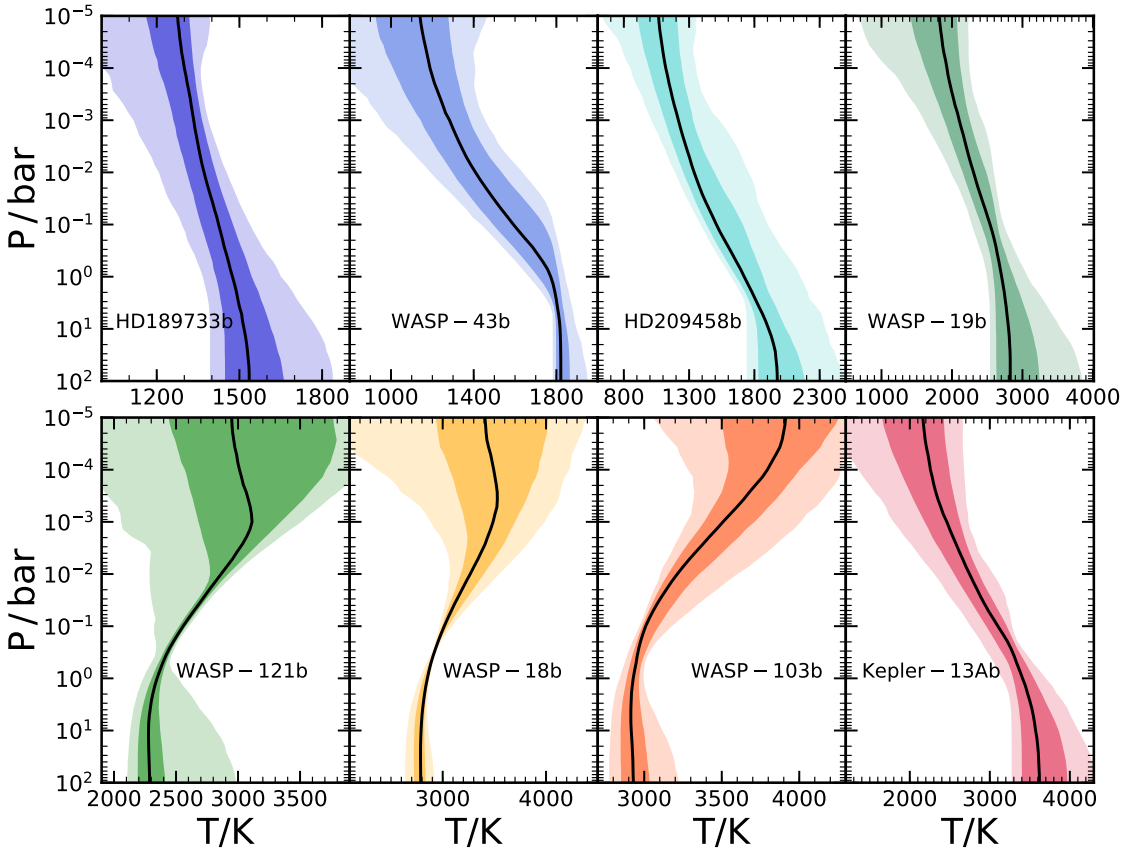

Fig. 7.9 Retrieved $P-T$ profiles for each of the planets in our study. The black curve represents the median temperature profile and the dark and light shaded regions the 1 and 2σ uncertainties respectively.

show signs of a thermal inversion which may be caused by the presence of visible absorbers such as TiO or VO as discussed below. Atmospheric temperature profiles of these planets are expected to be isothermal below the photosphere at P$\gtrsim$1 bar (Burrows *et al.*, 2008). Almost every planet in our sample shows the onset of this at which point the uncertainty on the temperature increases due to the insensitivity on the observed spectrum below this layer. Similarly the top of the atmosphere is also weakly constrained due to the low optical depth and thus negligible influence of these regions on the spectrum.

Thermal Inversions

Photospheric thermal inversions or stratospheres are seen in three of the eight planets we consider, WASP-121b, WASP-18b and WASP-103b (see fig. 7.9). These are some of the hottest exoplanets observed, with equilibrium temperatures $\gtrsim$2500 K. These thermal inversions are of particular relevance given that they have such a strong spectral signature. These inversions can cause emission features to occur in the WFC3 spectra. However, for all of these systems the retrievals point to an atmosphere that is inherently depleted of H_2O below the solar value, even with the inclusion of dissociation. This is due to the featureless spectra (see fig. 7.3). The inversion for WASP-18b and WASP-103b is in fact most strongly constrained from the CO abundance, obtained from the Spitzer 3.6 μm and 4.5 μm band. These photometric observations indicate a thermal inversion from the emission features from CO in the 4.5 μm band.

We do observe constraints for VO in one planet, WASP-121b, but no conclusive detection and no constraint on the other planets. Temperatures above 2000 K are predicted to have gaseous TiO and VO present in the atmosphere. If present at sufficient abundance their strong visible opacities can lead to inversions (chapter 4). This is caused by absorption of the incident stellar flux in the upper atmosphere, which results in the upper layers heating to a greater extent compared to the deeper layers of the atmosphere. Predicted thermal inversions with VO from 1-D radiative-convective equilibrium models do indicate that the abundance retrieved, $\log(\mathrm{VO}) = -6.9^{+0.8}_{-5.2}$, may not be sufficient to cause an inversion at solar abundance (Evans *et al.*, 2017; Fortney *et al.*, 2008; Spiegel *et al.*, 2009). However, as we have shown in chapter 4, an atmospheric C/O ratio of 1 lowers the required abundance for VO in order to form an inversion. At a C/O ratio of 1, an abundance as low as $\log(\mathrm{VO}) = -8.7$ may be enough for an inversion to occur due to the lower infrared opacity from the reduced H_2O abundance.

As well as TiO and VO, previous studies have shown that a range of other opacity sources are capable of giving thermal inversions at such high temperatures, particularly when H_2O abundances may be low (see chapter 4). Species such as Fe, SiO, Na, K and other metal hydrides are also capable of absorbing a large fraction of the stellar flux, which may lead to a stratosphere in the atmosphere without TiO or VO present (Lothringer *et al.*, 2018; Mollière *et al.*, 2015). Unfortunately these species cannot be constrained from infrared observations such as WFC3, due to their lack of significant opacity at such wavelengths. Observations of emission spectra in the visible is not possible given the brightness of the star and the weaker planetary signal. Observations through transmission spectroscopy with visible wavelengths may offer

a path to constrain such species, particularly with recent improvements through ground-based observations (Nugroho *et al.*, 2017; Sedaghati *et al.*, 2017).

Lack of Inversions on Other Systems

The cooler planets such as WASP-43b, HD189733b and HD209458b do not show signs of thermal inversions. These planets have an equilibrium temperature of ∼1200-1450 K, where the TiO and VO are likely condensed out of the upper atmosphere (Spiegel *et al.*, 2009). Thus on such planets there is insufficient visible opacity from TiO/VO to lead to thermal inversions. However, sulphur based species have been proposed to cause thermal inversions at these relatively cool temperatures (Zahnle *et al.*, 2009). As well as this, species such as Na and K have also been proposed at high C/O ratios which may also lead to stratospheres on such atmospheres (Mollière *et al.*, 2015). However, we do not see any signs of inversions in these planets.

Kepler-13Ab and WASP-19b also have temperatures high enough for gaseous TiO and VO to be present but the retrieved $P-T$ profiles show no inversions. Recently, work by Sedaghati *et al.* (2017) has detected TiO in the transmission spectrum of WASP-19b, but this has indicated a sub-solar abundance. Both of these planets show significant H_2O absorption and the spectra in fig. 7.3 clearly show absorption features from the non-inverted profiles. Therefore, it is unlikely that species such as TiO or VO are present at or near solar abundance as this would result in emission features from the stratosphere formed.

7.5 Discussion and Conclusions

We report a homogeneous retrieval of the atmospheric properties of eight transiting hot Jupiters using emission spectroscopy. The eight planets have some of the best signal to noise datasets available with the HST WFC3 spectrograph as well with Spitzer IRAC photometry. We perform a homogeneous retrieval of all of these planets using our HyDRA retrieval code from chapter 5. Our results show good agreement with previous analyses of these systems where retrievals have been reported (Evans *et al.*, 2017; Kreidberg *et al.*, 2014; Line *et al.*, 2016; Sheppard *et al.*, 2017). We constrain the atmospheric temperature profile with six retrieved parameters, and the atmospheric abundance of several other chemical species. These species are chosen based on their prominence in the near infrared spectrum in several theoretical studies (Moses *et al.*, 2013; Parmentier *et al.*, 2018).

7.5.1 Retrieved Abundances

We see strong H_2O absorption in several spectra, most notably WASP-43b, HD209458b, WASP-19b and Kepler-13Ab. All three of these systems show H_2O at abundances $\log(H_2O) \gtrsim -5$ at 3σ or greater. WASP-18b, WASP-121b and WASP-103b on the other hand show negligible H_2O absorption and thus the abundance retrieved is sub-solar and outside the solar value of $\log(H_2O) \approx -3.3$ by 1σ or more. The uncertainties in the H_2O abundances generally increase as $T_{eq} \gtrsim$2000 K, given that these hotter planets are observed to have weaker spectral features (see fig. 7.4).

There are several reasons why the retrieved H_2O abundance may be sub-solar, particularly on hotter planets with an equilibrium temperature in excess of 2000 K. One possible scenario is an atmospheric C/O ratio higher than the solar value of 0.54 (Asplund *et al.*, 2009). The C/O ratio of hot Jupiters strongly affects the H_2O abundance (Madhusudhan, 2012), and equilibrium chemical models have shown that C/O $\gtrsim$ 1 can deplete the H_2O by over 2 orders of magnitude at high temperatures (Madhusudhan, 2012; Moses *et al.*, 2013). The overall planetary C/O ratio is of great importance given its sensitivity to the formation of the planet and the migration to its current position (Öberg *et al.*, 2011). Formation of the planet beyond the CO/CO_2 snowline followed by disk-free migration results in a C/O ratio that is ∼1 for a solar composition disk (Madhusudhan *et al.*, 2014c). Thus for planets with an observed C/O ratio of unity we would expect them to have formed beyond these snowlines. The migration through the disk would also re-enhance the oxygen and therefore result in a planet with a near solar C/O ratio, thus for such planets with C/O∼1 disk-free migration must occur to preserve their ratio unless pebble accretion occurs without core erosion (Booth *et al.*, 2017; Madhusudhan *et al.*, 2016).

Photodissociation of species such as H_2O has also been proposed to explain the reduced feature of H_2O in the WFC3 bandpass seen for some planets (Arcangeli *et al.*, 2018; Lothringer *et al.*, 2018; Parmentier *et al.*, 2018). At high temperatures H_2O is expected to dissociate and therefore diminish the absorption feature at 1.4 μm. This is particularly the case for planets with a thermal inversion, as the dissociation occurs more significantly at higher altitudes where the high temperature drives H_2O depletion even further (Arcangeli *et al.*, 2018; Lothringer *et al.*, 2018; Parmentier *et al.*, 2018). It is proposed that such hot Jupiters with thermal inversions should therefore show H_2O depletion in their spectra. We also observe this trend, and the three planets with a thermal inversion all show largely featureless WFC3 spectra (see fig. 7.3). As well as the reduced H_2O abundance in the atmosphere, the strength of the absorption feature in the spectrum is also reduced by the $\tau_\nu \approx 1$ surface being in a narrower zone in

the atmosphere, reducing the temperature range probed. However, very hot planets ($\gtrsim$2000 K) are required for this to be significant (Parmentier *et al.*, 2018). In any case, even accounting for dissociation, our retrievals point to an inherently sub-solar abundance, albeit with weaker constraints for these ultra-hot planets due to their weaker WFC3 features. Cooler planets are largely unaffected in the photosphere where the bulk of the spectrum is generated, unless extremely irradiated (Moses *et al.*, 2013).

The surface gravity is also an important quantity in determining the photospheric H_2O abundance due to dissociation. Planets with a higher gravity such as Kepler-13Ab have a photosphere at higher pressures, i.e deeper in the atmosphere, where the dissociation of H_2O is less significant. On the other hand, planets with a low gravity ($\sim$1000 cm/s^2) such as WASP-121b will have a photosphere at a higher altitude in the atmosphere, and are therefore more susceptible to dissociation (Parmentier *et al.*, 2018).

A reduced metallicity of the planet would also deplete the H_2O, given that there is a lower quantity of oxygen available. However, an excellent probe of the overall metallicity is the CO abundance, given that it does not vary significantly with C/O ratio (Madhusudhan, 2012), nor does it photodissociate readily on hot Jupiters (Moses *et al.*, 2013; Parmentier *et al.*, 2018) and is thus largely unaffected by temperatures $\gtrsim$1200 K. A CO constraint may thus allow for the testing of several formation/migration models. A low metallicity has been proposed from some core-accretion and gravitational instability models with disk-free migration (Madhusudhan *et al.*, 2014c, 2016). Future instrumentation with higher spectral coverage, particularly the $\sim 5\mu$m CO feature, will allow us to study and constrain this further. Due to the complexity and diversity of these exoplanets, it may be the case that multiple such scenarios occur on these hot giant exoplanets.

We retrieve H- for five of the planets which have equilibrium temperatures in excess of 2000 K. For three of these planets the H- is unconstrained. For the remaining two a very high H- seems to be required to fit the data. We observe some constraints on H- for WASP-121b and WASP-18b, but these are significantly super-solar, $\sim 10^4\times$ the expected solar value for both planets. This is in contrast to Arcangeli *et al.* (2018), who used equilibrium models and suggested the H- to be solar. The H- abundances are determined by the final few data points in the WFC3 range, which probe the H- spectral feature at $\sim$1.64 μm (see fig. 6.1). For both WASP-18b and WASP-121b, a dip is seen at this end of the WFC3 range in the data, which constrain a very high H- abundance in order to fit the observations. On the other hand models without H- for both of these planets fit just as well. Further dayside emission observations for some of

the very hottest systems such as these may help us to obtain better constraints and determine the role that H- plays in the observed spectra.

7.5.2 Retrieved $P-T$ Profile

We see thermal inversions on three of the planets we study, WASP-121b, WASP-103b and WASP-18b, consistent with previous retrievals and forward models of these planets (Evans *et al.*, 2017; Kreidberg *et al.*, 2018; Sheppard *et al.*, 2017). These planets are some of the hottest (see fig. 7.9), with temperatures in excess of 2000 K, and fall into the category of ultra-hot Jupiters (Fortney *et al.*, 2008). The photospheres of these atmospheres are hot enough for species such as TiO and VO to remain gaseous and lead to thermal inversions owing to their strong visible opacity. Kepler-13Ab on the other hand shows no signs of thermal inversions, despite being the hottest planet that we observe. It has been proposed that a higher log(g) for planets such as Kepler-13Ab may reduce the vertical mixing and suppress the heavier gases such as TiO and VO and thus prevent a thermal inversion (Beatty *et al.*, 2017a,b). This is a possibility given that this planet is one of the more massive that we observe, which may also reduce thermal dissociation of H_2O as discussed above.

It is interesting to note that all of the planets in our study which possess thermal inversions also show inherently sub-solar H_2O. This is despite retrievals being conducted accounting for the dissociation in the atmosphere. These indicate that even accounting for the loss of H_2O due to thermal dissociation, the planets still show depleted H_2O. Simulated retrievals with WASP-18b quality datasets showed that a thermal inversion at solar H_2O with thermal dissociation could be accurately retrieved given the quality of the observations. Hence, the thermal inversions or the dissociation model are unlikely to bias the retrievals. However, without a conclusive detection of H_2O it is difficult to further quantify what this suggests for the atmospheres of these planets other than that a super-solar C/O ratio is implied given the low constraints.

The H_2O abundance seen for Kepler-13Ab may also be a reason for the lack of a thermal inversion, due to the greater infrared opacity, which acts to cool the atmosphere (chapter 4). Semi-analytic models of exoplanets predict that for a thermal inversion to occur in the atmosphere, the visible opacity, $\kappa_{\rm vis}$, must exceed the infrared opacity, $\kappa_{\rm ir}$ (Guillot, T., 2010). This emanates from the fact that thermal emission of radiation out of the planet increases with $\kappa_{\rm ir}$ whereas the absorption of stellar radiation increases with $\kappa_{\rm vis}$. Therefore a stronger $\kappa_{\rm ir}$ would lead to a temperature profile that decreases radially upward for the same $\kappa_{\rm vis}$. Given the higher water abundance, $\kappa_{\rm ir}$ is much greater for WASP-19b and Kepler-13Ab than for WASP-121b, WASP-103b or WASP-

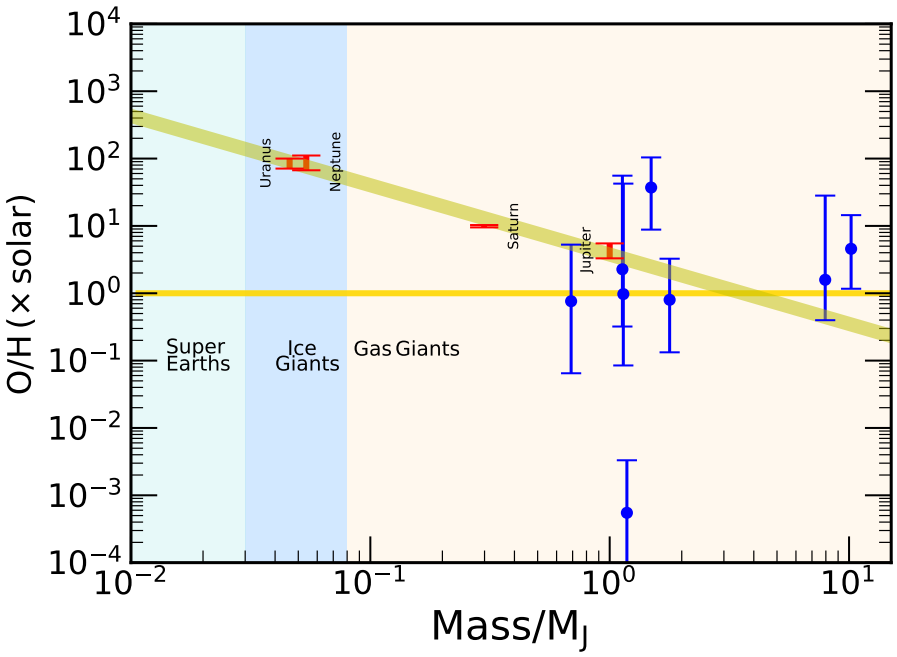

Fig. 7.10 Retrieved O/H ratio for the hot Jupiters against mass (shown in blue). Also shown for reference are the metallicities for the solar system giant planets.

18b. Therefore, assuming that the visible opacity is nearly constant, these systems show no signs of thermal inversions. Such planets with significant H_2O would need a much higher κ_{vis} in order for a thermal inversion. Future observations of these systems, particularly in the visible through transmission spectroscopy, would enable us to constrain species such as TiO/VO on these planets.

7.5.3 Mass-Metallicity Relation

The O/H ratio of each planet versus mass is shown for the eight hot Jupiters in figure 7.10. Here we use the O/H abundance as a proxy for metallicity for hot Jupiters, and we show the metallicity of the solar system planets via their CH_4 abundances for reference. We combine the retrieved abundances for all of the oxygen bearing species to give the overall oxygen abundance of a hot Jupiter atmosphere. However, given that we cannot constrain the CO abundance for many of these planets, there is a larger uncertainty in the O/H ratio.

Our derived O/H ratios provide initial clues on their trends with planet mass, as shown in fig. 7.10. The solar system planets show a metallicity trend that decreases with mass as a power law. The uncertainties on our O/H ratios do not allow a

definitive trend to be derived for exoplanets with the current data. However, most of our planets are consistent with solar metallicity while allowing for sub-solar and super-solar values. All but three of them are also consistent with the trend in metallicity for the solar system planets. The three outliers are WASP-103b, WASP-18b, and WASP-121b. While WASP-121b is clearly below solar system predictions, WASP-103b and WASP-18b are above. For these systems, the main O/H constraint comes from the retrieved CO abundance given that the H_2O is so poorly constrained. However, the uncertainty in these retrieved values for CO do not allow us to place constraints on the O/H ratio which are as reliable as for other planets, given that the CO abundance is determined primarily by only the 4.5 μm Spitzer point (see below). The majority of the other planets lie near the Jupiter mass and metallicity range. With increased spectral coverage and higher resolution spectra for such atmospheres becoming available future observations may provide further insights into the mass-metallicity relation for exoplanets.

With instrumentation such as the upcoming JWST with greater precision and spectral coverage we will be able to further constrain other molecular species. This will also allow us to explore the atmospheric processes that occur on hot Jupiters and study smaller more earth-like planets in the future. Constraints on species such as CH_4, NH_3 and HCN would greatly improve our knowledge of the composition and metallicity, and help us further understand the formation and migration processes of these planets.

Chapter 8

Detecting Species in Hot Jupiters with High Resolution Spectroscopy

"We're in the endgame now."
- Doctor Strange, Infinity War

This chapter discusses my work on high resolution spectroscopy of exoplanets. I have generated grids of model templates for various chemical species at very high resolution using the GENESIS model as discussed in chapter 3. These spectral templates have been used for detections of H_2O, CO and HCN in two hot Jupiters, HD209458b and HD189733b, based on observations in the near infrared at R$\sim$100,000 obtained using the CRIRES spectrograph on the VLT in Chile. The data was analysed by my collaborators Mr Samuel Cabot and Mr George Hawker, and their analysis pipeline is discussed in section 8.2. My work on the modelling is discussed in section 8.3. The results and discussion include analysis from the published works in Hawker *et al.* (2018) and Cabot *et al.* (2019), which I have co-authored.

8.1 Introduction

High resolution Doppler spectroscopy (HRS) from ground based observations has been used to detect chemical species in the atmospheres of hot Jupiters. This is pursued through the monitoring of numerous transition lines of a given species present in the atmosphere as these lines are Doppler shifted while the planet traverses around its host star. These can be identified over the stellar signal as the planetary velocity is significantly higher compared to the stellar orbital velocity. HRS has recently come to the fore thanks to stable high resolution spectrographs in the infrared allowing for the

planetary signal to be robustly extracted (Snellen *et al.*, 2010). Telescopes such as the Very Large Telescope (VLT), Keck and Subaru have all been used to explore HRS of a number of nearby hot giant planets.

Atmospheric characterisation with HRS should be contrasted with low resolution spectroscopy, where broad molecular bands of species are used for their detections. Detections of chemical species with HRS are carried out through cross correlation of template models with the data. Each template model spectrum is generated with a number of chemical species in the atmosphere at a given temperature profile. We typically cross correlate $\sim 10^2$-10^3 individual transition lines in the spectrum due to the contribution to the opacity from each species. These individual transition lines can be resolved thanks to the R$\sim$100,000 observations. The template models which most closely match the data have the highest cross correlation. Cross correlation against a grid of model templates can thus be used to place constraints on the abundances and temperature profiles. This method has led to a number of detections of molecular species such as H_2O and CO in nearby hot Jupiters through infrared spectroscopy using VLT and Keck (Birkby *et al.*, 2013, 2017; Brogi *et al.*, 2012; Rodler *et al.*, 2013). More recently, detections of atomic and molecular metal-rich species have also been made through high resolution observations at optical wavelengths (Hoeijmakers *et al.*, 2018; Nugroho *et al.*, 2017). In the coming decade telescopes such as the Extremely Large Telescope (ELT) and Giant Magellan Telescope (GMT) have the potential to probe an even wider range of species and smaller exoplanets, perhaps even opening up the possibility for characterisation of rocky exoplanets (Rodler and López-Morales, 2014).

HRS offers unparalleled insight into atmospheric composition without the degeneracies between chemical species interfering significantly with detections. Low resolution observations, e.g. with the Hubble Space Telescope (HST), are prone to inherent degeneracies between broad molecular features of various species (Kreidberg *et al.*, 2014; MacDonald and Madhusudhan, 2017). High resolution observations on the other hand make use of the uniqueness of the frequency of each transition for a given species. Thus when comparing numerous lines over the spectral range of observations, degeneracies between species are ruled out leading to unambiguous detections. HRS is thus complimentary to low resolution transit spectroscopy in many ways for the characterisation of exoplanetary atmospheres. The latter is typically sensitive to the temperature profile and species with broad absorption features, while the former is more sensitive to a wider range of species given that it probes the cores of spectral lines. Therefore many more species with weaker spectral features are potentially observable

through HRS. The probing of just the cores of these lines does however mean that constraints on the continuum opacity and temperature gradients are much less precise. Thus the possibility of combined low and high resolution spectroscopy is an exciting prospect (Brogi *et al.*, 2017).

Another significant strength of Doppler spectroscopy is that planetary transit is not required for detections of species. A number of species have been detected on non-transiting exoplanets such as 51 Pegasi b and τ Boo b (Birkby *et al.*, 2017; Brogi *et al.*, 2012), not possible through lower resolution observations which typically require the planets to transit. In addition, the high resolution of the observations allow for constraints on dynamical processes, such as meridional winds. This was first carried out for HD209458b (Snellen *et al.*, 2010) and has great potential for the future for exoplanets orbitting bright stars.

This chapter discusses the molecular detections of H_2O, CO and HCN made using VLT observations of HD209458b and HD189733b published in Hawker *et al.* (2018) and Cabot *et al.* (2019) respectively, both of which I co-authored. Central to these detections is the construction of high resolution spectral models which form the basis for model templates and thus the cross correlation with the data. I describe the data reduction and detrending for the high resolution observations in section 8.2. I then describe how to generate the high resolution model templates for cross correlation in section 8.3. This is followed by the results in section 8.4 where I discuss multiple potential molecular detections in the atmospheres of two well studied hot Jupiters.

8.2 Observations and Reduction

This section discusses the the data analysis carried out by my collaborators Samuel Cabot and George Hawker. I describe the data reduction pipeline that they have developed and the detrending methods they use for the detections of H_2O, CO and HCN in HD209458b and HD189733b.

We obtain spectroscopic observations of the two planets with the CRyogenic high-resolution InfraRed Echelle Spectrograph (CRIRES; Kaeufl *et al.* (2004)) on the Very Large Telescope (VLT), in Chile, made available through the European Southern Observatory (ESO) Science Archive. For HD209458b and HD189733b, the CRIRES observations cover two spectral ranges (2.29 - 2.35 μm and 3.18 - 3.27 μm) and have been obtained over multiple nights at a spectral resolution of R$\sim$100,000. We begin by describing the data reduction.

We use the `Esorex` reduction pipeline to perform initial processing and extraction of the one-dimensional spectra obtained at various times throughout the night of observations. Some bad pixels remain in the data which our post-processing scripts correct. We also normalise spectra according to their seeing conditions, i.e due to variations of the Earth's atmosphere and cloud throughout the night. We also remove (or mask) wavelengths with telluric contamination, those regions where absorption from the species in the Earth's atmosphere prevents any signal being detected (see figure 8.1). We align all spectra obtained over the course of a night to a common wavelength grid and calibrate the wavelengths for each spectrum. This calibration is carried out by aligning wavelengths where telluric absorption is strongest against a synthetic transmission spectrum (Lord, 1992). We then use our custom-built pipeline (X-COR 2.0) for analysis of phase-resolved high-resolution spectroscopy of exoplanetary atmospheres.

8.2.1 Detrending

After initial processing the reduced spectra are dominated by the stellar signal and deep telluric absorption lines caused by the Earth's atmosphere. Planetary emission leaves a characteristically unique imprint on the time-varying spectra from its varying Doppler shift over the course of the night, while other features are approximately static in time. Our next step involves separating the planetary signal from the stellar and telluric features. As such, robust detrending methods are required to remove the non-planet signals from the data.

Two key approaches have been used in previous studies for detrending (Birkby, 2018). The first is based on modelling airmass and telluric residuals and the other using the SYSREM algorithm (Tamuz *et al.*, 2005). The second of these, SYSREM, is designed to identify and subtract time-invariant signals, systematics and environmental effects and has been used in some studies (Birkby *et al.*, 2013, 2017; Nugroho *et al.*, 2017). This removes the majority of systematics without affecting the planet signal after a sufficient number of iterations. Airmass variation on the other hand affects the overall extinction caused by the atmosphere, and the depth of methane and water telluric absorption lines. Early high-resolution detections of CO in HD209458b involved fitting and removing trends due to airmass (Snellen *et al.*, 2010) and has also been commonly adopted in recent work (Brogi *et al.*, 2012, 2013, 2014, 2016; Schwarz *et al.*, 2015). This fitting of the airmass variation prevents atmospheric affects from dominating the cross-correlation function. We adopt the SYSREM detrending method for our

HD209458b results, but we adopt both airmass-based detrending and SYSREM and compare the performance of both for our HD189733b observations.

After this is done we apply a high pass filter to the data and normalise their values by their uncertainty. The final step is done to avoid noisy pixels from affecting cross correlation. Figure 8.1 panel (a) shows the extracted spectra in the 3.2 μm spectral band. Panel (b) shows the normalised data with masking, panel (c) depicts the detrended data, and panel (d) shows the data with a 40$\times$ model injection prior to detrending.

We then perform cross-correlation between each detrended spectrum and model templates over a wide range of radial velocities. Following previous analyses (Brogi *et al.*, 2012), we construct these model templates from Gaussian functions fit to the locations and depths of the strongest absorption features in the spectral model (see below). Previous studies (Brogi *et al.*, 2012; Snellen *et al.*, 2010) motivate this technique since it ignores the continuum baseline, noisier weak lines, and broad-band components (removed earlier by high-pass filter). This improves the correlation with intrinsic spectral features.

For a given $\Delta\phi$, the planet's radial velocity variation is determined by a velocity semi-amplitude (K_p) and systemic velocity (V_{sys}). Using the model templates we sample the $K_p - V_{sys}$ parameter space by Doppler shifting each template to the planetary radial velocity to result in a Cross-Correlation Function (CCF) matrix. The results for all values of K_p are presented in the array, normalised by its standard deviation to give a signal-to-noise (S/N) array as shown in fig. 8.5. A high S/N at the known V_{sys} and planetary K_p thus indicates the presence of a given molecular species. The CCFs, shifted into the rest frame of the planet, are shown in fig. 8.2 for both the data (left) and with a model injection at two times nominal strength (right). Dark trails are visible at the known value of V_{sys}.

8.3 Spectral Modelling

In order to cross correlate with the data we generate high-resolution model atmospheric spectra using the GENESIS code (chapter 3). Figures 8.3 and 8.4 show the model spectra for HD189733b and HD209458b respectively. The models involve line-by-line radiative transfer computed via the Feautrier method to obtain the emergent spectra in the observed bands at a spectral resolution of $R \gtrsim$300,000. The models assume a plane-parallel atmosphere in hydrostatic equilibrium and local thermodynamic equilibrium. These spectra form the basis of the model templates discussed earlier in section 8.2.1.

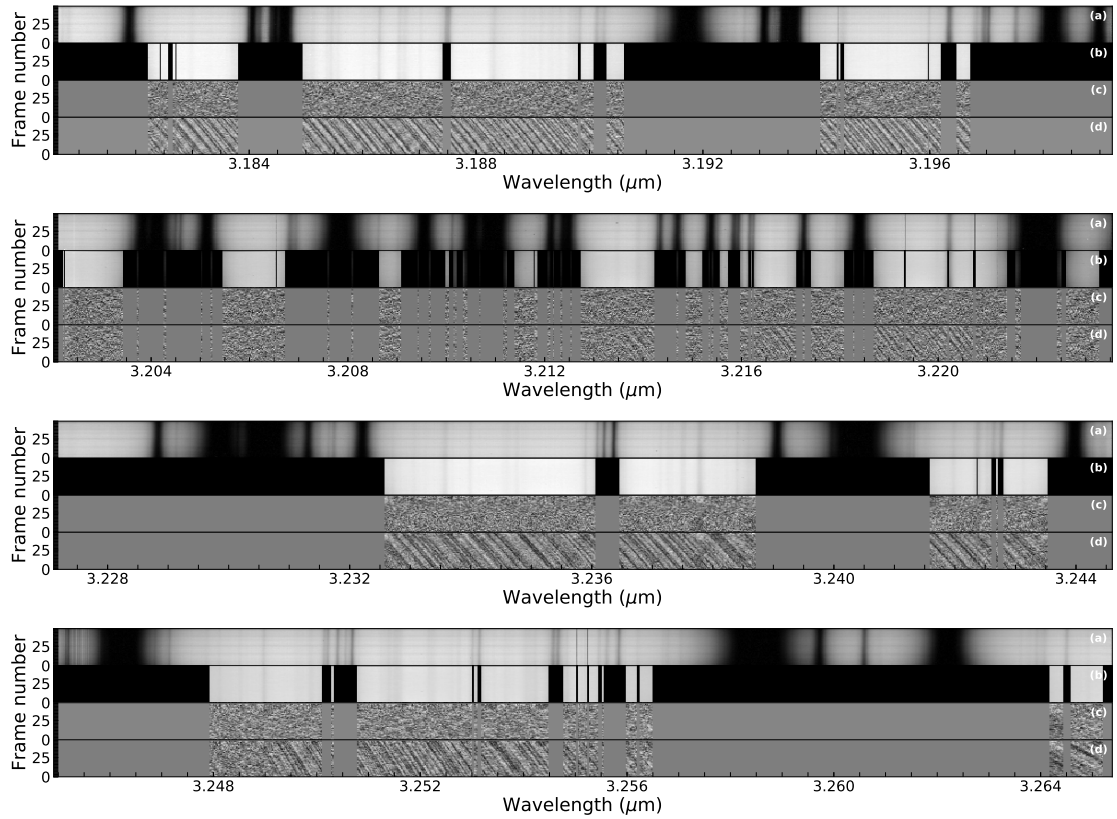

Fig. 8.1 Stages of detrending for the observations of HD209458b, for detectors 1–4 and the set of VLT CRIRES observations taken on 2011 July 25. The x-axis corresponds to wavelength, and the y-axis corresponds to frame number, increasing in time. Panel (a): spectra immediately after reduction of nodding frames. Heavy telluric contamination is evident (e.g. at 3.1915 μm). Poor seeing conditions manifest as dark horizontal bands. Panel (b): reduced spectra after wavelength calibration, alignment, additional cleaning, normalisation, and masking. This image (excluding masked regions) is the input of our detrending algorithm. Panel (c): data subject to column-wise mean subtraction, the optimal number of SYSREM iterations, a 15-pixel standard-deviation high-pass filter, and column-wise standard-deviation division. Panel (d): the same as in Panel (c), but with the injection of our planet model at 40x its nominal strength prior to detrending. The preserved planetary absorption features appear as dark trails that stretch over $\sim 0.0008\,\mu$m.

Figure 8.3 shows the $P-T$ profile and model spectra over both of the observed CRIRES spectral ranges for the planet HD189733b. For the purpose of this work we have generally ignored radiative-convective equilibrium and chemical equilibrium and generated grids of model spectra with fixed abundances and $P-T$ profiles. However, for completeness, each of the detections has been verified against radiative-convective

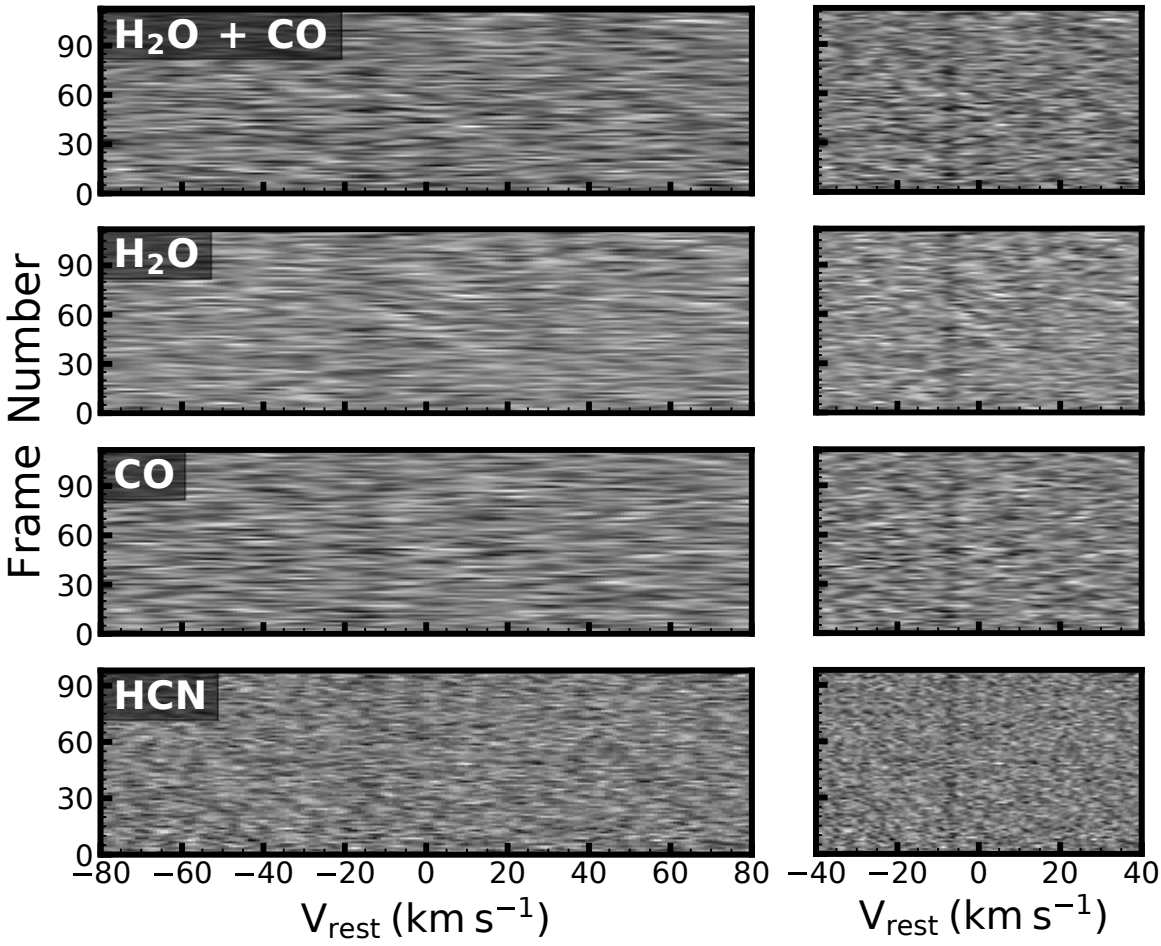

Fig. 8.2 Frame-by-frame cross correlation values as a function of velocity for the observations of HD209458b. The CCFs are shifted into the planetary rest frame by the peak significance K_p, for each model template (HCN, H_2O, CO, and their combination). The right panel shows the CCF with a model injection at two times nominal strength. Each CCF contains a dark vertical trail at approximately the known systemic velocity of -14.8 km s^{-1} from alignment between the model template and intrinsic features.

equilibrium as well as best-fit retrieved $P-T$ profiles from low resolution studies (chapter 7). We explore grids of abundances ranging from $\log(X_i) = -8$ to -3 for species i = H_2O, CO and HCN. The $P-T$ profiles also span a wide range of temperatures, between 500-2000 K but without a thermal inversion in the atmosphere, in accordance with previous low resolution observations (Crouzet *et al.*, 2014; Line *et al.*, 2016). We additionally extend the top of our model atmosphere to 10^{-8} bar. This was because the high resolut ion observations probe the spectral line cores, and thus the emission occurs from lower pressures higher up in the atmosphere given the strong opacity in

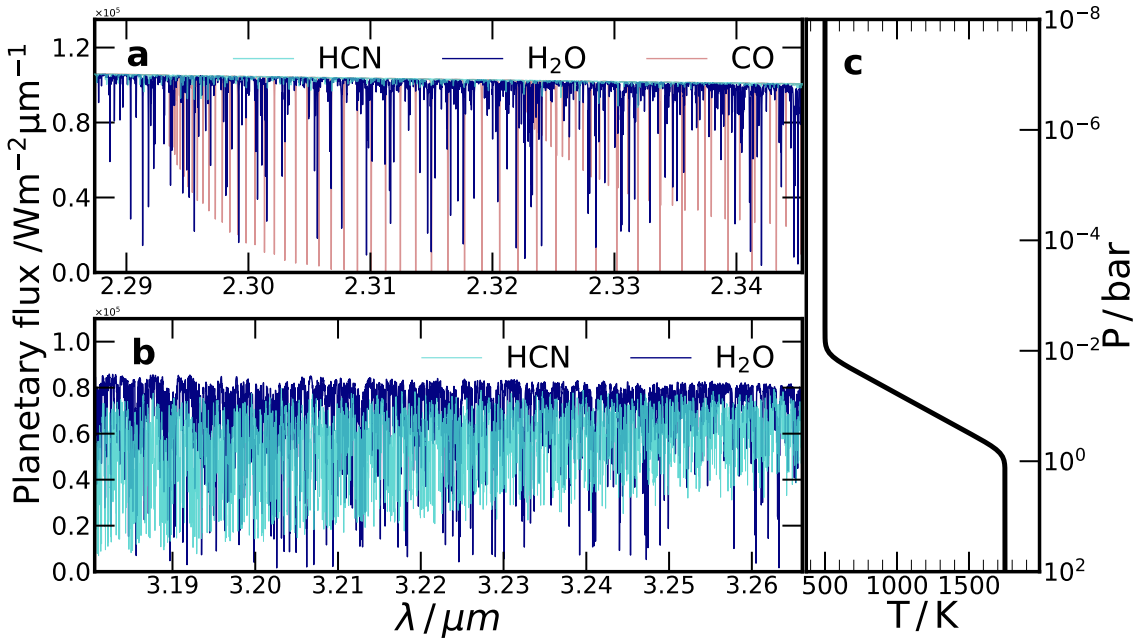

Fig. 8.3 Planetary spectra of the model atmosphere of HD189733b with different molecular species present. Panel a shows the 2.28-2.35 μm spectral range and panel b shows the 3.18-3.27 μm range. Spectra were generated with HCN (turquoise), H_2O (blue) and CO (red) with a wavenumber spacing of 0.01 cm^{-1} using the GENESIS code (chapter 3). Panel c shows the $P-T$ profile used to generate the spectra.

their line cores. Due to the greater range in observable pressures the atmosphere now comprises 150 model layers evenly spaced in log(P) for pressures from 10^{-8}-100 bar.

Our opacity sources are discussed in section 2.2.3 and referenced in table 2.2. We generate spectra with H_2O, CO and HCN, which are particularly conducive to high-resolution spectroscopy given their large number of rovibrational transitions in the near-infrared. These species are also known to be amongst the spectroscopically strong oxygen, carbon, and nitrogen carriers in the high-temperature H_2-rich atmospheres of hot Jupiters (Madhusudhan, 2012; Moses *et al.*, 2013). The line lists contain ∼750,000 transitions for HCN in the 3.15-3.30 μm, and the 2.25-2.37 μm range contains ∼1.6×10^6 transitions for H_2O and ∼2,800 transitions for CO. We consider ∼10^2-10^3 of the strongest spectral lines in our cross-correlation templates. The cross sections of these species are shown in fig. 2.2 and generated at a 0.01 cm^{-1} wavenumber spacing, which corresponds to a resolution of R$\gtrsim$300,000 in both the 2.3 μm and the 3.2 μm bands. In addition to molecular absorption from these species, we also include collisionally induced absorption (CIA) from hydrogen and helium interactions (Richard

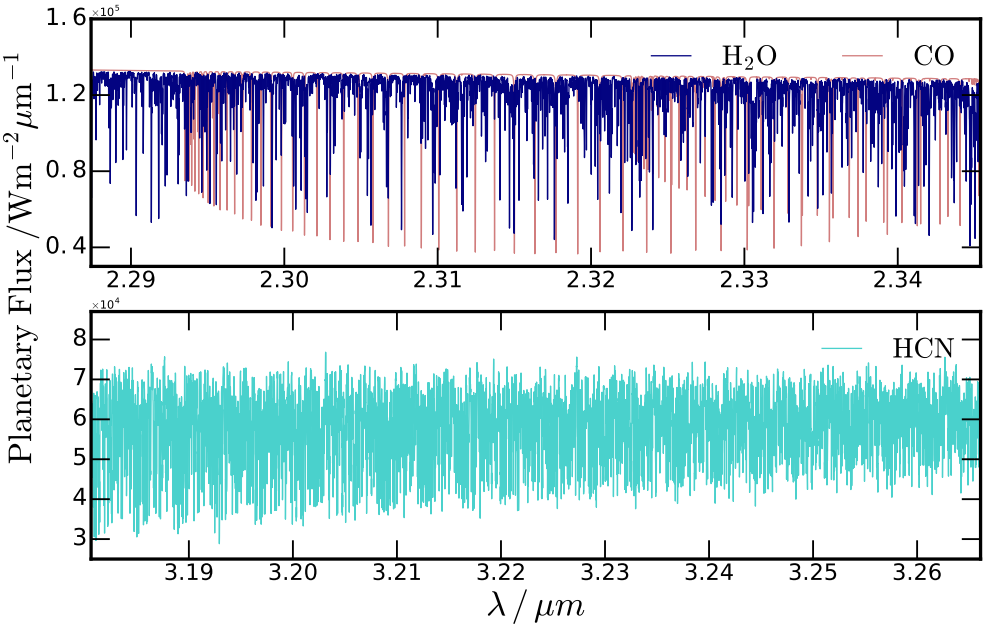

Fig. 8.4 High-resolution model spectra of HD209458b showing line features of HCN, H_2O, and CO in the observed bands at 2.28-2.35 μm and 3.18-3.27 μm.

et al., 2012) and Rayleigh scattering from molecular hydrogen as discussed in chapter 2.

Accurate line positions for each of the molecular transitions is critical to detect species in the atmosphere with high resolution spectroscopy. This is because the cross correlation requires accurate line positions in frequency (or wavelength) of the molecular species for detection. The cross correlation with the observations is maximised only when many strong transition lines are aligned in order to produce a strong significance peak. Therefore very precisely aligned line lists are required determine the transition frequencies to sufficient accuracy. Species such as CO are simple molecules and thus have much more precisely determined line positions, thus enabling detection of CO without difficulty. On the other hand, larger molecules such as H_2O and CH_4 have historically been much harder to obtain very accurate line positions from theoretical studies. This is because the energy levels for the molecules cannot be as well determined due to their complex shape. Therefore, accurate experimental comparisons of energy levels for each molecule is critical for HRS. This need for experimentally aligned line lists was demonstrated by Hargreaves *et al.* (2015), who showed differences between the CH_4 observed and theoretical transmittance at temperatures of ∼1000 K. Line lists for H_2O have also shown differences. In our work we use the HITEMP line list (Rothman

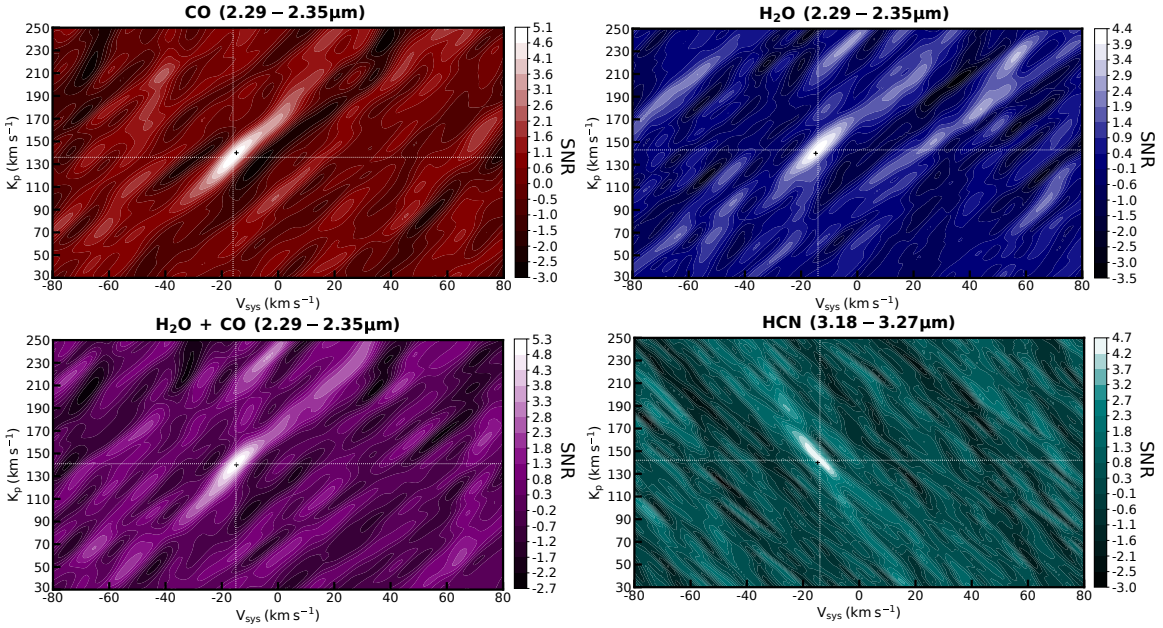

Fig. 8.5 Cross correlation S/N for CO, H_2O, and HCN as a function of systemic velocity and peak radial velocity of HD209458b. Cross correlation in the 2.29-2.35 μm spectral band yields an S/N of 5.1 with the CO template, and 4.4 with H_2O individually. A combined CO + H_2O model yields a boosted S/N of 5.3. HCN yields an S/N of 4.7 in the 3.18-3.27 μm spectral band. The white crosshairs denote the K_p and V_{sys} for the peak S/N which agree with the black cross corresponding to known orbital parameters.

et al., 2010). While less complete than some others, this offers a high temperature line list where many of the transitions have accurate line positions as they have been empirically determined. Recent work by EXOMOL has included many more H_2O transitions, also using empirically determined energy levels where available, to increase the accuracy of the line positions (Polyansky *et al.*, 2018).

8.4 Results

We now discuss the results and report the evidence for each species in the atmospheres of HD209458b and HD189733b. We have used the observations made with the VLT as part of CRIRES survey of hot Jupiters (Snellen *et al.*, 2011). Both of these planets are transiting and have also been previously observed with HST WFC3 and Spitzer photometric observations under transmission and emission spectroscopy. This means that the planetary K_p and V_{sys} are known parameters and have been independently measured. In our studies we see evidence for all three species, H_2O, CO and HCN

within the K-band and L-band observations. We describe each of the detections before comparing each of the detrending methods below.

8.4.1 HD209458b

In this section we discuss the results for the hot Jupiter HD209458b. We use both the 2.3 μm and 3.2 μm band archival VLT observations for our detections, made as part of the CRIRES survey of hot Jupiters (Snellen *et al.*, 2011). For this hot Jupiter we have detrended the data using the SYSREM algorithm as discussed in section 8.2.1. We find evidence for the presence of CO and H_2O in the 2.3 μm band and HCN in 3.2 μm band which we discuss below.

The cross-correlation signal-to noise (S/N) for each molecule over a grid of K_p and V_{sys} are shown in fig. 8.5. In the 2.3 μm window, cross correlation with H_2O and CO templates yield a S/N of 4.4 ($K_p = 143^{+15}_{-13}$ km s^{-1} and V_{sys} = -14$^{+6}_{-5}$ km s^{-1}) and 5.1 ($K_p = 136^{+15}_{-14}$ km s^{-1} and V_{sys} = -16$^{+6}_{-5}$ km s^{-1}), respectively. Using a combined H_2O + CO model gives a boosted S/N of 5.3 at $K_p = 141^{+11}_{-14}$ km s^{-1} and V_{sys} = -15$^{+4}_{-4}$ km s^{-1}. Cross correlation with an HCN template yields a peak S/N of 4.7 at $K_p = 142^{+21}_{-13}$ km s^{-1} and V_{sys} = -14$^{+5}_{-7}$ km s^{-1} in the 3.2 μm spectral window. The cross-correlation signal for HCN is made possible by its high molecular opacity in the 3.2 μm band, and a dense forest of deep absorption lines. The presence of CO is consistent with previous detections, both in transmission (Snellen *et al.*, 2010) and emission (Brogi *et al.*, 2017; Schwarz *et al.*, 2015). The K_p and V_{sys} of our detections are in agreement with those determined in previous studies (Mazeh *et al.*, 2000) as well as previous high resolution studies (Snellen *et al.*, 2010).

Figure 8.4 shows the planetary flux for both spectral ranges for H_2O, CO, and HCN. The peak cross correlations were found using volume mixing ratios of CO = 10^{-3}, H_2O = 10^{-4} and HCN = 10^{-5}. The CO spectrum in the 2.3 μm range shows deep absorption features resulting from the prominent absorption lines. The H_2O shows weaker features owing to its weaker opacity in this band (see fig. 2.2). Our H_2O detection arises as a result of the dense forest of lines as shown in fig. 8.4. These are more numerous but weaker than the CO, hence CO yields a higher S/N than H_2O in this spectral range (figure 8.5). The 3.2 μm range also shows significant absorption features in the spectrum arising from the numerous strong HCN lines. Despite the lower abundance of HCN we are able to obtain strong features in the spectrum at this wavelength thanks to its large molecular cross section.

8.4.2 HD189733b

In this section we discuss the detections of H_2O, CO and HCN on the hot Jupiter HD189733b. As with HD209458b in the previous section, the data was obtained as part of the CRIRES survey (Snellen *et al.*, 2011) in the 2.3 μm and 3.2 μm band. We use the model templates to cross correlate with the data using two detrending methods. We first discuss our detections using SYSREM and then airmass detrending.

The signal-to-noise ratio for each method of detrending for each species is shown in fig. 8.6. Using SYSREM, we detect CO with a peak detection signal-to-noise (S/N) of 4.7 at $V_{sys} = 0.0^{+3.0}_{-3.0}$ km s^{-1} and $K_p = 148.0^{+8.0}_{-11.0}$ km s^{-1}. These are consistent with the literature values (Bouchy *et al.*, 2005) of $V_{sys} = -2.361$ km s^{-1} and $K_p = 152$ km s^{-1} to which we optimised. The peak H_2O S/N is 4.9 at $V_{sys} = -2.0^{+6.0}_{-4.0}$ km s^{-1} and $K_p = 151.0^{+11.0}_{-14.0}$ km s^{-1}. The peak HCN detection S/N is 5.0 at $V_{sys} = -4.0^{+4.0}_{-5.0}$ km s^{-1} and $K_p = 155.0^{+13.0}_{-9.0}$ km s^{-1}. An HCN mixing ratio of 10^{-6} yields the peak detection significance reported above. The shape of the contours in fig. 8.6 is due to the degeneracy in K_p and V_{sys} when the CCF is nearly aligned to the rest frame. The orientation is determined by $\Delta\phi$. The detections of CO and H_2O are consistent with previous studies analysing these data (Birkby *et al.*, 2013; de Kok *et al.*, 2013).

Using airmass-based detrending, we find evidence for CO absorption with a peak detection S/N of 3.7 at $V_{sys} = 1.0^{+22.0}_{-9.0}$ km s^{-1} and $K_p = 146.0^{+12.0}_{-37.0}$ km s^{-1}. The peak H_2O S/N is 3.8 at $V_{sys} = -1.0^{+6.0}_{-9.0}$ km s^{-1} and $K_p = 151.0^{+18.0}_{-16.0}$ km s^{-1}. The peak HCN detection is at a S/N of 3.4 at $V_{sys} = -2.0^{+19.0}_{-19.0}$ km s^{-1} and $K_p = 152.0^{+28.0}_{-40.0}$ km s^{-1}. While the detection peaks are consistent with the expected K_p and V_{sys}, they are less well-constrained as demonstrated by larger error bars.

We have also conducted additional tests for the HD189733b observations to validate the significance of our results and compared the detections via both detrending methods. Previous high resolution studies use Welch T-tests to obtain the probability that values of pixels from within the CCF trail are drawn from the same parent distribution as those outside the trail (Birkby *et al.*, 2013, 2017; Brogi *et al.*, 2012; Nugroho *et al.*, 2017). The 'out-of-trail' values are consistent with Gaussian noise out to $\sim 4.0\sigma$ in a quantile-to-quantile comparison. The Welch T-test rejects the hypothesis that the two samples are drawn from the same parent distribution at confidences of 6.12σ, 6.23σ, 6.70σ, 6.81σ for CO, H_2O, HCN, and the combined H_2O+HCN model respectively. However, we choose to report the detection significances above from the more conservative signal-to-noise metric as shown in figure 8.6.

8.4.3 Robustness of HRS Detections

We have explored multiple detections of HCN, H_2O and CO in the 2.3 μm and 3.2 μm spectral ranges with the VLT CRIRES observations. The detrending step for these detections is critical and must be performed carefully in order to remove nuisance signals but not significantly degrade the weak planet signal. The optimal methodology for detrending depends on several factors, such as the strength of the planet signal compared to the noise level, the amount of data, and the presence of telluric and systematic effects on individual detectors. The best method to remove telluric contamination is yet to be determined (Birkby, 2018). We use both the SYSREM based and airmass based detrending method in our analyses, which are two of the most widely used methods. Figure 8.6 shows summed-CCF detection significance plots from cross-correlation with CO, H_2O, HCN, and combined H_2O+HCN templates for the HD189733b dataset. The results from the two methods, SYSREM and airmass fitting, are shown in the top and bottom rows of fig. 8.6 respectively. For both wavelength regimes and detrending methods we identify the optimal level of masking via model injection and recovery.

SYSREM

In all cases, we obtain peak detection significances at K_p and V_{sys} consistent with the known values. In both wavelength regimes, SYSREM consistently outperforms airmass-based detrending, with more than $+1\sigma$ higher detection significances. This performance is most likely related to the severe telluric contamination. de Kok *et al.* (2013) and Birkby *et al.* (2017) mention several possible sources of trends, including airmass, Adaptive Optics Strehl Ratio, and temperature. Since SYSREM is not restricted to specific columns of the data, it can more easily model these systematics, environmental variations and telluric variation. While the component removed in the first iteration of SYSREM resembles airmass, components removed by further iterations can pertain to subtle, higher-order trends which are less understood. The optimal number iterations for a detection has a strong dependence on the masking applied to telluric regions. This optimal number is set for each detector individually by recovery of an injected model, following similar studies (Birkby *et al.*, 2013, 2017; Nugroho *et al.*, 2017).

As expected, varying the amount of masking also has a significant effect on the detection significances. However, when optimising to other local maxima in K_p-V_{sys} space, in some cases we are able to obtain cross-correlation S/N values ≥ 4 at locations inconsistent with the expected K_p and V_{sys} of the planet. This raises some concern about potential false positives, especially if such a signal should happen to coincide

with the known K_p and V_{sys} or if K_p and V_{sys} are not known from another method. We find that the Welch T-test metric is similarly vulnerable and returns even higher estimates of the signal significances, hence we choose to use the more conservative S/N metric for our detections. An ideal statistical metric for detection significances should account for false positives and the sensitivities inherent to the method.

Airmass Detrending

Previous high-resolution studies have also adopted airmass-based detrending. We apply the procedure to the observations of HD189733b spanning a single night. As with SYSREM, we determine the appropriate amount of masking by injecting a planetary signal, and maximising the significance of its recovery. Cross-correlation with a CO template yields evidence for absorption at a significance of 3.2σ. The detection peak is at a location consistent with the expected planet K_p and V_{sys} (Bouchy *et al.*, 2005; Triaud *et al.*, 2009), within uncertainty. However, spurious positive and negative contours obtain comparable amplitudes ($\sim 3\sigma$) as the peak significance; thus we cannot conclusively classify the peak as a detection. This is similar for the 3.2 μm band, which also shows weaker signal to noise ratios than SYSREM as shown in fig. 8.6.

In order to avoid degrading the planet signal, some previous studies mask columns that are expected to contain strong absorption features from parts of the detrending process (Schwarz *et al.*, 2015; Snellen *et al.*, 2010). It is also common to either exclude detectors (e.g. because of odd-even interference) (Birkby *et al.*, 2013, 2017; Brogi *et al.*, 2012, 2014, 2016) or weight contributions from individual detector CCFs (Brogi *et al.*, 2017). In this study, however, we focus strictly on methods which use all available data, and treat the data equally with minimal prior knowledge of the planetary system.

We also perform the airmass detrending on the HD209458b observations. However, we are unable to obtain an S/N ≥ 3 from cross correlation with the HCN template in the 3.2 μm band. This may be partly due to the presence of remaining systematics which SYSREM is more effective at removing. We find that, applied to the 2.3 μm, the alternative detrending method produces a similarly inconclusive ($\sim 3\sigma$) potential CO detection in agreement with Schwarz *et al.* (2015). It also suggests that it is indeed worse at removing telluric systematics.

8.5 Discussion and Conclusion

We have performed cross correlation of high resolution VLT CRIRES spectra in the K-band (2.3 μm) and L-band (3.2 μm) and detected multiple species in the atmospheres

of the two hot Jupiters HD209458b and HD189733b. These are two of the most well studied hot Jupiters, with observations with HST WFC3 and Spitzer IRAC photometric bands (Crouzet *et al.*, 2014; Diamond-Lowe *et al.*, 2014; Line *et al.*, 2016). We report detections of H_2O and CO in the emission spectrum of the two planets, consistent with previous detections under transmission and emission spectroscopy including the current datasets (Birkby *et al.*, 2013; Brogi *et al.*, 2017; de Kok *et al.*, 2013; Snellen *et al.*, 2010). We additionally also report evidence for HCN using the SYSREM detrending method, with a much weaker signal for detrending using air mass fitting.

We considered a range of abundances when performing the cross correlation. We obtained the strongest CO signals for both planets using a mixing ratio of 10^{-3}. This is in agreement with previous high-resolution analysis (Birkby *et al.*, 2013; de Kok *et al.*, 2013; Snellen *et al.*, 2010). We obtained the H_2O signal for HD209458b using a mixing ratio of 10^{-4}, consistent with previous estimates using low-resolution spectra (Brogi *et al.*, 2017; MacDonald and Madhusudhan, 2017; Madhusudhan *et al.*, 2014b). Our HCN detections on the other hand used a template with a lower mixing fraction of 10^{-6}-10^{-5}. We found that a minimum log(HCN) of -6.5 in the planet is required to obtain a S/N of ≥ 3 from injection and recovery of such spectra. If confirmed, such a minimum atmospheric abundance of HCN could imply a high C/O ratio ($\sim$1 or higher) in the dayside atmosphere of the planet (Madhusudhan, 2012; Madhusudhan *et al.*, 2011b; Moses *et al.*, 2013).

The HCN detections and thus C/O ratio constraints also provide important constraints on the formation location and migration mechanism of the planet. The N/O and C/O ratios in both gas and solid phases in a protoplanetary disk change as a function of distance from the host star. The gas phase C/O and N/O ratios increase progressively beyond the H_2O, CO_2, and CO snow lines (Madhusudhan *et al.*, 2014c; Öberg *et al.*, 2011; Piso *et al.*, 2016); the snow line of N_2 lies beyond the CO. In particular, the gas phase N/O ratio can increase by 2$\times$ solar beyond the H_2O snow line and by $\sim$10$\times$ solar beyond the CO snow line. Such an enhancement in N/O can be caused due to condensation of the oxygen-rich ices as well as desorption of pebbles rich in N_2-ice within the N_2 snow line (Booth *et al.*, 2017; Piso *et al.*, 2016). Therefore, a high C/O and N/O ratio in the giant planet can be caused by accretion of gas beyond the CO_2/CO snow lines during the planet's formation. On the other hand, retention of these ratios at their primordial values would also require that the planet migrated to its present close-in orbit by dynamical 'disk-free' scattering mechanisms, as migrating through the disk would lead to accretion of oxygen-rich gas in the inner disk thereby lowering the C/O and N/O ratios (Madhusudhan *et al.*, 2014c, 2017).

Several advancements may help to further improve the robustness of chemical detections using high-resolution spectroscopy. The accumulation of datasets over multiple nights of observations lead to the strongest, most robust detections (Brogi *et al.*, 2012). Ideally, these observations span different orbital phase ranges so that K_p and V_{sys} contours overlap and constrain the planetary signal. Additionally, confidences may improve with wider wavelength coverage, as cross-correlation will involve more spectral features. The upcoming CRIRES+ spectrograph on the VLT (Follert *et al.*, 2014) will provide dramatic improvements upon the existing instrument, including 10× the wavelength coverage. As discussed in Brogi *et al.* (2017), high-resolution spectroscopy may also be combined with low-resolution observations to better constrain molecular detections and abundances. Additionally it might be useful to compare observations of identical objects obtained from different spectrographs (e.g. CRIRES, GIANO and NIRSPEC). This might help in distinguishing between spurious peaks due to noise and detection peaks from intrinsic features. The host of existing and upcoming instruments indicates great potential for high-resolution spectroscopy to make new chemical detections and to constrain compositions of exoplanet atmospheres.

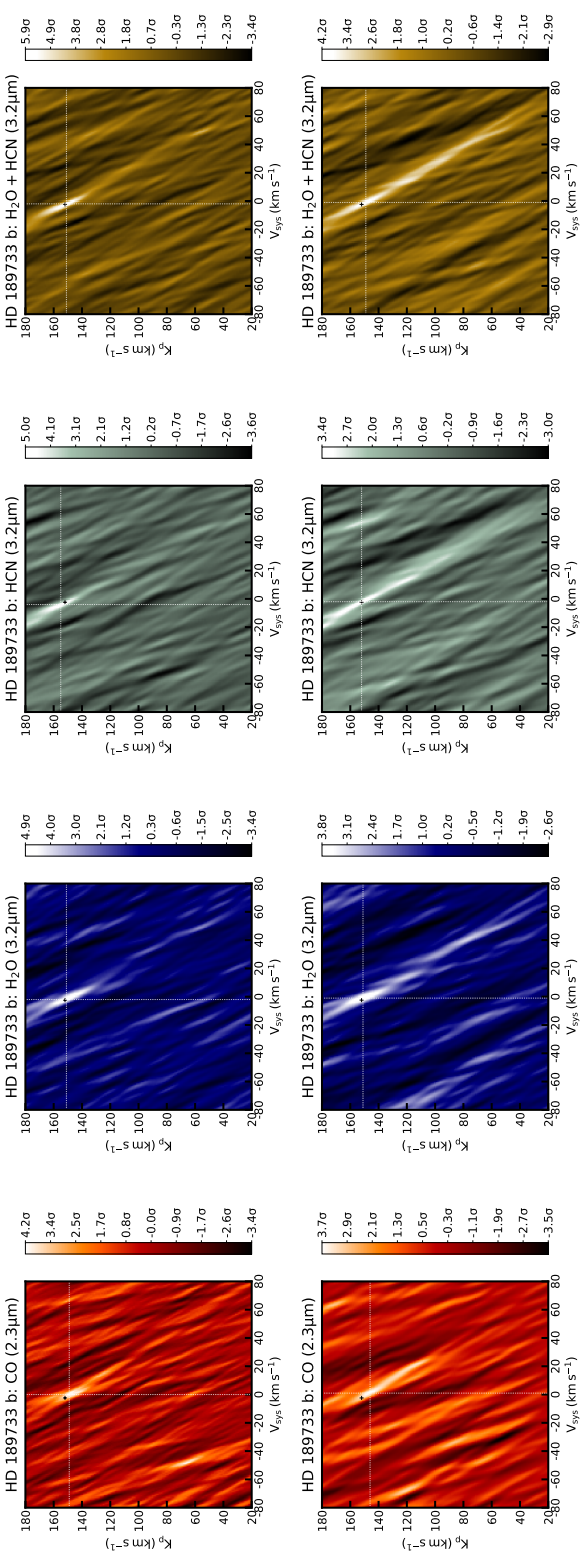

Fig. 8.6 Molecular detection significances for HD189733b using the two detrending methods. From left to right: detection significances of CO in the 2.3 μm band, and of H_2O, HCN, and combined H_2O + HCN in the 3.2 μm band. The black plus indicates the expected planetary K_p and V_{sys}. The top row of detections are made using the SYSREM detrending method. The bottom row of detections use airmass fitting.

Chapter 9

Conclusions

"Exit, pursued by a bear."
- The Winter's Tale, W. Shakespeare

In this thesis I have explored various aspects of atmospheric modelling through self-consistent and retrieval models. This work has formed the basis for multiple studies on exoplanetary atmospheres including both theory and interpretation of data. I now summarise my work, and consider the future directions of exoplanetary characterisation in each of the areas explored in this thesis as well as a general overview of the future of the field.

9.1 Molecular Opacity

Chapter 2 details the cross sections for several chemical species expected to be prominent in hot Jupiter atmospheres. I have calculated the cross section of each species from the spectral broadening of transition lines (Hill *et al.*, 2013). The line lists for these species are obtained from various databases such as HITEMP, HITRAN and EXOMOL (Rothman *et al.*, 2010, 2013; Tennyson *et al.*, 2016) (see table 2.2). These cross sections form the basis for opacities in both the self-consistent and the retrieval models. This work has led to chemical detections in a number of transiting exoplanets. These include constraints on H_2O in several prominent hot Jupiters using the Hubble Space Telescope Wide Field Camera 3 (HST WFC3) between 1.1-1.7 μm under both transmission and emission spectroscopy (Gandhi and Madhusudhan, 2018; Pinhas *et al.*, 2019). The cross sections have also been used to detect CO from HST WFC3 and Spitzer observations (Sheppard *et al.*, 2017) and for detections of other species made using ground-based spectroscopy. These include the first detection of TiO in the atmosphere

of the hot Jupiter WASP-19b (Sedaghati *et al.*, 2017) and detections of Li, Na, K in the super-Neptune WASP-127b (Chen *et al.*, 2018). In addition, my work on high resolution spectroscopy has led to detection of HCN in HD209458b and HD189733b using VLT CRIRES observations in the near infrared (Cabot *et al.*, 2019; Hawker *et al.*, 2018). With more observations on the horizon this work is vital for accurate modelling of exoplanetry atmospheres.

9.2 Self-Consistent Modelling

Accurate theoretical models of exoplanetary spectra are essential for reliable characterisation of their atmospheres. Such models provide a basis for our theoretical understanding of atmospheric processes and chemistry. Several such models have been reported in the literature with varying levels of sophistication and several have been adapted from other applications (Hubeny, 2017). My work has been to develop a new equilibrium model custom built for exoplanets and use it to explore various aspects of hot Jupiter atmospheres.

9.2.1 GENESIS

I have developed a new self-consistent atmospheric model to explore exoplanetary atmospheres, GENESIS (chapter 3). The model treats line-by-line radiative transfer through the Feautrier method and radiative-convective equilibrium through the Rybicki Complete Linearisation method in a plane parallel atmosphere (Hubeny and Mihalas, 2014). This allows for a detailed exploration of radiative processes and chemical compositions and their effects on observed emission spectra. This model has been demonstrated on both irradiated and non-irradiated planets over a wide range of exoplanetary parameter space. I have modelled the effect of C/O ratio, metallicity and equilibrium temperature on the emergent dayside spectrum from an atmosphere.

Several key developments have been achieved using GENESIS models. They have been used for comparisons with low resolution observations with HST as well as to generate high resolution spectral templates for cross-correlation as discussed in chapter 8. They have also been used to integrate retrieval and self-consistent frameworks (chapter 5). Below I discuss the application of GENESIS to thermal inversions (chapter 4) and future directions for self-consistent modelling.

9.2.2 New Avenues for Thermal Inversions

Thermal inversions (or stratospheres) have been observed on a number of hot Jupiter atmospheres. Visible absorbers such as TiO and VO have traditionally been proposed to cause these atmospheric thermal inversions in hot Jupiters (Fortney *et al.*, 2008; Hubeny *et al.*, 2003). Such species are of great significance given their importance in determining the overall temperature profile and hence spectrum from the dayside atmosphere. I have also found that many hot Jupiters which are expected to show thermal inversions through these species show isothermal or even non-inverted profiles. To explore this further I have explored how the visible and infrared opacity determine these inversions, and proposed multiple new species which are capable of producing inversions on these hot giant planets.

By exploring a range of metal-rich species I have found that four new species (AlO, CaO, NaH and MgH) provide visible opacities comparable to TiO/VO and can cause strong inversions with reasonable abundances (chapter 4). This key development has been possible due to the more complete line lists (e.g. from the EXOMOL and HITEMP databases, see table 2.2). I have used these to compute cross sections for these species as well as the GENESIS self-consistent model. I have explored the effect of these species as a function of their overall atmospheric abundance as well as determining the required abundance for each of these species to form an inversion.

Secondly, I showed that a low infrared opacity caused by a low H_2O abundance can also lead to strong thermal inversions even with sub-solar abundances of the visible absorbers. The effect of the infrared opacity on the overall equilibrium temperature profile has previously been suggested (Mollière *et al.*, 2015). I have expanded on that to consider visible and infrared opacities independently. I found that decreasing the H_2O abundance requires lower abundances of the visible absorbers such as TiO/VO as well as the newly proposed species in order for an inversion to form. This is due to the large infrared cross section of H_2O, which dominates the overall infrared opacity. At C/O ratios of $\sim$1, the atmosphere is depleted of H_2O and thus requires a lower abundance of visible absorbers in order to form and inversion. As a demonstration of this work I have shown that the thermal inversion on WASP-121b can be explained by all the visible absorbers listed above.

9.2.3 Future Directions

The GENESIS model can easily be extended to include more complex atmospheric processes and chemistry as our observations improve. So far, GENESIS has been used

to model H_2-rich giant planets. I have primarily focused on chemical compositions including the dominant volatile species (e.g. H_2O, CH_4), Na, K and some metallic species such as TiO and VO. This can be extended by including equilibrium chemical models of exoplanetary atmospheres with significantly more species into the GENESIS framework (e.g. Madhusudhan, 2012; Moses *et al.*, 2013; Seager *et al.*, 2005; Woitke *et al.*, 2018). These will greatly enhance the chemical network of species considered and thus may increase the possibilities of inversion causing species for such atmospheres (Lothringer *et al.*, 2018). Any photochemical or dynamical effects have also thus far been ignored. Models with these non-equilibrium phenomena can be included into this work in the future (e.g. Moses *et al.*, 2013). This will increase the physical plausibility of the self-consistent models and allow us to explore a wider range of parameters and their influence on the spectrum. Finally, the GENESIS model can also be easily extended to considering lower mass planets with significantly different compositions from the H_2-rich atmospheres explored in the current work.

As more species are included into the models, their opacity will also be needed. The latest molecular and atomic line list databases will be required with the most complete high temperature line lists (e.g. Rothman *et al.*, 2010, 2013; Tennyson *et al.*, 2016; Yurchenko *et al.*, 2013). Additionally, the opacity databases used in the present model are also continually updated with newer and more complete line lists. Newer line lists with a greater number of lines and higher accuracy energy levels are already becoming available thanks to advances in numerical modelling and experimental measurements (e.g. Hargreaves *et al.*, 2015; McKemmish *et al.*, 2019; Polyansky *et al.*, 2018). Cross sections and thus spectra generated with these will undoubtedly increase the accuracy of atmospheric modelling.

In addition to absorption, scattering from clouds and hazes in the atmosphere can also strongly inflruence the spectrum. Previous work in this area has shown that clouds/hazes of varying compositions may exist in these hot Jupiters and non-irradiated planets (e.g. Barman *et al.*, 2015; Helling *et al.*, 2008; Madhusudhan *et al.*, 2011c; Marley *et al.*, 2012). The current GENESIS model also assumes transfer of energy from day to night by adjusting the incident stellar flux with a parametric factor ($f_{\rm star}$). Meridional circulation of material and thermal flux can be incorporated in a more consistent manner by using sources and sinks of heat on the dayside and nightside respectively, as previously pursued by Burrows *et al.* (2008). With atmospheric observations at higher precision and higher resolution in the near future an accurate self-consistent modelling framework is thus vital for accurate atmospheric characterisation.

9.3 Retrievals

Retrievals of emission spectra perform spectral fits to the observations to determine the atmospheric composition and temperature profiles of exoplanetary atmospheres (Madhusudhan, 2018). These have been instrumental in the detection of various molecular and atomic species in the atmospheres of hot Jupiters both through transmission and emission spectroscopy. Traditional retrieval codes allow detailed constraints on chemical abundances and temperature profiles but have been unable to ascertain the physical plausibility of the derived temperature profiles. My work has been to address this issue and to constrain not just chemical and atmospheric properties but also deviations from equilibrium predictions. Central to this is a consistent framework with a shared architecture between retrievals and self-consistent models which allows us to make detailed predictions and disequilibrium analyses.

9.3.1 HyDRA

I developed a new hybrid retrieval method for exoplanetary emission spectra, HyDRA, which uses the latest atmospheric modelling tools to explore a wide range of parameter space (chapter 5). This determines the temperature profile and abundances of various species present in the dayside atmosphere to high accuracy through their emission spectra. These retrieved abundances are then used to explore disequilibrium process which may be present through integration into the GENESIS self-consistent model. Such a framework allows constraints on departures of the temperature structures from radiative-convective equilibrium as well as chemical compositions from thermochemical equilibrium. This paradigm combines the advantages of both atmospheric retrieval as well as self-consistent models and allows us to both test our current understanding of atmospheric processes as well as constrain the dynamical processes which may lead to these deviations.

This model has been demonstrated on the observed emission spectrum of the hot Jupiter WASP-43b (Gandhi and Madhusudhan, 2018), where I found the atmosphere to be consistent with the expectations from thermochemical and radiative-convective equilibrium. The emission retrieval code in HyDRA has also been used as a stand alone in the first detection of CO in the atmosphere of WASP-18b (Sheppard *et al.*, 2017) (see chapter 6) and H_2O in the atmospheres of several prominent hot Jupiters (chapter 7).

9.3.2 High Temperature Retrievals

In recent years thermal emission spectra have been observed for several strongly irradiated giant planets. A new class of ultra-hot Jupiters has emerged (Fortney *et al.*, 2008), with photospheric temperatures in excess of ∼2500 K. Observations of some of these systems with HST WFC3 spectra show featureless emission spectra (Kreidberg *et al.*, 2018; Sheppard *et al.*, 2017). A number of theories have been put forward to explain the lack of spectral features, particularly the lack of H_2O, from isothermal $P-T$ profiles to super-solar C/O ratios and the presence of H- and/or thermal dissociation (e.g. Lothringer *et al.*, 2018; Madhusudhan, 2012; Moses *et al.*, 2013; Parmentier *et al.*, 2018).

I explore each of these possibilities to retrieve the spectrum of a known hot Jupiter, WASP-18b, with some of the most precise WFC3 observations to date (Arcangeli *et al.*, 2018, 2019; Sheppard *et al.*, 2017). The retrievals already explore a range of atmospheric temperatures, encompassing non-inverted, inverted and isothermal $P-T$ profiles. In addition, HyDRA is also able to explore a wide range in chemical abundances by setting the volume mixing fraction of each species as a free parameter. The retrieval framework was extended to include opacity from H- (see chapter 2.3) and thermal dissociation of species such as H_2O, H-, TiO, and VO. This work thus marks a crucial step towards atmospheric characterisation of such strongly irradiated planets. I found that the H- abundance or dissociation cannot be well constrained due to the lack of any significant spectral feature. Thus the largely featureless HST WFC3 spectrum of WASP-18b remains a mystery.

The HyDRA retrieval model was further used to retrieve the HST WFC3 and Spitzer observations of several known hot Jupiters, including some of the hottest known exoplanets which fall into the category of ultra-hot Jupiters. For such systems I have included a range of chemistry, including H- and dissociation for the ultra-hot planets. The H_2O abundances for these systems were constrained primarily through their WFC3 observations. The $P-T$ profiles and in some cases CO abundances were constrained through both Spitzer and HST observations, and show that some of these exoplanets exhibit thermal inversions in the photosphere (see chapter 7).

9.3.3 Future Directions

A number of species have been proposed as potentially causing thermal inversions as discussed in chapter 4. These species are of great interest given the strong signature thermal inversions have on the emergent spectrum. While many of these species

have strong opacity in the visible, their opacity in the infrared is often much weaker making them difficult to detect through emission spectroscopy. However, transmission spectroscopy can be used in the visible to constrain these species. Recently, low resolution observations have been made of several hot Jupiters from ground based telescopes such as VLT and GTC (Chen *et al.*, 2018; Sedaghati *et al.*, 2017; von Essen *et al.*, 2019). High resolution observations have also recently been developed to probe exoplanetary atmospheres (Hoeijmakers *et al.*, 2018; Nugroho *et al.*, 2017). These observations have shown evidence for TiO, AlO, Na, K, Li, Fe and Ti in the day/night terminator of these planets. Further observations may improve upon these and constrain many more species with strong visible opacity. This will allow us to explore each of the proposed species capable of thermal inversions (e.g. Fortney *et al.*, 2008; Hubeny *et al.*, 2003; Lothringer *et al.*, 2018; Zahnle *et al.*, 2009) and study their physical plausibility with HyDRA. Any differences between the observations and equilibrium models may point towards dynamical effects present in the atmosphere, which may thus be detectable. Through improved ground-based and space-based observations we will be able to further constrain such deviations on hot Jupiters as well as cooler rocky planets. Such research will also be vital for future work given that O_3, a biosignature, can cause thermal inversions in Earth-like atmospheres, as it does in our own stratosphere.

Another extension to the retrieval framework would be exploring the planetary parameters as a function of orbital phase. Work has already begun looking into phase resolved spectroscopy (Stevenson *et al.*, 2017), combining dayside and nightside retrievals dependant on the observational geometry. Modification of the retrieval to retrieve a temperature profile that varies with orbital phase will be required, as this may vary significantly between the planet's day and night side. The temperature structure of the planet is sensitive in emission spectroscopy, so a good understanding here is required to get precise planetary properties. Hence the future of retrievals is promising given the significant influx of high quality and precision data on the horizon.

9.4 High Resolution Spectroscopy

High resolution spectral observations have recently been used for the detection of multiple molecular and atomic species, in particular H_2O and CO, in the atmospheres of several hot Jupiters (e.g. Birkby *et al.*, 2017; Brogi *et al.*, 2012). Such studies are now becoming possible thanks to improved facilities and observational techniques. Key to the detection of these trace species are the spectral model templates to cross-correlate

with the observed spectra, which often require high-efficiency and accurate radiative transfer and the most up-to-date molecular opacities.

I have used my GENESIS model to generate spectral templates for a number molecular species prevalent in hot Jupiter atmospheres. These very high resolution (R∼300,000) spectral templates have led to the first evidence of HCN in two hot Jupiters, HD189733b and HD209458b, using VLT CRIRES observations (chapter 8). We have also confirmed previous detections of H_2O and CO in these two planets through this technique.

9.4.1 Future Directions

In the future such high resolution spectroscopy has great potential for new chemical detections due to its sensitivity to trace species and shows great promise in the detection of such species on smaller rocky planets. Therefore being able to analyse and model exoplanetary atmospheres at high resolution is key going forwards, particularly with the wealth of new instruments coming online in the next few years as discussed below. The techniques I have developed during the course of this work will be instrumental in characterising these planetary atmospheres with JWST and large future ground based facilities such as TMT, GMT and ELT.

9.5 Landscape of Atmospheric Characterisation

With improvements in observational facilities over the coming years, we are at the beginning of an extraordinary growth curve in the field of atmospheric characterisation of exoplanets. Near and long term forecasts show great promise through both ground based and space based observations. With many new exoplanet surveys coming up in the next decade such as TESS (Ricker *et al.*, 2014) there will be an abundance of exoplanets, including smaller and cooler planets, for us to investigate with follow up observations. As well as this, ground based direct imaging of exoplanets with surveys such as GPI and SPHERE open up non-transiting planets at large orbital distances for us to explore. Hence we will be able to fill the exoplanet parameter space (e.g. fig. 1.1) with an even larger population. Alongside this, many new ground and space based surveys are going to improve our efforts to characterise these newly discovered planets.

One of the key developments in space based exoplanet characterisation is the James Webb Space Telescope (JWST), which is due to come online in the next few years. This promises significant improvements for atmospheric characterisation of

transiting exoplanets, allowing for greater precision, resolution and spectral coverage up to ∼28 μm. Thus JWST promises to revolutionise our current knowledge of hot Jupiters, warm Neptunes, even beginning to delve into the atmospheres of cooler rocky planets thanks to its greater sensitivity. Studies have already begun to explore the constraints possible from such observations (Batalha *et al.*, 2018; Greene *et al.*, 2016), with tight constraints possible for chemical abundances and $P-T$ profiles. The exciting possibility of detecting multiple species such as H_2O, CH_4 and CO in the atmosphere allows us to place robust constraints on C/O ratios, metallicities and thus formation and migration mechanisms for such planets.

Ground based high resolution spectroscopy (HRS) also has extraordinary potential for the near term progress of the field. Instruments such as ESPRESSO on the VLT and EXPRES on the DCT promise high resolution observations in the visible and CARMENES/CAHA, GIANO/TNG and CRIRES+/VLT promise such in the infrared. Visible high resolution spectroscopy has already shown promise for the detection of many species in the atmospheres of hot Jupiters (e.g. Hoeijmakers *et al.*, 2018; Nugroho *et al.*, 2017), and an exciting prospect for the future is the combination of JWST and HRS. Additionally, infrared HRS has led to the detection of H_2O and CO in numerous hot Jupiters, both transiting and non-transiting (e.g. Birkby *et al.*, 2017; Brogi *et al.*, 2012; Snellen *et al.*, 2010). Work has already begun in combining low and high resolution spectroscopy (Brogi *et al.*, 2017), and holds great potential in the detection of trace species on warm Neptunes and rocky planets in the future (Rodler and López-Morales, 2014; Snellen *et al.*, 2017). A detailed review of the future of HRS can be found in Birkby (2018) and Madhusudhan (2019).

The long term future of exoplanet characterisation is also exciting. Missions such as ARIEL will enable atmospheric characterisation for a large population of exoplanets. Large ground based telescopes such as ELT, GMT and TMT will detect Earth sized planets and open up the possibility for detecting biosignatures. Looking further into the future telescopes such as LUVOIR (Bolcar *et al.*, 2016) allow the characterisation of Earth-like planets around Sun-like stars. Thus finding Earth analogues and characterising their atmospheres, one of the main goals of exoplanetary science, is possible in the not too distant future. All of the near and long term exoplanet projects mean that detecting exoplanets and characterising their atmospheres is a major emerging frontier in modern science.

References

Abel, M. et al (2011). Collision-Induced Absorption by H2Pairs: From Hundreds to Thousands of Kelvin. *Journal of Physical Chemistry A*, **115**(25), 6805–6812.

Abel, M. et al (2012). Infrared absorption by collisional H_2-He complexes at temperatures up to 9000 K and frequencies from 0 to 20 000 cm^{-1}. *Journal of Chemical Physics*, **136**(4), 044319–044319.

Ackerman, A.S. and Marley, M.S. (2001). Precipitating Condensation Clouds in Substellar Atmospheres. *ApJ*, **556**, 872–884.

Amundsen, D.S. et al (2014). Accuracy tests of radiation schemes used in hot Jupiter global circulation models. *A&A*, **564**, A59.

Anglada-Escudé, G. et al (2016). A terrestrial planet candidate in a temperate orbit around Proxima Centauri. *Nature*, **536**, 437–440.

Apai, D. et al (2013). HST Spectral Mapping of L/T Transition Brown Dwarfs Reveals Cloud Thickness Variations. *ApJ*, **768**, 121.

Arcangeli, J. et al (2018). H^- Opacity and Water Dissociation in the Dayside Atmosphere of the Very Hot Gas Giant WASP-18b. *ApJ*, **855**, L30.

Arcangeli, J. et al (2019). Climate of an Ultra hot Jupiter: Spectroscopic phase curve of WASP-18b with HST/WFC3. *arXiv e-prints*.

Asplund, M. et al (2009). The Chemical Composition of the Sun. *ARA&A*, **47**, 481–522.

Atreya, S.K. et al (2016). The Origin and Evolution of Saturn, with Exoplanet Perspective. *ArXiv e-prints*.

Barber, R.J. et al (2006). A high-accuracy computed water line list. *MNRAS*, **368**(3), 1087–1094.

Barber, R.J. et al (2014). ExoMol line lists - III. An improved hot rotation-vibration line list for HCN and HNC. *Mon. Not. R. Astron. Soc.*, **437**, 1828–1835.

Barman, T.S., Hauschildt, P.H. and Allard, F. (2001). Irradiated planets. *The Astrophysical Journal*, **556**(2), 885.

Barman, T.S., Hauschildt, P.H. and Allard, F. (2005). Phase-dependent properties of extrasolar planet atmospheres. *The Astrophysical Journal*, **632**(2), 1132.

Barman, T.S. et al (2015). Simultaneous Detection of Water, Methane, and Carbon Monoxide in the Atmosphere of Exoplanet HR8799b. *ApJ*, **804**, 61.

Barton, E.J. et al (2017). Pressure-dependent water absorption cross sections for exoplanets and other atmospheres. *J. Quant. Spectrosc. Radiative Transfer*, **187**, 453–460.

Batalha, N.E. et al (2018). Strategies for Constraining the Atmospheres of Temperate Terrestrial Planets with JWST. *ApJ*, **856**, L34.

Beatty, T.G. et al (2017a). Evidence for Atmospheric Cold-trap Processes in the Noninverted Emission Spectrum of Kepler-13Ab Using HST/WFC3. *AJ*, **154**, 158.

Beatty, T.G. et al (2017b). The Broadband and Spectrally Resolved H-band Eclipse of KELT-1b and the Role of Surface Gravity in Stratospheric Inversions in Hot Jupiters. *AJ*, **154**, 242.

Bell, K.L. and Berrington, K.A. (1987). Free-free absorption coefficient of the negative hydrogen ion. *Journal of Physics B Atomic Molecular Physics*, **20**, 801–806.

Benneke, B. (2015). Strict Upper Limits on the Carbon-to-Oxygen Ratios of Eight Hot Jupiters from Self-Consistent Atmospheric Retrieval. *ArXiv e-prints*.

Benneke, B. and Seager, S. (2013). How to Distinguish between Cloudy Mini-Neptunes and Water/Volatile-dominated Super-Earths. *ApJ*, **778**, 153.

Birkby, J.L. (2018). Exoplanet Atmospheres at High Spectral Resolution. *ArXiv e-prints*.

Birkby, J.L. et al (2013). Detection of water absorption in the day side atmosphere of HD 189733 b using ground-based high-resolution spectroscopy at 3.2 μm. *MNRAS*, **436**, L35–L39.

Birkby, J.L. et al (2017). Discovery of Water at High Spectral Resolution in the Atmosphere of 51 Peg b. *Astrophys. J.*, **153**, 138.

Blecic, J. et al (2014). Spitzer Observations of the Thermal Emission from WASP-43b. *ApJ*, **781**, 116.

Blecic, J., Harrington, J. and Bowman, M.O. (2016). TEA: A Code Calculating Thermochemical Equilibrium Abundances. *ApJS*, **225**, 4.

Bolcar, M.R. et al (2016). Initial technology assessment for the Large-Aperture UV-Optical-Infrared (LUVOIR) mission concept study. In *Space Telescopes and Instrumentation 2016: Optical, Infrared, and Millimeter Wave*, volume 9904 of *Proc. SPIE*, page 99040J.

Bonnefoy, M. et al (2014). Physical and orbital properties of β Pictoris b. *A&A*, **567**, L9.

Booth, R.A. et al (2017). Chemical enrichment of giant planets and discs due to pebble drift. *Mon. Not. R. Astron. Soc.*, **469**, 3994–4011.

Bouchy, F. et al (2005). ELODIE metallicity-biased search for transiting Hot Jupiters. II. A very hot Jupiter transiting the bright K star HD 189733. *Astron. Astrophys.*, **444**, L15–L19.

Brogi, M. et al (2012). The signature of orbital motion from the dayside of the planet τ Boötis b. *Nature*, **486**, 502–504.

Brogi, M. et al (2013). Detection of Molecular Absorption in the Dayside of Exoplanet 51 Pegasi b? *Astrophys. J.*, **767**, 27.

Brogi, M. et al (2014). Carbon monoxide and water vapor in the atmosphere of the non-transiting exoplanet HD 179949 b. *Astron. Astrophys.*, **565**, A124.

Brogi, M. et al (2016). Rotation and Winds of Exoplanet HD 189733 b Measured with High-dispersion Transmission Spectroscopy. *ApJ*, **817**, 106.

Brogi, M. et al (2017). A Framework to Combine Low- and High-resolution Spectroscopy for the Atmospheres of Transiting Exoplanets. *Astrophys. J. Lett.*, **839**, L2.

Buchner, J. et al (2014). X-ray spectral modelling of the AGN obscuring region in the CDFS: Bayesian model selection and catalogue. *A&A*, **564**, A125.

Burgasser, A.J. (2014). The SpeX Prism Library: 1000+ low-resolution, near-infrared spectra of ultracool M, L, T and Y dwarfs. In *Astronomical Society of India Conference Series*, volume 11 of *Astronomical Society of India Conference Series*.

Burningham, B. et al (2017). Retrieval of atmospheric properties of cloudy L dwarfs. *MNRAS*, **470**, 1177–1197.

Burrows, A. (2009). The Role of Dust Clouds in the Atmospheres of Brown Dwarfs. In T. Henning, E. Grün, and J. Steinacker, editors, *Cosmic Dust - Near and Far*, volume 414 of *Astronomical Society of the Pacific Conference Series*, page 115.

Burrows, A. and Volobuyev, M. (2003). Calculations of the far-wing line profiles of sodium and potassium in the atmospheres of substellar-mass objects. *The Astrophysical Journal*, **583**(2), 985.

Burrows, A. et al (2007). Theoretical Spectral Models of the Planet HD 209458b with a Thermal Inversion and Water Emission Bands. *ApJ*, **668**, L171–L174.

Burrows, A., Budaj, J. and Hubeny, I. (2008). Theoretical Spectra and Light Curves of Close-in Extrasolar Giant Planets and Comparison with Data. *APJ*, **678**, 1436–1457.

Cabot, S.H.C. et al (2019). On the robustness of analysis techniques for molecular detections using high-resolution exoplanet spectroscopy. *MNRAS*, **482**, 4422–4436.

Cartier, K.M.S. et al (2017). Near-infrared Emission Spectrum of WASP-103b Using Hubble Space Telescope/Wide Field Camera 3. *AJ*, **153**, 34.

Castelli, F. and Kurucz, R.L. (2004). New Grids of ATLAS9 Model Atmospheres. *ArXiv Astrophysics e-prints*.

Cavalié, T. et al (2008). Observations of CO on <ASTROBJ>Saturn</ASTROBJ> and <ASTROBJ>Uranus</ASTROBJ> at millimeter wavelengths: new upper limit determinations. *A&A*, **484**, 555–561.

Cavalié, T. et al (2010). A cometary origin for CO in the stratosphere of Saturn? *A&A*, **510**, A88.

Charbonneau, D. et al (2002). Detection of an extrasolar planet atmosphere. *The Astrophysical Journal*, **568**(1), 377.

Chen, G. et al (2018). The GTC exoplanet transit spectroscopy survey IX. Detection of Haze, Na, K, and Li in the super-Neptune WASP-127b. *ArXiv e-prints*.

Crossfield, I.J.M. et al (2016). 197 candidates and 104 validated planets in k2's first five fields. *The Astrophysical Journal Supplement Series*, **226**(1), 7.

Crouzet, N. et al (2014). Water Vapor in the Spectrum of the Extrasolar Planet HD 189733b. II. The Eclipse. *ApJ*, **795**, 166.

Dalgarno, A. and Williams, D.A. (1962). Rayleigh Scattering by Molecular Hydrogen. *ApJ*, **136**, 690–692.

de Kok, R.J. et al (2013). Detection of carbon monoxide in the high-resolution day-side spectrum of the exoplanet HD 189733b. *Astron. Astrophys.*, **554**, A82.

Deming, D. et al (2013). Infrared transmission spectroscopy of the exoplanets hd209458b and xo-1b using the wide field camera-3 on the hubble space telescope. *The Astrophysical Journal*, **774**(2), 95.

Diamond-Lowe, H. et al (2014). New analysis indicates no thermal inversion in the atmosphere of hd 209458b. *The Astrophysical Journal*, **796**(1), 66.

Drummond, B. et al (2016). The effects of consistent chemical kinetics calculations on the pressure-temperature profiles and emission spectra of hot Jupiters. *A&A*, **594**, A69.

Dullemond, C. P., van Zadelhoff, G. J. and Natta, A. (2002). Vertical structure models of t tauri and herbig ae/be disks. *A&A*, **389**(2), 464–474.

Ehrenreich, D. et al (2015). A giant comet-like cloud of hydrogen escaping the warm Neptune-mass exoplanet GJ 436b. *Nature*, **522**, 459–461.

Espinoza, N. et al (2019). ACCESS: a featureless optical transmission spectrum for WASP-19b from Magellan/IMACS. *MNRAS*, **482**, 2065–2087.

Evans, T.M. et al (2016). Detection of h2o and evidence for tio/vo in an ultra-hot exoplanet atmosphere. *The Astrophysical Journal Letters*, **822**(1), L4.

Evans, T.M. et al (2017). An ultrahot gas-giant exoplanet with a stratosphere. *Nature*, **548**, 58–61.

Faure, A. et al (2013). Pressure broadening of water and carbon monoxide transitions by molecular hydrogen at high temperatures. *J. Quant. Spectrosc. Radiative Transfer*, **116**, 79–86.

Feroz, F. and Hobson, M.P. (2008). Multimodal nested sampling: an efficient and robust alternative to Markov Chain Monte Carlo methods for astronomical data analyses. *MNRAS*, **384**, 449–463.

Feroz, F., Hobson, M.P. and Bridges, M. (2009). MULTINEST: an efficient and robust Bayesian inference tool for cosmology and particle physics. *MNRAS*, **398**, 1601–1614.

Feroz, F. et al (2013). Importance Nested Sampling and the MultiNest Algorithm. *ArXiv e-prints*.

Fischer, D.A. et al (2016). State of the field: Extreme precision radial velocities. *Publications of the Astronomical Society of the Pacific*, **128**(964), 066001.

Follert, R. et al (2014). CRIRES+: a cross-dispersed high-resolution infrared spectrograph for the ESO VLT. In *Ground-based and Airborne Instrumentation for Astronomy V*, volume 9147 of *Proc. of SPIE*, page 914719.

Fortney, J.J., Marley, M.S. and Barnes, J.W. (2007). Planetary radii across five orders of magnitude in mass and stellar insolation: Application to transits. *The Astrophysical Journal*, **659**(2), 1661.

Fortney, J.J. et al (2008). A Unified Theory for the Atmospheres of the Hot and Very Hot Jupiters: Two Classes of Irradiated Atmospheres. *APJ*, **678**, 1419–1435.

Gandhi, S. and Madhusudhan, N. (2017). genesis: new self-consistent models of exoplanetary spectra. *MNRAS*, **472**, 2334–2355.

Gandhi, S. and Madhusudhan, N. (2018). Retrieval of exoplanet emission spectra with HyDRA. *MNRAS*, **474**, 271–288.

Gandhi, S. and Madhusudhan, N. (2019). New Avenues for Thermal Inversions in hot Jupiters. *arXiv e-prints*.

Gaudi, B.S. et al (2017). A giant planet undergoing extreme-ultraviolet irradiation by its hot massive-star host. *Nature*, **546**(7659), 514–518.

Gillon, M. et al (2016). Temperate Earth-sized planets transiting a nearby ultracool dwarf star. *Nature*, **533**, 221–224.

Greene, T.P. et al (2016). Characterizing Transiting Exoplanet Atmospheres with JWST. *ApJ*, **817**, 17.

Grimm, S.L. and Heng, K. (2015). HELIOS-K: An Ultrafast, Open-source Opacity Calculator for Radiative Transfer. *ApJ*, **808**, 182.

Guillot, T. (2010). On the radiative equilibrium of irradiated planetary atmospheres. *A&A*, **520**, A27.

Hansen, B.M.S. (2008). On the Absorption and Redistribution of Energy in Irradiated Planets. *ApJS*, **179**, 484–508.

Hargreaves, R.J. et al (2015). Empirical Line Lists and Absorption Cross Sections for Methane at High Temperatures. *ApJ*, **813**, 12.

Harris, G.J. et al (2006). Improved HCN/HNC linelist, model atmospheres and synthetic spectra for WZ Cas. *Mon. Not. R. Astron. Soc.*, **367**, 400–406.

Hauschildt, P. (1992). A fast operator perturbation method for the solution of the special relativistic equation of radiative transfer in spherical symmetry. *Journal of Quantitative Spectroscopy and Radiative Transfer*, **47**(6), 433 – 453.

Hauschildt, P.H. and Baron, E. (1999). Numerical solution of the expanding stellar atmosphere problem. *Journal of Computational and Applied Mathematics*, **109**(1–2), 41 – 63.

Hawker, G.A. et al (2018). Evidence for Multiple Molecular Species in the Hot Jupiter HD 209458b. *ApJ*, **863**, L11.

Haynes, K. et al (2015). Spectroscopic evidence for a temperature inversion in the dayside atmosphere of hot jupiter wasp-33b. *The Astrophysical Journal*, **806**(2), 146.

Hebb, L. et al (2010). WASP-19b: The Shortest Period Transiting Exoplanet Yet Discovered. *ApJ*, **708**, 224–231.

Hedges, C. and Madhusudhan, N. (2016). Effect of pressure broadening on molecular absorption cross sections in exoplanetary atmospheres. *MNRAS*, **458**, 1427–1449.

Hellier, C. et al (2011). WASP-43b: the closest-orbiting hot Jupiter. *A&A*, **535**, L7.

Helling, C. et al (2008). A comparison of chemistry and dust cloud formation in ultracool dwarf model atmospheres. *Monthly Notices of the Royal Astronomical Society*, **391**(4), 1854–1873.

Heng, K. and Lyons, J.R. (2016). Carbon Dioxide in Exoplanetary Atmospheres: Rarely Dominant Compared to Carbon Monoxide and Water in Hot, Hydrogen-dominated Atmospheres. *APJ*, **817**, 149.

Heng, K. and Showman, A.P. (2015). Atmospheric Dynamics of Hot Exoplanets. *Annual Review of Earth and Planetary Sciences*, **43**, 509–540.

Heng, K. and Tsai, S.M. (2016). Analytical Models of Exoplanetary Atmospheres. III. Gaseous C-H-O-N Chemistry with Nine Molecules. *ApJ*, **829**, 104.

Heng, K., Mendonça, J.M. and Lee, J.M. (2014). Analytical Models of Exoplanetary Atmospheres. II. Radiative Transfer via the Two-stream Approximation. *ApJS*, **215**, 4.

Hill, C., Yurchenko, S.N. and Tennyson, J. (2013). Temperature-dependent molecular absorption cross sections for exoplanets and other atmospheres. *Icarus*, **226**, 1673–1677.

Hoeijmakers, H.J. et al (2018). Atomic iron and titanium in the atmosphere of the exoplanet KELT-9b. *Nature*, **560**, 453–455.

Hubeny, I. (2017). Model atmospheres of sub-stellar mass objects. *MNRAS*, **469**, 841–869.

Hubeny, I. and Lanz, T. (1995). Non-LTE line-blanketed model atmospheres of hot stars. 1: Hybrid complete linearization/accelerated lambda iteration method. *ApJ*, **439**, 875–904.

Hubeny, I. and Mihalas, D. (2014). *Theory of Stellar Atmospheres*. Princeton University Press.

Hubeny, I., Burrows, A. and Sudarsky, D. (2003). A Possible Bifurcation in Atmospheres of Strongly Irradiated Stars and Planets. *ApJ*, **594**, 1011–1018.

John, T.L. (1988). Continuous absorption by the negative hydrogen ion reconsidered. *A&A*, **193**, 189–192.

Kaeufl, H.U. et al (2004). CRIRES: a high-resolution infrared spectrograph for ESO's VLT. In A. F. M. Moorwood and M. Iye, editors, *Ground-based Instrumentation for Astronomy*, volume 5492 of *Proc. of SPIE*, pages 1218–1227.

Karman, T. et al (2019). Update of the HITRAN collision-induced absorption section. *Icarus*, **328**, 160–175.

Kataria, T. et al (2015). The Atmospheric Circulation of the Hot Jupiter WASP-43b: Comparing Three-dimensional Models to Spectrophotometric Data. *ApJ*, **801**, 86.

Kippenhahn, R., Weigert, A. and Weiss, A. (2012). *Stellar Structure and Evolution*. Astronomy and Astrophysics.

Knutson, H.A. et al (2008). The 3.6-8.0 μm Broadband Emission Spectrum of HD 209458b: Evidence for an Atmospheric Temperature Inversion. *ApJ*, **673**, 526–531.

Knutson, H.A. et al (2009). Detection of A Temperature Inversion in the Broadband Infrared Emission Spectrum of TrES-4. *ApJ*, **691**, 866–874.

Knutson, H.A., Howard, A.W. and Isaacson, H. (2010). A correlation between stellar activity and hot jupiter emission spectra. *The Astrophysical Journal*, **720**(2), 1569.

Konopacky, Q.M. et al (2013). Detection of Carbon Monoxide and Water Absorption Lines in an Exoplanet Atmosphere. *Science*, **339**, 1398–1401.

Kramida, A. et al (2018). NIST Atomic Spectra Database (ver. 5.6.1), [Online]. Available: `https://physics.nist.gov/asd` [2019, February 6]. National Institute of Standards and Technology, Gaithersburg, MD.

Kreidberg, L. (2015). batman: BAsic Transit Model cAlculatioN in Python. *Publications of the Astronomical Society of the Pacific*, **127**, 1161.

Kreidberg, L. et al (2014). A precise water abundance measurement for the hot jupiter wasp-43b. *The Astrophysical Journal Letters*, **793**(2), L27.

Kreidberg, L. et al (2018). Global Climate and Atmospheric Composition of the Ultra-hot Jupiter WASP-103b from HST and Spitzer Phase Curve Observations. *AJ*, **156**, 17.

Kurucz, R.L. (1979). Model atmospheres for G, F, A, B, and O stars. *ApJS*, **40**, 1–340.

Kurucz, R.L. (1992). Atomic and Molecular Data for Opacity Calculations. *Rev. Mex. Astron. Astrofis.*, **23**.

Lavie, B. et al (2016). HELIOS-Retrieval: An Open-source, Nested Sampling Atmospheric Retrieval Code, Application to the HR 8799 Exoplanets and Inferred Constraints for Planet Formation. *ArXiv e-prints*.

Lavie, B. et al (2017). HELIOS-RETRIEVAL: An Open-source, Nested Sampling Atmospheric Retrieval Code; Application to the HR 8799 Exoplanets and Inferred Constraints for Planet Formation. *AJ*, **154**, 91.

Lee, J.M., Fletcher, L.N. and Irwin, P.G.J. (2012). Optimal estimation retrievals of the atmospheric structure and composition of HD 189733b from secondary eclipse spectroscopy. *MNRAS*, **420**, 170–182.

Line, M.R. et al (2012). Information Content of Exoplanetary Transit Spectra: An Initial Look. *ApJ*, **749**, 93.

Line, M.R. et al (2013). A Systematic Retrieval Analysis of Secondary Eclipse Spectra. I. A Comparison of Atmospheric Retrieval Techniques. *ApJ*, **775**, 137.

Line, M.R. et al (2014). A Systematic Retrieval Analysis of Secondary Eclipse Spectra. II. A Uniform Analysis of Nine Planets and their C to O Ratios. *ApJ*, **783**, 70.

Line, M.R. et al (2016). No Thermal Inversion and a Solar Water Abundance for the Hot Jupiter HD 209458b from HST/WFC3 Spectroscopy. *AJ*, **152**, 203.

Lodders, K. and Fegley, B. (2002). Atmospheric Chemistry in Giant Planets, Brown Dwarfs, and Low-Mass Dwarf Stars. I. Carbon, Nitrogen, and Oxygen. *Icarus*, **155**, 393–424.

Lord, S.D. (1992). A new software tool for computing Earth's atmospheric transmission of near- and far-infrared radiation. Technical report, NASA Technical Memorandum 10395.

Lothringer, J.D., Barman, T. and Koskinen, T. (2018). Extremely Irradiated Hot Jupiters: Non-Oxide Inversions, H- Opacity, and Thermal Dissociation of Molecules. *ArXiv e-prints*.

MacDonald, R.J. and Madhusudhan, N. (2017). HD 209458b in new light: evidence of nitrogen chemistry, patchy clouds and sub-solar water. *MNRAS*, **469**, 1979–1996.

Macintosh, B. et al (2015). Discovery and spectroscopy of the young jovian planet 51 Eri b with the Gemini Planet Imager. *Science*, **350**, 64–67.

Madhusudhan, N. (2012). C/O Ratio as a Dimension for Characterizing Exoplanetary Atmospheres. *APJ*, **758**, 36.

Madhusudhan, N. (2018). *Atmospheric Retrieval of Exoplanets*, page 104. Handbook of Exoplanets, ISBN 978-3-319-55332-0. Springer International Publishing AG, part of Springer Nature, 2018, id.104.

Madhusudhan, N. (2019). Exoplanetary Atmospheres: Key Insights, Challenges and Prospects. *arXiv e-prints*.

Madhusudhan, N. and Seager, S. (2009). A Temperature and Abundance Retrieval Method for Exoplanet Atmospheres. *APJ*, **707**, 24–39.

Madhusudhan, N. and Seager, S. (2010). On the Inference of Thermal Inversions in Hot Jupiter Atmospheres. *APJ*, **725**, 261–274.

Madhusudhan, N. and Seager, S. (2011). High metallicity and non-equilibrium chemistry in the dayside atmosphere of hot-neptune gj 436b. *The Astrophysical Journal*, **729**(1), 41.

Madhusudhan, N. et al (2011a). A high C/O ratio and weak thermal inversion in the atmosphere of exoplanet WASP-12b. *Nature*, **469**, 64–67.

Madhusudhan, N. et al (2011b). Carbon-rich Giant Planets: Atmospheric Chemistry, Thermal Inversions, Spectra, and Formation Conditions. *ApJ*, **743**, 191.

Madhusudhan, N., Burrows, A. and Currie, T. (2011c). Model Atmospheres for Massive Gas Giants with Thick Clouds: Application to the HR 8799 Planets and Predictions for Future Detections. *ApJ*, **737**, 34.

Madhusudhan, N. et al (2014a). Exoplanetary Atmospheres. In H. Beuther, R. S. Klessen, C. P. Dullemond, and T. Henning, editors, *Protostars and Planets VI*, page 739.

Madhusudhan, N. et al (2014b). H_2O Abundances in the Atmospheres of Three Hot Jupiters. *ApJ*, **791**(1), L9.

Madhusudhan, N., Amin, M.A. and Kennedy, G.M. (2014c). Toward Chemical Constraints on Hot Jupiter Migration. *ApJ*, **794**, L12.

Madhusudhan, N. et al (2016). Exoplanetary Atmospheres-Chemistry, Formation Conditions, and Habitability. *Space Sci. Rev.*, **205**, 285–348.

Madhusudhan, N. et al (2017). Atmospheric signatures of giant exoplanet formation by pebble accretion. *Mon. Not. R. Astron. Soc.*, **469**, 4102–4115.

Malik, M. et al (2017). HELIOS: An Open-source, GPU-accelerated Radiative Transfer Code for Self-consistent Exoplanetary Atmospheres. *AJ*, **153**, 56.

Mandell, A.M. et al (2013). Exoplanet Transit Spectroscopy Using WFC3: WASP-12 b, WASP-17 b, and WASP-19 b. *ApJ*, **779**, 128.

Markwardt, C.B. (2009). Non-linear Least-squares Fitting in IDL with MPFIT. In D. A. Bohlender, D. Durand, and P. Dowler, editors, *Astronomical Data Analysis Software and Systems XVIII*, volume 411, page 251.

Marley, M.S. and McKay, C.P. (1999). Thermal structure of uranus' atmosphere. *Icarus*, **138**(2), 268 – 286.

Marley, M.S. et al (2012). Masses, Radii, and Cloud Properties of the HR 8799 Planets. *ApJ*, **754**, 135.

Marois, C. et al (2008). Direct Imaging of Multiple Planets Orbiting the Star HR 8799. *Science*, **322**(5906), 1348.

Marois, C. et al (2010). Images of a fourth planet orbiting HR 8799. *Nature*, **468**, 1080–1083.

Maxted, P.F.L. et al (2013). Spitzer 3.6 and 4.5 μm full-orbit light curves of WASP-18. *MNRAS*, **428**, 2645–2660.

Mayor, M. and Queloz, D. (1995). A Jupiter-mass companion to a solar-type star. *Nature*, **378**, 355–359.

Mazeh, T. et al (2000). The Spectroscopic Orbit of the Planetary Companion Transiting HD 209458. *ApJ*, **532**(1), L55–L58.

McCullough, P.R. et al (2014). Water vapor in the spectrum of the extrasolar planet hd189733b. i. the transit. *The Astrophysical Journal*, **791**(1), 55.

McKay, C.P., Pollack, J.B. and Courtin, R. (1989). The thermal structure of Titan's atmosphere. *Icarus*, **80**, 23–53.

McKemmish, L.K., Yurchenko, S.N. and Tennyson, J. (2016). ExoMol line lists - XVIII. The high-temperature spectrum of VO. *MNRAS*, **463**, 771–793.

McKemmish, L.K. et al (2019). ExoMol Molecular linelists - XXXIII. The spectrum of Titanium Oxide. *arXiv e-prints*, page arXiv:1905.04587.

Menou, K. (2012). Thermo-resistive Instability of Hot Planetary Atmospheres. *ApJ*, **754**, L9.

Mihalas, D. (1978). *Stellar atmospheres (2nd edition)*. San Francisco, W. H. Freeman and Co.

Mollière, P. et al (2015). Model atmospheres of irradiated exoplanets: The influence of stellar parameters, metallicity, and the c/o ratio. *The Astrophysical Journal*, **813**(1), 47.

Mollière, P. et al (2017). Observing transiting planets with JWST. Prime targets and their synthetic spectral observations. *A&A*, **600**, A10.

Moreno, R. et al (2003). Long-term evolution of CO, CS and HCN in Jupiter after the impacts of comet Shoemaker-Levy 9. *Planet. Space Sci.*, **51**, 591–611.

Moses, J.I. et al (2010). On the abundance of non-cometary HCN on Jupiter. *Faraday Discussions*, **147**, 103.

Moses, J.I. et al (2011). Disequilibrium Carbon, Oxygen, and Nitrogen Chemistry in the Atmospheres of HD 189733b and HD 209458b. *ApJ*, **737**, 15.

Moses, J.I. et al (2013). Chemical consequences of the c/o ratio on hot jupiters: Examples from wasp-12b, corot-2b, xo-1b, and hd 189733b. *The Astrophysical Journal*, **763**(1), 25.

Nikolov, N. et al (2014). Hubble Space Telescope hot Jupiter transmission spectral survey: a detection of Na and strong optical absorption in HAT-P-1b. *MNRAS*, **437**, 46–66.

Nugroho, S.K. et al (2017). High-resolution Spectroscopic Detection of TiO and a Stratosphere in the Day-side of WASP-33b. *AJ*, **154**, 221.

Nymeyer, S. et al (2011). Spitzer Secondary Eclipses of WASP-18b. *ApJ*, **742**, 35.

Öberg, K.I., Murray-Clay, R. and Bergin, E.A. (2011). The Effects of Snowlines on C/O in Planetary Atmospheres. *Astrophys. J. Lett.*, **743**, L16.

Oreshenko, M. et al (2017). Retrieval Analysis of the Emission Spectrum of WASP-12b: Sensitivity of Outcomes to Prior Assumptions and Implications for Formation History. *ArXiv e-prints*.

Owen, J.E. (2018). Atmospheric Escape and the Evolution of Close-in Exoplanets. *arXiv e-prints*, page arXiv:1807.07609.

Parmentier, V. et al (2018). From thermal dissociation to condensation in the atmospheres of ultra hot Jupiters: WASP-121b in context. *ArXiv e-prints*.

Patrascu, A.T., Yurchenko, S.N. and Tennyson, J. (2015). ExoMol molecular line lists - IX. The spectrum of AlO. *MNRAS*, **449**, 3613–3619.

Pinhas, A. et al (2019). H_2O abundances and cloud properties in ten hot giant exoplanets. *MNRAS*, **482**, 1485–1498.

Piso, A.M.A., Pegues, J. and Öberg, K.I. (2016). The Role of Ice Compositions for Snowlines and the C/N/O Ratios in Active Disks. *Astrophys. J.*, **833**, 203.

Polyansky, O.L. et al (2018). ExoMol molecular line lists XXX: a complete high-accuracy line list for water. *MNRAS*, **480**, 2597–2608.

Rey, M. et al (2016). TheoReTS - An information system for theoretical spectra based on variational predictions from molecular potential energy and dipole moment surfaces. *Journal of Molecular Spectroscopy*, **327**, 138–158.

Richard, C. et al (2012). New section of the HITRAN database: Collision-induced absorption (CIA). *J. Quant. Spectrosc. Radiative Transfer*, **113**, 1276–1285.

Ricker, G.R. et al (2014). Transiting Exoplanet Survey Satellite (TESS). In *Space Telescopes and Instrumentation 2014: Optical, Infrared, and Millimeter Wave*, volume 9143 of *Society of Photo-Optical Instrumentation Engineers (SPIE) Conference Series*, page 914320.

Rivlin, T. et al (2015). ExoMol molecular line lists - X. The spectrum of sodium hydride. *MNRAS*, **451**, 634–638.

Rodler, F. and López-Morales, M. (2014). Feasibility Studies for the Detection of O_2 in an Earth-like Exoplanet. *ApJ*, **781**, 54.

Rodler, F., Kürster, M. and Barnes, J.R. (2013). Detection of CO absorption in the atmosphere of the hot Jupiter HD 189733b. *Mon. Not. R. Astron. Soc.*, **432**, 1980–1988.

Rothman, L.S. et al (1998). The HITRAN Molecular Spectroscopic Database and HAWKS (HITRAN Atmospheric Workstation): 1996 Edition. *J. Quant. Spectrosc. Radiative Transfer*, **60**, 665–710.

Rothman, L.S. et al (2010). HITEMP, the high-temperature molecular spectroscopic database. *JQSRT*, **111**, 2139–2150.

Rothman, L.S. et al (2013). The HITRAN2012 molecular spectroscopic database. *JQSRT*, **130**, 4–50.

Rybicki, G. (1971). A modified feautrier method. *Journal of Quantitative Spectroscopy and Radiative Transfer*, **11**(6), 589 – 595.

Schwarz, H. et al (2015). Evidence against a strong thermal inversion in HD 209458b from high-dispersion spectroscopy. *A&A*, **576**, A111.

Seager, S. (2010). *Exoplanet Atmospheres: Physical Processes*. Princeton University Press.

Seager, S. and Deming, D. (2010). Exoplanet Atmospheres. *ARAA*, **48**, 631–672.

Seager, S. and Sasselov, D.D. (1998). Extrasolar giant planets under strong stellar irradiation. *The Astrophysical Journal Letters*, **502**(2), L157.

Seager, S. et al (2005). On the Dayside Thermal Emission of Hot Jupiters. *APJ*, **632**, 1122–1131.

Sedaghati, E. et al (2017). Detection of titanium oxide in the atmosphere of a hot Jupiter. *Nature*, **549**, 238–241.

Sharp, C.M. and Burrows, A. (2007). Atomic and Molecular Opacities for Brown Dwarf and Giant Planet Atmospheres. *ApJS*, **168**, 140–166.

Sheppard, K.B. et al (2017). Evidence for a Dayside Thermal Inversion and High Metallicity for the Hot Jupiter WASP-18b. *ApJ*, **850**, L32.

Showman, A.P. et al (2009). Atmospheric circulation of hot jupiters: Coupled radiative-dynamical general circulation model simulations of hd 189733b and hd 209458b. *The Astrophysical Journal*, **699**(1), 564.

Shporer, A. et al (2019). TESS Full Orbital Phase Curve of the WASP-18b System. *AJ*, **157**(5), 178.

Sing, D.K. et al (2016). A continuum from clear to cloudy hot-Jupiter exoplanets without primordial water depletion. *Nature*, **529**, 59–62.

Skilling, J. (2004). Nested Sampling. In R. Fischer, R. Preuss, and U. V. Toussaint, editors, *American Institute of Physics Conference Series*, volume 735 of *American Institute of Physics Conference Series*, pages 395–405.

Snellen, I. et al (2011). Exoplanet atmospheres at high spectral resolution: A CRIRES survey of hot-Jupiters. In A. Sozzetti, M. G. Lattanzi, and A. P. Boss, editors, *The Astrophysics of Planetary Systems: Formation, Structure, and Dynamical Evolution*, volume 276 of *IAU Symposium*, pages 208–211.

Snellen, I.A.G. et al (2010). The orbital motion, absolute mass and high-altitude winds of exoplanet HD209458b. *Nature*, **465**, 1049–1051.

Snellen, I.A.G. et al (2017). Detecting Proxima b's Atmosphere with JWST Targeting CO_2 at 15 μm Using a High-pass Spectral Filtering Technique. *AJ*, **154**, 77.

Spiegel, D.S., Silverio, K. and Burrows, A. (2009). Can TiO Explain Thermal Inversions in the Upper Atmospheres of Irradiated Giant Planets? *ApJ*, **699**, 1487–1500.

Stevenson, K.B. et al (2010). Possible thermochemical disequilibrium in the atmosphere of the exoplanet GJ 436b. *Nature*, **464**, 1161–1164.

Stevenson, K.B. et al (2014). Thermal structure of an exoplanet atmosphere from phase-resolved emission spectroscopy. *Science*, **346**, 838–841.

Stevenson, K.B. et al (2017). Spitzer Phase Curve Constraints for WASP-43b at 3.6 and 4.5 μm. *AJ*, **153**, 68.

Sudarsky, D., Burrows, A. and Hubeny, I. (2003). Theoretical Spectra and Atmospheres of Extrasolar Giant Planets. *APJ*, **588**, 1121–1148.

Tamuz, O., Mazeh, T. and Zucker, S. (2005). Correcting systematic effects in a large set of photometric light curves. *Mon. Not. R. Astron. Soc.*, **356**, 1466–1470.

Tennyson, J. et al (2016). The ExoMol database: Molecular line lists for exoplanet and other hot atmospheres. *Journal of Molecular Spectroscopy*, **327**, 73–94.

Toon, O.B. et al (1989). Rapid calculation of radiative heating rates and photodissociation rates in inhomogeneous multiple scattering atmospheres. *J. Geophys. Res.*, **94**, 16287–16301.

Tregloan-Reed, J., Southworth, J. and Tappert, C. (2013). Transits and starspots in the WASP-19 planetary system. *MNRAS*, **428**, 3671–3679.

Triaud, A.H.M.J. et al (2009). The Rossiter-McLaughlin effect of CoRoT-3b and HD 189733b. *Astron. Astrophys.*, **506**, 377–384.

Trotta, R. (2008). Bayes in the sky: Bayesian inference and model selection in cosmology. *Contemporary Physics*, **49**, 71–104.

Vallis, G.K. (2006). *Atmospheric and Oceanic Fluid Dynamics*. Cambridge University Press.

Vaz, L.P.R. and Nordlund, A. (1985). The reflection effect in model stellar atmospheres. I - Grey atmospheres with convection. *A&A*, **147**, 281–299.

Venot, O. et al (2012). A chemical model for the atmosphere of hot Jupiters. *A&A*, **546**, A43.

von Essen, C. et al (2019). An optical transmission spectrum of the ultra-hot Jupiter WASP-33 b. First indication of aluminum oxide in an exoplanet. *A&A*, **622**, A71.

Wakeford, H.R. et al (2016). Marginalizing Instrument Systematics in HST WFC3 Transit Light Curves. *ApJ*, **819**, 10.

Waldmann, I.P. et al (2015). Tau-REx I: A Next Generation Retrieval Code for Exoplanetary Atmospheres. *ApJ*, **802**, 107.

Wilzewski, J.S., Gordon, I.E. and Rothman, L.S. (2015). CO2, H2 and He Line Broadening Coefficients and Pressure Shifts for the HITRAN Database. In *Venus Science Priorities for Laboratory Measurements*, volume 1838 of *LPI Contributions*, page 4001.

Wishart, A.W. (1979). The bound-free photo-detachment cross-section of H-. *MNRAS*, **187**, 59P–61.

Woitke, P. et al (2018). Equilibrium chemistry down to 100 k - impact of silicates and phyllosilicates on the carbon to oxygen ratio. *A&A*, **614**, A1.

Wong, I. et al (2016). 3.6 and 4.5 μm Spitzer Phase Curves of the Highly Irradiated Hot Jupiters WASP-19b and HAT-P-7b. *ApJ*, **823**, 122.

Wong, M.H. et al (2004). Updated Galileo probe mass spectrometer measurements of carbon, oxygen, nitrogen, and sulfur on Jupiter. *Icarus*, **171**, 153–170.

Wyttenbach, A. et al (2015). Spectrally resolved detection of sodium in the atmosphere of HD 189733b with the HARPS spectrograph. *A&A*, **577**, A62.

Yadin, B. et al (2012). ExoMol line lists - I. The rovibrational spectrum of BeH, MgH and CaH in the X $^2\Sigma^+$ state. *MNRAS*, **425**, 34–43.

Yurchenko, S.N., Barber, R.J. and Tennyson, J. (2011). A variationally computed line list for hot NH_3. *MNRAS*, **413**, 1828–1834.

Yurchenko, S.N. et al (2013). Vibrational transition moments of CH_4 from first principles. *Journal of Molecular Spectroscopy*, **291**, 69–76.

Yurchenko, S.N. et al (2016). ExoMol molecular line lists - XIII. The spectrum of CaO. *MNRAS*, **456**, 4524–4532.

Yurchenko, S.N. et al (2017). A hybrid line list for CH_4 and hot methane continuum. *A&A*, **605**, A95.

Yurchenko, S.N., Al-Refaie, A.F. and Tennyson, J. (2018). EXOCROSS: a general program for generating spectra from molecular line lists. *A&A*, **614**, A131.

Zahnle, K. et al (2009). Atmospheric Sulfur Photochemistry on Hot Jupiters. *ApJ*, **701**, L20–L24.

Zhou, Y. et al (2017). A Physical Model-based Correction for Charge Traps in the Hubble Space Telescope's Wide Field Camera 3 Near-IR Detector and Its Applications to Transiting Exoplanets and Brown Dwarfs. *AJ*, **153**, 243.

Appendix A

Computational Methods for Self-consistent Atmospheric Modelling

A.1 Solving the Transfer Equation

In this section we describe how to solve the radiative transfer equation using the Feautrier method. Discretising equation 3.17 for a layer of the atmosphere i, frequency k and angle m results in

$$\frac{\mu_{k,m}^2\ j_{i-1,k,m}}{\Delta\tau_{i-\frac{1}{2},k,m}\Delta\tau_{i,k,m}} - \frac{\mu_{k,m}^2\ j_{i,k,m}}{\Delta\tau_{i,k,m}}\left(\frac{1}{\Delta\tau_{i-\frac{1}{2},k,m}} + \frac{1}{\Delta\tau_{i+\frac{1}{2},k,m}}\right) + \frac{\mu_{k,m}^2\ j_{i+1,k,m}}{\Delta\tau_{i+\frac{1}{2},k,m}\Delta\tau_{i,k,m}} = j_{i,k,m} - S_{i,k,m}, \quad \text{(A.1)}$$

for the transfer equation, with μ being the cosine of the angle. Given the source function from the previous iteration (or taken to be the planck function for the first iteration) we can calculate the values of $j_{i,k,m}$. Then

$$J_{i,k} = \sum_m w_m\ j_{i,k,m}, \quad \text{(A.2)}$$

is the mean intensity of radiation for a layer i and frequency k, the mth angle for some weight function w.

The definitions of $\Delta\tau$ are

$$\Delta\tau_{i\pm\frac{1}{2},k} \equiv \frac{1}{2g}((\kappa_{i\pm1,k}+\sigma_{i\pm1,k})/\rho_{i\pm1}+(\kappa_{i,k}+\sigma_{i,k})/\rho_i)|P_{i\pm1}-P_i| \ , \tag{A.3}$$

$$\Delta\tau_{i,k} \equiv \Delta\tau_{i+\frac{1}{2},k}+\Delta\tau_{i-\frac{1}{2},k} \ , \tag{A.4}$$

which come directly from the definition of $d\tau$ and hydrostatic equilibrium.

A.2 Complete Linearisation

To compute the equations of radiative transfer numerically, all of the major equations need to be discretised, as well as constraints and boundary conditions in section 3.3.3. Doing this for equation 3.9 and the corresponding equation for $g \equiv H_\nu(0)/K_\nu(0)$ gives

$$f_{i,k} = \frac{\sum_m w_m\mu^2 \ j_{m,i,k}}{\sum_m w_m \ j_{m,i,k}} \ , \tag{A.5}$$

$$g_k = \frac{\sum_m w_m\mu \ j_{m,ND,k}}{\sum_m w_m \ j_{m,ND,k}} \ . \tag{A.6}$$

The weights are denoted by w. Discretising equations 3.18 and 3.24 for ND layers (indexed by i) and NF frequencies (indexed by k), numbered from 0 at the bottom of the atmosphere, gives

$$\frac{f_{i-1,k}}{\Delta\tau_{i-\frac{1}{2},k}\Delta\tau_{i,k}}J_{i-1,k} - \frac{f_{i,k}}{\Delta\tau_{i,k}}\left(\frac{1}{\Delta\tau_{i-\frac{1}{2},k}}+\frac{1}{\Delta\tau_{i+\frac{1}{2},k}}\right) J_{i,k} + \frac{f_{i+1,k}}{\Delta\tau_{i+\frac{1}{2},k}\Delta\tau_{i,k}}J_{i+1,k} = \frac{\kappa_{i,k}}{\kappa_{i,k}+\sigma_{i,k}}J_{i,k} - \frac{\kappa_{i,k}}{\kappa_{i,k}+\sigma_{i,k}}B_{i,k}, \tag{A.7}$$

for layers $i = 2,3...ND-1$,

$$\frac{f_{ND-1,k}J_{ND-1,k} - f_{ND,k}J_{ND,k}}{\Delta\tau_{ND-\frac{1}{2},k}} = g_kJ_{ND,k} - H_k^{\text{ext}} + \frac{\Delta\tau_{ND-\frac{1}{2},k}}{2}\left(\frac{\kappa_{ND,k}}{\kappa_{ND,k}+\sigma_{ND,k}}J_{ND,k} - \frac{\kappa_{ND,k}}{\kappa_{ND,k}+\sigma_{ND,k}}B_{ND,k}\right), \tag{A.8}$$

for layer $i = ND$ at the top of the atmosphere and

$$\frac{(f_{1,k}J_{1,k} - f_{2,k}J_{2,k})}{\Delta\tau_{\frac{3}{2},k}} = \frac{1}{2}(B_{1,k} - J_{1,k}) + \frac{1}{3}\frac{B_{1,k} - B_{2,k}}{\Delta\tau_{\frac{3}{2},k}} - \frac{\Delta\tau_{\frac{3}{2},k}}{2}\left(\frac{\kappa_{1,k}}{\kappa_{1,k}+\sigma_{1,k}}J_{1,k} - \frac{\kappa_{1,k}}{\kappa_{1,k}+\sigma_{1,k}}B_{1,k}\right), \quad \text{(A.9)}$$

for the bottom of the atmosphere layer $i = 1$. The equations of radiative equilibrium become

$$\sum_{k=1}^{NF} w_k \kappa_{i,k}(J_{i,k} - B_{i,k}) = 0, \quad \text{(A.10)}$$

$$\sum_{k=1}^{NF} w_k \left(\frac{f_{i,k}J_{i,k} - f_{i+1,k}J_{i+1,k}}{\Delta\tau_{i+\frac{1}{2}}}\right) = \frac{\sigma_R}{4\pi}T_{\text{int}}^4, \quad \text{(A.11)}$$

where the quadrature weights are given by w and the last line is only valid for layers up to $i = ND - 1$. With the additional convective flux these become

$$\sum_{k=1}^{NF} w_k \left(\kappa_{i,k}(J_{i,k} - B_{i,k})\right) + \frac{\rho_i g}{4\pi}\frac{F_{\text{conv},i-\frac{1}{2}} - F_{\text{conv},i+\frac{1}{2}}}{\frac{1}{2}(P_{i-1} - P_{i+1})} = 0, \quad \text{(A.12)}$$

$$\sum_{k=1}^{NF} w_k \left(\frac{f_{i,k}J_{i,k} - f_{i+1,k}J_{i+1,k}}{\Delta\tau_{i+\frac{1}{2}}}\right) + \frac{F_{\text{conv},i+\frac{1}{2}}}{4\pi} = \frac{\sigma_R}{4\pi}T_{\text{int}}^4. \quad \text{(A.13)}$$

The $\Delta\tau$ term is linearised by

$$\frac{d\Delta\tau_{i\pm\frac{1}{2}}}{dT_i} = \frac{\Delta\tau_{i\pm\frac{1}{2}}}{\omega_i + \omega_{i\pm1}}\frac{d\omega_i}{dT_i}, \quad \text{(A.14)}$$

where $\omega_i = (\kappa_i + \sigma_i)/\rho_i$. The κ (and σ) term is linearised by

$$\frac{d\kappa_i}{dT_i} = \frac{\partial\kappa_i}{\partial T_i} + \frac{\partial\kappa_i}{\partial P_i}\frac{dP_i}{dT_i}. \quad \text{(A.15)}$$

For an ideal gas, dP/dT is simply P/T.